Modelling and Experimental Analysis of Low Concentrating Photovoltaic for Use in Building Integrated and Attached Photovoltaic (BIPV/BAPV) Systems

Homan HADAVINIA

This thesis is submitted in partial fulfilment of the requirements of the University for the Award of PhD

Supervised by:

Dr Harjit Singh

College of Engineering, Design and Physical Sciences

Brunel University London

March 2018

Dedicated to

I dedicate this PhD to my mother and father who supported me through all my study. I also like to thank my sisters Mahsa and Mahshid without them I could not finish this work.

Declaration

I Homan Hadavinia hereby certify that I had personally carried out the work presented in this thesis entitled *Modelling and Experimental Analysis of Low Concentrating Photovoltaic for Use in Building Integrated and Attached Photovoltaic (BIPV/BAPV) Systems* except where otherwise indicated and acknowledged. The work presented is original and has been carried out under supervision of my Director of Study Dr Harjit Singh.

Signature …….

Homan Hadavinia

Date …….

Abstract

This thesis studies stationary, low concentration ratio, non-imaging reflective concentrators to generate power at a lower cost for applications in Building-Integrated Photovoltaics (BIPV). Stationary solar energy concentrators are a promising option for decreasing the price of photovoltaic electricity in BIPV.

Two geometrically equivalent non-imaging concentrators parabolic V-trough and CPC are investigated routes to increasing the efficiency of solar cells employed in BIPVs. In this work V-trough and CPCs concentrators were modelled in COMSOL at various geometries and configurations. Each configuration was separately studied at various light angles of incidence. In addition, the effect of CPC truncation and V-trough side wall angle for BIPV implementation was also studied. The results showed big increases in angle of acceptance, reductions in height profile and V-trough-like characteristics past the original CPC design acceptance angles, with consequence in reducing material consumption for the manufacture of CPC and therefore reduction in the cost of the system.

For ray tracing analysis a variety of direct and iterative solvers were tested and the generalized minimal residual method (GMRES) was used for 2D and 3D analysis of concentrators. A drop of performance was observed for both concentrators at increased light incidence angles; however, V-trough showed a better ability to dampen the loss as incidence angle increased. In terms of net concentration ratio, a truncated CPC at equal height shows a net concentration ratio of $C_{opt} = 2.70$ whilst V-trough hovered around $C_{rnet} = 2.37 - 2.70$ resulting in a net performance increase of 31% for CPC adoption. Results showed V-trough having lower concentration ratios but better performance at high angles of incidence compared to CPCs. Truncated CPCs showed equal optical efficiency to their full height parents but a lower concentration ratio due to a reduction in inlet aperture size.

The modelled 50mm CPC concentrator designed for BIPV shows a greater overall concentrating performance, with significantly improved concentration up to the acceptance half angle, a small loss compared to the V-trough from the acceptance half angle to around 30° light incidence, and again an improvement over the V-trough from ~30° onwards. All truncated CPCs also show V-trough-like behaviour past their acceptance angles, making them suitable for BIPV incorporation. On the other hand, the V-trough concentrator showed better uniformity of flux distribution, this was especially pronounced at lower light angles of incidence.

The experimental investigation was carried out on two candidates compound parabolic concentrator and a V-trough reflector on the optical and energy conversion characteristics. Two prototype LCPV systems based on dimensions of the selected concentrators have been manufactured and placed through outdoor testing conditions. The aim was to measure the solar radiation incident at the aperture and the PV cell surface using a pyranometer for times 10:00 to 14:00 equivalent to light incidence angles of -30° to +30°. The analysis of the experimental data showed good correlation with ray tracing simulations, showing similar behaviour with changing light angles of incidence. Experimental analysis showed that CPC had an overall 2.4% higher power output compared to V-trough concentrator. This agreed with the ray tracing studies. Although this was lower than the difference predicted by modelling analysis, this was put down to the non-uniformity of the concentrated light on the CPC absorber area and differences between the ideal and manufactured parabolic reflector. Based on these complexities some future work was recommended.

Acknowledgments

This dissertation is the result of four years of hard work. First and most of all I would like to thank my Director of Study Dr Harjit Singh who supervised this project. He continuously guided me through my PhD, the queries that I came across and always being available when I needed help. I would also like to thank Professor Hari Upadhyaya for his guidance with many aspects of Dye Sensitized Solar Cell.

I would like to thank Mr Costas Xanthos for helping me in various testing setups and advice with regards to all aspects of fluid mechanics and thermal dynamics apparatus, Paul Yates for assisting me in CNC fabrication of the V-trough and CPC concentrators.

Special thanks to Ms Nastaran Faridamin for helping me in carrying out the experimental testing.

I would also like to thank the library staff at Brunel University for helping me to find the information I needed and how to reference my work accordingly.

Finally, I enjoyed working and having good time with my friends, Reza, Amin and Parvaneh for supporting me throughout my PhD.

Homan Hadavinia (**MSc, BEng**)

Brunel University
05 March 2018

Table of Contents

List of Figures

List of Tables

Chapter 1 Introduction

1.1. Motivation and Scope

Humanity is facing the biggest challenge in its history and that is to find a sustainable energy sources for running the economy. This challenge is growing bigger as the world population is rising and fossil fuel resources are depleting. In addition, the use of fossil fuels leads to CO_2 and other greenhouse gas emissions, complicating the situation and making the world's energy supply a bigger issue. The nuclear power option is also facing resistance from environmentalists due to production of hazardous waste. In view of these facts, and the current state of technology, renewable energy sources and energy efficiency are the only viable options to satisfy the global energy demand for a sustainable economy. As a result, large scale implementation of solar and wind energy in many countries are underway. Many countries around the globe have embarked on large scale renewable energy projects and newly installed renewable power capacity set new records in 2016, with 161 GW added, increasing the global total (not including hydro) by almost 9% relative to 2015 to 921GW [1]. The bulk of this is from solar 307.8 GW (33.4%) and wind energy 487 GW (~52.9%). Solar photovoltaic (PV) accounted for approximately 303 GW and concentrating solar thermal power technologies about 4.8 GW. In 2017 the installed capacity for solar PV grew to 400 GW and solar thermal to 5 GW. This is projected to rise to 687 GW for PV, reaching almost 40% of installed renewable share and 8 GW for solar thermal.

Investment in renewable energy is growing year on year. This trend is shown in Figure 1.1 with a breakdown of total renewable investment into its four subcategories: wind, solar, biofuel and others. Wind and solar represent the bulk of the renewable investment.

In solar energy sector photovoltaic is the most popular and favoured technology (>98%) as it directly converts the solar energy to electricity without the need of intermediary technology such as steam powerplants. Solar PVs can be used at small scales to power households eliminating the power transmission loss of up to 15% and produce electricity at the point it is generated, as well as large scales to meet commercial and industrial demands. An emerging market for electric vehicles also presents an opportunity to replace one of the biggest sources of CO_2 emissions. Almost half of all EU carbon emissions are generated in the built

environment, and the deployment of renewable energy, specifically PV, in these areas has a great potential to both generation and saving of energy.

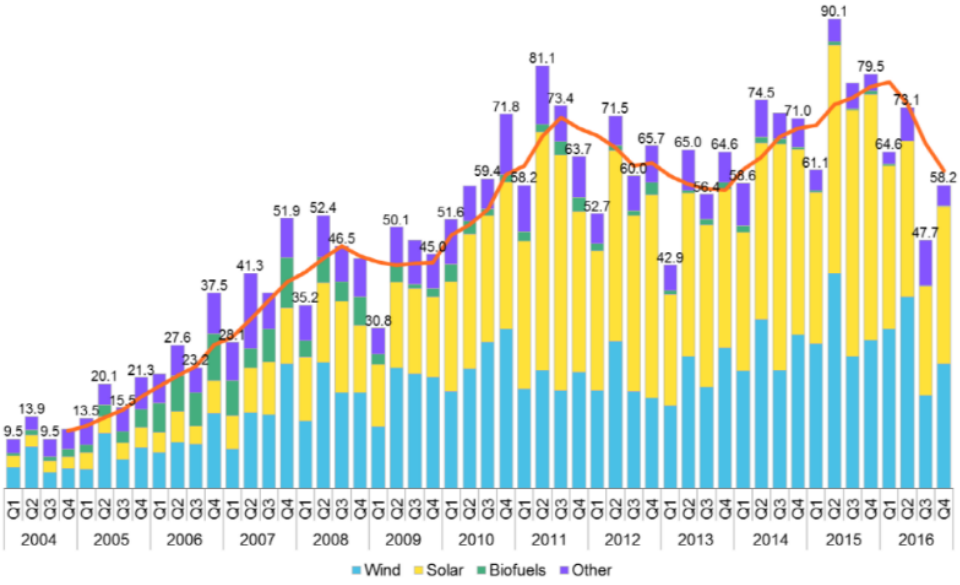

Figure 1.1. Investment in clean energy by sector 2004-2016 (BNEF 2017)

The cost of crystalline silicon and the thin-film PV modules, with both offering low cost per Watt-peak as shown in Figure 1.2 has been reduced to historical lows with a trend set to continue.

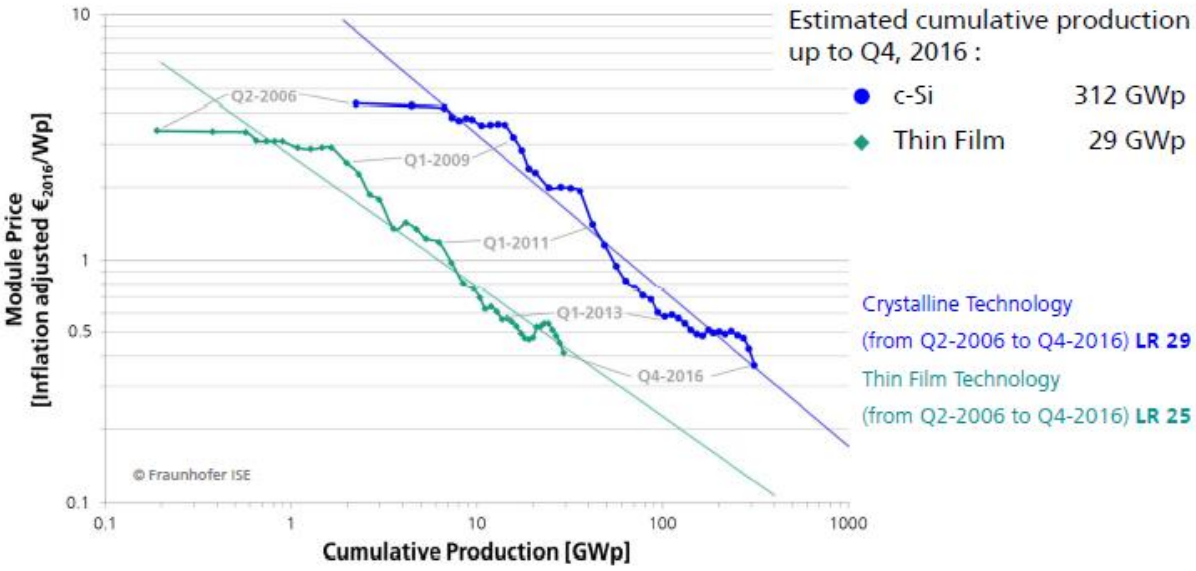

Figure 1.2. Cumulative production of c-Si and thin film up to Q4. 2016 [2].

This cost can be decreased further through improvements to the PV efficiency. PV cell efficiency can be improved by increasing the incident solar flux using concentrating optics [3]. Even high concentrating (500x) multi-junction PVs have been shown to require an equal sized

power generation area to power an apartment as reported by Akinyele et al. [4]. One way to solve the problem of space constraint is unlocking the vertical surfaces of medium rise apartments and high-rise buildings through the implementation of Building Integrated Photovoltaics (BIPVs). Concentrators are used to focus light from a large aperture area onto a solar cell, increasing the exposure of the solar cell to higher solar irradiance. Figure 1.3 a typical standard PV and concentrator PV (CPV) is demonstrated.

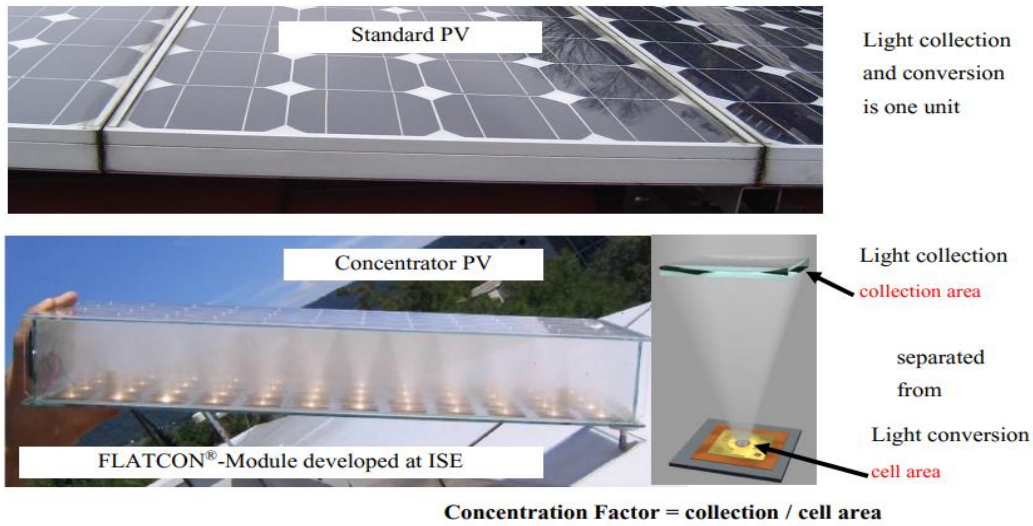

Figure 1.3. Standard PV and concentrator PV [5].

Building-integrated photovoltaics (**BIPV**) are photovoltaic materials that are used to replace conventional building materials in parts of the building envelope such as the roof, skylights, or facades. They are increasingly being incorporated into the construction of new buildings as a principal or ancillary source of electrical power, although existing buildings may be retrofitted with similar technology. The advantage of integrated photovoltaics with respect to common non-integrated systems is the initial cost saving from reducing building materials consumption and labour. At present these benefits make BIPV one of the fastest growing segments of the photovoltaic industry. The term building-applied photovoltaics (**BAPV**) is sometimes used to refer to photovoltaics that are a retrofit – integrated into the building after construction is complete. Most building-integrated installations are actually BAPV. Classification of BIPVs is shown in Figure 1.4.

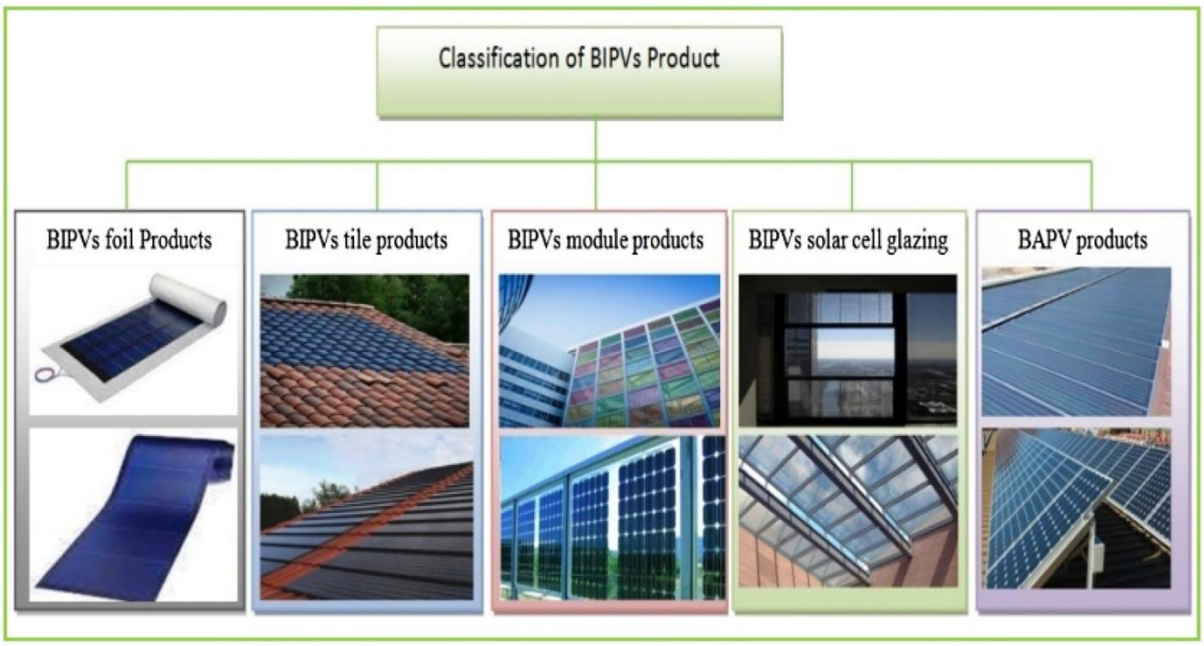

Figure 1.4. Classification of BIPV and BAPV [6].

Advances in computer power and improvements in optical modelling using computer software have grown substantially. Early optical models of compound parabolic concentrators (CPCs) were based on using multiple programs for ray-tracing analysis. Ray tracing is used for estimation of the amount and distribution of concentrated solar energy that the receiver is experiencing. At present, there are many commercial integrated computer aided design (CAD)/simulation software for optical modelling capable of building the geometry, adding the light source and analysing the collectors' behaviours by the ray-tracing method. These software are broadly classified to three categories: sequential ray tracing, non-sequential ray-tracing and finite-difference time domain (FDTD) simulation types [7].

Sequential ray-tracing interacts with the light from a user-defined source by propagating the light through each surface in the optical system one at a time in a pre-defined order. These types of programs are typically used to model optical behaviour of cameras, endoscopes, microscopes, telescopes etc. Examples of such programs are CODE V and ASAP. Non-sequential programs allow the ray interaction with any surface multiple times without any predetermined sequence. These type of programs are typically used to model imaging systems, light pipes, backlights. Examples of such programs are COMSOL, FRED, Light Tools, Optics Lab, OSLO, TracePro and ZEMAX [7].

Optical simulation software had been reportedly used to simulate the performance of nonimaging optics of CPCs [8, 9, 10]. It is known that by increasing geometric concentration ratio of a CPC, the height increases greatly. As a result, more materials are required for making

the large reflector while at the same time optical performance deteriorate. Xie et al. [11, 12] studied CPC truncation position to improve the trade-off between cost reduction and optical performance using optical simulation software and the truncated CPC with lowest truncation position is designed by eliminating multiple reflections. The performance is investigated by the material consumption assessment. They managed to design a CPC with considerable reduction in material consumption for reflectors while keeping the optical performance including uniformity and optical efficiency the same [11] .

In this thesis COMSOL software is used for ray tracing of various CPCs and V-trough collectors and their truncated configurations.

1.2. Motivation

Photovoltaics (PV) are increasingly used as an integral part of the building's façade, windows, walls, and roofs. Concentration of the light into a smaller area of PV, gives the potential to reduce the electricity production cost for building integrated photovoltaic (BIPV) products with a potential to reduce the cost of the PV system. As light is concentrated, the cost-benefit analysis of higher efficiency cells shifts, making them more economically viable and ultimately permitting a higher per-unit-area power output. Both CPCs and V-trough concentrators perform well for stationary and passive tracking systems at concentration ratios up to 10x making them particularly suitable for use BIPVs.

The use of Concentrating BIPVs would also lead to additional useful outputs such as thermal energy. Something that would be considered waste output in industrial scale electricity production and require more investment and energy to cool, can become a source of hot water or central heating due to close proximity to point of consumption.

1.3. Aim and Objectives

1.3.1. Aim of the study

The aim of this study is to investigate the efficient use of stationary low concentrated nonimaging concentrators in building integrated photovoltaic (BIPV) to improve the efficiency and reduce the cost of the system.

This thesis will outline recent developments and suggested designs in CPC and V-trough concentrators and provide design parameters for the use of these concentrators for building integrated applications of PV systems.

1.3.2. Specific objectives

The investigated concentrators are parabolic compound (CPC) and V-trough concentrators with low cost reflector materials such as aluminium or steel. The following are the main objectives of this study:

1. Mapping the state-of-the-art of nonimaging collectors and discussing various novel applications of collectors for integration in BIPVs systems.
2. To investigate the nature of the solar resources, appreciate the performance and limitations of solar conversion technologies.
3. Improvement of Dye Sensitized Solar Cell (DSSC) performance and development of modelling and characterisation techniques.
4. Analysis of local irradiance distribution perturbations due to concentrators over a wide range of light incident angles and concentration factors.
5. Develop reliable models using COMSOL software ray-tracing algorithms and investigate the optical efficiency of the selected solar concentrators to facilitate feasibility studies on new concentrator design for application in BIPV technologies.
6. Improvement of optical performance of CPC and V-trough concentrators by modifying the geometry and topology of the concentrators for BIPV applications.
7. Model validation by getting real data from experiments on CPC and V-trough.

1.4. Thesis layout

A comprehensive investigation of the modelling and experimental analysis of low concentrating photovoltaic for use in building integrated and attached photovoltaic (BIPV/BAPV) systems are conveyed in this thesis in seven chapters as described below:

Chapter 1: A brief background, motivation and problem definition of this research, aims and objectives and importance of this research are highlighted.

Chapter 2: An in-depth literature review of PVs and their operation and the principles of DSSCs including the existing research that has been carried out on PV systems and the details of various concentrating PV/T systems. Concentrating systems are presented and categorised into low, medium and high concentrating systems. Finally, the principles of tracking and their modes of operation are presented.

Chapter 3: The fabrication of Dye-Sensitized Solar Cells (DSSC) is discussed. A new modified black-dye is used to fabricate multiple configurations of DSSCs, a

second batch is fabricated simultaneously using the same process with N719 dyes for control and comparison purposes.

Chapter 4: A summary of the recent developments and designs in CPC and V-trough are presented and mathematical models for optical performance of CPC and V-trough are discussed. The principles of ray optics, including a comparison to wave optics are given. The optical modelling performed on various V-trough and CPC designs through ray-tracing modelling is presented. A novel method is implemented to allow the COMSOL Multiphysics solver to automatically generate and update both geometries and boundary conditions and model them. Finally, the concentrator efficiency limits are calculated using Carnot, Landsberg and hybrid models.

Chapter 5: This chapter explains the steps from concept through fabrication to experimental testing of the CPC and V-trough concentrators. The testing conditions are described including the impact of diffuse radiation and the values for the UK.

Chapter 6: Presents the results for Chapters 3 through 5. That is, the results of the Dye Sensitized Solar Cell fabrication, V-trough and CPC modelling results and finally the experimental V-trough and CPC results. A cost study is performed for the CPVs and the effect of diffuse radiation is considered.

Chapter 7: Lastly, a summary of the findings is presented and the concluding remarks of this research are summarised. Recommendations for future works to explore further the possibility of using stationary concentrator in BIVP has been made.

Chapter 2 Literature Review

Solar energy is a promising source of supplying the energy demands. The annual potential of solar energy is 1575–49837 exajoules (EJ), which is 1.8–58 times over the estimated future world energy consumption of 860 EJ in 2040 [13].

This PhD research covers three main areas i.e. Dye-Sensitized Solar Cells (DSSC), modelling of low concentrating V-trough and compound parabolic concentrators (CPC) and manufacturing and testing of a Concentrated Photovoltaic/Thermal (CPVT) system. As a result, in this chapter the fundamental of working principles of photovoltaics are discussed. Then the third-generation solar cells DSSC is briefly reviewed. Finally concentrated photovoltaic thermal (CPVT) solar collectors' technologies have been reviewed. Many researchers have explored CPVTs' high efficiency, and multi-output nature through many innovative designs. The review covers CPVTs' characteristics and design considerations in addition to an overview of the principals and technological advances in the solar thermal collectors, solar concentrator optics, concentrated solar technologies, and application areas which are required in that construction of various CPVTs.

2.1. Photovoltaics

Photovoltaics are a category of power generation which convert light into electricity directly using solar cells. In practice, this is achieved by using semiconducting materials which exhibit photovoltaic effect. First observed by French physicist Alexandre-Edmond Becquerel in 1839, Becquerel noted the photovoltaic effect of silver chloride immersed in an iodide solution and connected to platinum electrodes [14]. Photovoltaic effect is the excitation of light from the valence band to the conduction band of the material. In semiconductors, electrons are confined to a finite number of bands of energy meaning there is a single energy gap between the valence and conductions bands called the *band gap*. Figure 2.1 illustrates the band gap principle, in order for the jump from the valence band to the conduction band to occur, an electron needs the minimum required energy (E_g) by absorbing a photon (light) or phonon (heat). This transfer of electrons leaves behind a hole which is sometimes considered a positively charged particle with the ability to move around.

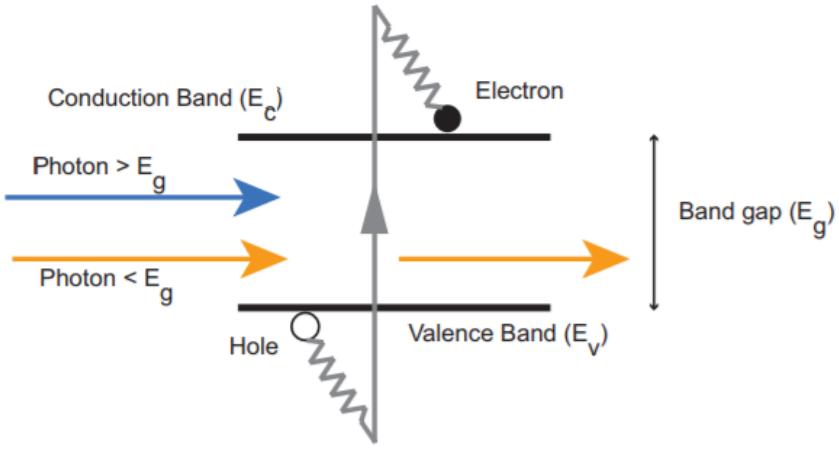

Figure 2.1. Electron band gap promotion.

2.1.1. Semiconductor Materials

Semiconductor materials come from different groups in the periodic table but share similarities. The atoms in a semiconductor either come from group IV, combined group III and group V (called III-V semiconductors) or combined group II and group VI (II-VI semiconductors). Silicon is the mused use semiconductor, a group IV atom. Figure 2.2 shows a relevant section of the periodic table with semiconductor atoms highlighted. Group IV atoms have four valence electrons, allowing them to bond to themselves creating single element structures. An example is shown in Figure 2.3 where silicon atoms bond together creating a lattice structure. Each atom forms covalent bonds with four adjacent atoms, sharing electron pairs to create an overall stable electronic configuration whilst being overall neutrally charged.

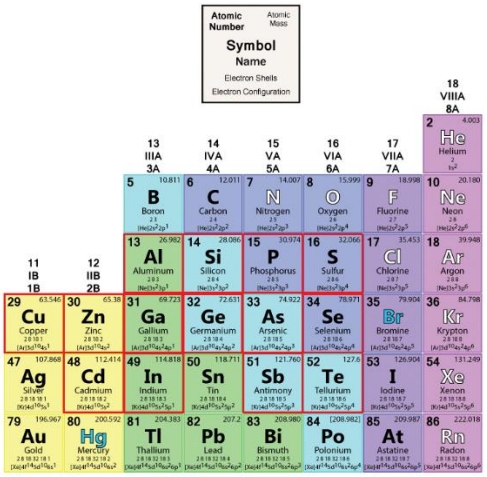

Figure 2.2. A semiconductor can be either of a single element, such as Si or Ge, a compound, such as GaAs, InP or CdTe, or an alloy mixture.

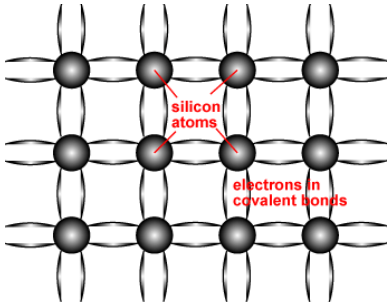

Figure 2.3. Silicon crystal lattice.

Silicon is the most widely used semiconductor used in fabrication for a few reasons:

- It is extremely abundant, forming 28% of the Earth's crust available as silica and quartz.
- Silicon wafer manufacturing techniques have become extremely economical.
- Silicon's energy band gap of 1.12eV at 0K is stable when compared to other group IV elements such as Germanium reducing current leakage.
- Crystalline structure of Silicon is 34% densely packed allowing easy substitution of impurities leading to high doping concentration potential ~10^{23} atoms/cm^3.
- Silicon oxide is extremely stable, beneficial in microelectronics as an electric insulator [15].

Silicon dioxide, also known as silica, with the chemical formula SiO_2 as shown in Figure 2.4, most commonly found in nature as quartz and in various living organisms.

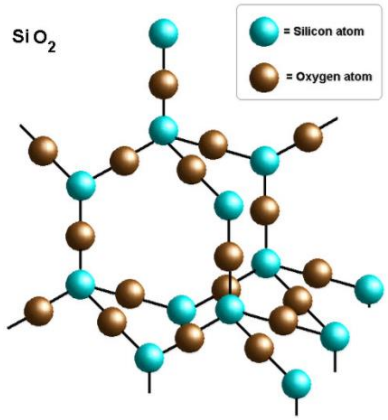

Figure 2.4. Silicon Dioxide structure.

2.1.2. Why semiconductors

One question that arises upon considering the principle operation of solar cells is "why use semiconductors". By definition, the lower the bandgap of the material used, the more photon-excitations occur. It follows that conductors have a lower bandgap than semiconductors; in

fact, these bands can overlap each other. Figure 2.5 shows the relative bandgaps of conductors, semiconductors and insulators.

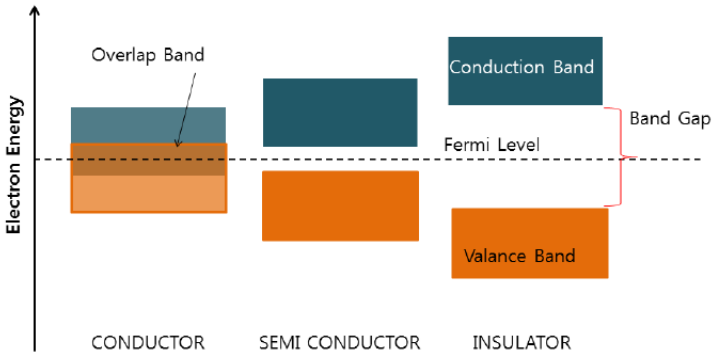

Figure 2.5. Bandgaps of Conductors, semiconductors and insulators.

It is important to note that free electrons do not necessarily mean flow of current. A current is formed when free electrons move in a specific direction, whereas in conductors, electrons move randomly creating a net flow of 0. It is the presence of the PN junction in semiconductors, blocking the mixing of the holes and electrons of either side of the junction that creates an electric field. This electric field creates a net current flow in one direction.

2.1.3. Light properties

Light is radiation within parts of the electromagnetic radiation spectrum which is divided into several groups including radio, microwaves, infrared, the visible light, ultraviolet, x-rays and gamma rays depending on the wavelength ranging from $10^{-16}\ m$ to $10^{8}\ m$. The frequency and wavelength have an inverse relationship (Eq. 2.1) meaning longer wavelength radiation has lower frequency and vice versa.

$$\lambda = \frac{c}{v} \tag{2.1}$$

Where:

- λ is the wavelength (m)
- v is the frequency of the wave (Hz)
- c is the speed of the light (m/s)

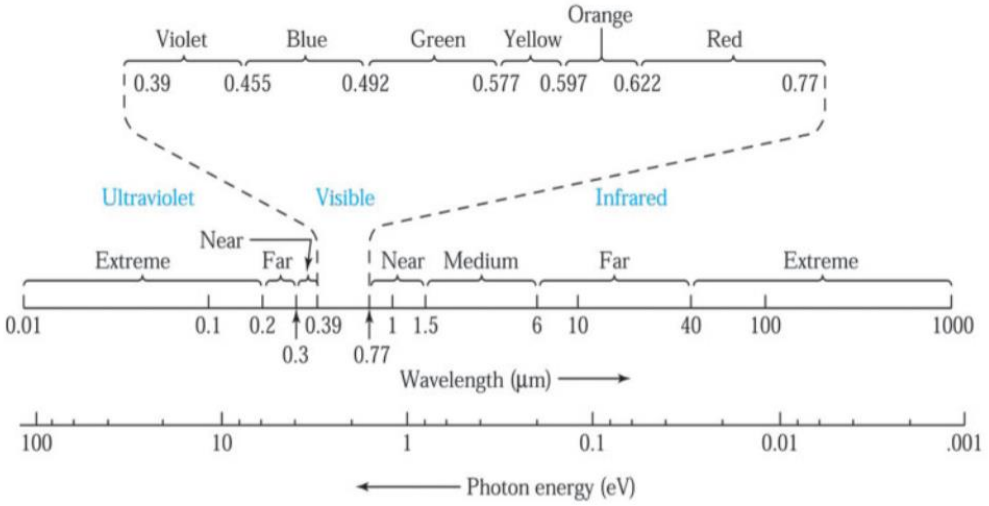

Figure 2.6. Electromagnetic spectrum *[16, 17]*.

The electromagnetic spectrum band is shown in Figure 2.6. Visible light, which is a small band that human eye can detect within the radiation spectrum ranges between 300 nm to 780 nm from ultraviolet with the shortest wavelength to infrared with the longest wavelength [17].

Electromagnetic radiation is a stream of the tiniest massless (zero rest mass) particles called *photons* which move at the speed of light and exhibit wave/particle duality [18]. Each photon carries an energy called photon energy, which is inversely proportional to its wavelength as shown:

$$E = \frac{hc}{\lambda} \tag{2.2}$$

Where E is the energy of the photon (J)

λ is the wavelength (m)

h is the Planck constant= 6.62606896(33) $\times 10^{-34}$ (J·s)

and c is the speed of light= 299,792,458 (m/s)

In addition, the electronvolt (eV) is a common unit that is used for the measurement of photon energy instead of joule (J). An electronvolt is the energy required to raise an electron by 1 volt, thus a photon with an energy of 1 eV = 1.602 × 10^{-19} J.

By multiplying *h* and *c* to *1.99 × 10^{-25}* Joules-m, or *1.24 eV-μm*. After re-writing the Eq. (2.2), we get the often-cited equation:

$$E(eV) = \frac{1.24}{\lambda(\mu m)} \tag{2.3}$$

2.2. Solar Cell Operation

As mentioned previously, semiconductors act as insulators at low temperatures and conduct electricity at higher temperatures. This occurs because at higher temperatures, the increased electron energy allows it to break free from the covalent bonds and travel freely. When electrons gain enough energy to break their covalent bonds, they are called *"free electrons"* and are in a *high energy state* and together with the hole constitute the two types of charge carriers. Conversely, electrons covalently bound between the Si atoms are in a *low energy state*. It is this difference between the high and low energy state that determines the bandgap: the minimum energy required for the creation of an electron-hold (e-h) pair. Shizuo Fujita [19] presented a review of wide-bandgap semiconductor materials and the issues which need to be addressed before reaching "full bloom". Table 2.1 presents the physical properties of some common semiconductors and diamond for reference. Figure 2.7 shows the relationship between the bandgap and bond length of compound semiconductors of interest.

Table 2.1. Basic physical properties of various wide-bandgap semiconductor single crystals.

	Si	***GaAs***	***ZnO***	***Diamond***
Bandgap (eV)	1.12	1.4	3.4	5.6
Band Structure	Indirect transition	Direct transition	Direct transition	
Electron mobility ($cm^2V^{-1}s^{-1}$)	1,450	8,500	300	4,000
Hole mobility ($cm^2V^{-1}s^{-1}$)	450	400		3,800
Breakdown electric field (MV/cm)	0.3	0.4		10
Thermal conductivity (W/cmK)	1.3	0.54	~1	20
Electron saturation velocity (cm/s)	1×10^7	2×10^7	3×10^7	3×10^7
Relative permittivity	11.7	12.9	~8	5.7

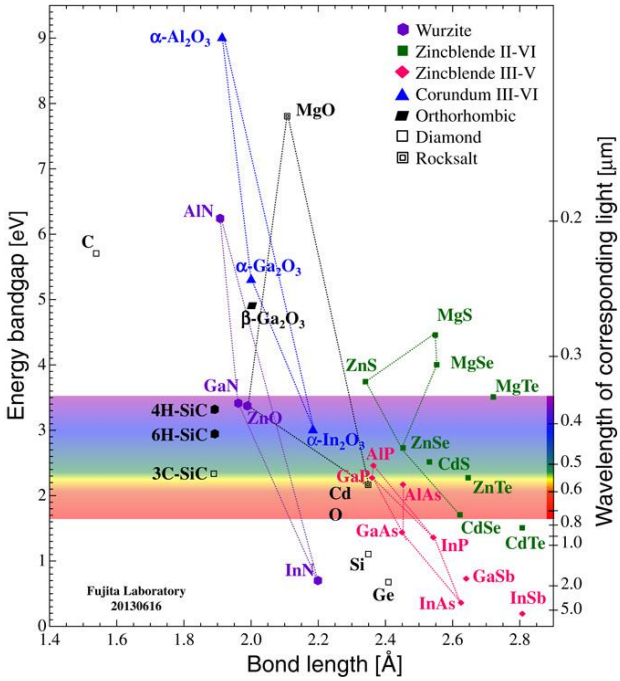

Figure 2.7. Relationship between energy bandgap and bond length for various compound semiconductors promising for practical applications. [19]

2.2.1. Intrinsic carrier concentration

At thermal equilibrium and without any excitations caused by light, pressure or an electrical field, continual thermal agitation leads to the excitation of electrons from the valence band to the conduction band, giving rise to a pair of electron hole carriers in both bands. Electrons and holes participating in conduction are called *intrinsic carriers* and their concentration is based on the bandgap and temperature of the material. The term *intrinsic* refers to the fact that these carriers are a result of the natural unaltered material with inconsequential amounts of impurities.

It is logical that at higher temperatures, increased thermal excitation leading to a higher intrinsic carrier concentration and conversely, a larger bandgap requires a bigger *jump*, hence energy meaning larger bandgaps lower intrinsic carrier concentration. This intrinsic carrier concentration, n_i is one of the biggest determinants of solar cell efficiencies.

To obtain the electron density, i.e. the normalized number of electrons (per unit volume), we get the product of the *density of states* $N(E)$ by the *Fermi-Dirac probability distribution* $F(E)$. This is done incrementally in steps dE and integrated from the bottom of the conduction band E_c to the top of the conduction band E_{top} giving:

$$n = \int_{E_c}^{E_{top}} n(E)dE = \int_{E_c}^{E_{top}} N(E)\,F(E)\,dE \qquad (2.4)$$

$N(E)$, the *density of states* is the number of allowed energy states per unit energy per unit volume ($states/eV/cm^{-3}$). It is described by:

$$N(E) = 4\pi \left(\frac{2m_n}{h^2}\right)^{\frac{3}{2}} \sqrt{E} \qquad (2.5)$$

Where m_n is the density-of-states effective mass of electrons.

The effective mass of an electron is usually given as a multiple of the *rest mass of an electron* having the value $9.11 \times 10^{-31}\ kg$. Remarkably, the *effective mass* can become *negative* when the band curves downwards. The result is that these electrons behave as though they have positive charge both electrically and magnetically describing the behaviour of valence band holes found in semiconductors [20]. Table 2.2 presents the electron and hole density-of-states effective mass of some common semiconductors [21, 17, 22].

Table 2.2. Density-of-states effective mass of electron (m_n) and holes in selected semiconductors [21, 17, 22].

Group	Material	Electron	Hole
IV	Si (4 K)	1.06	0.59
	Si (300 K)	1.09	1.15
	Ge	0.55	0.37
III-V	GaAs	0.067	0.45
	InSb	0.013	0.6
II-VI	ZnO	0.29	1.21
	ZnSe	0.17	1.44

$F(E)$ is the probability that an electron occupies an energy state (range) E. It is given by the Fermi-Dirac distribution [23]:

$$F(E) = \frac{1}{1+e^{\left(\frac{E-E_F}{kT}\right)}} \qquad (2.6)$$

Where *k* is the Boltzmann constant equal to $8.6173303 \times 10^{-5}\ eV \cdot K^{-1}$,
T is the absolute temperature (K),
E_F is the fermi-level, that is the state at which an electron has exactly $\frac{1}{2}$ chance of occupying.

Figure 2.8 shows a visual plot of the fermi-distribution (eq. 2.6) vs. $E - E_F$ at various temperatures through a simple MATLAB script:

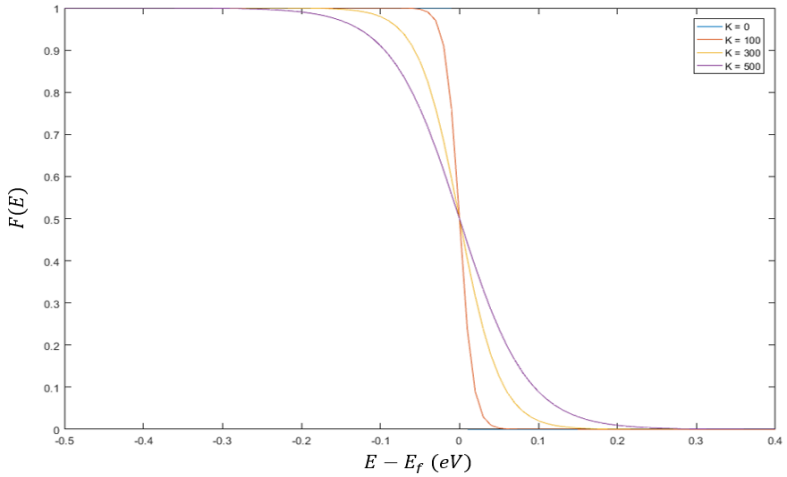

Figure 2.8. Fermi-Dirac distribution F(E) vs. (E-E_F)

It can be seen from Figure 2.8 that $F(E)$ is symmetrical around the fermi-level E_F (0.5). The location of E_F is important in determining the electrical behaviour of the material.

In *conductors*, E_F is located within a delocalized band and there are a large number of states active and ready to carry current. Conversely in *insulators* E_F lies at the centre of a large band gap, a long distance from any states able to support charge carriers. Finally, in *intrinsic semiconductors*, E_F is still in a bandgap but the distance to the conductor and valence band is short enough that a small number of thermally excited carriers can exist.

Figure 2.9 visualizes this concept by showing the different bands of metals (conductors), semiconductors and insulators. The top bands are the conduction bands and the bottom bands are the valence bands. The height is the energy level and the width represents the density of available states. The bands are shaded based on the Fermi-Dirac probability distribution and it can be seen that in insulators the conduction band is purely white meaning there are no electrons filling the conduction band states. On the other hand, the metals have a band intersecting E_F and are able to intrinsically carry current. Semiconductors lie between conductors and insulators: an intrinsic semiconductor has a small number of conduction states filled (small black shading at the bottom of the conduction band). Doping, a concept explained more thoroughly in section 2.2.2 shifts the bands up or down (it does not move E_F) which directly affects the number of electrons occupying the conduction band and holes occupying the valence band. That is *n*-type semiconductors move the conduction band closer to E_F and *p*-type semiconductors move the valence band closer to E_F.

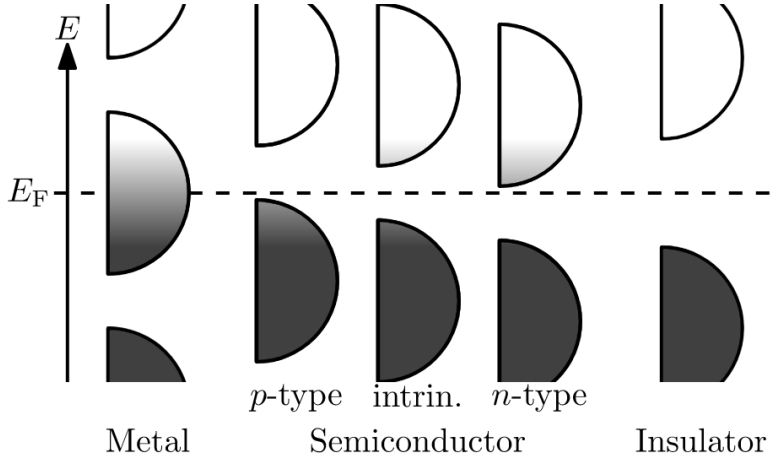

Figure 2.9. Relative band positions of metals, semiconductors and insulators and their Fermi levels. Shading represents Fermi-Dirac distribution with black being all states fill and white meaning no states filled.

In 1991, Sproul and Green [24] attempted to improve the values of intrinsic carrier concentration recorded between 275-375 K from measurements of injected minority carrier flows in narrow base *p-n* junction diodes. Sproul found the resulting n_i to be $1.00 \times 10^{10}\ cm^{-3}$ with a one standard deviation uncertainty of 3%. This was a corroboration of earlier work in 1990 by Green [21] which measured $n_i = 1.08 \times 10^{10}\ cm^{-3}$ and Wasserab [25] at $1.02 \times 10^{10}\ cm^{-3}$. This was a major revision, with the common value being used at the time at $n_i = 1.45 \times 10^{10}\ cm^{-3}$ [17, 26, 27, 28].

It was reassessed again by Altermatt et al. [29] who measured the intrinsic carrier concentration of silicon at $9.65 \times 10^{9}\ cm^{-3}$ at 300K (~room temperature).

The relation of the intrinsic carrier concentration of silicon as a function of temperature was developed in 1993 by Misiakos [30] by finding the best fit of accurate experimental results carried out using a technique based on the capacitance measurement of a p^+-i-n^+ diode biased in high injection. Misiakos found $n_i = (9.7 \pm 0.1) \times 10^{9} cm^{-3}$ at 300K agreeing closely with the work of Altermatt et al. [29] leading to Eq. (2.7) and plotted in Figure 2.10.

$$n_i(T) = 5.29 \times 10^{19} \left(\frac{T}{300}\right)^{2.54} e^{\left(\frac{-6726}{T}\right)} \qquad (2.7)$$

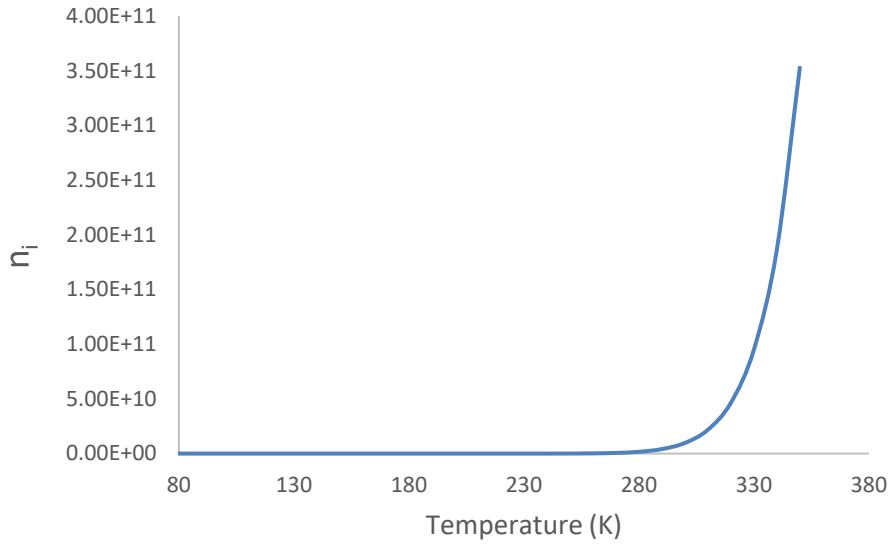

Figure 2.10. Intrinsic carrier concentration for silicon at T = 80 - 350K.

Whilst semiconductors show conducting properties at room temperature, the number of charge carriers are still relatively small. For this reason, and to control the flow of holes and electrons, impurities are introduced to the material by *doping*.

2.2.2. Doping

Doping a semiconductor with impurities allows us to control the number of electrons and holes. For this to happen, a small concentration of a *doping* material is introduced to the crystal lattice structure. Taking silicon, a group IV material, as an example, each silicon atom has 4 outer electrons which share covalent bonds with 4 neighbouring silicon atoms creating a stable configuration with all outer shells filled. If on the other hand a silicon atom was replaced with a group V element, four of the five outer electrons would bond with neighbouring silicon as before, but there would be a spare electron left. This fifth electron has a weak binding energy and can be ionized at low temperatures to becoming a charge carrier. This electron is considered to be *donated* to the conduction band and the group V atom is called a ***donor*** atom. This creates what is called an *n*-type semiconductor due to the overall net availability of negative charge carriers (electrons). An example of a donor atom is arsenic and the structure is shown in Figure 2.11 (a) [31].

If a group IV atom such as silicon is *doped* with a group III element, then only three valence electrons exist. Therefore, to form bonds with all four neighbouring silicon atoms, an extra electron needs to be *accepted* from the lattice, creating a *hole*. This *doping* material is called an ***acceptor*** and it creates an overall excess of *holes* creating a *p*-type semiconductor. An

example of a group III atom typically bonded with silicon is boron, and Figure 2.11. (a) n-type Si with donor (arsenic) and (b) p-type Si with acceptor (boron). Figure 2.11(b) shows the structure of a *boron-doped* silicon structure [31].

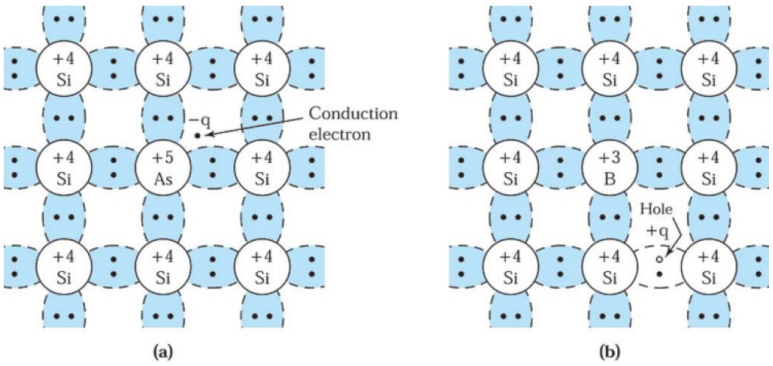

Figure 2.11. (a) n-type Si with donor (arsenic) and (b) p-type Si with acceptor (boron). [31]

Doped semiconductors are called *extrinsic semiconductors* due to the external changes made to their natural form and behaviour.

To understand the operation of solar cells, one needs to consider the workings of p-n junctions.

2.2.3. P-N Junctions

P-n junctions are the building blocks of many semiconductor devices. These range from diodes, bipolar transistors and thyristors [17], metal-oxide semiconductor field-effect transistors (MOSFETs) and microwaves. Important to this work, *p-n* junctions can also act as a photonic device.

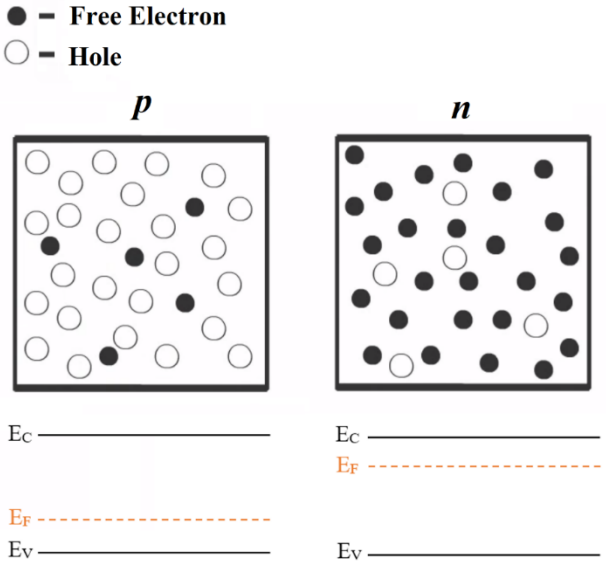

Figure 2.12. p-type and n-type *doped* semiconductors.

Imagine you have a *p*-doped and *n*-doped semiconductor of uniform doping as shown in Figure 2.12, the *p*-type semiconductor contains a high concentration of holes and tiny concentration of electrons and the *n-type* contains a high concentration of electrons and small concentration of holes.

If the *p*-type and *n*-type semiconductors are joined together, the large carrier concentration gradient causes holes to *diffuse* from the *p*-doped region to the *n*-doped region and electrons to *diffuse* from the *n*-doped region to the *p*-doped region. This is called the *diffuse current* and occurs across the *p*-*n* junction, the surface where the *p*-and *n*-type material meet. The pairing of electron-holes at the junction creates a region with a lack of free electrons and holes called the depletion region (Figure 2.13).

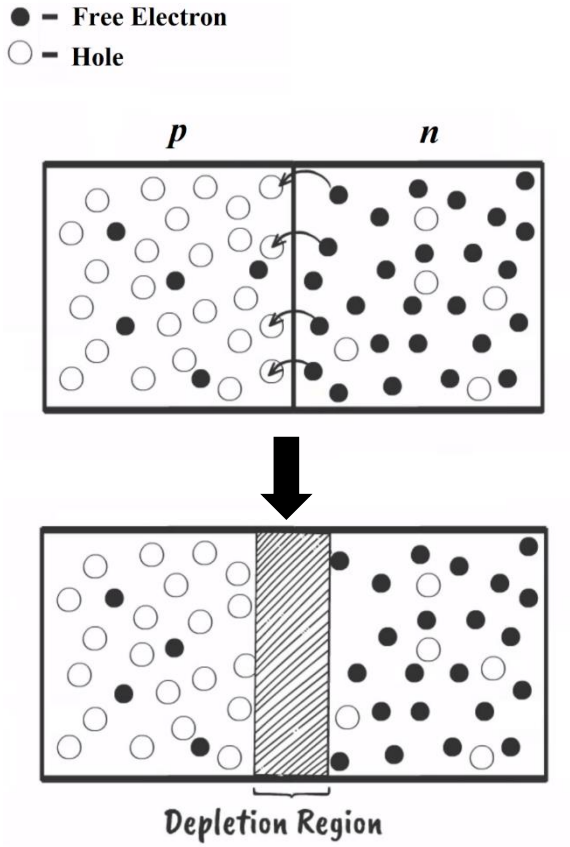

Figure 2.13. Formation of the depletion region due to electron hole pairing at the p-n junction.

A *p*-type semiconductor is neutrally charged because the *holes* and *acceptor ions* are equal. Similarly, an *n*-type semiconductor is neutral due to the balance of *free electrons* and *donor ions*. However, when the *p* and *n* materials are joined, the diffusion of electrons and holes causes the overall charge of the *p*-side depletion region to become negative due to uncompensated negative acceptor ions (N_A^-) and the *n*-side depletion region to become positive

due to uncompensated positive donor ions (N_D^+). This charge gradient creates a static electric field directed form the positive charge to the negative charge (Figure 2.14).

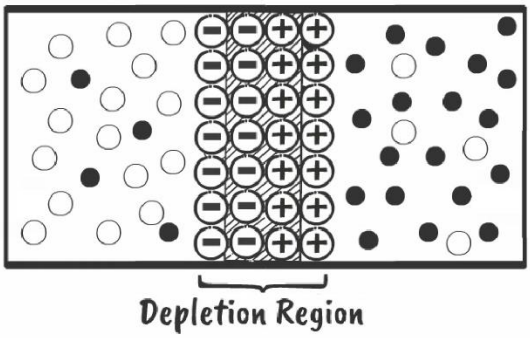

Figure 2.14. Static electric field due to depletion region.

This leads to a *drift current* that transports free electrons and holes in the opposite direction of the *diffuse current*. This is shown in Figure 2.15, in the lower part of the graph, holes diffuse from the left (*p*-type) to the right (*n*-type) at the same time as holes *drift* from the right to the left due to the electric field. Similarly, electrons diffuse from the right to the left and drift from the left to the right.

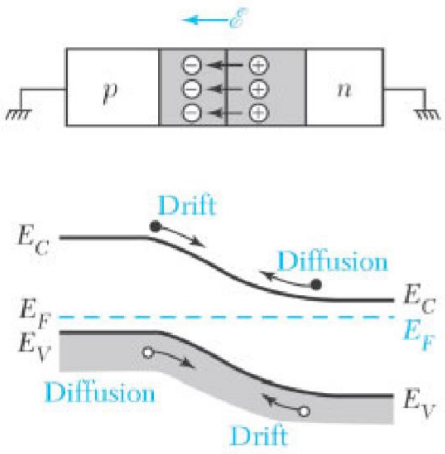

Figure 2.15. Drift and diffusion caused by the depletion region of a p-n junction.

The *drift* and *diffusion* occur until a steady-state is reached where the net transfer of electrons and holes across the depletion region is zero. This is the basis of a diode.

If a *forward-bias* potential V_F is applied to the *p*-*n* junction, that is we apply a voltage with the anode (+) connected to the *p*-side and the cathode (-) connected to the *n*-side, the static electric field is reduced leading to the narrowing of the *depletion region*. This smaller gap is now easily traversable by the charge carriers and current can flow if the applied voltage is bigger than that

of the barrier potential. This is shown in Figure 2.16 (a), for a silicon diode, the *forward-bias* barrier potential $V_{bi} = 0.7V$.

On the other hand, applying a *reverse-bias* potential V_R, i.e. connecting the cathode (+) to the *n*-side and the anode (-) to the *p*-side increases the width of the *depletion region* and hence the static electric field, making it extremely difficult for the charge carriers to traverse the gap. This is shown in Figure 2.16 (b) and the current is negligible with the diode in effect acting as an electrical insulator.

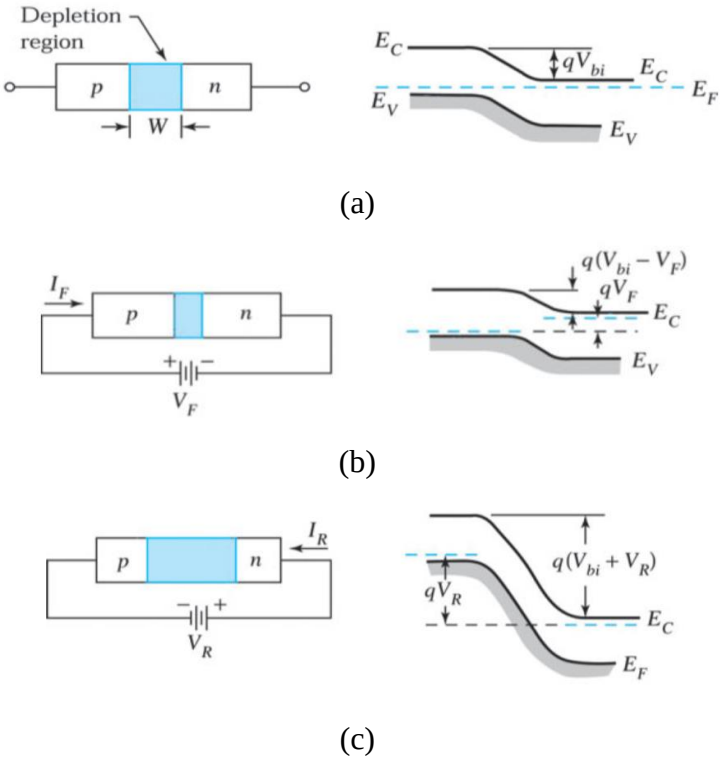

Figure 2.16. p-n junction under (a) thermal equilibrium, (b) forward bias, (c) reverse bias conditions.

Testing a typical silicon diode under an I-V sweep illustrates the properties of diodes. In the I-V curve shown in Figure 2.17. We can see that up to 0.7 V of forward-bias potential, current cannot pass through the *p-n* junction. Once the barrier potential V_{bi} is overcome, current is free to pass, and the resistance of the *p-n* junction is effectively zero. In the reverse-bias the *p-n* junction acts as an insulator allowing negligible current to pass. There is a reverse-bias breakdown voltage (V_B) where the electrons and holes *break down* through the junction resulting in the flow of a current. This breakdown, referred to as the *avalanche breakdown*

permanently damages the *p-n* junction due to the excess heat generated by the electrons and holes crossing the barrier.

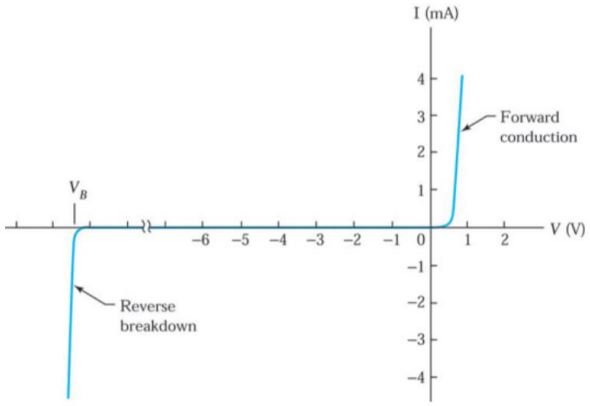

Figure 2.17. I-V characteristics of a silicon diode

2.2.4. LEDs, photodiodes and solar cells

p-n junctions are found in optoelectronic devices such as LEDs, photodiodes and solar cells. It is the *recombination* of holes and electrons within the *light emitting diode p-n* junction that produce light. The light emitted is the emission of photons, similarly the electrical current generated by photodiodes and solar cells are the results of absorption of photons.

It is the interactions between photons and electrons that determine the function of optoelectronic devices. They can be categorized as *absorption, spontaneous emission* and *stimulated emission*. If we consider E_1 being the energy level of an atom at the *ground state*, and E_2 the energy level at the *excited state* then any transition between these states must involve the emission or absorption of a photon. Recalling equations 2.1 - 2.3, we get $\lambda = \frac{c}{v} = \frac{hc}{hv} = \frac{1.24}{hv(eV)}\mu m$, we can give the energy of the photon emitted or absorbed by $hv_{12} = E_2 - E_1$. At room temperature, most of the atoms in solids are at the ground state. Under forward-bias condition, electrons are inserted from the *n*-side and holes are injected from the *p*-side as well as a lowering of the barrier potential. This leads to the injected carriers passing through the barrier and meeting at the junction. Here free electrons and holes are annihilated due to recombination and light is produced. The energy of the photons is determined by the material bandgap:

$$hv_{\Delta} = E_G + kT$$

The kT term is negligible and ignored, therefore the photon released has energy equal to E_G, i.e. $hv = E_G$.

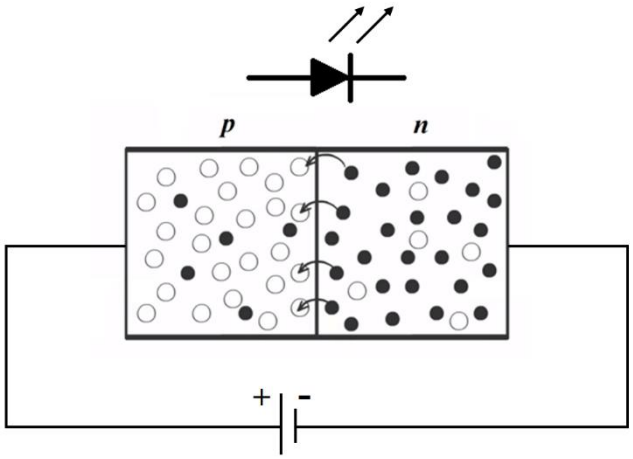

Figure 2.18. Light-Emitting Diode (LED) under forward-bias.

Radiative recombination is not the only process that occurs, the radiative recombination occurs alongside nonradiative ones. An LED can be characterized by the ratio of radiative versus nonradiative recombination. This is presented as the *internal quantum efficiency* (IQE) and is defined as:

$$\eta_{in} = \frac{number\ of\ photons\ \ emitted\ internally}{number\ of\ carriers\ passing\ junction} = \frac{R_r}{R_r + R_{nr}} \qquad (2.8)$$

Where R_r is the radiative recombination and R_{nr} is the nonradiative recombination.

Furthermore, not all emitted photons exit the device. There are a number of losses including absorption by the *p-n* material, absorption in the substrate, fresnel reflection and total internal reflection losses. *External quantum efficiency* (EQE) is therefore defined as follows:

$$\eta_{ex} = \frac{number\ of\ photons\ emitted\ externall}{number\ of\ carriers\ passing\ the\ junction} = \eta_{in}\eta_{op} \qquad (2.9)$$

Where η_{in} is the IQE and η_{op} is the *optical efficiency* and refers to all the losses stated above.

Solar cells are principally diodes that operate using the same fundamentals of LEDs. The difference is that in LEDs, injected electron and holes combine to release photons whilst in solar cells photons are absorbed by the cell to create *electron-hole pairs* (EHPs). The photocurrent is actually a reverse bias current because electrons flow toward the cathode and the holes flow to the anode.

The solar cell structure is composed of a *p-n* junction near the front surface. The *n-type* material is typically much shallower than the *p-type* material. This causes the shift of *p-n* junction required to the surface. Bus bars are constructed on the front surface to collect the charge

carriers and the back is attached to an ohmic electrode. Anti-reflection coating is usually applied to the front surface to minimize incident light reflection (Figure 2.19).

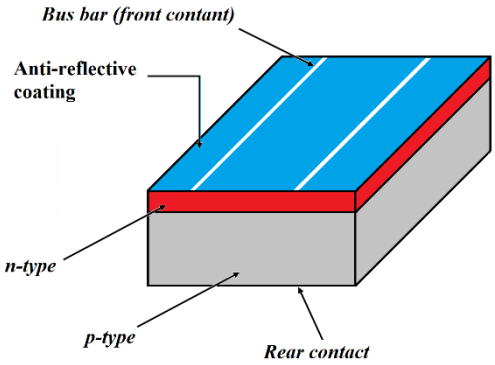

Figure 2.19. General schematic of a solar cell.

When the solar cell is illuminated (such as exposed to solar radiation), photons hit the *p-n* junction. If the photon energy is less than the bandgap of the material (E_G), then enough energy is not provided to the valence electrons in order to excite them to the conduction band. However, where the photon $E > E_G$, then electron-hole pairs (EHPs) are created at the depletion region of the *p-n* junction. An amount of energy equal to the bandgap (E_G) is hence contributed to the solar cell output, whilst the excess energy $\Delta E = E - E_G$ is converted into heat energy. The electric potential causes light generated electrons move to the *n-side* whilst the holes are transported to the *p-side*, here the charge carriers go on to exit through the cathode and anode as current.

2.2.5. I-V curve

PV cells act as diodes with the addition of a current source. For this reason, under dark conditions a solar cell has the I-V characteristics of a diode, and as current is generated with increasing solar exposure, the *I-V curve* is shifted in the current direction to present the power generation. A solar cell I-V curve goes from the short-circuit current I_{SC}, to the open-circuit voltage V_{OC}. The short-circuit current occurs when the negative and positive contacts of the cell are connected with zero resistance, at this point there is also zero potential difference between the two points meaning $V = 0$. Conversely at the open-circuit voltage V_{OC}, there is infinite resistance between the solar cell contacts and no current can pass, hence $I = 0$ but the potential difference (i.e. voltage) is at a maximum. All points in between are achieved by applying a variable load (resistance) and looking at the generated current and voltage, hence the name I-V curve. The operating I-V curve is the *superposition* of the solar cell dark diode (solar cell with no light exposure) down to the fourth quadrant. This means the solar I-V curve

can be expressed as the *"diode law"* with an additional term for light generation represented current [32]:

$$I = I_0 \left(e^{\left(\frac{qV}{nkT}\right)} - 1 \right) - I_L \qquad (2.10)$$

Where I is the cell output current,

I_L is the current generated by solar illumination

V is the voltage

$q = 1.6021766208 \times 10^{-19}\ C$, is the elementary electron charge

k is the Boltzmann constant, $(8.6173303 \times 10^{-5}\ eV \cdot K^{-1})$

T is the absolute temperature of the cell (K).

A typical solar cell I-V curve is shown in Figure 2.20 below, the orange curve (a) is the I-V curve of the solar cell under dark condition, note the current is virtually zero until it rises due to the applied voltage surpassing the barrier potential (V_{bi}) of a typical *p-n* junction diode. In fact, the curve is the same as a diode under forward-bias operation as presented in Figure 2.17. The red curve (b) is the I-V curve of the cell under light irradiation, a shift can be seen directed down with the magnitude of the shit, i.e. the difference between the orange and red curve current representing the light generation current I_L. The shift is down to the fourth quadrant because solar cells are producing *reverse-bias* current.

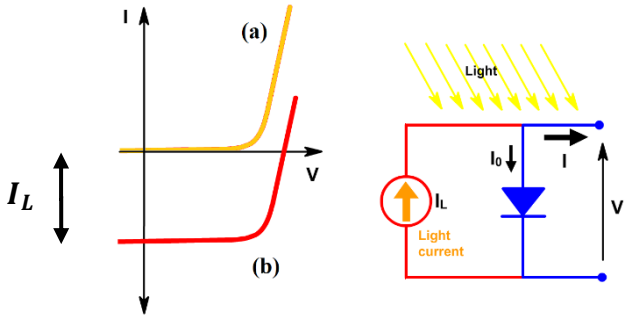

Figure 2.20. I-V curve of solar cell under (a) dark condition, (b) exposure to light.

By convention, due to the generation of power, the current is inverted, moving the I-V curve to the first quadrant to give:

$$I = I_L - I_0 \left(e^{\left(\frac{qV}{nkT}\right)} - 1 \right) \qquad (2.11)$$

The "−1" term in the equation can be ignored as the exponential term >> 1 under operating conditions. More so, the light generated current I_L becomes much larger than I_0 as the cell is illuminated. Therefore, the above equation can be simplified to:

$$I = I_L - I_0 \left(e^{(\frac{qV}{nkT})}\right) \tag{2.12}$$

And the inverted I-V characteristic as:

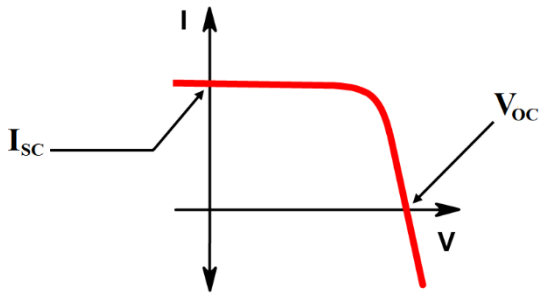

Figure 2.21. Inverted solar cell I-V curve

Power generated is calculated as $P = I \times V$, therefore at I_{SC} power is $I_{SC} \times 0 = 0\ W$. Likewise, at V_{OC} the power is also $V_{OC} \times 0 = 0\ W$ since by definition the short-circuit current has zero voltage and the open-circuit voltage has zero current. Power is only generated within the bounds of these two points and in order to get the *peak power point* it is useful to create an overlapping plot of the power-voltage characteristic. The plot is simply $P = I \cdot V$ vs. V and the graph would look something like Figure 2.22. Maximum power is generated at the current and voltage corresponding to point P_{Max}, i.e. the peak of the P-V curve, they are denoted at I_{MP} and V_{MP}.

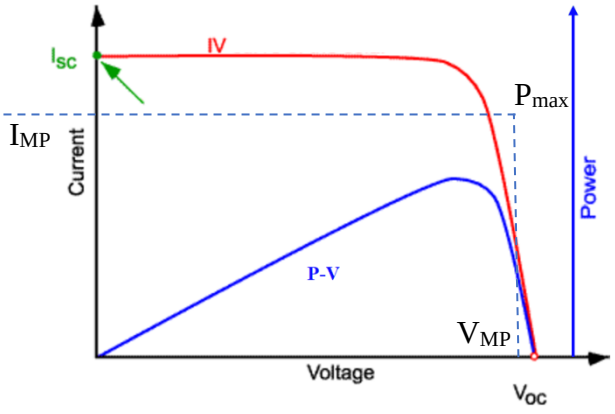

Figure 2.22. Overlapping I-V, P-V characteristic curves

2.3. Fill Factor

One measure of the quality of a solar cell is the fill factor, FF. Fill factor is the ratio of the *maximum power generated* to the power that would be generated by $V_{OC} \times I_{SC}$. The maximum power generated can be represented as the area of the I-V curve by the intersecting lines V_{MP} and I_{MP} (area A in Figure 2.23). A similar area can be drawn by crossing I_{SC} and V_{OC} (area B in Figure 2.23).

Since the area represented by square $A = V_{MP} \cdot I_{MP}$ and the area represented by square $B = V_{OC} \cdot I_{SC}$, the *fill factor* is defined as:

$$FF = \frac{Area\ A}{Area\ B} = \frac{\boldsymbol{V_{MP} \cdot I_{MP}}}{\boldsymbol{V_{OC} \cdot I_{SC}}} \tag{2.13}$$

Since the denominator is the area of a square, fill factor is essentially the squareness of the I-V curve of the solar cell.

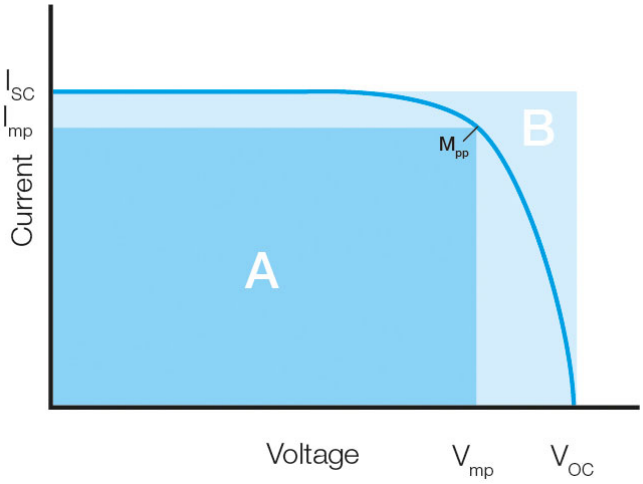

Figure 2.23. Fill factor A/B of a solar cell

2.3.1. Parasitic Resistances

There is a presence of parasitic resistances in solar cells. The most common resistances are referred to as the *series resistance* R_S and the *shunt resistance* R_{SH}. The impact of these resistances is reduction in the FF and in effect the solar cell efficiency. An equivalent circuit incorporating the series and shunt resistances is shown in Figure 2.24.

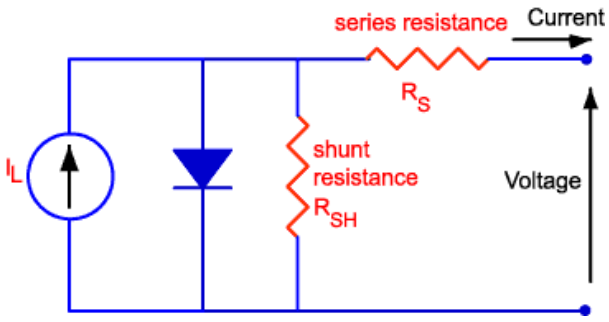

Figure 2.24. Equivalent circuit of a solar cell with series and shunt parasitic resistance.

Series resistance R_S is the largest source of resistance [33, 34] which results from the ohmic loss on the front surface of the solar cell. Photon induced electrons generated in the solar cells need to traverse the *n-type* material to the buss bars shown in Figure 2.24 which introduces a series resistance. There are some series resistances present in the *p-type* material as well, but due to the larger size of the *p*-material in solar cells this effect is much smaller. The series resistance is a factor of a combination of *junction depth*, *doping intensity* and the *front surface contacts*. It has been shown the series resistance decreases as the junction depth (barrier height) is increased and is also reduced with increased doping concentration of the semiconductor material. The effect of R_S is to decrease the intensity of the slope between the maximum power point P_{Max} and V_{OC} (see Figure 2.25).

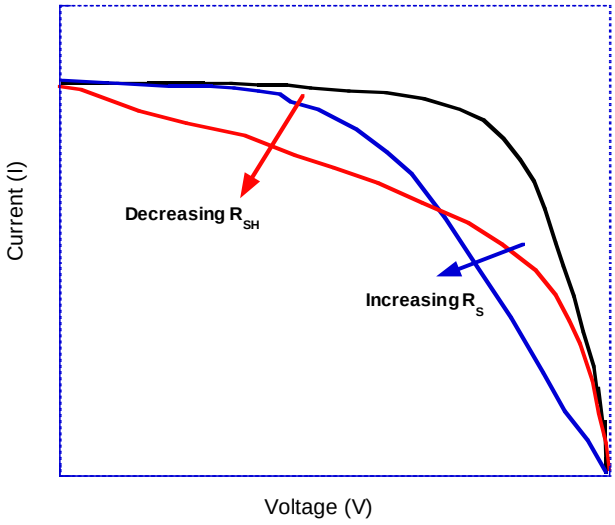

Figure 2.25. Effect of series and shunt resistance on solar cell I-V curve.

The effect of series resistance on the ideal I-V curve gives the amended equation:

$$I = I_L - I_0\left(e^{\left(\frac{q(V+IR_S)}{nkT}\right)}\right) \tag{2.14}$$

With the additional term R_S representing the effect of series resistance. The inclusion of I on both sides of the equation makes this an *implicit function* meaning the equation can only be solved through numerical methods. Another method of graphing the I-V curve whilst including the series resistance is to vary the voltage across the solar cell and plot the output.

Shunt resistance R_{SH} is represented as the shorting of the equivalent circuit and is the effect of photo-generated current passing through the crystal surface and grain boundaries rather than travelling to the collection contact. Shunt resistance is due to the presence of manufacturing defects and can be characterised by altering the ideal solar cell I-V curve equation to:

$$I = I_L - I_0\left(e^{\left(\frac{qV}{nkT}\right)}\right) - \frac{V}{R_{SH}} \tag{2.15}$$

Where R_{SH} is the shunt resistance of the solar cell.

The effect of shunt resistance R_{SH} is to lower the top part of the I-V curve by increasing the slope intensity of the line connecting I_{SC} to P_{MAX} Figure 2.25. If R_{SH} is increased high enough, V_{OC} can be lowered.

In an ideal solar cell, the series resistance is zero and the shunt resistance is infinite. It is therefore possible to use the slopes of the I-V curve to find the series and shunt resistances, where R_S is the inverse of the vertical slope difference between the ideal solar cell I-V curve and the measured I-V curve and R_{SH} is the inverse of the horizontal slope compared to an ideal I-V curve [35] as shown in Figure 2.26.

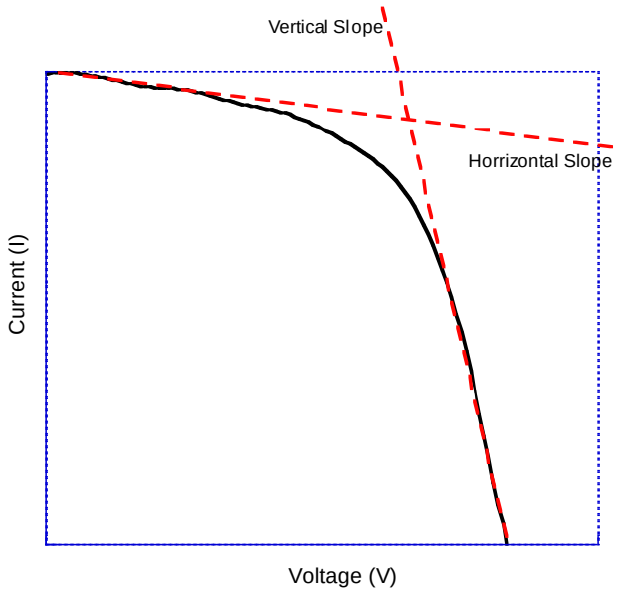

Figure 2.26. Horizontal and vertical slope of I-V curve

2.3.2. Recombination

Recombination is the opposite process of the useful work carried out by solar cells. A solar cell uses incident light photons to create electron-hole pairs (EHPs) which are separated and carried in opposite directions. This process occurs simultaneously to recombination, a parasitic loss whereby holes and electrons recombine to release photons (the useful work of an LED). Recombination causes losses in both current collection and forward-bias current injection. This means both the I_{SC} and V_{OC} are affected. Recombination occurs in the bulk of the solar cell material, the surface of the solar cell and also in the depletion region of the *p-n* junction. They are referred to as *bulk recombination*, *surface recombination* and *depletion-region recombination*, respectively. The majority of recombination occurs in the bulk region and surface of the solar cell.

There are three types of recombination processes in effect for monocrystalline semiconductors: *radiative recombination*, *Auger recombination* [36] and *Shockley-Read-Hall recombination* [37, 38].

The dominant recombination effect in *direct bandgap* semiconductor solar cells is *radiative* or *band-to-band* recombination. In radiative recombination, an electron in the conduction band emits a photon, dropping to the valence band where it pairs with an available hole. This causes emission of a photon and is where the name *radiative* recombination originates (Figure 2.27). The energy released is approximately the bandgap of the material. It should be noted that silicon is an *indirect-bandgap* material where radiative recombination is negligible. Cells used in satellites and space applications, as well as high concentrating photovoltaic systems which are often multi-junction in nature, use *direct-bandgap* semiconductor materials such as GaAs.

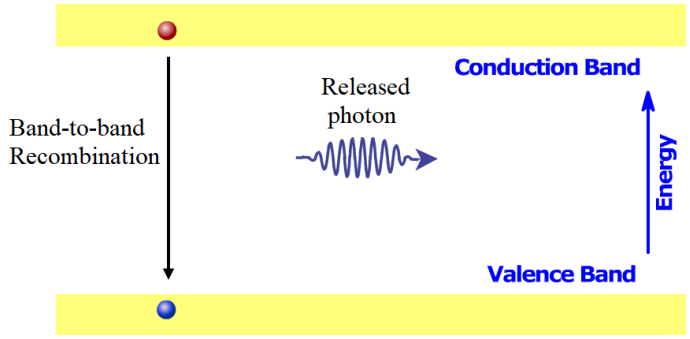

Figure 2.27. Radiative (band-to-band) recombination of electron-holes.

Shockley-Read-Hall (SRH) recombination is due to the presence of defects in the material (see Figure 2.28). These defects can be due to fabrication process limitations or intentional doping

of the semiconductor material. This causes an available energy state in the *forbidden region* within the bandgap of the material. The electron drops to an energy state in the forbidden region, releasing photon(s) equivalent to the energy drop. From here the electron further drops to the valence band, pairing with a hole and releasing an additional photon.

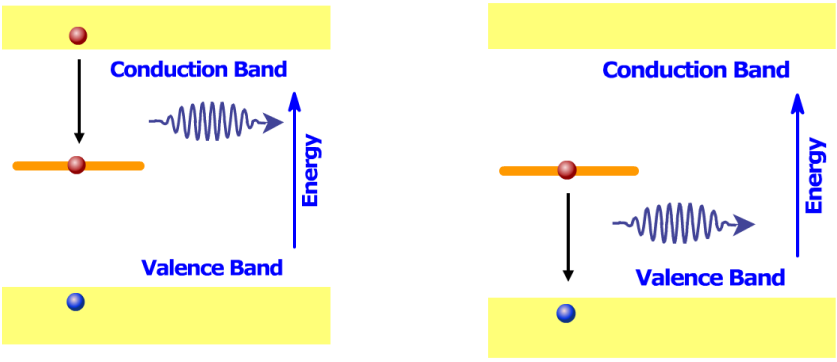

(a) Electron moves to energy state in the forbidden region releasing photon

(b) Electron moves again to the valence band to combine with a hole releasing another photon

Figure 2.28. Shockley-Read-Hall Recombination

The position of the energy state in the forbidden region is important in determining the rate of recombination: in energy states close to the conduction or valence band, the most likely outcome of an electron/hole moving to those bands is that they travel back to the band they are originated from. The highest recombination occurs when the energy states are midpoint between the valence band and conduction band, this is the peak at which electrons and holes are most likely to go to their counterpart band and recombine.

Auger recombination occurs when an electron and hole combine but give the energy to a second electron (conduction band) instead of thermal or light radiation (see Figure 2.29). This electron moves to a higher energy level still within the conduction band for a period, after which it will radiate thermal energy and drop back down to the edge of the conduction band.

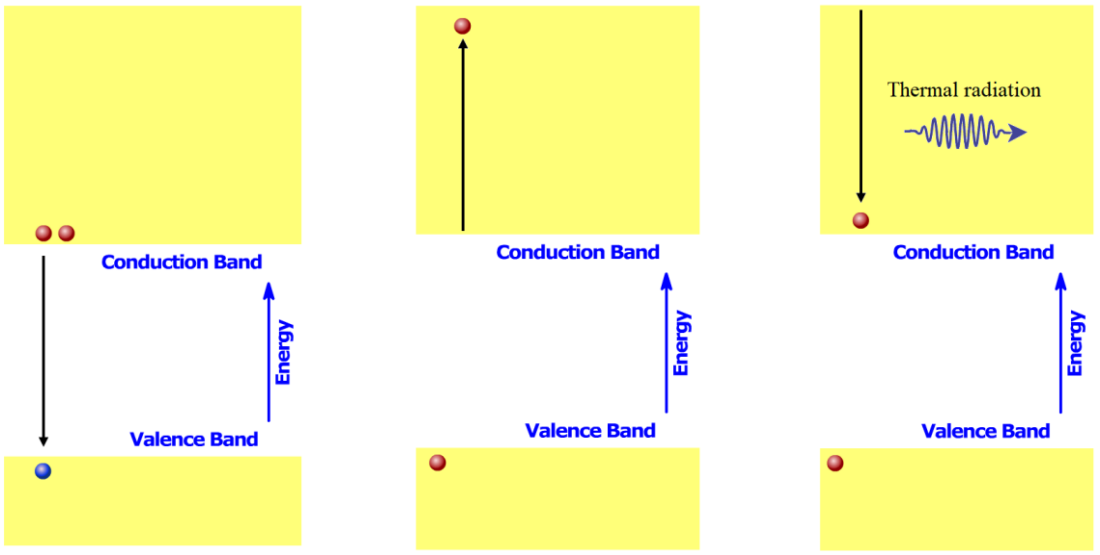

(a) Electron and hole combine, energy released to a third carrier

(b) Affected electron moves to higher energy states of the conduction band

(c) Electron drops back down to the edge of the conduction band radiating thermal energy

Figure 2.29. Auger Recombination

Since Auger recombination causes energy released to a nearby electron, the chance increases as carrier concentration goes up, a property that increases as the doping of the semiconductor is increased. Furthermore, cells operating under increased sunlight, for example due to concentrators, undergo increased carrier injection. The result is that the carrier lifetime is reduced leading to a lower solar cell operating efficiency.

2.4. Solar Cells Technologies

Solar cell technologies are typically categorised into three groups:

- First generation solar cells based on crystalline Silicon.
- Second generation solar cells including thin film and amorphous Silicon (a-Si).
- Third generation solar cells constitute a wide range of emerging PV technologies. These include Dye-Sensitized Solar Cells (DSSC), Perovskite cells, Organic PVs (OPV) and Quantum Dot (QD) cells.

2.4.1. Shockley–Queisser limit

William Shockley and Hans-Joachim Queisser published a study in 1961 looking at the theoretical limits of single *p-n* junction solar cells [39]. They took into account the effects of *blackbody radiation*, *recombination*, *spectrum losses* and *impedance matching*.

2.4.1.1. Laws of thermodynamics

There are four laws of thermodynamics

The ***zeroth law of thermodynamics*** states that if two thermodynamic systems are in equilibrium with a third, then they are in equilibrium with each other i.e. if A=B and C=B then A=C. It gets its term zeroth due to the fact that it was defined after the first law of thermodynamics but is considered more fundamental.

The ***first law of thermodynamics***, known as the Law of Conservation of Energy, states that energy cannot be created or destroyed within an isolated system, i.e. the total energy must remain constant. This is typical described by:

$$\Delta U = \Delta Q - \Delta W$$

Where ΔU is the internal energy of the isolated system, ΔQ is the energy supplied to (or given off) the system and ΔW is the work done by (or to) the system.

The ***second law of thermodynamics*** states that the entropy of an isolated system tends to the maximum. That is, it is either constant (ideal scenario) or increases. The entropy is defined as:

$$S = k \ln W$$

Where S is the entropy of the system, k is the Boltzmann constant ($1.38064852 \times 10^{-23}$ J·K^{-1}), and W is the number of microstates in the system.

The ***third law of thermodynamics*** states that as the temperature of a system approaches absolute zero (-273.15°C, 0 K), entropy approaches zero. At absolute zero, W, the number of microstates in the system becomes 1, that is:

$$S = k \ln 1 = k \cdot 0 = 0$$

2.4.1.2. Blackbody radiation

Blackbody radiation is energy lost to heat due to radiation of any material that is not at 0 Kelvin. For solar cells this accounts for ~7% of energy falling on the cell at room temperature (300 K). However, since all losses of a solar cell are converted to heat, the temperature of a solar cell even at room temperature will increase until an equilibrium is reached. This equilibrium temperature can be as high as 86.8 °C. This means cells without cooling devices will operate at lower efficiencies than their room temperature rating.

2.4.1.3. Recombination

Recombination of electron-hole pairs releasing photons occurs in solar cells alongside the dominant reverse process of *generation* (creation of electron-hole pairs due to absorption of photons). Shockley-Queisser found the recombination rate is a factor of $\exp(V/V_c)$, where V_c is the voltage equivalent of the temperature effects on the cell given by:

$$V_c = kT_c/q \tag{2.16}$$

Where k is the Boltzmann constant and q is the charge of an electron.

The rate of recombination was therefore given by the product of the *blackbody radiation* and this $\exp(V/V_c)$ factor:

$$Q(\nu_g, T_s) = \int_{\nu_g}^{\infty} \frac{1}{\exp\left(\frac{h\nu}{kT_c}\right)-1} \exp\left(\frac{q\nu}{kT_c}\right) \frac{2\pi\nu^2}{c^2}\, d\nu \tag{2.17}$$

This integral turned out to be an accurate approximation. Ruppel-Wurfel [40] and De Vos-Pauwels [41] improved the expression to:

$$Q(\nu_g, T_s) = \int_{\nu_g}^{\infty} \frac{1}{exp\left(\frac{h\nu-qV}{kT_c}\right)-1} \frac{2\pi\nu^2}{c^2}\, d\nu \tag{2.18}$$

2.4.1.4. Spectrum losses

Probably the dominant limit on solar cell efficiency is due to *spectrum losses*. This is based on two factors:

Firstly, for a *p-n* semiconductor, the minimum energy an electron needs to recombine with a hole is the distance between the conduction and valence bands, the bandgap. Therefore, any photons below this bandgap cannot create an EHP and is lost.

Furthermore, under the assumption that each photon can only create one EHP, any excess energy induced by the photon is radiated as heat. Therefore, only photons with energy exactly equal to the bandgap will be fully absorbed by the solar cell:

- If a photon has less energy than the bandgap, it cannot create an EHP and is completely lost
- If a photon has more energy than the bandgap, the excess energy is lost as heat [42]

Shockley and Queisser calculated the spectrum losses alone would limit the efficiency of single *p-n* junction solar cells to 44%, referred by them as the *ultimate efficiency factor* which alone represents a 56% loss assuming perfect material bandgap and ideal conditions.

2.4.1.5. Impedance matching factor

As shown by previous chapters with I-V curves, at high resistances, the current will be very low (at open-circuit conditions the current is in fact zero) and vice versa at low load resistances the voltage is very low. The *peak power* generated is therefore the load resistance at which maximum power will be output by the solar system. Shockley-Queisser named the term *impedance matching factor* denoted by *m*. *m* was given as a function of the open-circuit voltage of a solar cell as shown in Figure 2.30 and at low illumination where $V_{oc} \gg V_c$, *m* goes to 0.25 and at large V_{OC} the impedance matching factor approaches 1.

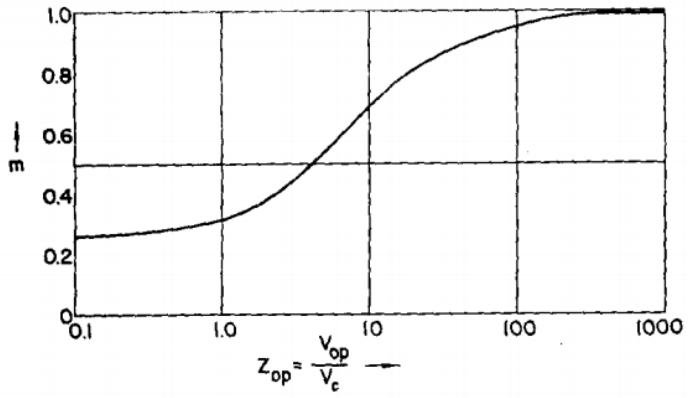

Figure 2.30. Relation of Impedance matching factor m and V_{oc}

The four losses were combined to give the overall efficiency function:

$$\eta(x_g, x_c, t_s, f) = \frac{I[V(max)]\mathrm{V[max]}}{\mathrm{P_{inc}}} = t_s u(x_g) v(f, x_c, x_g) m(v x_g / x_c) \quad (2.19)$$

$$x_g = V_g / V_s \quad (2.20)$$

$$x_c = V_c / V_s \quad (2.21)$$

Where $u(x_g)$ is the *ultimate efficiency* (spectrum losses), $v(f, x_c, x_g)$ is the *ratio of open-circuit to bandgap voltage*, *m* is the *impedance matching factor*, t_s is the probability that a photon with $hv > E_g$ creates an EHP, *f* is the geometrical and transmission factors together with the effect of excess recombination over radiative recombination.

The results were shown with a maximum theoretical efficiency limit of ~30% at a bandgap of 1.34eV (Figure 2.31). For comparison silicon semiconductors have a bandgap of 1.1 eV.

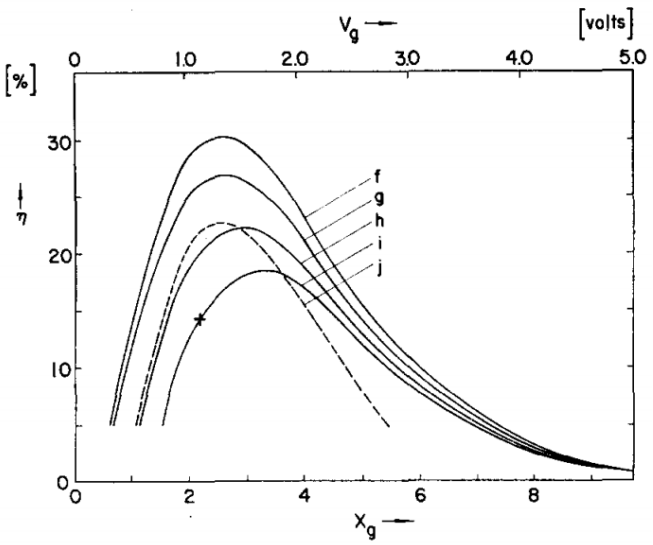

Figure 2.31. Efficiency limit of a solar cell at 300 K exposed to a blackbody sun at T=6000 K. Curve (f) is the detailed balance limit.

Rühle presented a tabulated list of the Shockley–Queisser limit for single junction solar cells and placed this efficiency at 33.7% with silicon limited to 32.23% efficiency [43]. The relation of bandgap to efficiency limit is shown in Figure 2.32.

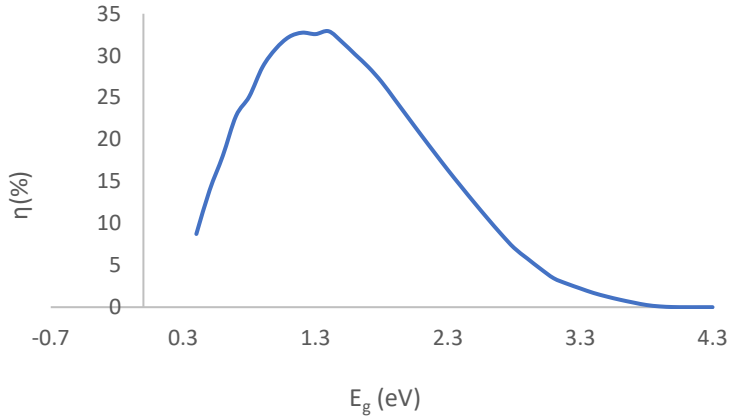

Figure 2.32. Theoretical limit on single p-n junction solar cells based on the semiconductor material bandgap

This limit applies to a single *p-n* junction solar cell. If multiple *p-n* junctions with different bandgaps are stacked in tandem, the efficiency can exceed this number. Alexis de Vos calculated the theoretical limit on a tandem solar cell (otherwise known as a multi-junction solar cell) by assuming a stack of an infinite number of solar cells. He found that such a system can convert a maximum of 68% of unconcentrated sunlight and 86% of concentrated sunlight [44].

2.4.2. Silicon Solar Cells

Crystalline Silicon (c-Si) solar cells are considered the first generation of solar cells. They are the most predominant solar cells in the market due to their high efficiency and high stability. Structure of a typical single-junction crystalline silicon PV cell is shown in Figure 2.33 [45]. Current recorded lab efficiencies are 26.7% [46] for mono-crystalline and 21.9% [46] for multi-crystalline solar cells. Commercial c-Si solar cells are also rated to last between 20-25 years. The cost of such cells has also reduced drastically, going from $76/watt in 1977 to just 30¢/watt in 2015.

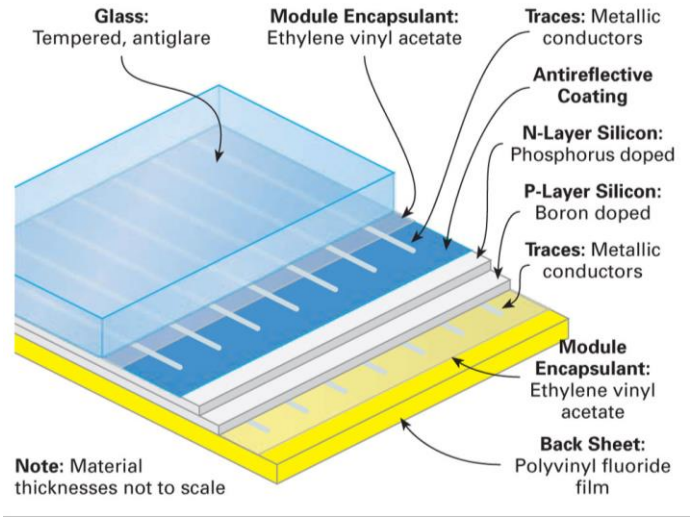

Figure 2.33. Typical structure of a single-junction crystalline silicon PV cell [45].

Crystalline silicon cells are categorised in two groups: mono-crystalline silicon solar cells and multi-crystalline silicon (or polycrystalline) solar cells.

Mono-crystalline or mono-Si solar cells are made from extremely pure silicon ingots typically prepared using the Czochralski process to cylinders of up to 2 meters (Figure 2.34). From here they are sliced into *wafers* which are used in semiconductor devices such as solar cells. A defining property of mono-Si is that the crystal structure is homogenous across the wafer making all properties constant throughout the material and lacking grain boundaries.

Figure 2.34. mono-crystalline silicon ingot. Source: Beijing Simic Boya Electric Technology Co.

Multi-crystalline solar cells are creating using poly-crystalline (poly-Si) silicon. Polycrystalline silicon derives its name from the fact that the material, produced using a chemical purification process called the *Siemens process*, consists of a batch of connected smaller crystals. This is apparent when looking at the material where the visible "flakes" represent each crystal boundary. The name multi-crystalline refers to the fact that the crystals are larger than 1mm. A schematic of the allotropic forms of silicon is shown in Figure 2.35.

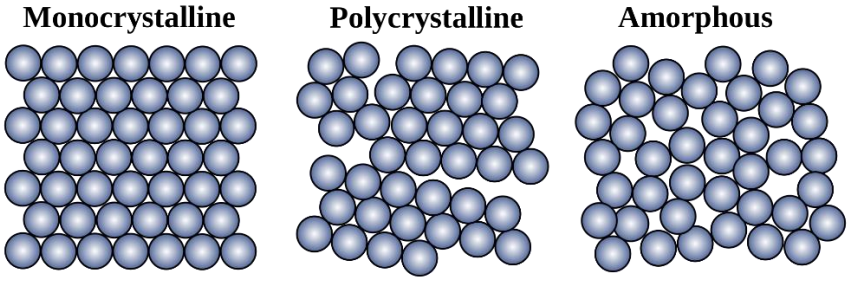

Figure 2.35. Mono-crystalline, poly-crystalline and amorphous silicon lattice.

Mono-Si cells are more expensive to make but are more efficient, for this reason, and due to the fact that mono-Si solar cells are produced from cylindrical mono-Si ingots which are expensive to fabricate, the cells contain large tapered edges. This more circular variation of a "square" improves the yield of cells from ingots. Multi-Si solar cells are less efficient; however, they are much cheaper than mono-Si making them the more cost-effective option. This makes mono-Si solar cells ideal for space-limited project and multi-Si solar cells suited for cases where the cost is more important than space. Figure 2.36 shows a comparison of multi/poly-crystalline and mono-crystalline solar cells. Currently, most of silicon solar cells produced globally are multi-Si solar cells (Figure 2.37).

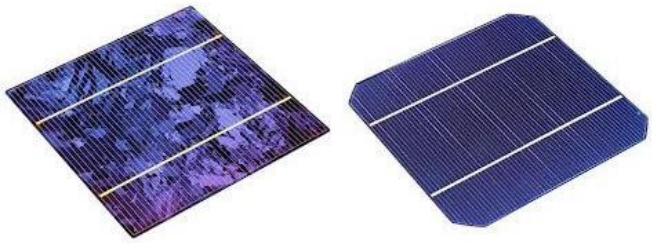

Figure 2.36. Left multi-crystalline (poly-Si), right mono-crystalline solar cell.

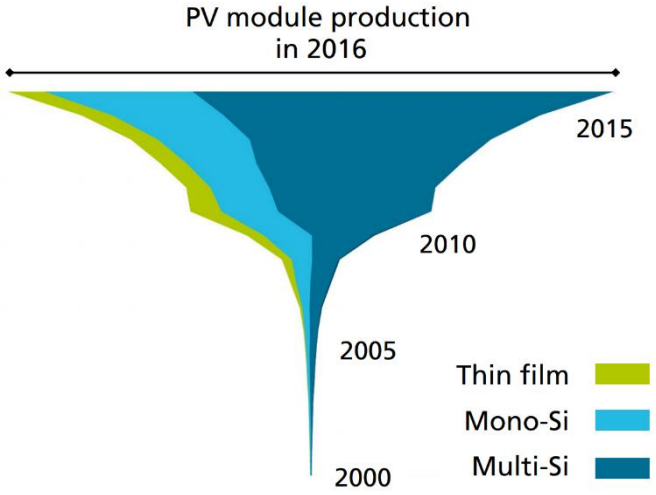

Figure 2.37. Global PV production breakdown by technology type. [46]

2.4.3. Thin Films

Second generation solar cells, based on thin films are varied in fabrication material. The most common thin film solar cells are amorphous silicon (a-Si) solar cells, Cadmium Telluride (CdTe) solar cells and Copper Indium Gallium Selenide (CIGS) solar cells.

Thin films have several advantages: thin films are flexible by nature, meaning flexible non-glass substrates can be used to create flexible solar cells. The materials of thin film solar cells can be designed, allowing their incorporation in tandem-PVs. The vacuum processing and high temperature treatment required for fabrication of thin films leads to high energy consumption in manufacturing. The use of rare earth metals also limits the production capacity, supply and cost of thin films, especially for mass adoption.

2.4.4. Third Generation Solar Cells

Third generation solar cells refer to a large number of emerging solar cell technologies. This includes but is not limited to Organic Photovoltaics (OPVs), Quantum Dot cells, Dye-Sensitized Solar Cells (DSSC) and their solid-state offshoot the Perovskite solar cell.

The history of DSSCs is deeply rooted in advances in photography. It is a convergence of photography and photoelectrochemistry, both rely on photo-induced charge separation at a liquid-solid interface [47]. In 1839, Edmond Becquerel observed the first photovoltaic effect of silver chloride immersed in an iodide solution and connected to platinum electrodes [14]. The silver halides have large band gaps (2.7-3.2eV), hence are insensitive to most of the visible spectrum in much the same way as TiO_2.

Silver halides are much more sensitive to blue and UV light than green and red light. In 1873, Vogel employed sensitizing dyes to extend the sensitivity of the silver halide in the green and orange region [48]. The first sensitization of a photoelectrode followed thereafter [49], with the clear connection between dye sensitization for photography and photovoltaics shown in 1965 by Namba et al. [50] and verification that the process is achieved by electron injection from the dye molecules to the conduction band of the n-type semiconductor in 1968 by Gerischer et al. [51].

The first semblance of modern DSSCs was developed in subsequent years with the realization that higher efficiencies could be achieved by chemisorbing the dye onto the semiconductor surface [52, 53, 54]. This was followed shortly by the usage of water cleavage to create surface complexes with a better interface [55]. Finally, it was discovered that increasing the surface roughness of the semiconductor greatly increases cell efficiency [56, 57].

In 1991 the first high efficiency cell was developed by Michael Gratzel and Brian O'regan demonstrating 7.1-7.9% efficiency [58]. This was improved progressively reaching 11.9%. Towards the end of 2012, solid state DSSCs overtook traditional cells in efficiency and are now the subject of increased interest.

2.4.5. DSSC Operation

DSSCs revolve around a layer of dye particles attached to a mesoporous oxide layer (see Figure 2.38), typically TiO_2. Under applied light, photons excite electrons within the dye particles resulting in electron injection to the conduction band of the semiconductor. The holes left behind in the dye are restored through electron donation by an electrolyte such as iodide/triiodide couple. Although some recombination occurs from the conduction band back to the dye molecules, the speed is much slower than regeneration from the iodide and hence is negligible in comparison. The electrolyte is regenerated by reduction of the triiodide due to election transfer from the cathode completing the circuit.

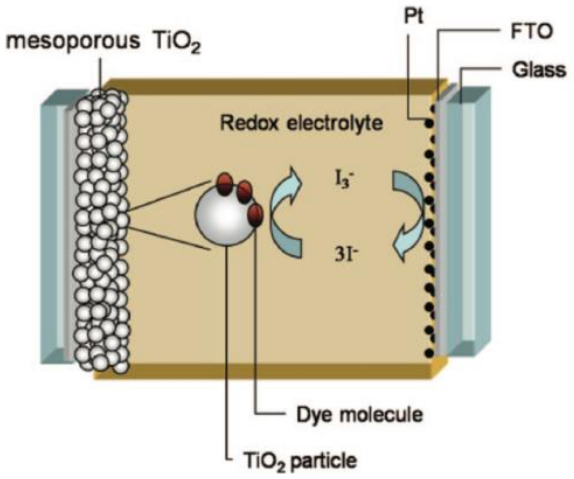

Figure 2.38. Physical schematic of a dye-sensitized solar cell

The DSSC process can be summarised as:

- The incident photon is absorbed by dye photosensitizers (such as Ru complex) absorbed on the semiconducting surface
- The photosensitizers are excited from the ground state (S) to the excited state (S^*). The excited electrons are injected into the conduction band of the TiO_2 electrode. This results in the oxidation of the photosensitizer (S^+).

$$S + hv \rightarrow S^*$$

$$S^* \rightarrow S^+ + e^-(Sc)$$

- The injected electrons in the conduction band of the semiconductor are transported between the semiconductor nanoparticles with diffusion toward the back contact TCO (Transparent Conducting Oxide). The electrons finally reach the counter electrode through the circuit completing the cycle.
- The oxidized photosensitizer (S^+) accepts electrons from the I- ion redox mediator leading to regeneration of the ground state (S), and the I^- is oxidized to the oxidized state, I_3^-.

$$S^+ + e^- \rightarrow S$$

- The oxidized photosensitizer (S^+) accepts electrons from the I- ion redox mediator leading to regeneration of the ground state (S), and the I^- is oxidized to the oxidized state, I_3^-.

$$S^+ + e^- \rightarrow S$$

- The oxidized redox mediator, I_3^-, diffuses toward the counter electrode and is then reduced to I^- ions.

$$I_3^- + 2e^- \rightarrow 3I^-$$

The electron conversion efficiency of a DSSC is dependent on four energy levels: the excited state (approximately lowest unoccupied molecular orbital, LUMO) and the ground state (highest occupied molecular orbital, HOMO) of the photosensitizer, the Fermi level of the semiconductor electrode and the redox potential of the mediator (I^-/I_3^-) in the electrolyte [59].

Due to the stable and non-hazardous properties and low cost readily available nature of the material, TiO_2 is the most widely used semiconductor in DSSCs. TiO_2, as well as other semiconductors used in DSSCs exhibit low spectral absorbance. The need for dye-sensitizers lead to the use of Ruthenium complexes (Figure 2.39), the most widely used ones being the N3 dye and its salt analogue N719 and the dye N749 commonly known as black dye.

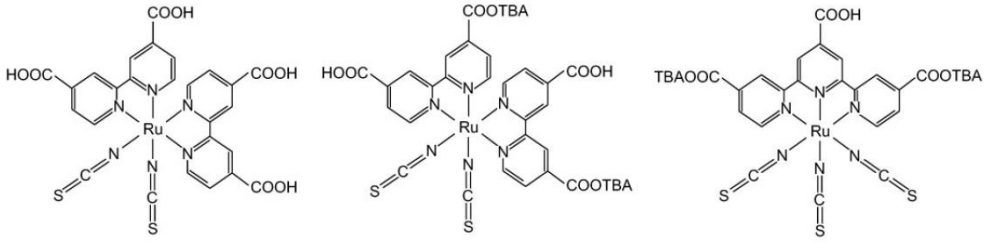

Figure 2.39. Common dyes in DSSCs from left to right N3, N719, N749 (Black Dye)

2.5. Modelling Dye Sensitized Solar Cells

Application of density functional theory (DFT) to DSSCs will take into consideration electron charge transport, recombination, light harvesting and interfacial kinetics. The kinetics of recombination are assumed to be electron density dependent.

A modified continuity equation proposed by Villanueva et al. [60] takes the form:

$$\frac{\partial n(x,t)}{\partial t} = G(x) + \frac{\partial}{\partial x}\left(D(n)\frac{\partial n(x,t)}{\partial x}\right) - k_R(n)(n(x,t) - n_0^0) + \frac{J_{TCO}}{ed} \qquad (2.22)$$

where $n(x,t)$ is the total number density of electrons, as a function of x, the distance to the working electrode and t, time.

$G(x)$ is the term describing the generation rate, $D(n)$ the diffusion coefficient, and $k_R(n)$ the recombination rate. An addition proposed by the authors in [60], $\frac{J_{TCO}}{ed}$ models the TCO/electrolyte interface, where *e* is the elementary charge.

2.5.1. Generation

The generation term describes the injection of electrons into the system due to photon excitation. Generation is a space-dependent function.

2.5.2. Diffusion

The electron diffusion coefficient, D, in the mesoporous oxide film was found to depend strongly on the electron density,

$$D(n) = D_{ref} f(n) = D_{ref} \left(\frac{n}{n_{ref}}\right)^{1-\alpha/\alpha} \quad (2.23)$$

D_{ref} is the diffusion coefficient at the reference density ($n_{ref} = n_0^0$, i.e. in dark condition and 0 bias at the contact). This has been derived from theoretical considerations by Bisquert et al. [61] and random walk simulation [62, 63, 64]. Here α represents the average energy distribution of the trap states below the conduction band, at $\alpha = 0.5$ the diffusion equation displays linear dependence between *D* and *n*.

2.5.3. Recombination

The model used by [60] applies the same principles of diffusion for recombination of electrons with dye molecules or electrolyte, taking them to be density dependent. This was based on literature by Anta et al. [65], the assumption being that since recombination is transport limited, k_R will be proportional to the diffusion coefficient [66, 67].

$$k_R = k_R^{ref} f(n) = k_R^{ref} \left(\frac{n}{n_{ref}}\right)^{1-\frac{\alpha}{\alpha}} \quad (2.24)$$

Where k_R^{ref} is the recombination constant at reference density (dark condition and zero bias at contact).

2.5.4. TCO/electrolyte interface

Villanueva et al. [60] presented an extra term describing the TCO/electrolyte interface based on the Butler-Volmer equation [68].

$$J_{TCO} = J_{TCO}^0 \left\{\exp\left[\frac{-(1-b)eV}{k_B T}\right] - \exp\left[\frac{beV}{k_B T}\right]\right\} \quad (2.25)$$

J_{TCO}^0 is the exchange current density and *b* is the cathodic transfer coefficient.

2.5.5. Extraction of model parameters

The model is dependent on five input parameters, these need to be acquired through experimental measurements.

- UV/Vis spectrum of the dye in solution
- Steady-state photocurrent vs. voltage curves at fixed light intensity
- Photocurrent rise upon application of light source
- Open circuit photovoltage vs. light intensity
- Open circuit voltage decay response of removal of light source

Villanueva et al. [60] compared the model with two dye sensitized solar cells: Cell T, a TiO_2 based cell with N719 dye and a low-viscosity organic electrolyte solution and Cell Z a ZnO_2 based cell sensitized with the same N719 dye and an ionic liquid electrolyte solution.

The results of current-voltage curves are shown in Figure 2.40 and show the models accurately predicting DSSC parameters and behaviours. In the case of ZnO Cell the model is nearly identical to experimental results with TiO_2 Cell closely matching the model for the duration of the linear region but falling off as the curve tails off.

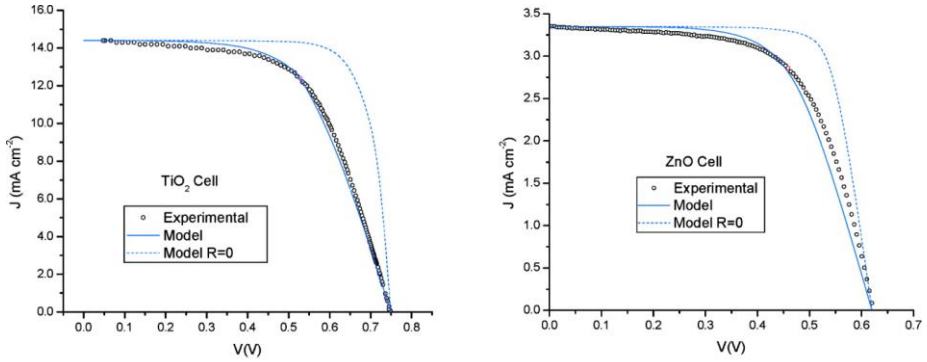

Figure 2.40. Current−voltage curves for the studied cells. The model data were obtained by solving the continuity Eq. (2.22) so that J is computed at different values of the voltage V.

2.6. Photovoltaic/thermal concentrator (PVT)

The technology of harvesting solar energy can be categorised in to the following three areas:

1) *Solar thermal system*: Captured heat from solar collector is directly converted into thermal energy. The output energy can be used for domestic hot water, space heating, agricultural drying and increased ventilation [69].
2) *Photovoltaic (PV) system*: A PV module directly converting sunlight captured by the PV solar panel to direct current electrical energy based on the photoelectric effect [70]
3) *Photovoltaic-Thermal (PV/T) system*: A combined solar thermal /photovoltaic system. The incident solar energy partly converted to electricity and partly to thermal energy [71].

In these devices, the PV modules are mounted together with heat recovery units, by which a circulating fluid flow extracts the heat from the PV panels so as to protect them and increase their efficiency in addition to collecting thermal energy from the sun. Active solar conversion technologies are shown in Figure 2.41.

During 2016, at least 75 GW of solar PV capacity and 0.1 GW concentrating solar thermal capacities were added worldwide. Up to 2017, the cumulative global solar PV and thermal capacity has increased to 303 GW and 4.7 GW, respectively [72]. In the solar thermal system, the evacuated tube or flat-plate are used to collect solar radiation to provide domestic hot water, to heat and cool space, to dry crops, to cook, to distillation, and to provide heat, steam or refrigeration for other industrial or commercial processes. However, the thermal system market is shrinking due to pressure from heat pump and the PV [73].

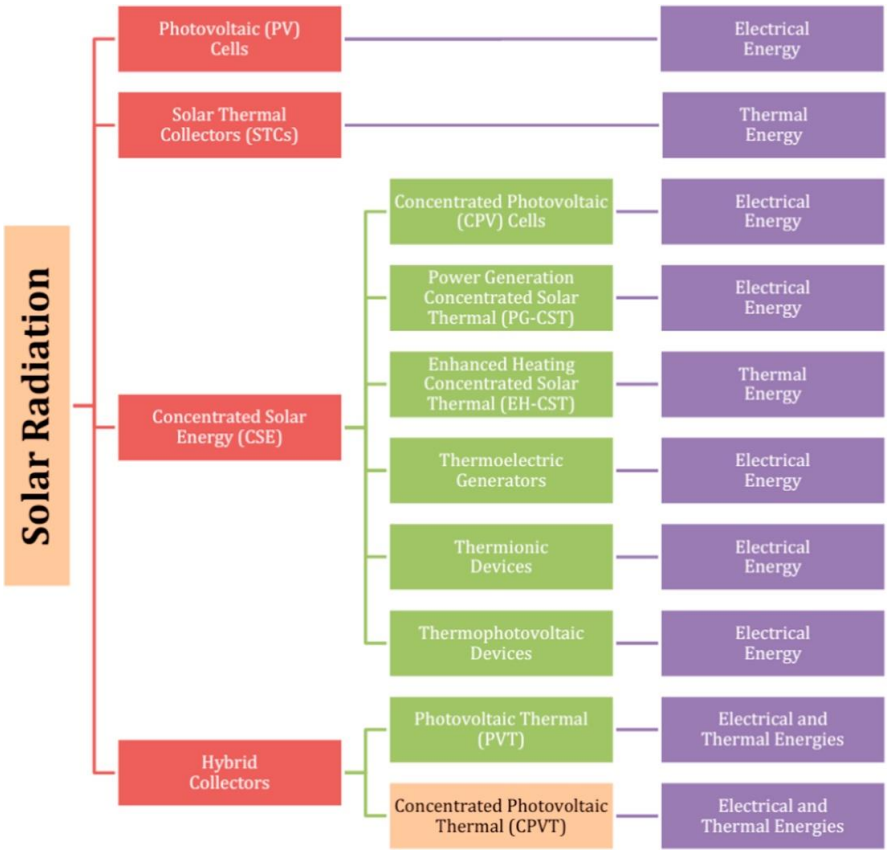

Figure 2.41. Direct conversion paths of main active solar-to-electrical and solar-to-thermal energy technologies [74].

Despite the great progress in PV technologies, the conversion efficiencies of PV systems still has potential for further improvement. Although the 4-junction PV solar cells manufactured by ISE institute of Fraunhofer has reached to 46% conversion efficiency record [75], the

conversion efficiencies of commercialized PV systems are still low; 14–20% for silicon solar cells and 25–30% for III–V multi-junction solar cells [76] where the balance of the remaining solar energy is wasted as heat. The efficiency of solar system can be improved by harnessing the dissipated heat in PV system using combining thermal systems.

As a result, the idea of combining photovoltaic (PV) with solar thermal together with reflective or refractive solar concentrators has been explored as an option for solar system design [77, 78]. The resulting system is known as a concentrated photovoltaic thermal (CPVT) system which is a hybrid combination of concentrated photovoltaic (CPV) and photovoltaic thermal (PVT) systems.

The combined system generates both thermal and electrical energy. Various studies have shown that PVT collectors have higher overall combined efficiencies and they are more cost effective than separate PV and solar thermal systems [79]. This is partly due to increase in the PV panel efficiency due to reduction of PV working temperature. A suitable PV technology for a CPVT system would have high efficiency under concentrated illumination and a low efficiency temperature coefficient. Kern and Russell applied this idea of combining the PV/T system in order to remove the heat on the PV surface so that the efficiency can be improved [80]. A study carried out by Othman et al. [81] reported that for every 1 °C increase in PV panel temperature, there is about 0.4–0.5% decrement in its efficiency. In addition, the bandgap energy of the selected PV should be in accordance with the concentration ratio and PV heat extraction method. The category of PV and PVT systems are shown in Figure 2.42.

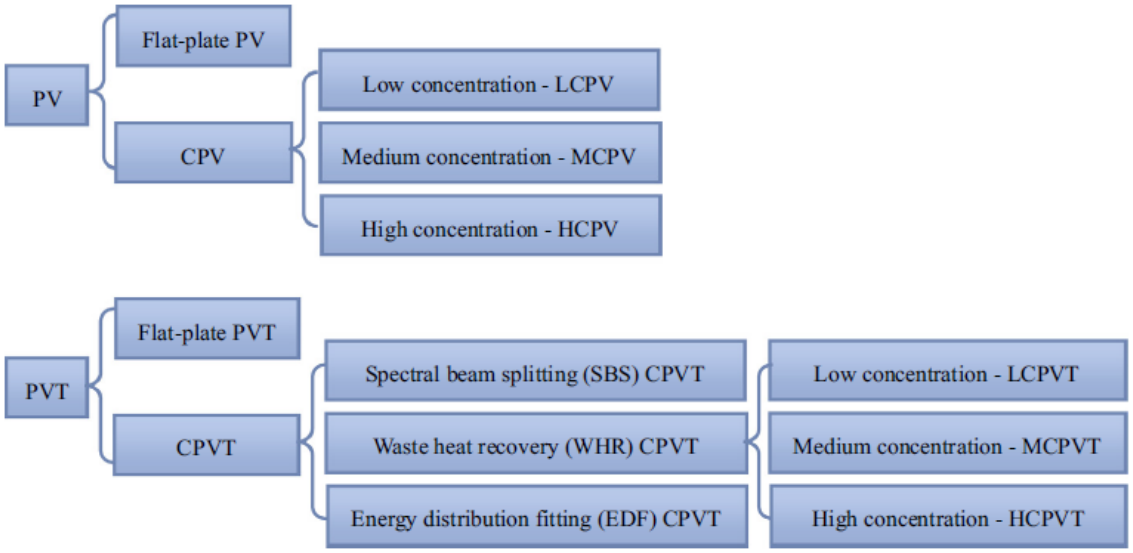

Figure 2.42. The category of PV and PVT systems [82].

Based on the distribution method and conversion sequence of energy flux, concentrating PVT systems (CPVT) are classified into three types: the waste heat recovery (WHR) CPVT, the spectral beam splitting (SBS) CPVT, and the energy distribution fitting (EDF) CPVT. Similar to the CPV systems, as the system configuration is mainly affected by the concentration ratio (CR) of optical concentrators, WHR CPVT systems are further categorized into three types: low CR system(LCPVT) where CR ≤ 10x, medium CR system(MCPVT) where 10x < CR ≤ 100x, and high CR system HCPVT) where CR > 100x [82]. The system configurations and energy flux of WHR, SBS, and EDF CPVT systems are shown in Figure 2.43.

There are various optical systems which have been used in the thermally coupled WHR CPVT systems. The most common ones are flat specular/diffuse reflectors, compound parabolic concentrators (CPCs), linear Fresnel reflectors, parabolic troughs, dish reflectors, tower-heliostats, and Fresnel lenses. The CR of the optical system influences significantly the thermal system design, the type of solar cells, the adoption of tracking systems, the electrical and thermal performance, and the system costs [82].

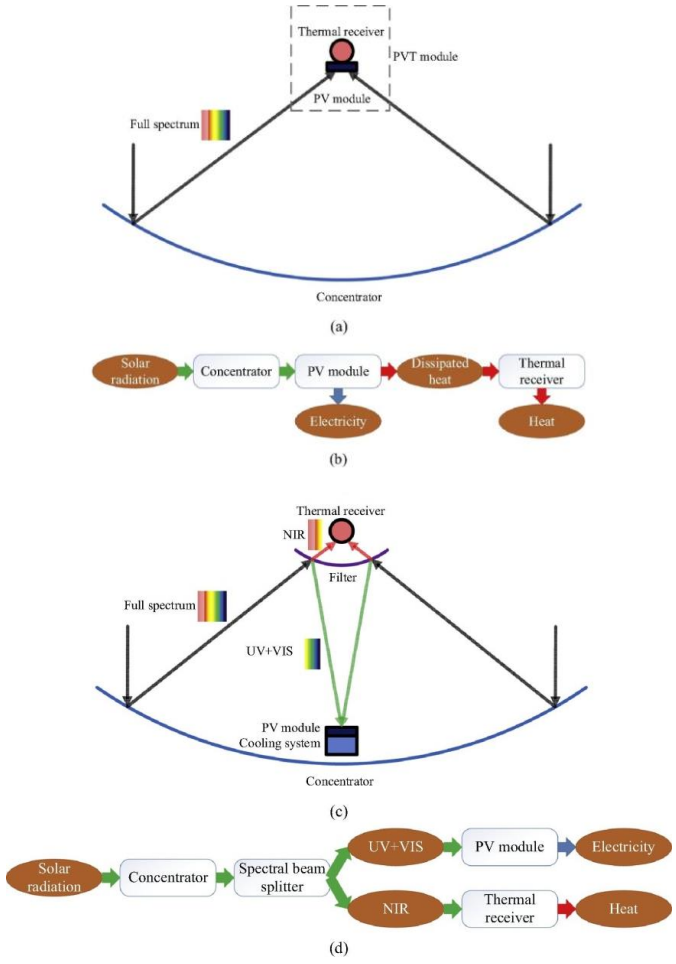

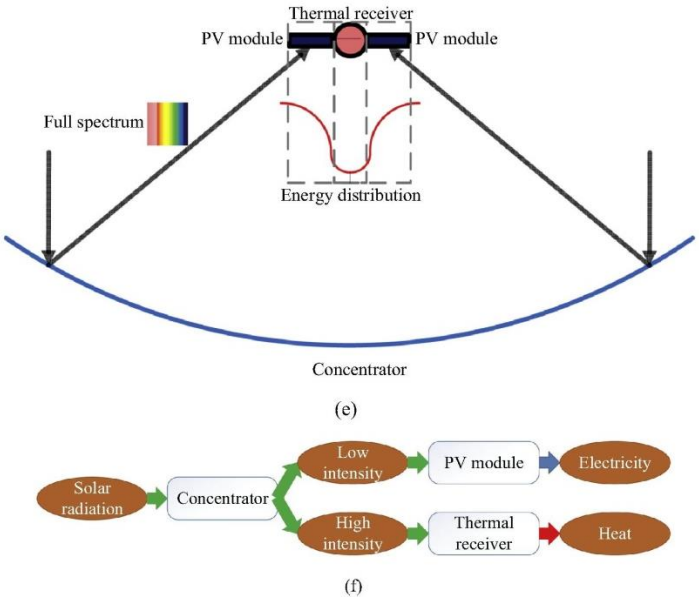

Figure 2.43. The classification of CPVT system: (a) basic system configuration of WHR CPVT; (b) energy flux of WHR CPVT; (c) basic system configuration of SBS CPVT; (d) energy flux of SBS CPVT; (e) basic system configuration of EDF CPVT; (f) energy flux of EDF CPVT [82].

2.6.1. Low concentrating PVT (LCPVT) systems

The LCPVT systems of CR < 10x are the simplest type of CPVT approaches. In LCPVT systems of CR < 4x, both the flat-plate reflector and V-trough are used as the concentrator (see Figure 2.44). The flat-plate specular boosters can be mounted either on one side or both top and bottom sides of the PVT panel. In this system PV solar panels connected in a row and bonded into flat-reflector/V-troughs acting as solar receivers. Water/air flows in pipes or tubes under the solar cells to harvest the wasted heat from solar cell modules.

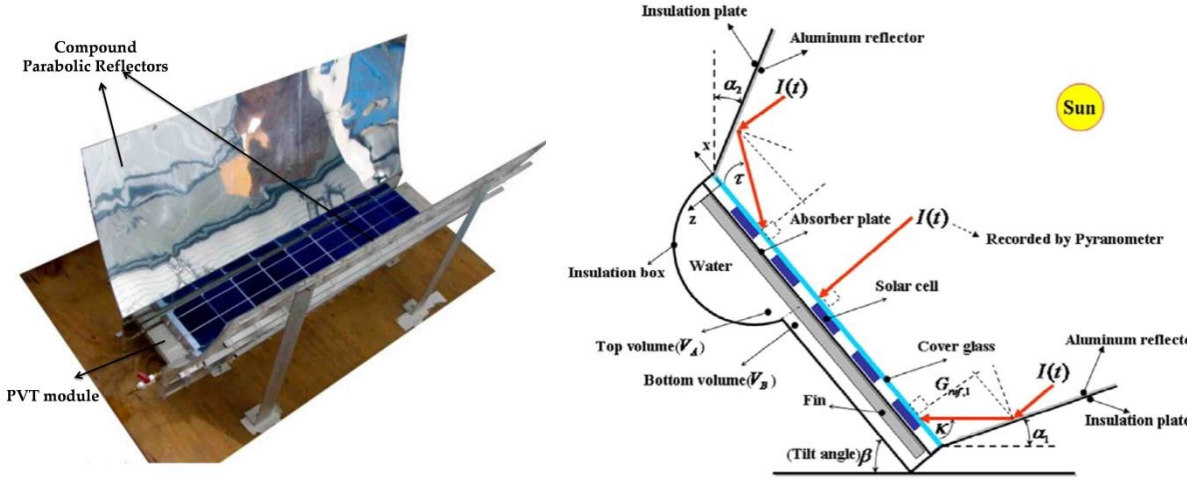

(a) (b)

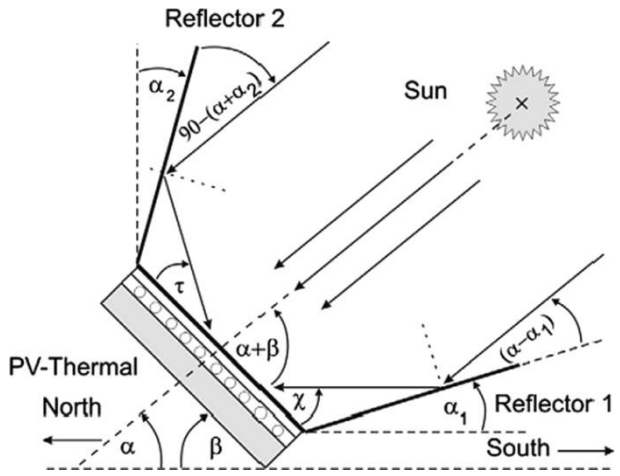

Figure 2.44. (a) Low concentrating CPVT module, (b) the passive cooling LCPVT system with a finned cooling chamber [83], (c) CPVT with booster reflectors [84].

Other design is the flat diffuse reflectors which could achieve smoother solar radiation distributions on the PV surface. In this design the CR on the surface of PV modules is usually lower than that of specular reflectors, however, the diffuse reflectors are cheaper and can be easily combined with standard PV modules. This design has also been used as the building integrated LCPVT (BI-LCPVT) system [85]. In the system shown Figure 2.45 flat aluminium plates are used as the booster diffuse reflectors. By mounting reflectors onto one side of PV panel, an optical CR of 1.35x has been achieved. The experimental results showed 16% improvement in electrical output in comparison to the PVT systems alone, and thermal heat extraction efficiency of 30% for air HTF and 60% for water HTF obtained.

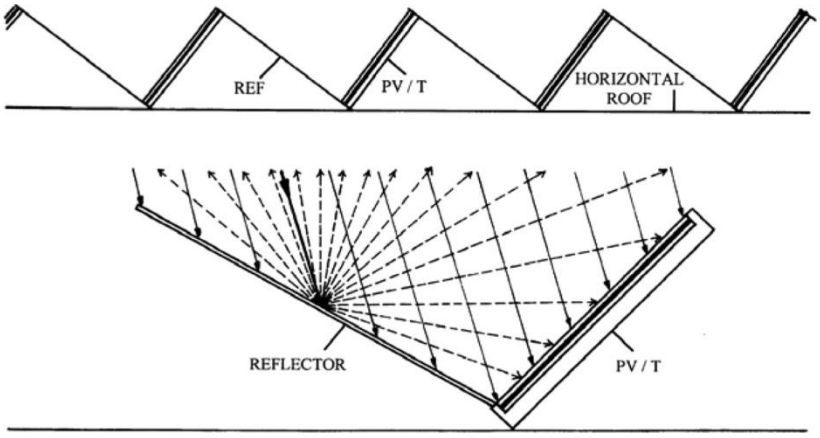

Figure 2.45. The BI-LCPVT system with a booster diffuse reflector [85].

2.6.2. Medium concentrating PVT (MCPVT) systems

MCPVT systems with CRs of 10–100 suns are more complex and usually have solar tracking with more effective cooling. They usually utilize parabolic troughs, linear Fresnel lenses and reflectors as the concentrators. As an example, Figure 2.46 shows a 0.6 mm thick aluminium trough wall Fresnel lens PV Concentrator (FPVC) with a concentration ratio of 100×.

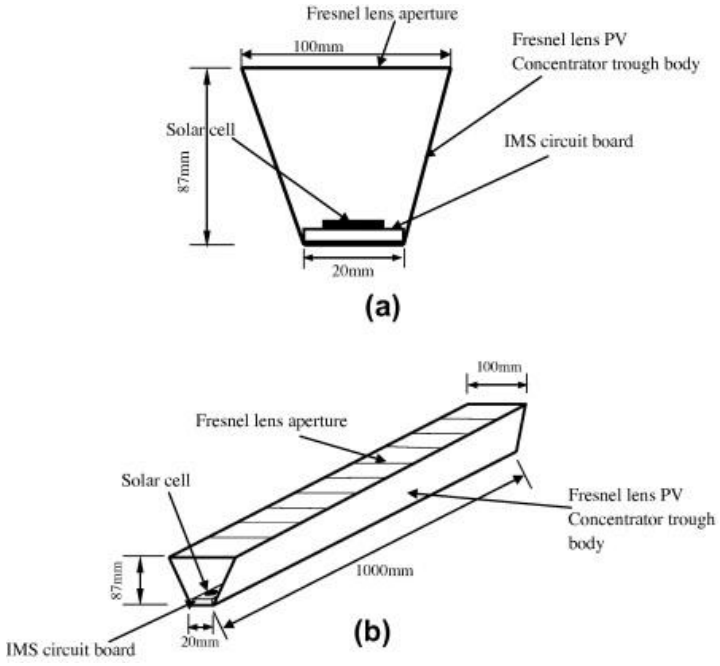

Figure 2.46. (a) Cross sectional view of the experimentally characterised FPVC system and (b) 3D diagram of the experimentally characterised FPVC system. [86]

The authors showed that when the FPVC system tested under a simulated solar radiation intensity of 1000 W/m^2 and ambient air temperature of 50 °C with no forced convection, the predicted silicon solar cell efficiency in the FPVC system was reduced to approximately half that at standard test conditions.

Feng et al. [87] calculated and designed the dimensions of each wedge-shaped element of Fresnel lens shown in Figure 2.47. They used the gallium arsenide high concentrated battery as the receiver and they tested the cylindrical compound transmissive Fresnel CPVT system in the real sky. They studied the performance of the FPVCT system in hazy and clear weathers. The hazy weather has great influence on power generation efficiency, but it has less effect on heat efficiency of cooling water. Test results showed that the total efficiency of thermal and electricity reached more than 55% at noon time (11:00–13:00).

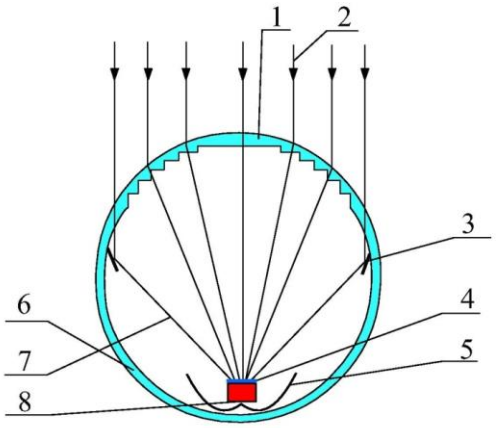

1. transmissive Fresnel solar concentrator; 2. incident light; 3. reflector; 4. gallium arsenide photovoltaic cell; 5. secondary reflector; 6. frame; 7. reflected light; 8. cooling water channel;

Figure 2.47. Working principle of a PV/T system with transmissive Fresnel solar concentrator. [87]

2.6.3. High concentrating PVT (HCPVT)

In CPVT systems subjected to CR > 100x, solar cells operate at very high energy flux and high temperature. These conditions affect the design of the CPVT system configurations in many aspects such as using 2 axis tracking system.

Solar tracking system increases the efficiency of CPVT system. Eke and Senturk [88] analysed the performance of two identical 7.9 kWp PV double axis sun tracking photovoltaic (PV) systems after one year of operation. The PV systems were first in a fixed position and then they controlled while tracking the sun in two axes (on azimuth and solar altitude angles). The test results showed that 30.8% more PV electricity is obtained in the double axis sun-tracking system when compared to the latitude tilt fixed system.

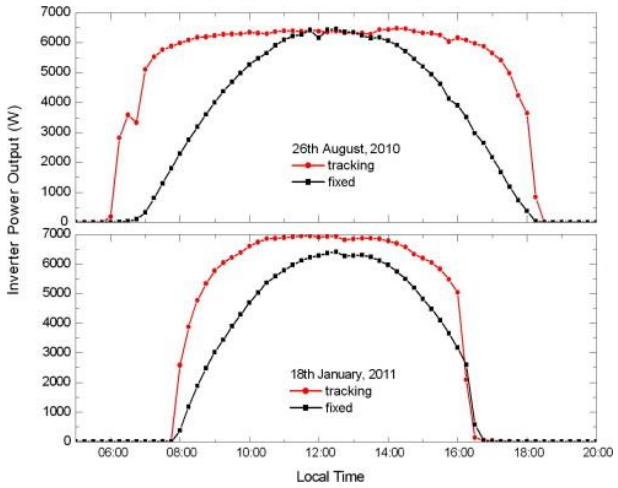

Figure 2.48. PV systems operation in representative days. [88]

Tripathi et al. [89] analysed partially covered Photovoltaic thermal (PVT)-compound parabolic concentrator (CPC) water collector (see Figure 2.49) coverall thermal energy gain and exergy gain four different cases; case (i) 25% PV coverage area, case (ii) 50% PV coverage area, case (iii) 75% PV coverage area and case (iv) 100% PV coverage area, on each collector. On the demand of electrical and overall exergy, case (iv) which covers the concentrator completely has been found to be maximum. On the other hand, when the demand of thermal gain is needed, case (i) which only covers a quarter of concentrator area is first choice producing overall thermal energy gain of five times greater than case (iv) (Figure 2.50).

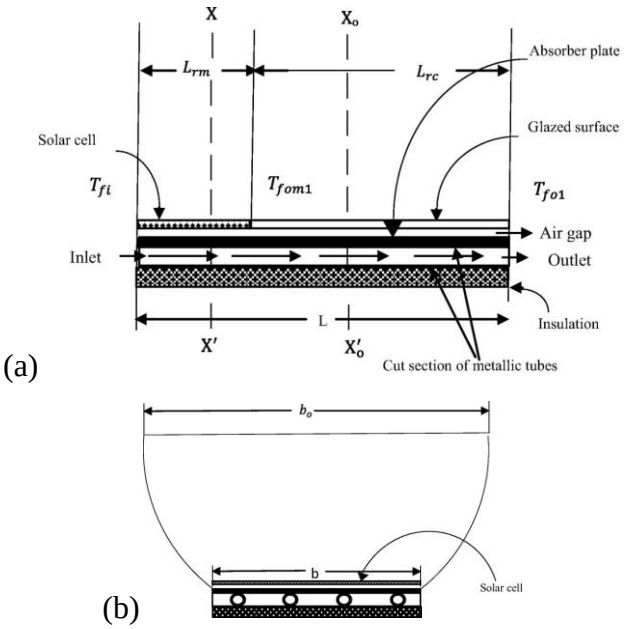

Figure 2.49. (a) Cross section side view of partially covered first of PVT-CPC collector with A_r = 1 m^2, A_{rm} = 0.25 m^2 and A_{rc} = 0.75 m^2, (b) Cut section XX' front view of partially covered of first of PVT-CPC collector where A_a = 2 m^2. [89]

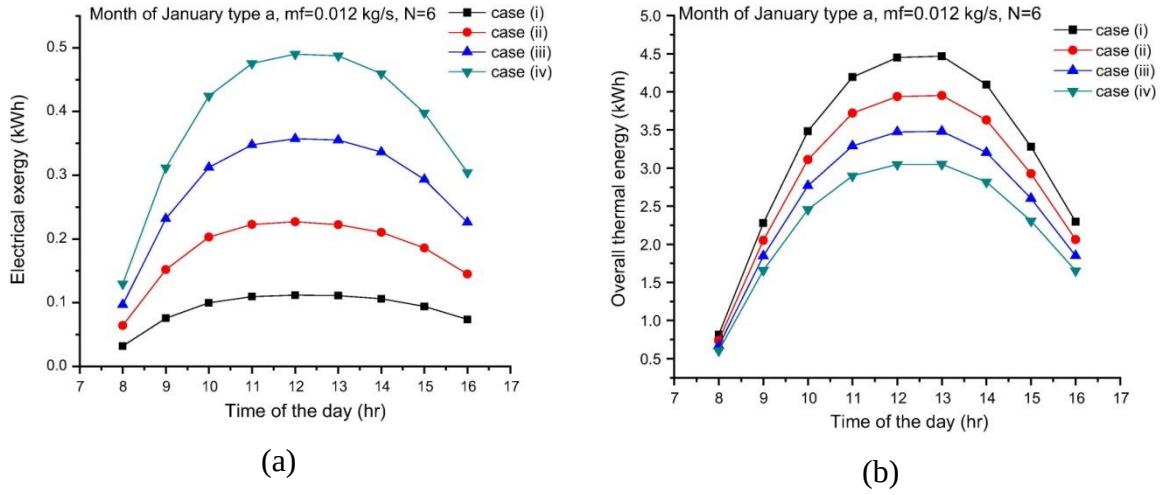

Figure 2.50. (a) Hourly variation of electrical exergy of a typical day in month of January for four different cases, (b) Hourly variation of overall thermal energy gain of a typical day in month of January for four different cases. [89]

Abdelhamid et al. [90] developed a novel double stage high-concentration hybrid solar photovoltaic thermal (PVT) collector (Figure 2.51) using nonimaging optics and world record thin film single-junction gallium arsenide (GaAs) solar cells. The system uses a parabolic trough (primary concentrator) to focus sunlight towards a secondary nonimaging compound parabolic concentrator (CPC) to simultaneously generate electricity from single junction GaAs solar cells, as well as high temperature dispatchable heat. The solar cells are placed inside the vacuum tube to act as spectrally selective mirrors for lower energy photons to maximize the system exergy, and the secondary concentrator allows the thermal component to reach a concentration ratio ~60. The maximum outlet temperature reached 365 °C, and on average the thermal efficiency of the experiment is around 37% and the maximum electrical efficiency is around 8% (Figure 2.52). The total system electricity generation is around 25% of incoming direct normal irradiance (DNI).

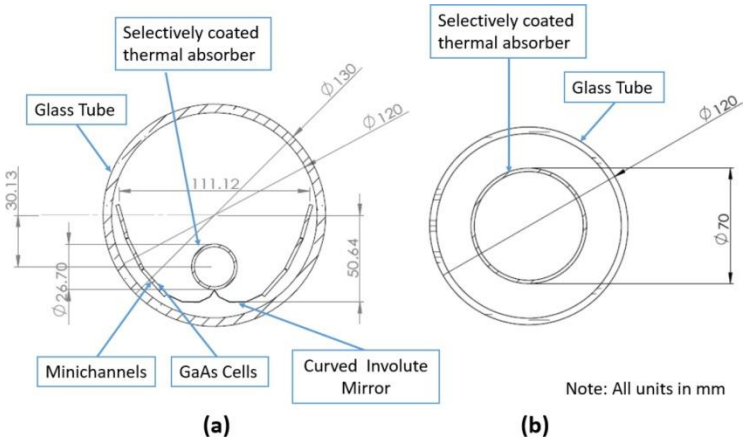

(c)

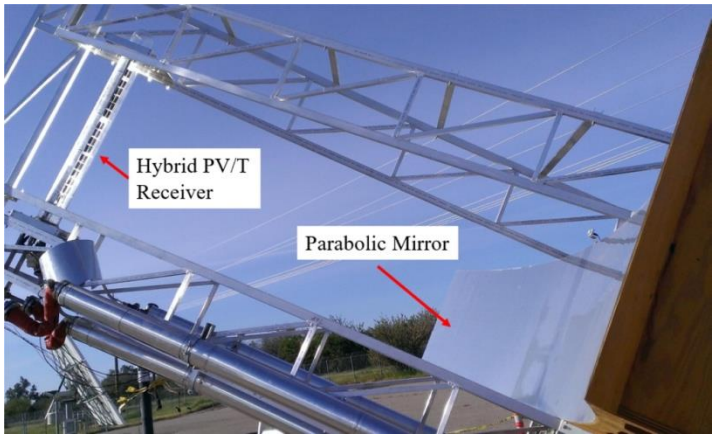

Figure 2.51. (a) Hybrid PV/T receiver (b) Standard receiver, (c) Parabolic mirror and hybrid PV/T receiver. [90]

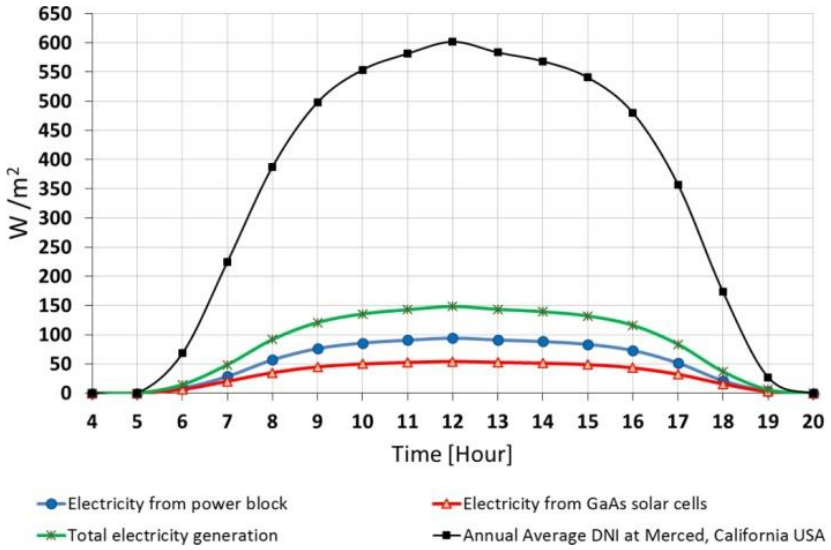

Figure 2.52. Average annual hourly direct normal irradiance (DNI) at Merced, CA and annual hourly average PV/T system electricity generated per system aperture area (W/m2). [90]

Some other designs of PV/T systems are summarised in Figure 2.53 below.

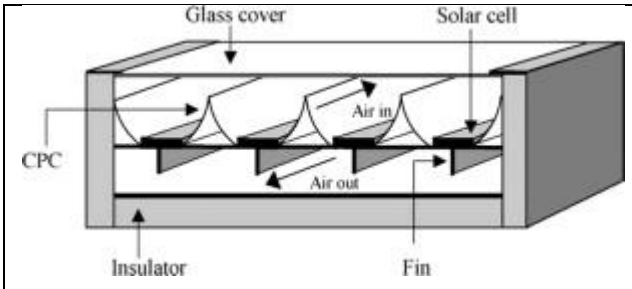

Schematic model of a double-pass photovoltaic thermal solar collector with CPC and fins [91]. Indication of diffuse reflected radiation on the PV panel [92].

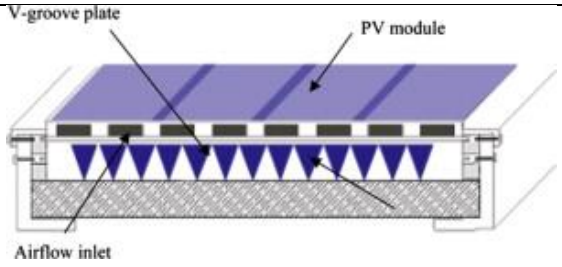

Schematic diagram of PV/T collector with V-groove absorber collector [81]. Cross-section of bi-fluid type PV/T design collector [93].

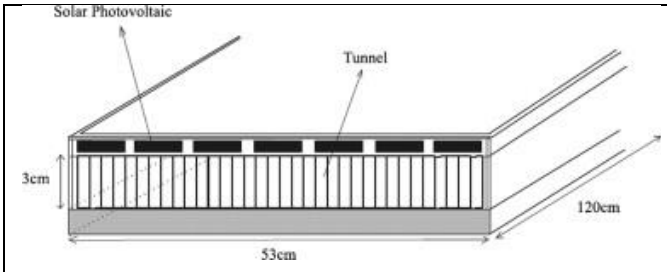

Schematic diagram of PV/T collector with rectangular tunnel absorber collector [81].

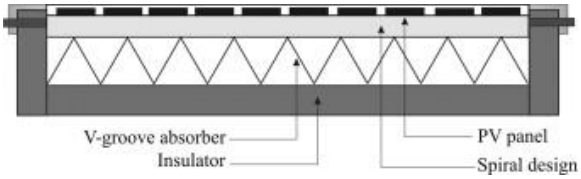

Schematic diagram of PV/T Combi with spiral and V-groove design for water and air absorbers, respectively.

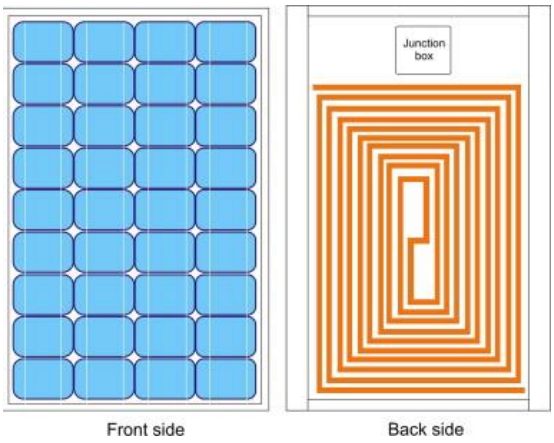

Position of spiral absorber underneath the PV module [94].

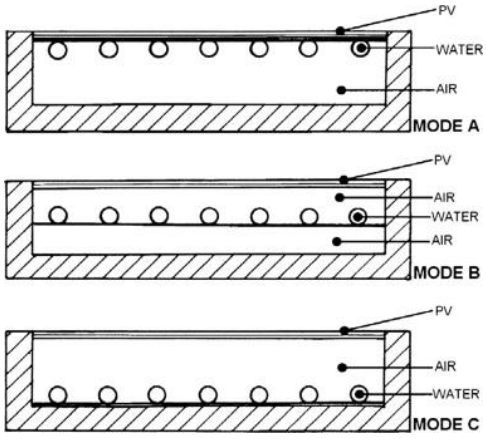

Designs of PV/T dual system [95].

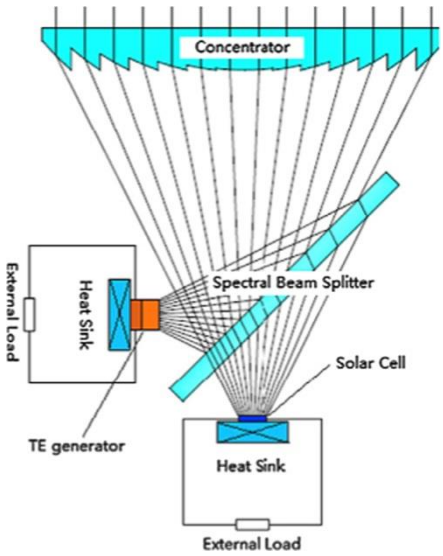

CPVT system with spectral beam splitter and thermoelectric generator [96].

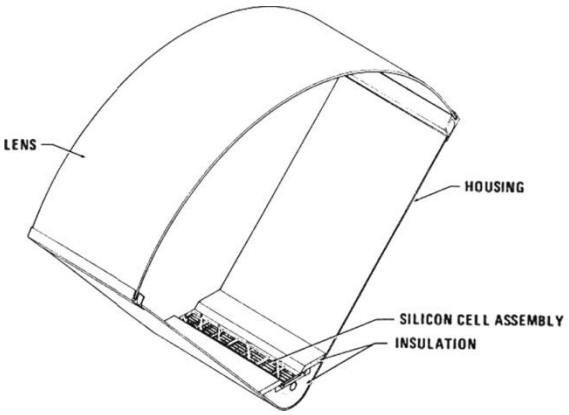

Schematic of a module of the linear Fresnel lens-based CPVT used at the DFW airport [131].

Figure 2.53. Various designs of PV/T systems

Kunnemeyer et al. [77] showed that the V-trough offered improved electrical yields from both concentrating radiation onto the photovoltaic cells and also by actively cooling them. Also, it

was shown that the V-trough could be made of a durable (long life) stainless steel, rather than the more reflective aluminium, while still offering a 25% increase in incident radiation over a typical year. However, it was noted that modifications would be needed to improve cooling and to increase the thermal efficiency by reducing heat losses [77].

2.7. Solar Concentrators

In order to increase the energy production there are two options either to increase the system scale (e.g. by increasing the number of receivers) or to concentrate the radiation flux by placing a concentrator (usually some kind of optical device) between the light source (sun) and the receiver. The most common concentrators are reflectors (mirrors) and refractors (lenses), which modify and redirect the incident sunlight beam. The design of the concentrating optics varies. Some of the examples of concentrating collectors, which involve diversely shaped mirrors, are shown in Figure 2.54, as they applied to the solar-to-thermal energy conversion.

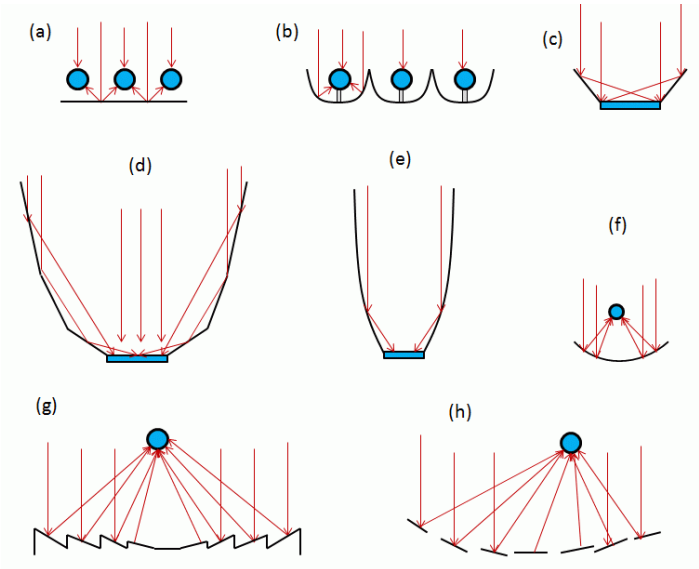

Figure 2.54. Types of concentrating sunlight collectors: (a) tubular absorbers with diffuse back reflector, (b) tubular absorbers with specular cusp reflectors, (c) plane receiver with plain reflectors (V-trough), (d) multisectional planar concentrator, (e) compound parabolic concentrator (f) parabolic trough, (g) fresnel concentrator, (h) array reflectors (heliostats) with central receiver. Concentration of light on the receiver is achieved by shaping the reflectors (mirrors) around the receiver (represented by blue circles) [97].

2.7.1. Concentrator Categories

Concentrated Photovoltaics (CPV) are typically broken down into three categories based on their concentration factors.

Low concentration PVs (LCPV) are systems with concentrations factors between 2-10. The systems emanate a low enough heat flux that the cells can be passively cooled rather than

actively. Furthermore, LCPVs have a wide acceptance angle meaning it is possible to design systems where active solar tracking does not occur.

Medium concentration PVs range from 10 to 300 concentration ratios. At these solar intensities, both active cooling and dual axis tracking would be required.

High concentration photovoltaics (HCPV) are systems that magnify the incoming light by factors of 300 and more. The economy of such a system makes usage of multi-junction PVs viable for terrestrial solar generators [98].

2.7.2. Parabolic Trough Concentrator

Parabolic Trough Concentrators (PTC) are trough-shaped parabolic concentrators which use reflective material to concentrate solar energy from their aperture area to a central tube, referred to as a Dewar tube. In most cases the output of interest is thermal energy in the form of heated liquids such as water. This is used either directly for consumption or fed to the steam turbine for power generation. A schematic of the PTC is shown in Figure 2.55 [99].

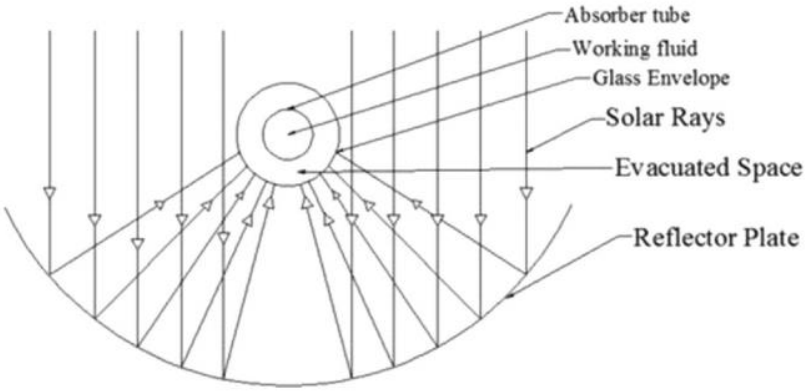

Figure 2.55. Parabolic Trough Concentrator schematic.

Two of the three parameters rim angle, aperture width and focal length are sufficient to determine the cross-section of a parabolic trough completely, i.e. shape and size.

ψ can be expressed as a function of the ratio of the aperture width to the focal length:

$$tan\psi = \frac{\frac{a}{f}}{2-\frac{1}{8}\left(\frac{a}{f}\right)^2} \tag{2.26}$$

As a result, the ratio of the aperture width to the focal length can be expressed as a function of the rim angle:

$$\frac{a}{f} = -\frac{4}{tan\psi} + \sqrt{\frac{16}{tan^2\psi} + 16} \qquad (2.27)$$

The surface area of a parabolic trough may be important to determine the material need for the trough. The area is calculated as follows:

$$A = \left(\frac{a}{2}\sqrt{1 + \frac{a^2}{16f^2}} + 2f.ln\left(\frac{a}{4f} + \sqrt{1 + \frac{a^2}{16f^2}}\right)\right).\ell \qquad (2.28)$$

Where *l* is the length of the parabolic trough concentrator.

For the collector the geometrical concentration ratio (C_G) is defined as the ratio of the collector aperture area ($A_{ap,c}$) to the receiver aperture area ($A_{ap,r}$):

$$C_G = \frac{A_{ap,c}}{A_{ap,r}} \qquad (2.29)$$

In many cases, the projected area of the absorber tube is chosen as the receiver aperture area. Hence

$$C_G = \frac{a.\ell}{d.\ell} = \frac{a}{d} \qquad (2.30)$$

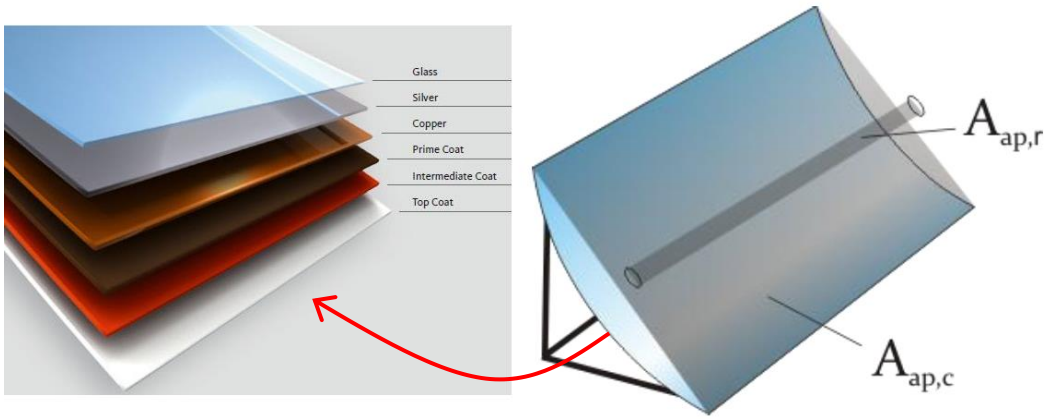

Figure 2.56. Collector aperture area and receiver aperture area with Flabeg multi-layered mirror. [100]

Another possibility is to take the irradiated absorber surface area as the receiver aperture area. In real parabolic troughs this would mean that the whole absorber tube surface area ($\pi.d.\ell$) is the receiver aperture area

$$C_G = \frac{a.\ell}{\pi.d.\ell} = \frac{a}{\pi d} \qquad (2.31)$$

This definition leads to a lower geometrical concentration ratio. However, the concentration ratio according to the projected areas is more commonly used.

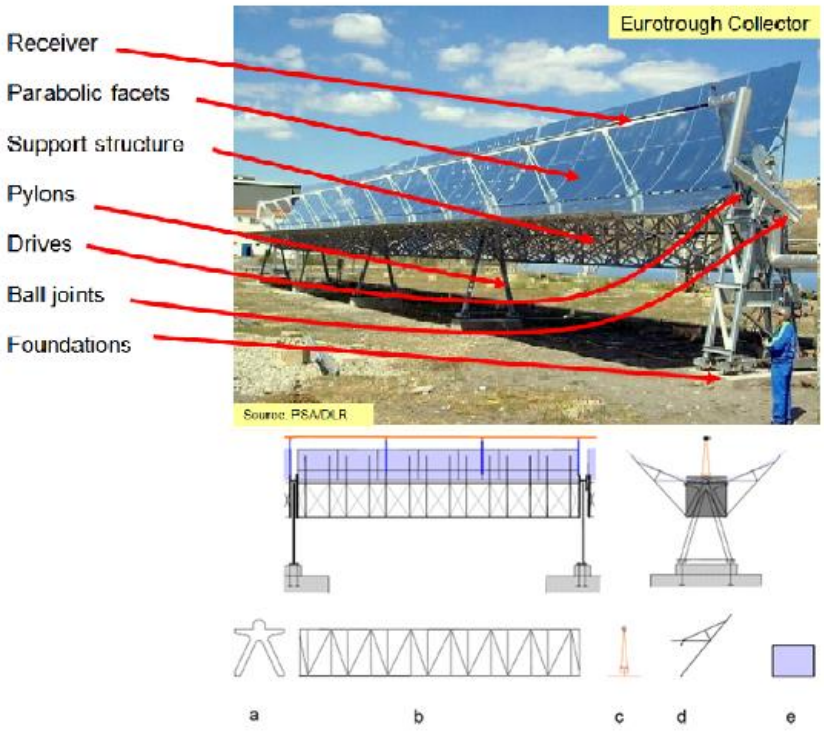

Figure 2.57. Eurotrough module structural elements: (a) front and rear endplates for mounting to the pylons, (b) space frame structure, (c) receiver supports, (d) cantilever arm, (e) mirror facet. [101]

2.7.3. Parabolic Dish Concentrator

Parabolic dish concentrators use satellite-like reflective dishes to concentrate sunlight onto a small focal area. Parabolic dish concentrators can go between 100-factor concentration for silicon solar cells to 500-factor concentration for group III-V devices (e.g. GaAs-based devices). The theoretical maximum concentration for a point-focus concentrator is $1/\sin^2 x$ based on geometrical anaylsis. However, point focused concentrators require tracking in 2-axis (x and y). Hijazi et al. (2016) described the design of a low cost parabolic solar dish concentrator [102] as shown in Figure 2.58.

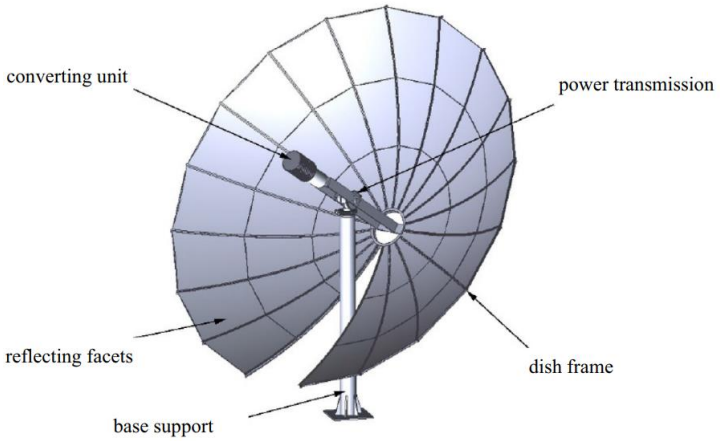

Figure 2.58. Schematic frame of a parabolic dish concentrator *[102]*.

2.7.4. V-trough Concentrator

V-trough concentrator uses linearly inclined reflectors to concentrate light from a wider inlet aperture, W_{ape} to an absorber area, W_{abs} as shown in Figure 2.59. Sangani and Soanki (2007) looked at a 2-sun V-trough concentrator which showed a 44% increased electrical output leading to a 24% overall reduction in cost of electricity [103].

Kunnemeyer et al. [77] showed that the V-trough can improve electrical yields from both concentrating radiation onto the photovoltaic cells and also by actively cooling them. Also, they showed that the V-trough made from a durable (long life) stainless steel, rather than the more reflective aluminium, offering a 25% increase in incident radiation over a typical year [77].

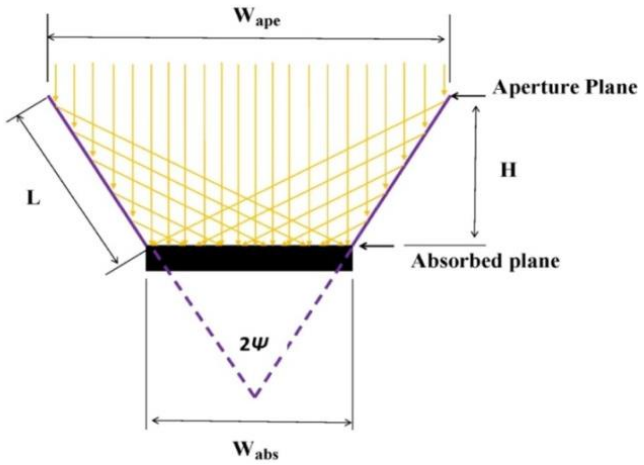

Figure 2.59. V-trough concentrator schematic *[104]*.

2.7.5. Compound Parabolic Concentrator (CPC)

The compound parabolic concentrators (CPC) are of nonimaging concentrators, which are capable of collecting both beam and diffuse available radiations and directing them to the receiver. In comparison to parabolic troughs concentrators, CPCs do not have the strict requirements for the radiation incidence angle. This makes CPCs attractive for system simplicity and flexibility. Like parabolic and other shapes, CPC concentrators can be applied in both linear (troughs) and three-dimensional (parabolocylinder) versions. The trough CPCs are most widespread for this type of concentrator. The structure of a CPC is shown in Figure 2.60. In Chapter 4 ray tracing for the design of CPCs is discussed in details.

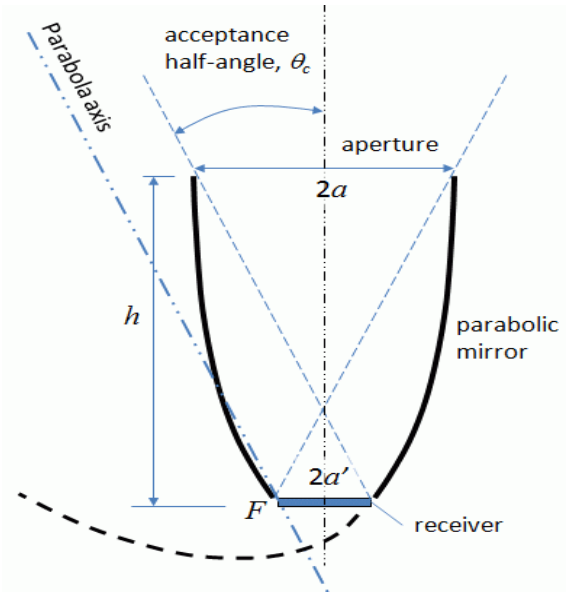

Figure 2.60. Composition of a Compound Parabolic Concentrator (CPC).

CPCs applications are classified in Figure 2.61 used in PV systems including variable-focus-parabolic (VPF) and rotationally asymmetrical compound parabolic concentrator (RACPC), in solar thermal for daylighting in either control or collection and other applications.

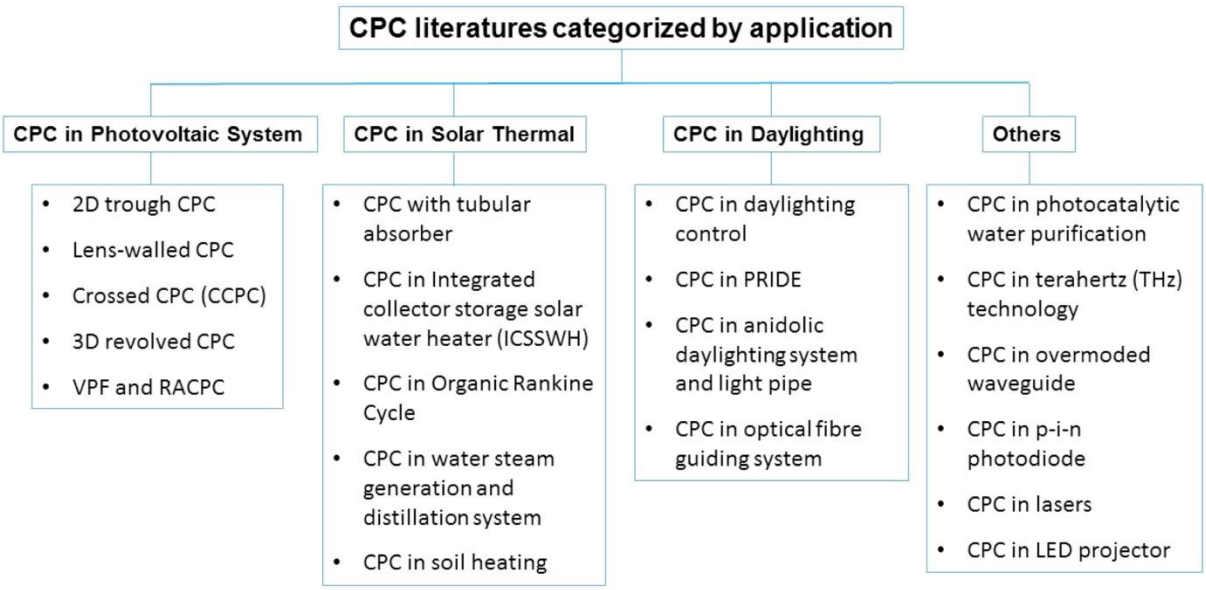

Figure 2.61. Various applications of CPCs [105]

2.7.6. Tracking

As the sun rises from the East to the West through the day and its path moves North-South during the year, the solar radiation incidence on the Earth's surface varies both based on the time of the day, and day of the year.

Surface incidence is governed by Lambert's *cosine law* which states that the intensity of light on a surface is proportional to the cosine of the AoI. This means that even for non-concentrating flat PV panels, there is a loss based on light incidence angle (shown in Figure 2.62). Wilson and Ross (NASA's Jet Propulsion Laboratory) conducted an analysis on the effects of AoI on PV cells including the effect of soiling and background [106].

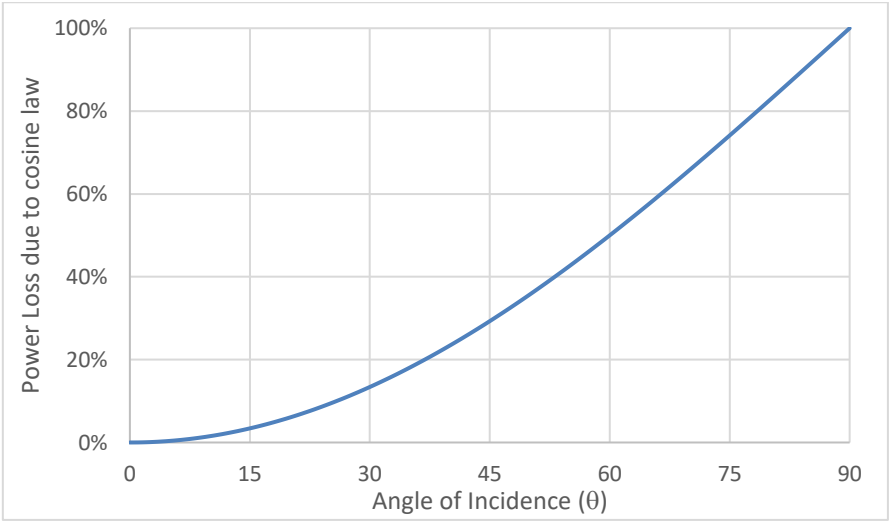

Figure 2.62. Power loss due to Lambert cosine law

Therefore, PVs perform best with light at normal incidence to the PV surface (i.e. 0° angle of incidence). Another method is to rotate the surface of the PV systems to face the sun as it moves across the sky such that rays hit normal to the surface: this is achieved through solar tracking systems.

The use of tracking systems is especially important when concentrating systems are employed. HCPV systems such as dish concentrators requires tracking with ~0.1° accuracy [107] for power output, dropping to virtually zero with any major deviations.

Tracking systems are classified by their modes of motion. A receiver surface such as a PV cell can rotate about three axes, two horizontal and one vertical (Figure 2.63). In single axis tracking systems, the surface rotates over one axis, this can be done parallel to the earth's axis (Figure 2.64(b)), coverage over an east-west range (Figure 2.64(d)) or a north-south range (Figure 2.64(c)). A combination of two axes can be employed to create a 2-axes tracking system (Figure 2.64(a)) allowing coverage over any altitude and azimuth angle.

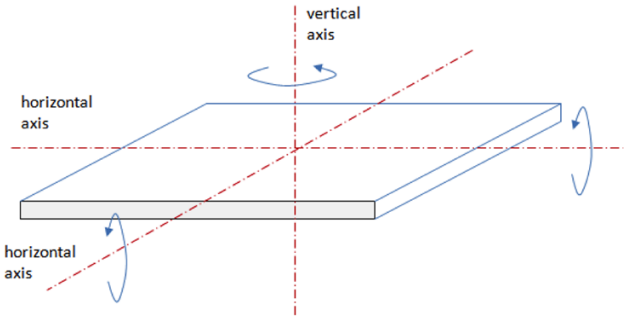

Figure 2.63. Three axes of rotation of a surface

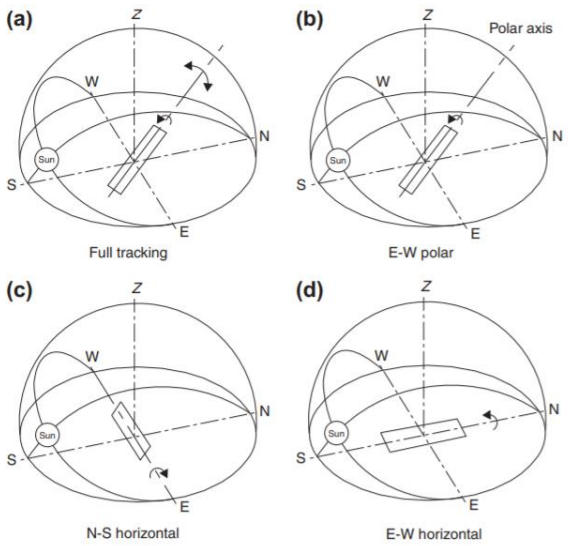

Figure 2.64. Various modes of tracking [108]

Sangani et al. [103] tested a V-trough (2-sun) concentrator using different sun trackers under three tracking modes [A] seasonal tracking, [B] 1-axis N-S tracking, [C] diurnal tracking. I-V and P-V characteristics under 900 Wm^{-2} are shown in Figure 2.65.

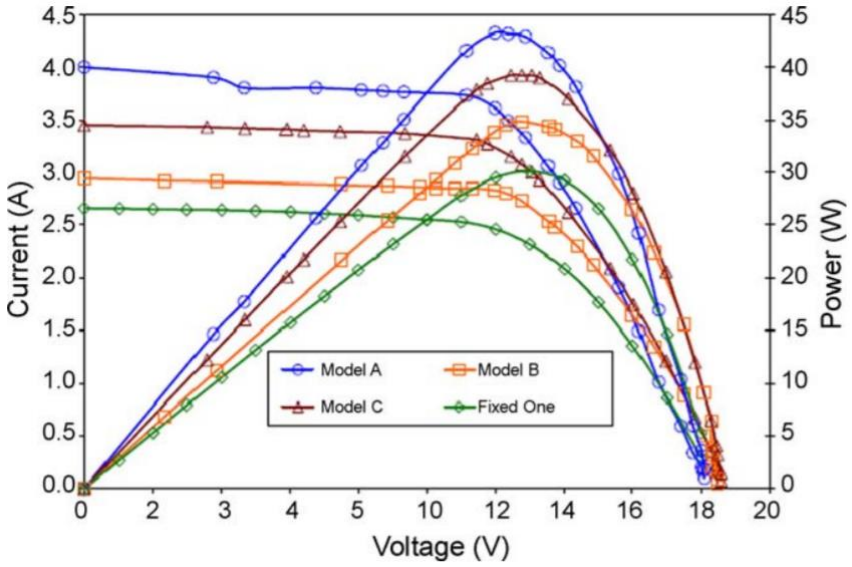

Figure 2.65. I-V and P-V curves of V-trough concentrator under various tracking modes and fixed condition [103]

Trackers can be categorized as shown in Figure 2.66 below:

Single Axis Trackers:

A. Horizontal single axis tracker (HSAT) – tracks daily E-W motion of the sun
B. Vertical single axis tracker (VSAT) – can be set up in N-S or E-W orientation to track the sun, rotating about a vertical axis relative to the ground
C. Tilted single axis tracker (TSAT) – axis of rotation between vertical and horizontal, the daily E-W motion of the sun is tracked by setting the axis of rotation to be parallel to the axis of the earth's rotation
D. Polar aligned single axis trackers (PSAT) – aligns to the polar star by ensuring tilt angle is the same as the location latitude

Dual Axis Trackers:

E. Tip–tilt dual axis tracker (TTDAT) – Tracks the E-W and N-S motion of sun through a combination of vertical and horizontal rotation axes
F. azimuth–altitude dual axis tracker (AADAT) - tracks E-W motion sun and N-S motion of the sun using a large ground-mounted ring mounted with a series of rollers

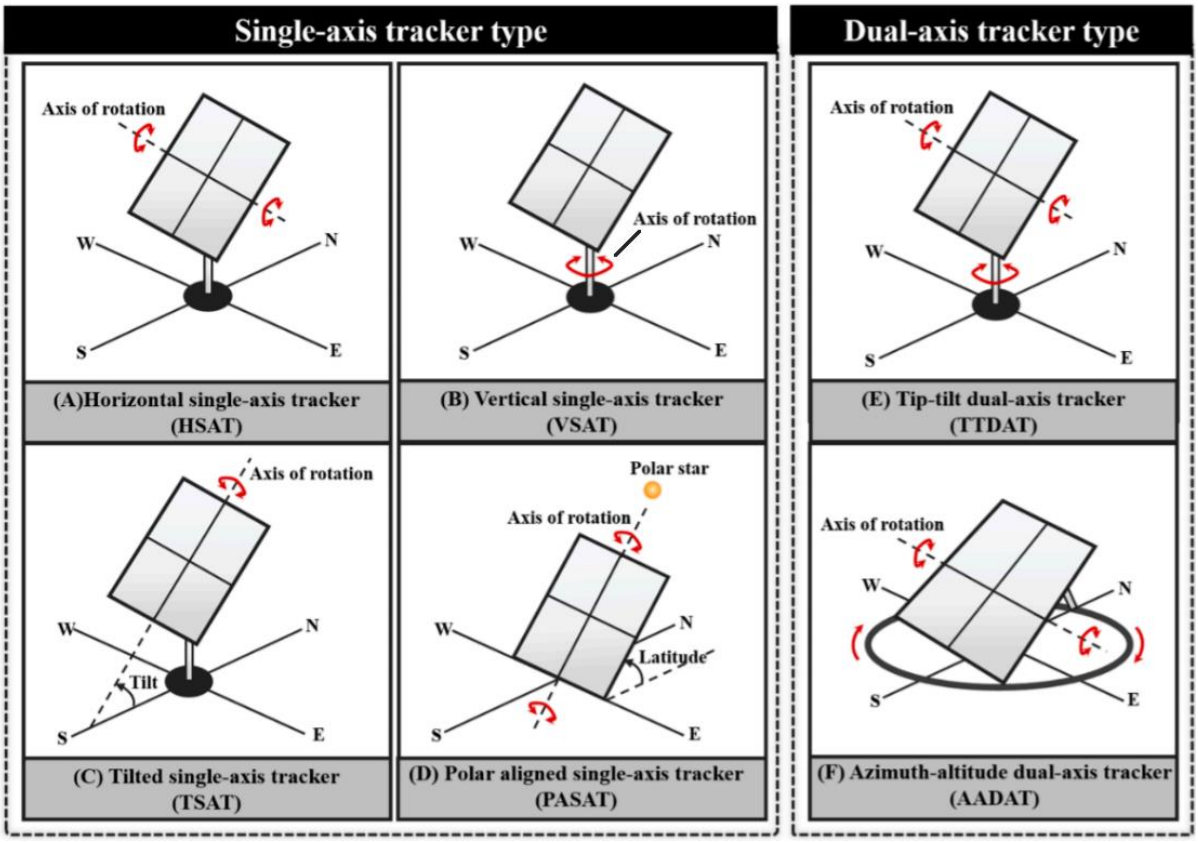

Figure 2.66. Single-axis and Dual-axis tracker types [109]

2.8. Summary

In this chapter the principal workings of PV systems and the details of various CPV/T has been discussed. The CPV/T has been categorised into low, medium and high concentrating systems. In Table 2.3 various features of different categories of CPV/T systems have been compared.

In Chapter 4 v-trough and compound parabolic concentrates have been modelled and the performance of the collector has been investigated both analytically and numerically using ray tracing software. Chapter 5 continues this by fabricating v-trough and CPC CPV/T systems to experimentally establish and verify the characteristics of the systems. The results are compared with the literature.

Table 2.3. Comparison of different CPVT systems.

Features of the system	LCPV/T systems	MCPV/T systems	HCPV/T systems
Optical	- The flat-plate reflectors and the CPC optical systems can provide geometrical CRs lower than 4 suns and optical CRs lower than 2.5 suns. - The systems are usually stationary to avoid the expensive tracking systems. - At a higher 4< CR < 10, the linear focused system with 1-axis tracking is used. - The integration of LCPVT system with building and greenhouse highly depends on its CR. - The diffuse radiation plays an important role in the LCPVT systems.	- The linear concentration optics, including the parabolic trough, linear Fresnel lens and reflector, can provide a CR of 10–100 suns. - Both 1-axis and 2-axis tracking systems are used. - The domed Fresnel lens is more popular than the flat one since domed Fresnel lens has advantages of reduced coma, minimum reflectance, and shorter focal length [110]. - For greenhouses and buildings with large surfaces and illumination demand, a stationary concentrator with a moving receiver is a viable choice.	- Concentrating optics such as dish reflectors or spot Fresnel lenses that concentrate sunlight to intensities of 100 suns or more. - The systems with 2-axis tracking parabolic trough or tower-heliostat are also used, but they are not considered as the main research object, as the CR and cost of 2-axis tracking parabolic trough are not competitive in HCPVT systems.
The PV subsystem	- At CR lower than 10 suns, the commercially available silicon solar cells, including monocrystalline, polycrystalline and amorphous silicon (c-Si, pc-Si and a-Si) solar cells, are usually selected in the LCPVT for economic reasons. The typical conversion efficiency of these solar cells is lower than 20%. - For LCPVT systems with flat specular or diffuse reflectors, the solar panels are directly applied, which would be easy to assemble. - For systems with V-trough, CPC trough, parabolic reflector and linear Fresnel lens solar collectors, the solar cells are connected linearly to make up the PVT absorber.	- Crystalline silicon solar cells, as the pc-Si and a-Si cells are not quite suitable to be operated at the CR over 10 suns. With the use of linear concentrators, the cells are packed linearly in nearly all designs. - At the CRs of over 10 suns, the uniformity of solar radiation plays an import role in the PV efficiency. - The system performance can be improved by better mirror reflectivity, and by pursuing a suitable focal line with uniform illumination.	- Multi-junction solar cells are currently favoured over silicon as they are more efficient at higher CRs and temperatures. - Though the cost of multi-junction GaAs solar cell is much higher than that of comparable silicon cells, the cell cost remains a small fraction of the cost of the overall HCPV system, and the system economics favour the multi-junction GaAs cells. - To achieve current matching, various PV connection methods were investigated, and the total cross tied (TCT) method achieved less mismatching loss [111].

The thermal subsystem	- Water or air is adopted as the main HTF - Flowing through a tube/channel with or without fins, the coolant temperature increases to 40–60 °C for tap water or local heating. - Can also provide illumination for greenhouse or buildings. - Passive cooling systems or thermosiphon systems are not commonly used in LCPVT systems, since active cooling systems can provide more convenient and controllable solutions. - to store the thermal energy, a water tank would be a regular solution. Other methods, including PCM heat storage, are still in the early stage.	- Thermal load on MCPVT systems increases, and passive cooling or thermosiphon methods are not suitable. - Channels with fins are more frequently adopted as the cooling structure - Water is considered as a primary HTF.	- For systems operating at over 100 suns high-capacity heat sinks are required to prevent thermal destruction - Microchannel heat sinks have the advantages of high heat transfer performance, easy integration with moving components, light weight, and high stability, and is a viable method to cope with the extremely high thermal load. - Water-glycol mixture and pressurized water are used as the cooling fluid at temperatures above 100 °C. - A closed thermal cycle and a secondary heat exchanger are necessary for these systems.

Chapter 3 Dye Sensitized Solar Cell

3.1. Introduction

Dye Sensitized Solar Cells (DSSCs) represent one of a 3rd generation of solar cells challenging traditional inorganic solid-state junction devices [112] typically made of silicon. One of the differentiating factors in DSSC devices is the separation of light absorption and charge carrier transport. This refers to the dislodging of electrons due to light absorbed by the dye sensitizer and injection into the semiconductor. This proves beneficial as the absorber dye can be separately optimised for spectral absorption and the semiconductor optimized for carrier transportation. This difference in electron injection rather than electron promotion also means a hole is not induced in the semiconductor and the rate of electron recombination to the dye is much slower than electrons gained by the dye (backflow) from the electrolyte causing DSSC cells to show exceptional low-light performance [113].

Unlike crystalline silicon solar cells which are based on rigid single or multi crystal wafers, dye sensitized solar cells are based on a multi-layer schematic of semiconductor paste material, sensitizer dye and electrolyte, all of which are flexible in nature. This means the choice of substrate becomes the dominant factor in the flexibility of the solar cell. Figure 3.1 shows some commercially manufactured DSSCs by GCell [114].

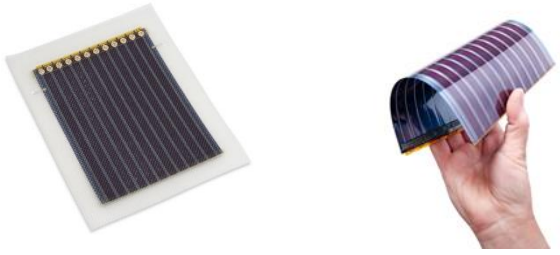

Figure 3.1. Flexible Commercial Dye Sensitized Solar Cell (manufactured by GCell UK)

The history of DSSCs is deeply rooted in advances in photography. It is a convergence of photography and photoelectrochemistry, both rely on photo-induced charge separation at a liquid-solid interface [47]. In 1839, Edmond Becquerel observed the first photovoltaic effect of silver chloride immersed in an iodide solution and connected to platinum electrodes [14].

The silver halides have large band gaps (2·7−3·2eV), hence are insensitive to most of the visible spectrum in much the same way as TiO2.

Silver halides are much more sensitive to blue and UV light than green and red light. In 1873, Vogel employed sensitizing dyes to extend the sensitivity of the silver halide in the green and orange region [26]. The first sensitization of a photoelectrode followed thereafter [49], with the clear connection between dye sensitization for photography and photovoltaics shown in 1965 by Namba et al. [50] and verification that the process is achieved by electron injection from the dye molecules to the conduction band of the n-type semiconductor in 1968 by Gerischer et al. [51].

The first semblance of modern DSSCs was developed in subsequent years with the realization that higher efficiencies could be achieved by chemisorbing the dye onto the semiconductor surface [53, 54, 52].This was followed shortly by the usage of water cleavage to create surface complexes with a better interface [55]. Finally, it was discovered that increasing the surface roughness of the semiconductor greatly increases cell efficiency [56, 57].

In 1991 the first high efficiency cell was developed by Michael Grätzel and Brian O'regan demonstrating 7.1-7.9% efficiency [58]. This was improved progressively reaching 11.9%, Figure 3.2 shows the progress of DSSCs. Towards the end of 2012 the solid state DSSCs overtook traditional cells in efficiency and is now the subject of increased interest.

Date	Innovation	Efficiency
1991	EPFL	6.3%
1995	EPFL	7.5%
1996	EPFL	11.0%
2006	IPCE improves due to increase in the haze of the TiO_2 electrodes, particularly in the near-IR region	11.1%
2011	Cobalt complexes used with custom made donor-π-acceptor zinc porphyrin molecules consensitized with Y123	12.3%
2012	donor-acceptor type coadsorbent used to avoid dye aggregation	11.4%

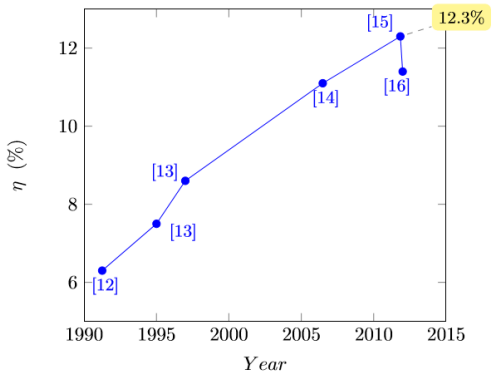

Figure 3.2. DSSC lab cell efficiencies

3.2. Interpolation Modelling

Min-Kyu et al. [115] discussed a simple model for dye-sensitized solar cells. Their aim was to produce a simple yet accurate model for determining the performance of DSSCs based on the thickness of the TiO_2 semiconductor layer. They used representative DSSCs to extract the coefficients proposed (α and β) and interpolated to create the I-V curve of the target TiO_2 thickness (T). The paper used this to find the best performing thickness, T for DSSCs at 20 μm.

The process is as follows:

- Select a lower and higher bound based on the thickness (T) of interest
- Extract the coefficients α and β
- Apply the coefficients to get new V and J (voltage and current density respectively)
- Iterating over standard J-V curve to get new J-V

The coefficients, α and β were derived from:

$$V_{TN} = V_{TL} - \frac{T-T_L}{T_H-T_L}(V_{TL} - V_{TH}) \quad (3.1)$$

$$J_{TN} = J_{TL} - \frac{T-T_L}{T_H-T_L}(J_{TL} - J_{TH}) \quad (3.2)$$

The values V_{TN} and J_{TN} were then used to get:

$$\alpha_T = \frac{V_{TN}}{V_{ST-OC}} \quad (3.3)$$

$$\beta_T = \frac{J_{TN}}{J_{ST-OC}} \quad (3.4)$$

Finally, the new voltage and current density were derived by looping over a standard test cell J-V curve from:

$$V_{NEW} = \alpha_T \cdot V_{STC} \quad (3.5)$$

$$J_{NEW} = \beta_T \cdot J_{STC} \quad (3.6)$$

Where *STC* denotes the values of the standard cells. The process is shown in *Figure* 3.3.

In the above formulae, T is the thickness being modelled, T_H and T_L are the lower and higher range thicknesses according to the modelled thickness and V_{TL}, J_{TL}, V_{TH} and J_{TH} are the lower and higher open-circuit voltage and short-circuit current densities. V_{ST-OC} and J_{ST-SC} are the respective values for the standard cell (chosen as 6 μm).

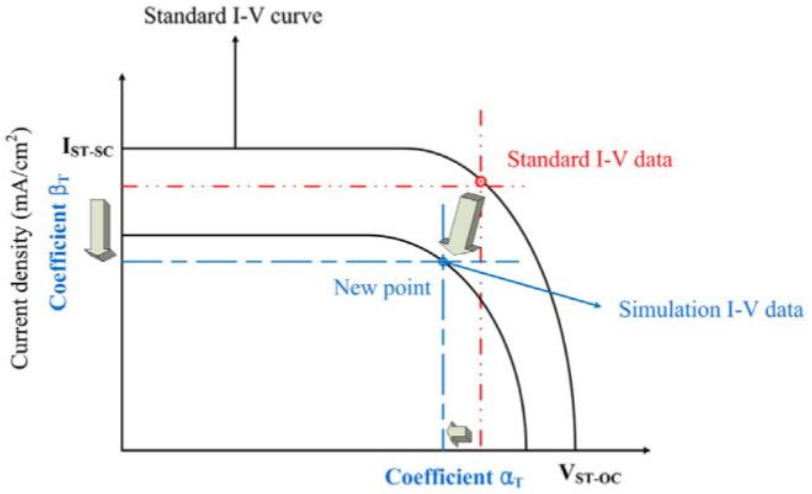

Figure 3.3. Interpolation in the V and J directions to achieve new curve [115].

Further scrutiny of the paper raised some important questions: The optimal *T* turned out to be exactly on one of the representative (experimental) values in the table (shown in Table 3.1). By applying their method, it turns out that using their proposed method, the only way to have reached the same conclusion they had, was by using the peak (20 μm) performance to reach the peak (20 μm data). This was due to the linear interpolation model used. As such, if the 20 μm data was removed from the *training set*, then the model would fail to predict the peak performing *T*.

Table 3.1. I-V characteristics of representative cells with different TiO_2 thicknesses.

	TiO_2thickness	**V_{OC} (V)**	**J_{SC} (mA/cm²)**	**FF**	**η (%)**
Standard DSSC	6 μm	0.75	7.88	0.74	4.37
Representative DSSC	3 μm	0.75	5.71	0.74	3.14
	8 μm	0.75	9.01	0.75	5.05
	12 μm	0.75	10.93	0.74	6.08
	20 μm	0.73	14.42	0.75	7.85
	26 μm	0.72	9.98	0.74	5.32

To improve accuracy of such a model, an update to the model is proposed: in this case, rather than using just the upper and lower bounds of the thickness of interest, the entire *training set* (i.e. representative cell data) is used. Furthermore, instead of using linear interpolation, a polynomial function is assessed to represent the data. This would achieve better modelling at curvatures which represent the greatest areas of interest in DSSC design.

3.2.1. Implementation

An initial function was written in FORTRAN, the Rosenbrock function to get an initial program and test the coupling capabilities with the external optimisation package DAKOTA [116]. The aim of DAKOTA integration is for implementation of automatic optimisation methods (stochastic and deterministic) as well as additional capabilities such as robustness analysis for the future.

Dakota (Design Analysis Kit for Optimization and Terascale Applications) was developed by Sandia National Laboratories, a US government-owned, contractor-operated (GOCO) national laboratory operated for the US Department of Energy.

According to the Dakota manual, the principal classes of Dakota algorithms are:

- **Parameter Studies** which employ deterministic (gradient based) designs to yield a sensitivity analysis by looking at the effect of design parameter changed on the simulation results. They can assess simulation characteristics such as smoothness, multi-modality, robustness and non-linearity [117].
- **Design of Experiments** using design and analysis of computer experiments (DACE) techniques to explore the parameter space of an engineering design problem. Whilst this can be similar to parameter studies, the primary objective is to get good coverage of the input parameter space.
- **Uncertainty Quantification** performs uncertainly propagation in which probability information for input parameters is mapped to probability information for output response functions. This includes stochastic methods such as Monte Carlo sampling, reliability methods and polynomial chaos expansions.
- **Optimization solvers** seek to minimize cost or maximize performance of a model. This is usually subject to constraints on input variables or response (output) functions of the model. This is achieved using deterministic or stochastic methods. Dakota allows multi-objective trade-off optimization as well as hybrid, multi-start and Pareto-set optimization.
- **Surrogate models** are used to reduce higher-order models into inexpensive approximations able to explore the design region without calling the original models.

In order to couple a user-created solver with Dakota, the two packages need to communicate. Dakota creates an input parameters file including the design parameters with optional sensitivity analysis and second order derivatives. Dakota also expected an output results file

with the simulation responses to the input parameters. This is shown in *Figure* 3.4 and construes the black-box approach taken in implementing the coupling wherein Dakota doesn't concern itself with the workings of the simulation and vice versa.

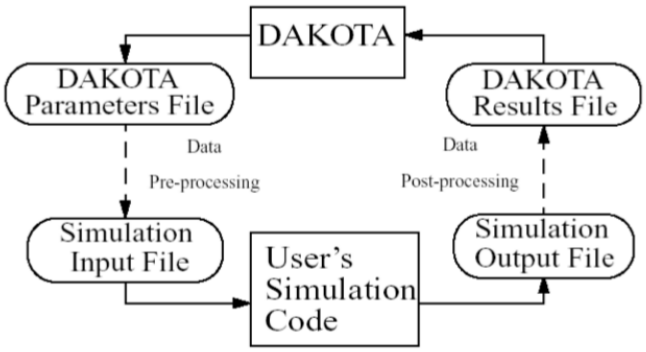

Figure 3.4. Black-box interface between DAKOTA and simulation code [117].

The names of the input file and output file are provided by Dakota to the solver through the command prompt. This is due to the dynamic nature of the naming process which can iterate over hundreds or thousands of designs, creating the need for equal number of input/output files (e.g. input1.dat-input100.dat).

The simulation was programmed such that the solver can be called using the below format:

```
solver input.dat output.dat
```

where *solver* is the name of the polynomial interpolation model executable and *input.dat* and *output.dat* are the DAKOTA input file and model output file respectively. DAKOTA creates an input file as shown in Figure 3.5(a). This includes the number of input variables, the variables' names and the expected outputs as well as optional information regarding the first and second order variable sensitivities.

The simulation should be run using the provided design variables and an output file created. A typical output file providing one output variable of value 202.37 and variable name f is shown in *Figure* 3.5*(b)*.

```
     2  variables
  0.85  x1
  -0.7  x2
     1  functions
     1  ASV_1:obj_fn
     1  derivative_variables
     1  DVV_1:x1
     2  DVV_2:x2
     0  analysis_components
```

(a) DAKOTA input file

```
202.37312499999999     f
```

(b) Model output file

Figure 3.5. Interfacing of Model and DAKOTA

A flowchart of the solver is shown in *Figure* 3.6.

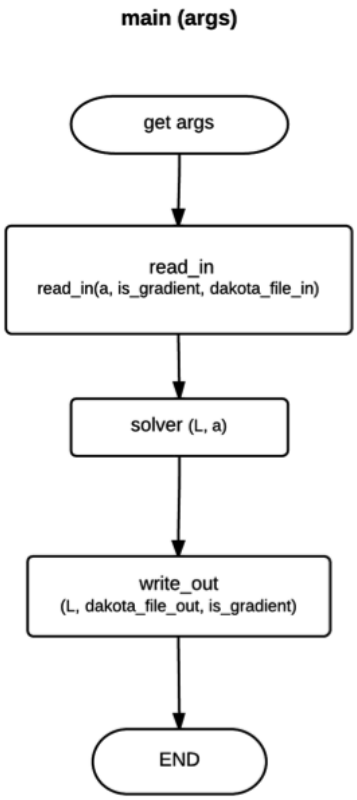

Figure 3.6. Solver model overview

3.2.2. Modularisation

Once the Rosenbrock solver was created, coupled and tested, the program was modularised: the core simulation model was moved to a separate module “solver m”. This allowed the model to be updated as required. This was followed by implementing the modified polynomial simple DSSC model presented by Min-Kyu et al. [115]. The general program process is outline in the flowchart shown Figure 3.6.

3.2.3. Polynomial Interpolation

Two methods of polynomial interpolation of a set of data is considered: the Lagrange polynomial interpolation and the Newton polynomial interpolation methods.

Lagrange polynomial interpolation:

The Lagrange interpolating polynomial is defined on a set of *n* data points $(x_1, y_1), \dots, (x_j, y_j), \dots, (x_n, y_n)$ where the polynomial $P(x)$ is of order $\leq (n-1)$, that is, at most one order less than the number of points being interpolated. It is given by:

$$P(x) = \sum_{j=1}^{n} y_j \ell_j(x)$$

Where

$$\ell_j(x) = \prod_{\substack{k=1 \\ k \neq j}}^{n} \frac{x - x_k}{x_j - x_k} = \frac{(x - x_1)}{(x_j - x_1)} \dots \frac{(x - x_{j-1})}{(x_j - x_{j-1})} \frac{(x - x_{j+1})}{(x_j - x_{j+1})} \dots \frac{(x - x_k)}{(x_j - x_k)}$$

Application of Lagrange interpolating polynomial

Assuming we have a data set as follows:

x	***F(x)=y***
1	1
4	16
6	36

The Lagrange interpolating polynomial is given by:

$$\begin{aligned} P(x) &= \left(1 \times \frac{x-4}{1-4} \times \frac{x-6}{1-6}\right) + \left(16 \times \frac{x-1}{4-1} \times \frac{x-6}{4-6}\right) + \left(36 \times \frac{x-1}{6-1} \times \frac{x-4}{6-4}\right) \\ &= \left(\frac{x^2 - 10x + 24}{15}\right) + 16\left(\frac{x^2 - 7x + 6}{-6}\right) + 36\left(\frac{x^2 - 5x + 4}{10}\right) \\ &= \left(\frac{1}{15} - \frac{16}{6} + \frac{36}{10}\right)x^2 + \left(-\frac{10}{15} + \frac{16 \times -7}{-6} + \frac{36 \times -5}{10}\right)x + \left(\frac{24}{15} + \frac{16 \times 6}{-6} + \frac{36 * 4}{10}\right) \\ &\boxed{= \boldsymbol{x^2}} \end{aligned}$$

Using Lagrange interpolation on a subset of the J_{SC} representative data set, we get the following polynomial function:

$$f(x) = -0.0039434523809524x^3 + 0.14470238095238x^2 - 1.10255952380952x + 10.1378571428571$$

Figure 3.7 graphs the results of the Lagrange polynomial and the experimental data. One concern of Lagrange interpolation is that the more data points are provided, the higher the order of the polynomial. This leads to functions that give large oscillations between the training data points. However, due to the low number of data points in this case it can be seen that in this case the polynomial given by Lagrange interpolation is reasonably robust.

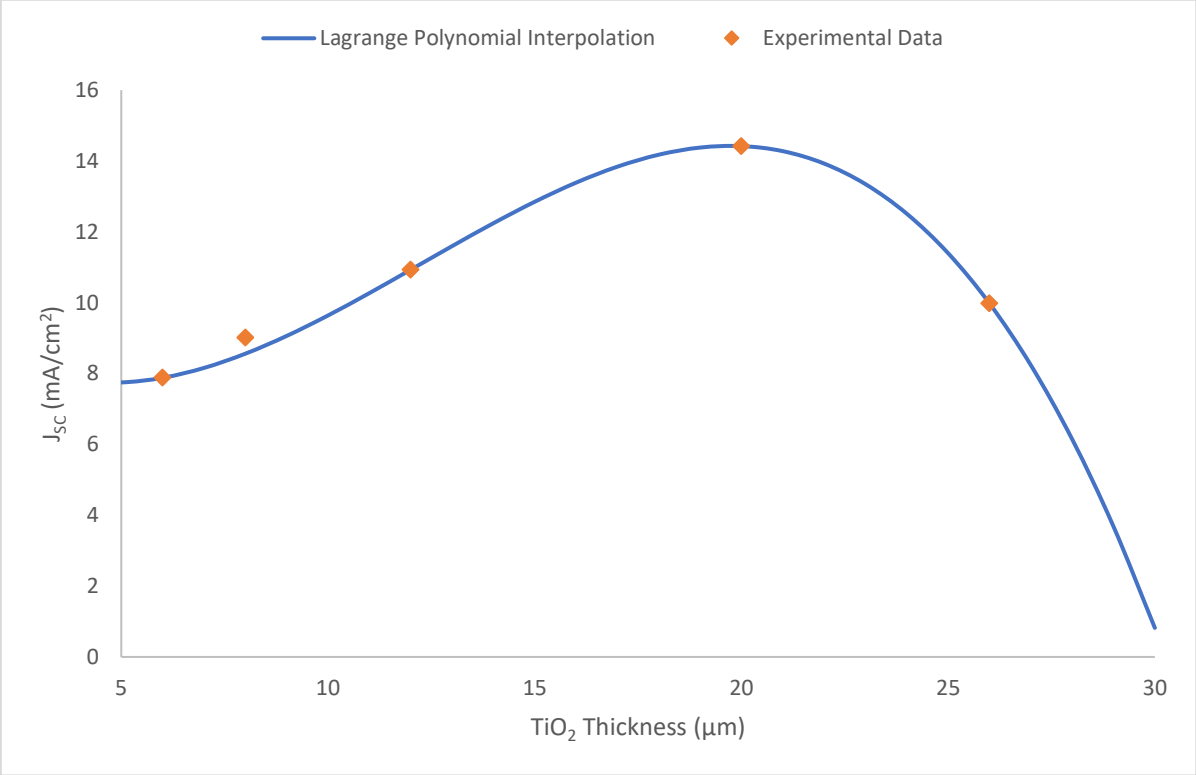

Figure 3.7. Plot of DSSC data set interpolation polynomial

An alternative is to use the *Newton interpolation polynomial*.

Newton polynomial interpolation

In order to get the Newton polynomial interpolation for a set of data points:

$$(x_0, y_0), \ldots, (x_j, y_j), \ldots (x_k, y_k)$$

where each *x* is unique:

$$N(x) = \sum_{j=0}^{k} a_j n_j(x)$$

$$= [y_0] + [y_0, y_1](x - x_0) + \cdots + [y_0, \dots, y_k](x - x_0)(x - x_1) \cdots (x - x_{k-1})$$

Where

$$n_j(x) = \prod_{i=0}^{j-1}(x - x_i)$$

$$for\ j > 0, n_0(x) = 1$$

$a_j = [y_0, \dots, y_i]$ is the *divided differences* as shown in

Table 3.2.

Table 3.2. divided differences for any data with points (x,y=f(x))

x	$y = f(x)$
1	5
2	11
3	21
4	35

x_0 $f(x_0)$

$$\frac{f(x_1) - f(x_0)}{x_1 - x_0}$$

x_1 $f(x_1)$ $$\frac{\left(\frac{f(x_2) - f(x_1)}{x_2 - x_1}\right) - \left(\frac{f(x_1) - f(x_0)}{x_1 - x_0}\right)}{x_2 - x_0}$$

$$\frac{f(x_2) - f(x_1)}{x_2 - x_1}$$

x_2 $f(x_2)$ $$\frac{\left(\frac{f(x_2) - f(x_1)}{x_2 - x_1}\right) - \left(\frac{f(x_1) - f(x_0)}{x_1 - x_0}\right)}{x_2 - x_0}$$

$$\frac{f(x_3) - f(x_2)}{x_3 - x_2}$$

x_3 $f(x_3)$

x	$f(x)$			
1	5			
		$\frac{11-5}{2-1}=6$		
2	11		$\frac{10-6}{3-1}=2$	
		$\frac{21-11}{3-2}=10$		0
3	21		$\frac{14-10}{4-2}=2$	
		$\frac{35-21}{4-3}=14$		
4	35			

The interpolation polynomial is given as:

$$f(x) = 5 + 6(x-1) + 2(x-1)(x-2) + 0(x-1)(x-2)(x-3)(x-4)$$
$$= 5 + 6x - 6 + 2x^2 + 6x + 4$$
$$\boxed{= 2x^2 + 3}$$

As can be seen in the above procedure, one advantage of the Newton interpolation polynomial method is that adding a data entry does not require a complete recalculation, only the end needs to be amended.

3.2.4. Model initial results

Although the input arguments are designed to allow DAKOTA to run instances of the model solver, we can interject and run single instances of the model. An example of a cell of the model with thickness of 6 μm is shown in Figure 3.8.

```
Homan:Rosen homanh$ ./rosenbrock test.in test.out
      0.59999999999999998
v_tn: 0.75000000000000000
j_tn: 7.6900001525878903
alpha: 1.0000000000000000   V_new: 0.75000000000000000
beta: 0.75000000000000000   J_new: 7.6900001525878903
```

Figure 3.8. Running solver in single-instance for 6 μm

For a thickness 6μm and using the lower thickness 3μm and higher thickness 8μm. We get the output Voltage: 0.75 and Current Density J: 7.69. For comparison the experimental results

show V: 0.75 and J: 7.88. The results are very close with V values being 100% accurate and J values being 97.6% accurate (2.4% difference).

Running the solver over a higher range, looking at 8um we get V=0.74 and J=10.81. In comparison the experimental values are V=0.75 and J=10.93. V is 98.7% accurate and J is 98.9% accurate. A comparison of the two methods is shown in Figure 3.9 for J_{SC}.

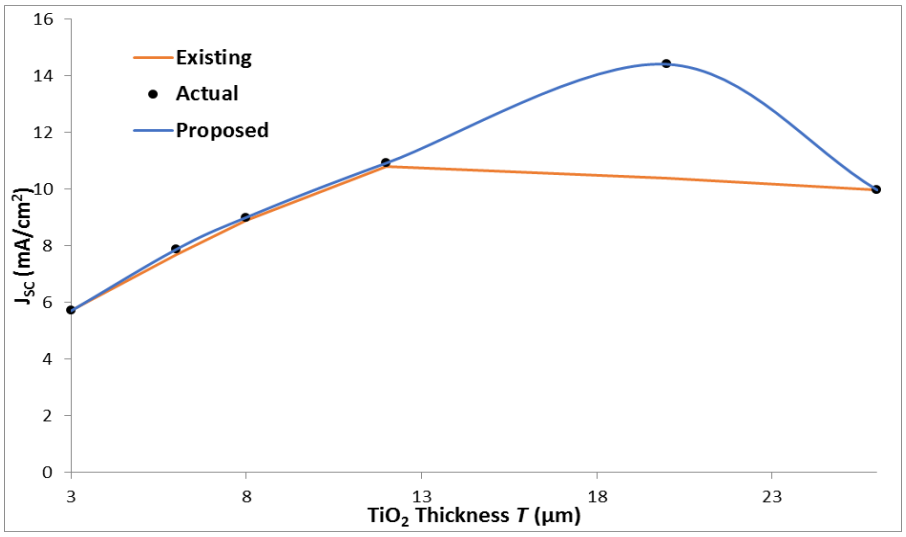

Figure 3.9. Comparison of linear (existing) interpolation model vs. proposed (Lagrangian polynomial interpolation) and experimental data

3.3. DSSC Fabrication

Two configurations of solar cells were made with both N719 and BD-HTB. One set was made using transparent only TiO2, another with transparent + active opaque TiO_2 semiconductors. The active opaque layer scatters light and increases the surface/volume ratio of the sintered film layer leading to improved performance. Outliers were removed at the end of testing, considered cells with failures or imperfections.

3.3.1. Solar Cell Substrate Cutting

Two substrate blocks were cut into cell sizes. One block was cut to 2.5mm x 1.5mm cells, the second block was cut into 2×2 cells measuring 5mm × 3mm. This is achieved by using a glass cutter to create scratches then snapping into smaller parts. The second batch was created in 2×2 formations for the future screen printing process.

3.3.2. Cleaning of Substrates

The cells were cleaned with 2% Hellmanex liquid using brush to take off impurities and FTO protective layer whilst rinsing with tap water. They were then rinsed with deionised water. The cells were stood upright in a beaker, submerged fully in deionised water and placed in an

ultrasonic vibrator bath for 10 minutes. The cells were then rinsed with Acetone and again submerged fully in Acetone. Due to fumes released the beaker was covered with a plastic film and again run through the ultrasonic vibrator bath for 10 minutes. Finally, the cells (inside the beaker) were again rinsed with Methanol and fully submerged in Methanol and sealed, then placed for 10 minutes in ultrasonic vibration bath.

3.3.3. Pre-treatment

Cells were dried and placed in UV/Ozone cleaner for 20 minutes. *An alternative is using Oxygen Plasma cleaner*. This is to make the substrate hydrophobic, ensuring the upcoming Titania layer is applied consistently and smoothly.

3.3.4. Screen Printing

Multiple layers of TiO_2 are applied with each layer offering a benefit in terms of light conversion efficiency:

3.3.5. Transparent Layer

The printing screen was cleaned with ethanol and the cells were taped down under the screen and the screen brought down to cover them. The TiO_2 transparent layer was applied with a printing blade with three strokes. Each stroke applied the Titania through the unmasked portion of the mesh onto the substrate. The cell was removed and placed under a beaker (on tissue) with Acetone applied to the tissue directly circumventing the beaker. The cell was held in this position for 45 seconds then placed on as 125 °C hotplate for 3:00 minutes. The cells were allowed to cool for 5 minutes and this entire process was repeated 3 times for the Transparent TiO_2 layer for each cell.

3.3.6. Scattering Layer

The same process as described in section 3.3.5 was performed. In this case the steps described were repeated 2 times for the Scattering TiO_2 layer for each cell. The cells were then placed on a hot plate ramping to 510 °C for a total of 85 minutes

3.3.7. Compact Layer Process (Post-treatment)

UV/Ozone or Oxygen Plasma treatment for 20mins/10mins respectively, making the FTO hydrophobic. FTO substrates were then placed in 40mM TiCl4 (in Di Water) with FTO facing up and submerged fully in liquid then placed on hotplate at 80 °C for 30minutes. They were washed with Di water and dried using Nitrogen. Finally, they were placed back in the ramp hot

plate ramping for 10 minutes to 450 °C and holding for 30 minutes. They were removed at ~80 °C.

Post treatment also applies a layer of compact TiO2. This is achieved again by placing the cells in TiCl4 @ 40mMolar (in Di water) on the hotplate at 80 °C for 30minutes. No UV/Ozone/Oxygen Plasma treatment is applied this time. They are washed with Di Water, rinsed again with Ethanol and dried using Nitrogen then again put through the ramp hot plate (above).

3.3.8. Cell Structure

The final structure is as follows:

- Glass substrate
- 500nm FTO layer (crystalline)
- 50-80nm compact/blocking TiO2 layer
- 9 micron layer of "transparent" TiO2 with 18-20 nm porous particle size
- 6 micron layer of "scattering" TiO2 with 200-400nm porous particle size
- 50-80nm compact/blocking TiO2 layer

The post processing increases the surface area of the surface for dye application and absorption. Each application of screen printing steps applies ~3microns of material, hence to get the 9micron transparent layer we apply 3 rotations of screen printing and for the 6micron dispersion layer, 2 rotations of the printing steps are used.

3.3.9. Dying Process

For the dying process N719 Dye and BD-HTB were used. This was created using 0.3-0.5 mM Dye Mixed with Aceto-Nitrile:Tert-butanol (1:1 ratio). The cells were submerged in the resultant dye solution and left overnight.

3.3.10. Counter Electrode

A sand blast machine cut the electrolyte injection hole 90% of the way on the counter electrode cells and completed using a fine (0.6mm diameter diamond tipped) drill to cut the final 10%. The smaller hole at the FTO side causes a smaller area to be wasted. The counter electrode substrates were then cleaned using the previous method.

3.3.11. Platinum catalyst

Platinum was applied to the counter-electrode substrate (back contact).

3.3.12. Sealant

Sealants were cut with an opening inner area slightly larger than the active cell size. The sealant was sandwiched between the substrates and placed on a hotplate for a few seconds until the sealant was absorbed by both contacts.

3.3.13. Electrolyte Application

The cells were placed in a vacuum chamber with drilled side facing up and the electrolyte solution was dripped on the drilled hole with a micropipette. The pump was turned on to create a semi-vacuum; this sucked the air out of the cell through the drilled hole. Once all the air was removed, the vacuum valve was opened to let air in, the cell absorbed the electrolyte solution through the drilled hole. This process was repeated until necessary.

3.4. Results and Discussion

The results of N719 and BD-HTB are shown in *Table* 3.3 and the I-V characteristics in Figure 3.10 below:

Table 3.3: Cell results for transparent and opaque cell configurations

Dye	TiO_2	Model	Jsc (mA/cm^2)	Voc (mV)	FF	%
BD-Htb	Scatter + Transparent	BO1	4.20	517	58%	1.258
		B02	3.93	510	58%	1.155
		BO3	1.29	532	55%	0.378
		BO4	3.35	504	62%	1.047
	Transparent	BT1	3.78	507	62%	1.186
		BT2	2.89	530	62%	0.942
N719	Scatter + Transparent	NO	17.38	656	46%	5.22
	Transparent	NT	15.48	663	43%	4.43

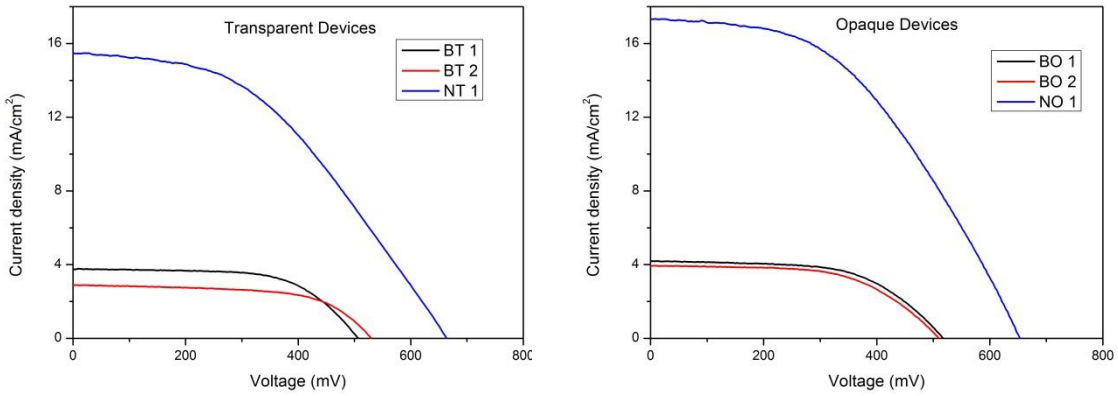

Figure 3.10. I-V characteristics of BD-HTB and N719

On the transparent only configuration, the BD-HTB cells averaged 1.06% efficiency, the equivalent N719 control cells averaged 4.43% efficiency. Similar pattern is seen in the transparent + active opaque scattering layer configuration. The scatter layer improved efficiency in both dyes as expected, with the BD-HTB variant averaging to 1.15%, providing a 9% improvement and N719 variant averaging 5.22% providing an 18% improvement.

On the other hand, in both cases the BD-HTB cells performed below the control cells N719. This is in spite of the fact that parent black dye solar cells outperform N719. The control cells' characteristics, at 5.2% and 4.4% efficiencies we great results for the lab fabrications at the facility. On top of the generally good performance, the cells showed consistency in their results across the cells. This is important as it validated the quality of the fabrication process of not just the N719 cells but more importantly the BD-HTB cells.

3.5. Conclusion

Whilst the low efficiencies of the BD-HTB modification as a dye sensitizer is disappointing, it represents progress in establishing the suitability of such materials for use in dye solar cell applications. The N719 cells on the other hand showed an improvement in the consistency of cell fabrication at the facility.

Future work being considered includes going back and different variants of the BD, synthesis of new dyes for use in DSSCs, and application of DSSCs in the field. Of particular concern to the author is the use of DSSCs in BIPVs and solar concentrators such as V-Trough and CPCs, as both standalone solar cells and part of multi-junction cells in tandem with Silicon cell or thin film technologies such as GaAs, CiGS or CdTe solar cells.

Chapter 4 Optical Modelling of V-trough and Compound Parabolic Concentrator

4.1. Introduction

From the total renewable power generation capacity of 921 GW (not including hydro) as per 2016 data [1], the contribution of solar photovoltaic (PV) is about 303 GW, and concentrating solar power technologies is about 4.8 GW. PV cell efficiency can be improved by increasing the light intensity and solar flux on the PV module using concentrating systems [3]. Concentrator Photovoltaic (CPV) technology has entered the market as a utility scale option for the generation of solar electricity with more than 370 MWp in cumulative installations, including several sites with more 30 MWp [118]. The top highest electricity production capacity are Golmud 1 plant with 57.96 MWp, and Golmud 2 plant with 79.83 MWp both in Golmud, Qinghai province, China and Touwsrivier project in Touwsrivier, Western Cape, South Africa at a capacity of 44.19 MWp[1]. A key advantage of a CPV system over other types of photovoltaic technologies is its higher efficiency. For a given peak power rating, a CPV system requires less land area than other photovoltaic technologies. The parabolic trough accounts for majority of the installed CVP worldwide due to its cost advantage. Most of the CPVs are actively tracking the Sun in order to achieve meaningful concentration. However, by using an active solar tracking mechanism which is often accompanied with an imaging concentrator, adds to the capital and O&M costs while consuming a fraction of the generated power [119]. Therefore, with all these disadvantages in view, nonimaging and stationary techniques of concentrating solar radiation are more cost effective. Application of the nonimaging optics techniques can deliver moderate level of concentration with completely stationary concentrators.

The key principle of CPV is the use of cost-efficient concentrating optics that dramatically reduce the PV cell area, uses less semiconductor components which are made from heavily

[1] See data at: http://cpvconsortium.org/projects

mined and relatively rare metals, enabling the use of more expensive, higher efficiency cells and potentially a levelized cost of electricity (LCOE) competitive with standard flat-plate PV technology [118, 120]. The history of the development of concentrating photovoltaic (CPV) is discussed in [121, 122, 123, 118, 124, 125]. The theoretical limit associated with solar-to-electricity conversion efficiency with bulk multi-junction solar cells (MJSC) is 86% [126], and >60% with three junctions [127]. The gap between the attained efficiencies and the theoretical value shows there is greater scope for performance improvement. Ways in which this can be achieved include using more junctions, increasing concentration, reducing substrate use, use of alternative materials, nanostructures, and removing heat from PV in CPVT system. CPVs are classified as LCPV and HCPV as described in Table 4.1.

Table 4.1.CPV classification.

CPV	**Concentration range**	**Tracking**	**Type of cell**
HCPV	300-1000	Two axes	III-V MJSC
LCPV	<100	One or two axes	c-Si or other cells

For increasing concentration optical elements with a higher concentration ratio are used. Higher concentration leads to smaller solar cells, higher photon flux and enhanced current production, but also a lower volume of metal contacts with which to conduct the current produced. Figure 4.1 show global installed HCPV/LCPV capacity from 2002-2016 derived from public announcements [2].

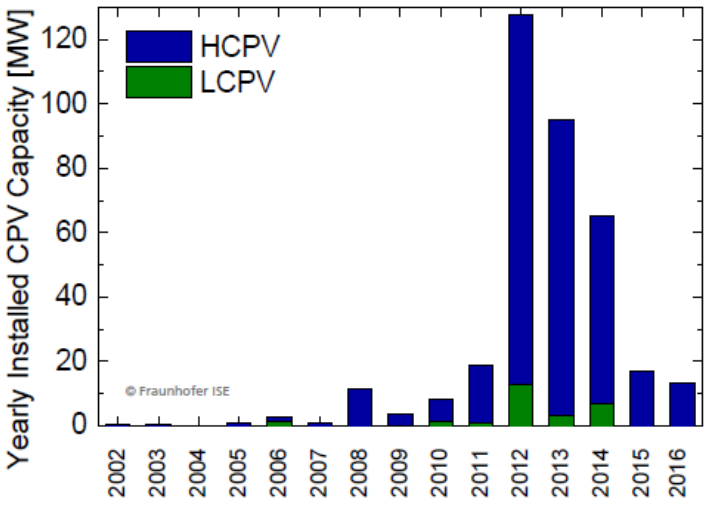

Figure 4.1. Yearly installed capacity of low and high concentrator PV systems (LCPV/HCPV) [2].

In this chapter the computer based optical modelling of V-trough and Compound Parabolic Concentrators (CPC) is presented. Many researchers have used ray-tracing technique for theoretical characterisation of a concentrating system for PV applications [128, 129] while others used experimental optical efficiency and solar energy flux distribution by various methods [130, 131, 129]. A multitude of nonimaging techniques for concentration of solar radiation in stationary or passive tracking applications will be examined. Numerical optical evaluation of the concentrating systems such as CPC and V-trough collectors using a ray-trace technique is discussed. The results of ray tracing analysis for designing CPCs and V-trough are presented in Chapter 6 together with experimental optical efficiency and solar energy flux distribution for a designed and manufactured isolated PV cell module.

4.2. Nonimaging solar concentrators

Radiation collectors that direct the radiative energy from the larger entry aperture area of the concentrator to the exit smaller aperture area with minimum optical losses are defined as nonimaging concentrators. This allows the design of optical systems with maximum geometric concentration permitted by physical conservation laws for a specified field of view. Contrary to imaging concentrators which produce an image of the sun by reflecting it on the receiver, nonimaging concentrators do not produce any optical image of the source and they are able to reflect to the receiver all the incident radiation, either beam or diffused, intercepted over a wide range of incidence angles. Nonimaging collector designs follow fundamental principle of the edge-ray principle, i.e. if the edge or boundary rays from a source to an optical system (reflective or refractive) can be directed to the edges of a target area, then all the rays in between these edge rays will also be directed to the target area. The most commonly used technology that takes full advantages of nonimaging optics is the compound parabolic concentrator (CPC) and V-tough concentrators. V-trough and Compound Parabolic Concentrators (CPC) are most common nonimaging concentrator discussed in this chapter.

4.2.1. V-trough concentrator

V-trough concentrators are part of a family of low concentration non-imaging reflective concentrators. It can be used both with and without sun tracking systems [103] and is cheaper to manufacture due to the simple geometries and linear surfaces employed [132]. Their lower thermal output [133] makes employment of V-trough in BIPVs ideal, as passive cooling can be used, leading to better integration and lower maintenance of such systems as well as improved solar cell efficiencies [134]. Lastly, the linear mirrors result in a near linear projection of light leading to high uniformity distribution of light onto the absorber area [132, 135].

Amanlou et al. [122] used the Monte Carlo ray tracing method (MCRTM) and evaluated the optical performance and flux distribution on the receiver PV panel. They showed that in V-trough concentrator by increasing the angle α shown in Figure 4.2, the concentration ratio is increasing but it does not exceed 3. The optical simulation indicates that flat concentrators make a uniform distribution of irradiation on the absorber as shown in Figure 4.2.

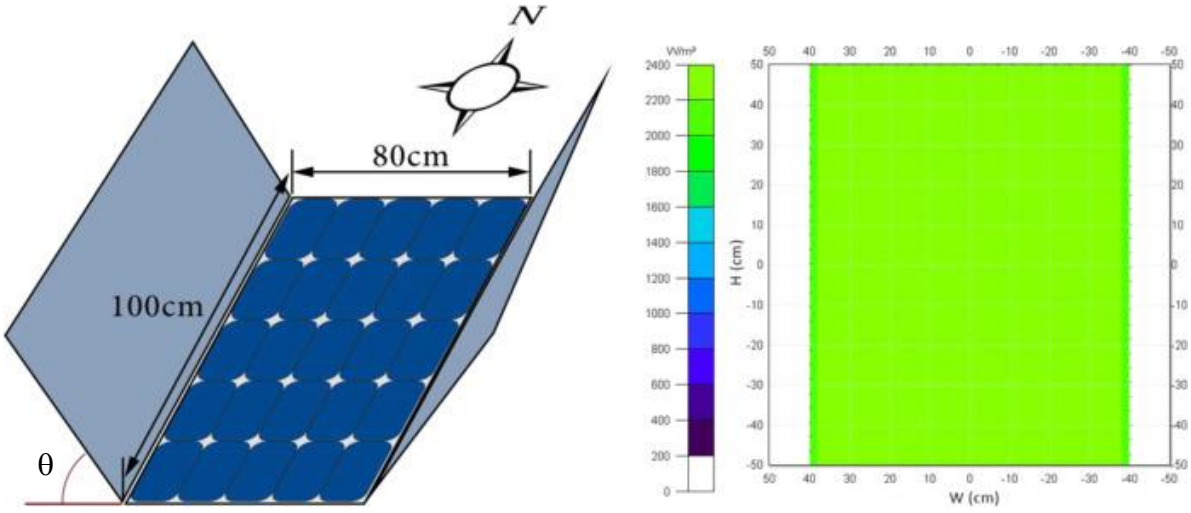

Figure 4.2. Irradiation and irradiation intensity distribution on a flat CPV system [122].

The schematic of a V-trough concentrator cross section as shown in Figure 4.3 comprises of an absorber aperture area W_{abs} connected on both sides to two inclined reflective surfaces at angle θ. The entry aperture is the wider plane created at the end of the inclined mirrors and is denoted by W_{ape}. The additional terms W and L represent the V-trough height and mirror length, respectively.

The geometric concentration ratio of the V-trough concentrator is defined as:

$$C = \frac{W_{ape}}{W_{abs}} \tag{4.1}$$

Fraidenraich and Almeida, 1991 [136] calculated the acceptance angle of the cavity as:

$$\theta = \sin^{-1}\frac{1}{C} \tag{4.2}$$

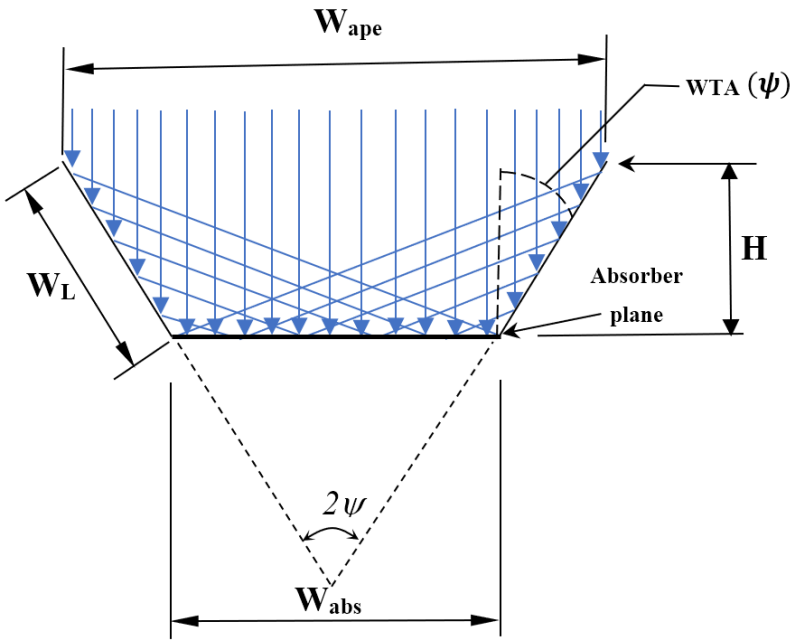

Figure 4.3. Cross section of V-trough cavity, ψ represents wall trough angle

A method of approximating the effective concentration ratio analytically through the solution of equations describing the number of reflections or rays through the V cavity is presented in [136, 137, 138, 139, 140]. The aperture width of the V-trough concentrator W_{ape}, can be divided into many regions based on the number of reflections the rays require to reach the absorber aperture. These regions are named $w_0, w_1, w_2, \ldots, w_n$ where n represents the number of reflections as shown in Figure 4.4. For example, rays entering in the w_0 region of the entry aperture fall directly to the absorber area [137]. The number of reflections to W_{abs} is collected experimentally by using a laser beam to point down from the entry aperture between region *(a)* and *(b)* (Figure 4.4) and check visually the number of reflections of the incident beam [141, 142, 143, 144, 145]. The data is used to determine the effective concentration ratio (C_{eff}) of the V-trough concentrator by:

$$C_{eff} = C \times \left[\frac{w_0+\rho w_1+\rho^2 w_2+\rho^3 w_3+\ldots+\rho^{nmax} w_{nmax}}{W_{ape}}\right] \qquad (4.3)$$

Where C is the *geometric concentration ratio* defined in Eq. (4.1) and ρ is the reflectivity of the material.

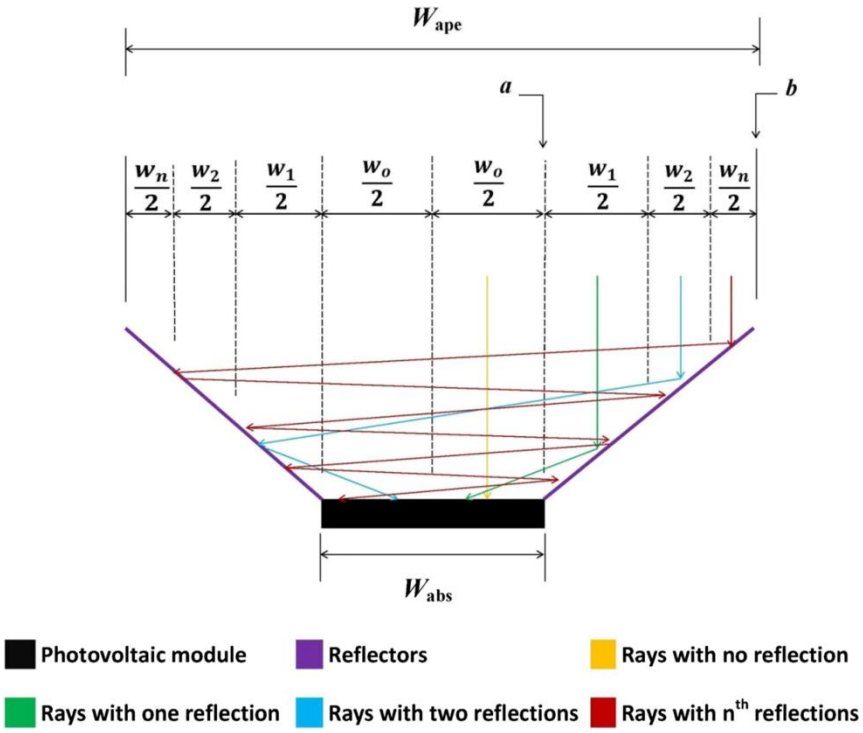

Figure 4.4. V-trough concentrator divided into sub regions based on number of reflections [xx]

There are some drawbacks to this analytical method: (i) The regions $w_0 - w_n$ are discretized by using laser visual analysis. This means the accuracy of the model will depend greatly on the number of steps the laser-analysis is performed, if the steps sizes are too large then the boundaries will be inaccurate, if they are too small then the sweep will become a laborious task and take too long. (ii) The process demonstrated in Figure 4.4 assumes a light angle of incidence of 0°. The process becomes more cumbersome as the incidence angle becomes more complex such as rays inclined on the 2D plane entering the cross-section cavity or if a combination 3D vector of the rays due to the solar azimuth angle and solar altitude angle hit a 3D V-trough concentrator model. (iii) More complex and asymmetric V-trough concentrators are more difficult to address analytically.

The use of computer modelling does not have the drawbacks presented above and has the advantage of not needing the manufactured system to analyse with lasers, allowing rapid design iterations before even the prototype stage.

4.2.2. Compound Parabolic Concentrators (CPCs)

Compound Parabolic Concentrators are a result of improvements on the *cone concentrator* through the application of edge-ray principle to prototype a series of nonimaging concentrators that approach an ideal concentrator with the maximum theoretical concentration ratio. CPC is considered the best static concentrator for solar radiation collection due to high optical

efficiency and the capability to collect both diffuse and direct radiations [146, 147]. Simultaneous work was done on CPCs by Hinterberger & Winston in 1966 [148, 149] and Baranov [150] and Baranov and Melnikov [151] in 1965 and 1966, respectively. This led to a publication on the suggestion of 3D CPC (termed as *Parabolatoroidal mirrors*) in 1966 by Baranov [152]. Finally, in 1974 the 2D CPC geometry was described by Winston in 1974 [153]. Various types of absorbers are used depending on the application of the CPC collector. O'Gallagher discussed more common design of CPCs including flat plate, vertical fin, wedged shape and cylindrical absorbers as shown in Figure 4.5 [154].

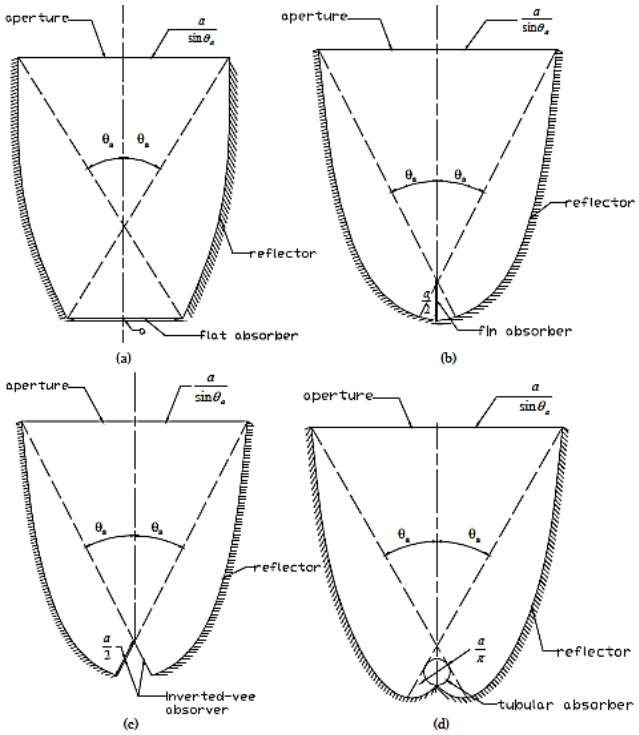

Figure 4.5. Two-dimensional CPC reflectors for four absorber configurations: (a) flat absorber, (b) vertical fin absorber, (c) wedged shape absorber and (d) cylindrical absorber. [4x]

CPCs use a combination of two symmetrical or asymmetrical parabolas to focus light onto an absorber aperture. The advantage is that unlike a parabolic dish, rather than focusing light onto a focus point, light is spread over a focal area. This also leads to a more robust acceptance of light, i.e. a CPC can accept light at different angles whilst fixed, as compared to a parabolic concentrator which needs to implement some sort of sun-tracking system. This makes CPCs a great candidate for BIPVs: firstly, because the spread of light over a greater area leads to better heat generation distribution, secondly because a BIPV CPC can passively track the sun within the acceptance angle. The stationary CPC has capability of concentrating solar radiation by a factor of ~3 and by seasonal adjustment can reach to a factor of ~10 [15]. CPC concentrators can be applied in both linear (troughs) and three-dimensional (parabolocylinder) versions. The

two-dimensional CPC also called linear CPC or trough-like CPC has a longitudinal axis. Various 3D CPCs were investigated by many researchers. Timinger et al. [155] optimized faceted CPCs by discretising the curvature of CPC in both the circumferential and axial directions as shown in Figure 4.6.

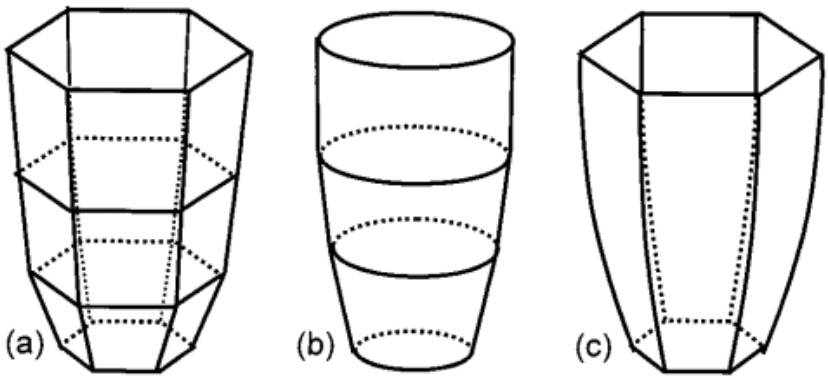

Figure 4.6. The concentrator in (a) has six circumferential and three axial subdivisions. In the limiting case of infinite circumferential subdivisions (b) the apertures have the form of circles. In the limiting case of infinite axial subdivisions (c) the axial profile has the shape of a smooth curve [155].

van Dijk, et al. [156] simulated the relationship between transmittance and concentration ratio (C) of circular, square and hexagonal concentrators with reflectance (R) of 95% as shown in Figure 4.7. The results show that by increasing the sides of CPCs apertures, the optical performance approaches closer to ideal transmittance.

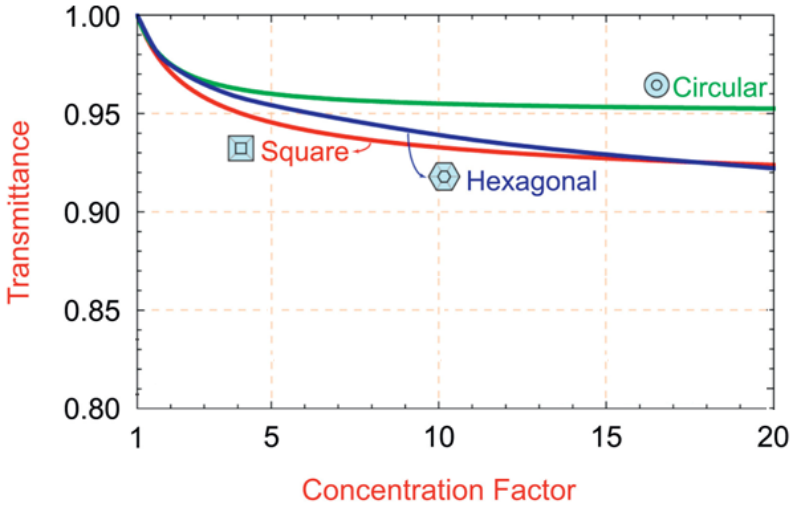

Figure 4.7. Plot of the transmittance of a circular, square and hexagonal concentrators as a function of the concentration factor (C) at a reflectance (R) of the concentrator surface set to 95%. The average number of reflections at the concentrators increases with C [156].

The study by Cooper et al. [157] also implies similar results, in which the optical properties of CPCs with polygonal apertures having 3, 4, 5, 6, 8, 12 sides and circular aperture were compared in Figure 4.8.

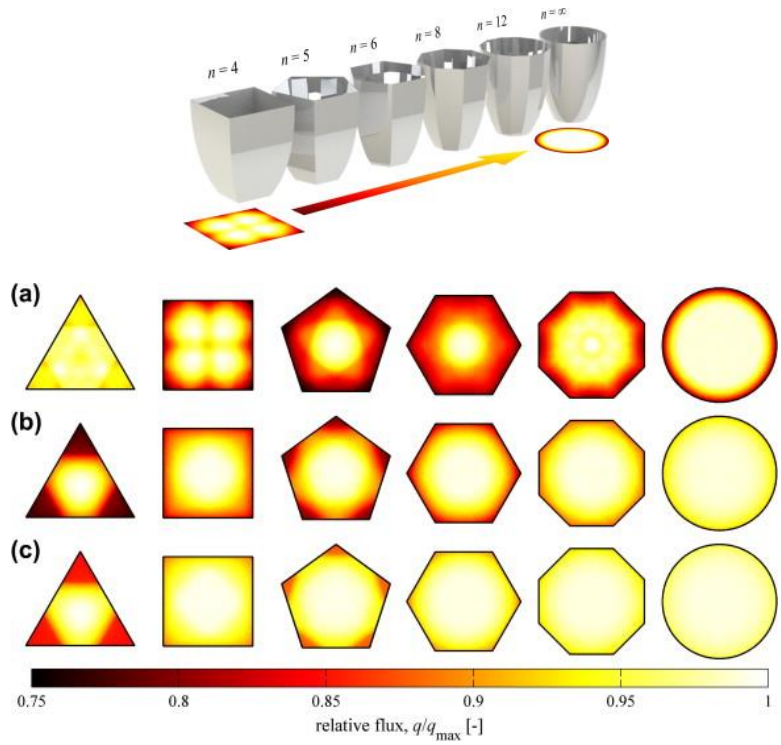

Figure 4.8. Flux distribution at the outlet of circular and various polygonal CPCs with half-acceptance angle (a) θ = 5°; (b) θ = 30°; and (c) θ = 45°. Calculated by Monte Carlo ray-tracing with 10^9 rays [157].

The shape of a CPC depends on two factors:

1. The area of the absorber plate
2. Acceptance angle

The name *compound parabolic concentrator* comes from the fact that the concentrator is comprised of two parabolic mirror segments with different focal points. Taking the CPC in image Figure 4.9 below, we can see that there are two parabolas: C-C' rotated to make its focus point A and D-D' rotated to make its focus point B. The CPC is created by cutting the two parabolas at the absorber surface (A-B) and at the top inlet aperture area (D-C). The aperture area is the point at which the slopes of parabolas C-C' and D-D' are zero, i.e. the entry aperture beyond that point will start to decrease and become smaller, decreasing the concentration ratio. The acceptance angle of incidence is $\theta°$. Unlike a V-trough concentrator, all light coming within the acceptance angle entering the aperture will reach the absorber surface assuming ideal conditions (such as perfect mirror reflectivity).

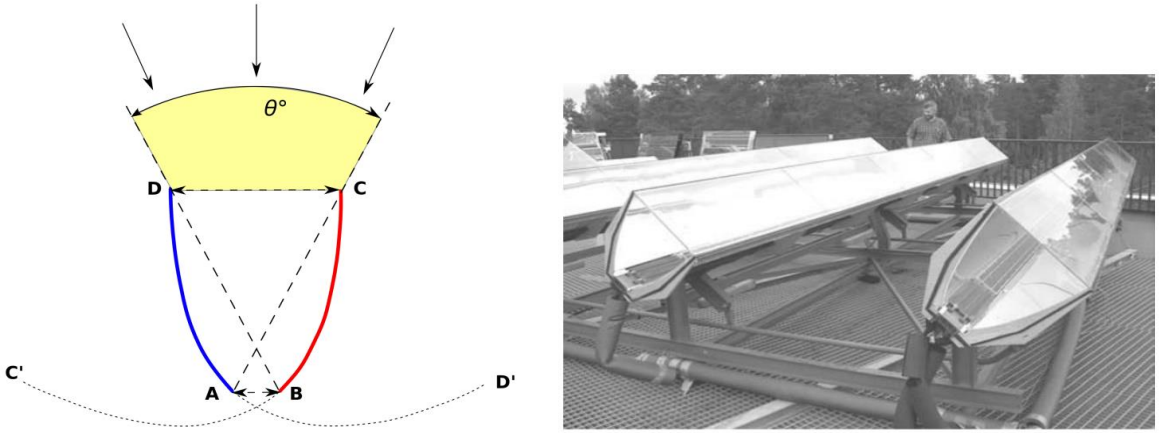

(a) (b)

Figure 4.9. (a) Schematic of Compound parabolic concentrator (CPC), (b) A CPC trough system [158]

The focal length of the parabola is given by:

$$f = a'(1 + \sin\theta_h) \tag{4.4}$$

Where θ_h is the *acceptance half angle*, a' is the absorber (exit) half aperture and a is the entry half aperture. The length (height) of the CPC is given by:

$$L = \frac{a'(1+\sin\theta_h)\cos\theta_h}{\sin^2\theta_h} \tag{4.5}$$

The radius of the inlet aperture is:

$$a = \frac{a'}{\sin\theta_h} \tag{4.6}$$

From the above two equations we get:

$$\begin{aligned} L &= \frac{a'(1+\sin\theta_h)\cos\theta_h}{\sin^2\theta_h} \\ &= \frac{a'(1+\sin\theta_h)\cot\theta_h}{\sin\theta_h} \\ &= a(1+\sin\theta_h)\cot\theta_h \\ &= (a + a\sin\theta_h)\cot\theta_h \end{aligned}$$

Substituting $a = \frac{a'}{\sin\theta_h} \rightarrow a' = a\sin\theta_h$ we get:

$$L = (a + a')\cot\theta_h \tag{4.7}$$

The concentration ratio of a CPC is defined as the ratio of the aperture area to the absorber surface area and is related to the acceptance angle and given by:

$$C_{max} = \frac{a}{a'} = \frac{\text{D-C}}{\text{A-B}} = \frac{1}{sin(\theta_h)} \tag{4.8}$$

If we want to make a CPC with a concentration ratio of ***4*** and an absorber surface area of ***50mm*** cross-section:

$$C_{max} = 4 = \frac{1}{\sin\theta_h} \tag{4.9}$$

Acceptance half angle:

$$\therefore \theta_h = \sin^{-1}(1/4)$$
$$= 14.48°$$

The total acceptance angle of the concentrator without refraction is therefore:

$$\theta = 14.48 \times 2 = 28.96°$$

The length of the CPC, *L* is given by:

$$L = (a + a')\cot\theta_h$$
$$= (25 + 100)\cot 14.48°$$
$$= \boldsymbol{484.04mm}$$

The focal length *f* is calculated as

$$f = a'(1 + \sin\theta_h)$$
$$= 25[mm]\ (1 + \sin 14.48°)$$
$$= \boldsymbol{31.25mm}$$

This is the distance A-F in Figure 4.10 from the vertex of the parabola to its focus point.

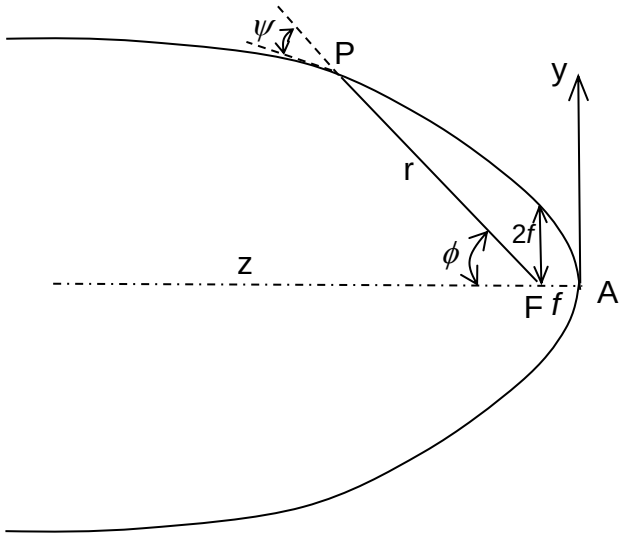

Figure 4.10. CPC parabola in polar coordinates with origin at the focus

The shape of the parabola is described by the equation in Cartesian form:

$$z = \frac{y^2}{4f} \tag{4.10}$$

It is usually easier to use the polar coordinate system to get the basic properties of the CPC, derived as:

$$r = \frac{2f}{1-cos\phi} = \frac{f}{\sin^2\frac{\phi}{2}} \tag{4.11}$$

The parabola is rotated by the acceptance half angle θ_{i_h} and truncated at its top (P') and bottom (Q') as shown in

Figure 4.11. The focus of the rotated parabola becomes Q.

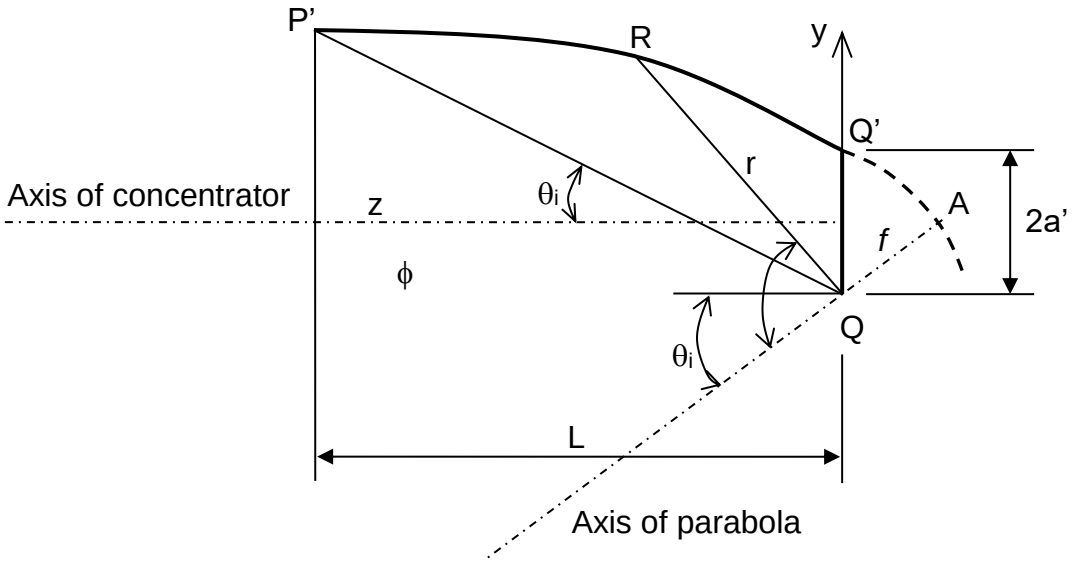

Figure 4.11. Rotated CPC parabola.

A similar parabola is created as explained above, this time the parabola is rotated in the opposite direction by θ_h degrees such that it passes through *Q* and has the focal point *Q'*. The resulting CPC is shown in Figure 4.12 by the shape *QPP'Q'*.

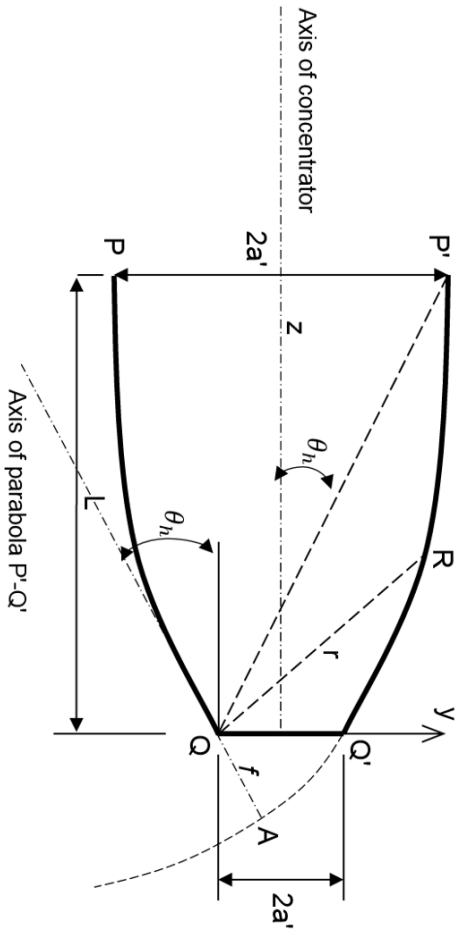

Figure 4.12. Final CPC design schema

It should be noted that simple calculations have shown that for a case of concentration ratio, C=10, a CPC uses 4.4 times the amount of material used by a simple parabolic concentrator (SPC), but CPC has 3.15 times more acceptance angle for the same case. A typical limiting value of concentration ratios of CPCs and SPCs in order to enable collection of circumsolar radiation was calculated to be 19.1 and 6.1, respectively, which corresponds to an acceptance angle of 3° [159].

4.3. Ray Tracing Modelling

Many software are available for ray tracing of solar concentrators. The most widely used software are:

APEX is an add-in of SOLIDWORKS for analysing optical and illumination system; the core of APEX is time-proven ray tracing engine; create, design and analyse in one program environment; simulate optical and illumination system with an easy-to-follow workflow.

COMSOL Multiphysics is a finite element analysis, solver and simulation software package; model and simulate coupled or Multiphysics phenomena simultaneously; incorporates various software such as SOLIDWORKS; simulate the electricity output of CPV system.

LightTools is a 3D optical engineering and design software; supports virtual prototyping, simulation, optimization and photorealistic renderings of illumination application; provide point-and-shoot ray tracing and Monte Carlo simulations; incorporates with SOLIDWORKS and other applications like Microsoft Excel or MATLAB.

MATLAB is a high-level language and interactive environment; for numerical computation, visualization and application development; new codes are required to be written for ray tracing simulation; optimize CPC geometry.

OPTIS software provides optical simulation in CAD/CAM with capability of optical design of luminaries, illumination, non-imaging, UV curing and disinfection, solar and day lighting, IR irradiation, industrial system, optical design for sensor systems, and optical design for consumer devices.

Photopia is a fast and accurate photometric analysis program; for non-imaging optical designs; the results are obtained based on probabilistic method; provides a large selection of sun and sky dome models and numerous material data; can be incorporated with AutoCAD and also available as an add-in for SOLIDWORKS.

RADIANCE Photon map (Pmap) Extension is a versatile lighting simulation system; use light-backwards ray-tracing method; photon map is based on a light particle transport simulation by a Monte Carlo sampling method; can obtain not only accurate ray-tracing results, but photon map for analysing the light source distributions in annual and climate-based daylight simulations.

TracePro is a commercial, fast and accurate optical engineering software program; incorporates with CAD products and the software using a Dynamic Data Exchange client/server interface; has an add-in to SOLIDWORKS; provides Monte Carlo simulations for CPCs.

ZEMAX is an optical and illumination design software; applied for both imaging and illumination system; provides standard sequential ray tracing through optical elements, non-sequential ray tracing for analysis of stray light and physical optics beam propagation; its versatile features meet the requirements of CPC analysis under either normal or special conditions.

In this work in order to model the characteristics of the V-trough and Compound Parabolic Concentrators, the COMSOL Multiphysics software package is employed and the *geometric optics* package is used to run ray tracing analysis.

4.3.1. Ray optics vs. wave optics

There are two archetypes of modelling the propagation of light through space available in COMSOL: Ray optics and RF or Electromagnetic Wave Optics modules, available in the Frequency Domain or Beam Envelopes. An important consideration is the scale of the geometry being modelled in comparison to the wave amplitude, i.e. will physics such as *diffraction* play a major part in the light propagation of the problem. Figure 4.13 shows the different optical methods in use when solving problems of varying geometries.

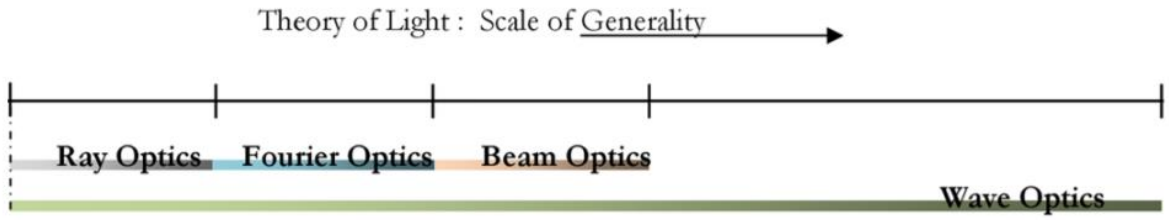

Figure 4.13. Problem scale and Optics suitability [160]

4.3.2. Wave Optics

Electromagnetic wave simulation uses finite element method (FEM) to solve the electric field amplitude of each electromagnetic wave using Maxwell's Equations. As a consequence, the finite element mesh needs to be small enough to solve each individual wavelength.

Maxwell's equations (shown in differential form) are defined as follows:

Gauss's law:

$$\nabla \cdot \vec{E} = \frac{\rho}{\varepsilon_0} \tag{4.12}$$

Where:

- E is the electric field vector
- ρ is the electric charge density
- ε is the electric permittivity of the free space, known as the *dielectric constant*

The Gauss's law states that electric charge creates electric fields diverging from it (Figure 4.14). Moreover, the net electric flux through any closed surface is proportional to the net electric charge.

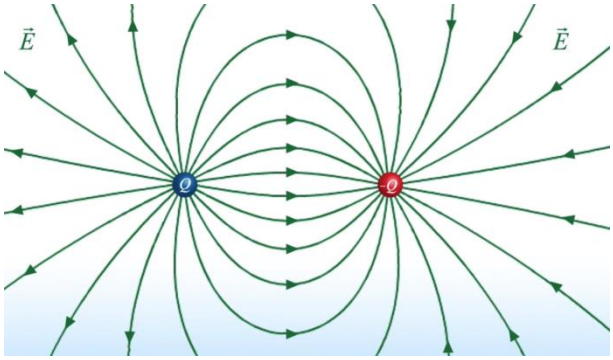

Figure 4.14. Electric field of two opposing but equal magnitude charges

Gauss's law for magnetism:

$$\nabla \cdot \vec{B} = 0 \tag{4.13}$$

Where *B* is the magnetic flux density vector.

This law states that the magnetic field $\vec{B}$ has a divergence of zero, i.e. that magnetic fields always come in di-poles north and south and magnetic monopoles do not exist.

Faraday's law of induction:

$$\nabla \times \vec{E} = -\frac{\partial \vec{B}}{\partial t} \tag{4.14}$$

Where

- *E* is the induced electric field vector
- $\underbrace{\nabla \times}_{dell\ cross\ operator}$ means "to take the curl"

States that time-varying magnetic fields create *curling* electric fields around them.

Ampere-Maxwell's Law:

$$\nabla \times \vec{B} = \mu_0 \left(\vec{J} + \varepsilon_0 \frac{\partial \vec{E}}{\partial t} \right) \tag{4.15}$$

Where:

- *B* is the magnetic field
- *J* is the electrical current density
- *E* is the electric flux density
- μ is the magnetic permittivity of free space
- ε is the electric permittivity of free space

This law states that the curl (curvature) of the magnetic field equals the electrical current density plus the time derivative of the electric flux density.

4.3.3. Ray Optics

Ray optics is the usage of ray tracing algorithms to approximate the solutions to Maxwell's Equations. Ray tracing assumes that the wavelength is extremely small relative to the geometry size. This means the electromagnetic waves are modelled as rays that can reflect and refract across material discontinuities (typically boundaries in a model).

When light is incident on such boundaries one of the following occurs:

- Light is partially or totally reflected at the boundary (Figure 4.15a)
- Light can be scattered in random directions at the boundary (Figure 4.15b)
- Light can be partly refracted at the boundary entering the second medium
- Light can be partly absorbed in either medium

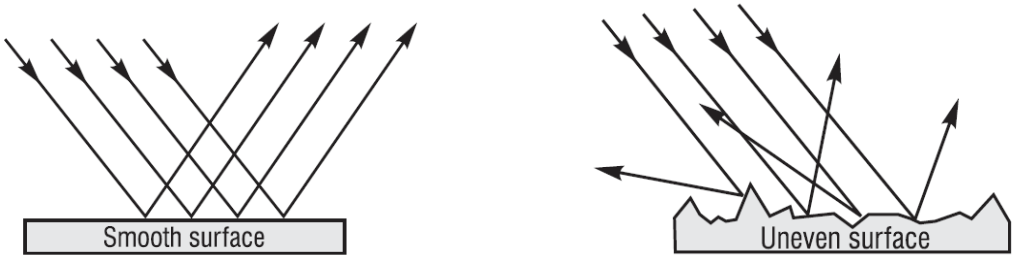

(a) Specular reflection (b) Diffuse reflection

Figure 4.15. Specular and diffuse reflection at boundaries [161]

Ray optics solves for ray position q and wave vector k, with optional equations able to be defined and solved for each variable like ray intensity, optical path length or phase.

Rays can travel through a homogeneous medium or a graded index medium (rays curve over medium due to constant change in refractive index). Figure 4.16 shows ray optics plot used to solve the focusing of light in a graded-index Luneburg lens. A Luneburg lens is a spherically symmetric gradient-index lens where refractive index n decreases radially from the centre to the outer surface. For certain index profiles, the lens will form perfect geometrical images of two given concentric spheres onto each other. There are an infinite number of refractive-index profiles that can produce this effect. The simplest such solution was proposed by Rudolf Luneburg in 1944 [162].

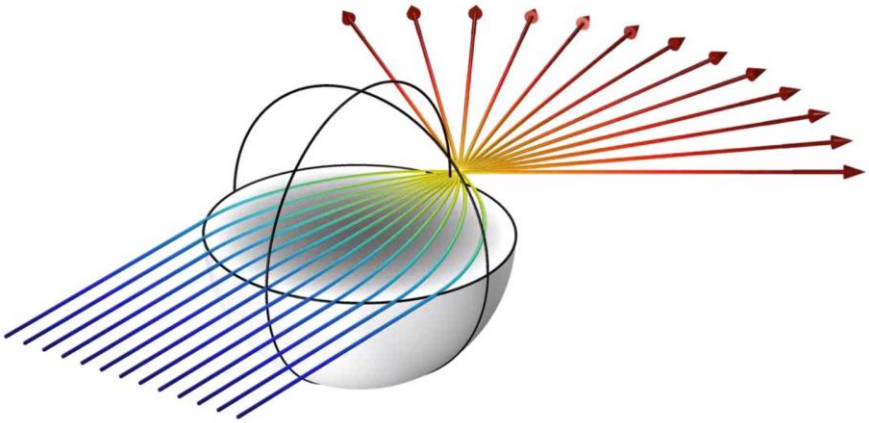

Figure 4.16. Rays focused by graded index of Luneburg lens in COMSOL Ray Optics [163]

Reflection and Refraction:

In ray optics, light is described as *rays* which propagate in straight lines with the paths governed by the laws of *reflection* and *refraction*. As such, whenever rays hit a boundary where the refractive index changes discontinuously, a refracted and reflected ray are both produced according to Snell's law.

Snell's law states that:

$$\frac{\sin\theta_1}{\sin\theta_2} = \frac{v_1}{v_2} = \frac{\lambda_1}{\lambda_2} = \frac{n_2}{n_1} \tag{4.16}$$

Where v is the velocity of light in the respective medium, λ is the wavelength of the light in the respective medium and n is the refractive index of the respective medium.

Since the order of the relation of the refractive indices is reversed, the relationship between the sine of the angle of light propagation and the refractive index across a boundary is best represented by the transposition:

$$n_1 \sin\theta_1 = n_2 \sin\theta_2 \tag{4.17}$$

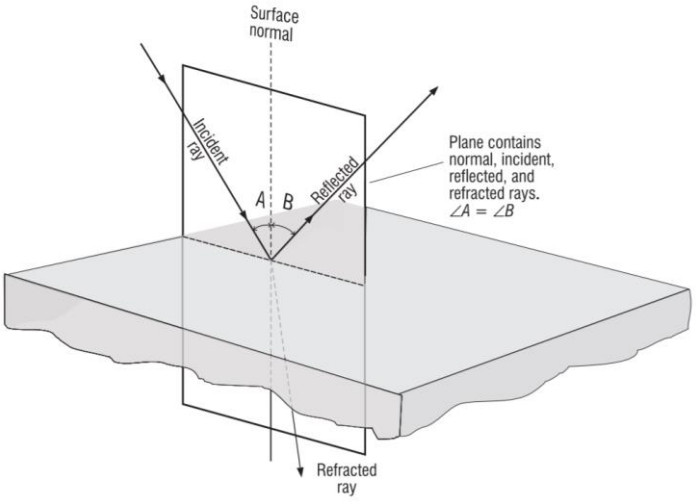

Figure 4.17. reflection and refraction across a material discontinuity [161]

In COMSOL, whenever rays hit a discontinuous boundary as shown in Figure 4.17, a reflected and refracted ray are both produced simultaneously based on Snell's law. Therefore, at any material discontinuity, a deterministic ray splitting occurs (rather than a probabilistic approach). Total internal reflection is automatically handled such that if there would be no refracted ray, only a reflected ray would be produced.

4.4. COMSOL Ray Tracing

There are three main reasons ray tracing was used to simulate the concentrators. First, due to the physical size of the geometry with respect to the wavelength of the incident light the refraction is taken to be negligible. Second, the distance the incident light travels to the concentrator and within the concentrator is considerable and would be computationally impractical. Finally, within COMSOL ray optics, only the boundaries need to be meshed. This reduces computation time, especially when rays travel large distances such as the sun or light source to a concentrator.

4.5. Direct vs. Iterative methods

4.5.1. Direct Methods

All direct solvers reach the same solution assuming a correctly set up model. This means in terms of results there is no difference between which direct solver is employed. COMSOL uses MUMPS, PARDISO and SPOOLES direct solvers all based on LU decomposition.

The difference comes down to computation cost, memory usage and scalability. PARDISO is typically the fastest solver with SPOOLES being the slowest. In terms of memory, SPOOLES uses the least amount of RAM however. Finally, the MUMPS solver offers support for parallel

computing, offering access to more memory than would otherwise be available on a single machine.

4.5.2. Iterative Methods

Iterative methods start at an initial condition, decided by the software based on the boundary conditions and physics or by the user prior to computation. The solver will approximate a solution to the problem and estimate the error, i.e. the difference between the current iteration and solution. In a well-defined problem, iterative methods gradually approach the solution. The rate of convergence can vary greatly depending on the problem with unsolvable or badly set up problems failing to converge or showing oscillating convergence plots. This successive approximation method also means that the different solvers will arrive at different solutions.

Non-linear problems almost universally require iterative methods, however even linear problems of large complexities and degrees of freedom are solved with iterative methods. In such cases direct methods would be extremely expensive computationally (processing power and memory).

4.6. 2D Geometry Models

4.6.1. Manual 2D Models

In the first phase of the investigation, the V-trough and CPC models were created using COMSOL geometry manually. For the v-trough this meant creating base receiver aperture as a flat plate (line) extended on both sides by two linear *mirror* straight surfaces. The top of the mirrors was capped using a straight surface representing the entry aperture. The result is shown in Figure 4.18.

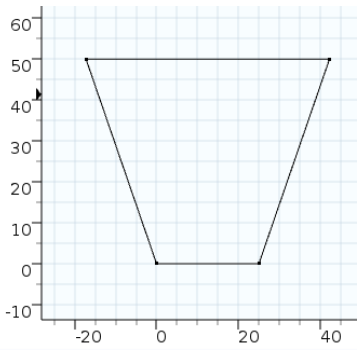

V-trough 2D geometry

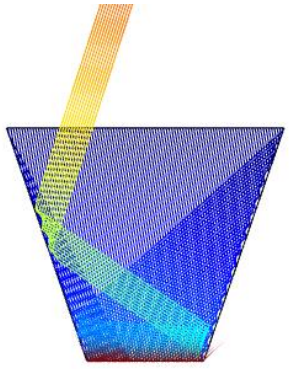

V-trough geometry with ray tracing

Figure 4.18. 2D v-trough model during (a) geometric creation and (b) ray tracing study

The CPC model similarly started with the receiver aperture created as a flat surface. The parabolic mirror is defined as a *parametric curve* feature in COMSOL. Here the expression for the parabola in Cartesian coordinates is defined (discussed in section 1 of this chapter). The parabola is then rotated by the acceptance half angle, and because a symmetric CPC is used, *mirror* transformation is applied to the parabola to get an equal and opposite curve. Finally, the top is capped with a linear surface at the appropriate height and the additional features trimmed. The process is shown in Figure 4.19.

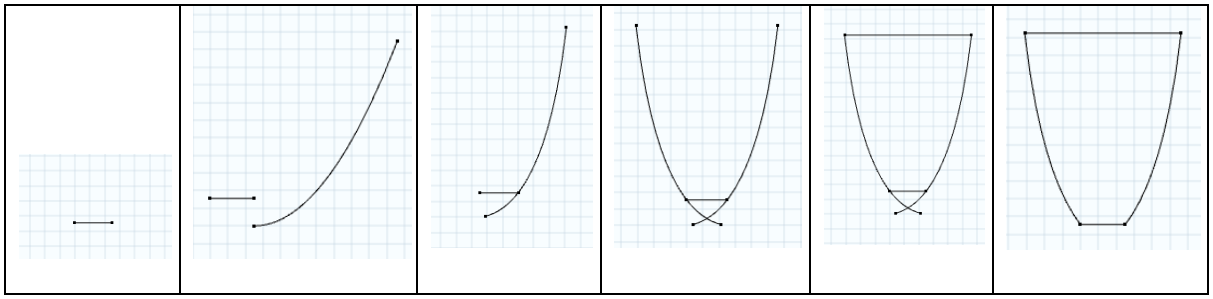

(a) Absorber (b) Parabola (c) Rotation (d) Mirror (e) Entry Ape. (f) Trim

Figure 4.19. CPC 2D Geometry Definition

The entry aperture does not represent a physical dimension but is used to a) find the geometric concentration ratio and b) release the sunrays at the concentrator.

A multitude of inlet boundary conditions were used to release the light rays into the ray tracing model. All the variations were physically equivalent and converged on the same result with the difference being the method used to achieve it: the goal was to allow easier transition into the *parametric driven geometry* [4.6.3] which would allow COMSOL to automatically adjust both the geometry and boundary conditions on-the-fly. These included releasing the rays at the bounds of the entire model, a distance above the entry aperture with the inlet released from a line tilted by the light angle of incidence and finally from the mirrors through a COMSOL boundary type called *illuminated surface*.

By using the inlet aperture cap method shown in Figure 4.20, it can be ensured that regardless of the direction vector of the light rays, the number and position of rays released would match exactly those that would be entering the concentrator system. Comparing this to the original manual system shown in Figure 4.21, where the rays were released at a light source, a set distance above the system, two steps of the process are improved:

- Only the light rays that would have entered the system are considered, making the optical efficiency easier to calculate. In Figure 4.20, all rays not reaching the absorber

surface is considered rejected rays [red rays]. However, in Figure 4.21 a series of rays do not enter the system at all and need to be ignored entirely. Because this number changes based on the direction vector of the light rays, it creates a stumbling block for creating the automated solver.

- As the direction vector becomes steeper, the location the inlet rays are released shifts, for example, at 89° light AoI, the release location of the rays in Figure 4.21 would move very far to the left. By using the capped method (Figure 4.20), the light ray vector has no impact on the location of the boundary condition.

By using the aperture cap method, the efficiency of the concentrator defined as:

$$\eta_f = \frac{rays\ hitting\ absorber}{rays\ released} \tag{4.18}$$

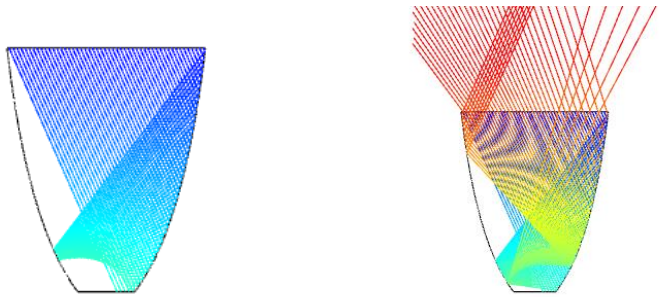

(a) Rays released (b) Rejected rays exit

Figure 4.20. Rays released at entry aperture

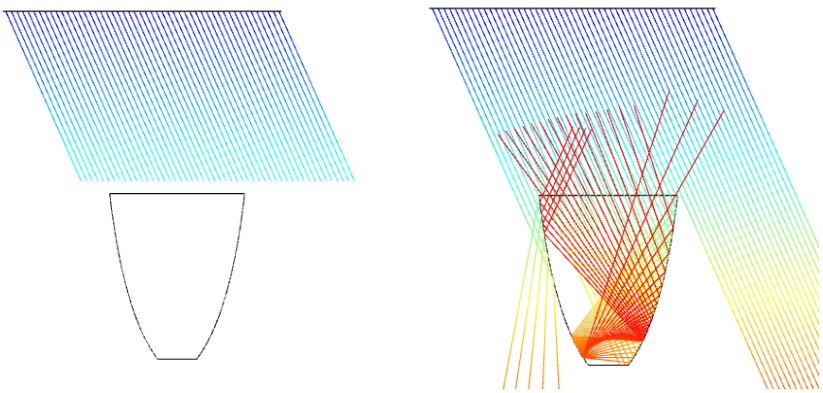

(a) Rays released (b) Rejected rays exit

Figure 4.21. Rays released set distance above concentrator

4.6.2. Parametric Sweep

An important feature in COMSOL Multiphysics is the option of running a *Parametric Sweep* study. In a parametric sweep, COMSOL will run a simulation multiple times with each iteration changing one or more parameters of the problem. For example, rather than hard setting the light angle of incidence and running the solver for each angle we would like to investigate, the model can be set up such that the *inlet* boundary condition is based on a parameter variable added under *Global Definitions* called "angle" which would hold the light angle of incidence. These variables can be changed during solver run-time, and importantly can be tied into the boundary conditions (such as *angle*) and geometries of the model, such that changing the parameters will change the BC or model geometry.

Under the *study* component of the simulation a parametric sweep is added where the parameters of the sweep can be selected. The values to be studied and the unit is defined here, where value can take the form of a number, a list or a range. For example, if we want to run the simulation for all light incidence angles 0-45 degrees in a 5° step interval the parameter would be set up as shown in Table 4.2

Table 4.2. Parameters for COMSOL ray tracing simulation.

Parameter name	**Parameter value list**	**Parameter Unit**
angle (Inlet light angle of incidence)	range(0,5,45)	deg

This would run the simulation a total of 10 times with the angle looping over the list {0, 5, 10, 15, 20, 25, 30, 35, 40, 45}.

4.6.3. Parametric Driven Geometry

The number of simulations required to model every design over the wide array of conditions is prohibitively large. For the V-trough, modelling Angle of Incidence (AoI) of 0-45° and Trough Wall Angle (TWA) of 0-45°, a total of 46×46 (2116) simulations will need to be performed. This is assuming only symmetrical V-trough is to be considered, if asymmetrical V-troughs (those with left and right reflector sides having different lengths) are modelled then the total simulations required would grow exponentially. The same principle applies to CPC concentrators; every CPC design and every truncation level needs to be modelled for every AoI.

A novel approach was used to convert the geometries in both 2D and 3D from manual CAD drawings to parametrically driven geometries. The aim once completed is that the solver (COMSOL Multiphysics) is given a range of various parameters and is able to automatically create and update the geometries and boundary conditions, allowing significant numbers of simulations to run automated.

4.6.3.1. V-trough

For the purpose of modelling, four parameters, *inlet light*, *wall trough angle (ψ)*, *wall length (W_L)* and *wall length horizontal component (W_x)*, were defined as described in Eq. (4.19) and (4.20).

Here the model was re-created and defined as functions of the angle of wall being simulated and the height limit of 50mm. Four parameters were added: *inlet light*, *wall angle*, *wall length* and *wall horizontal component*, where:

$$W_L = \frac{50}{\cos(\theta)} \tag{4.19}$$

$$W_x = W_L \sin(\theta) \tag{4.20}$$

In COMSOL Multiphysics, a *Bézier polygon* allows the creation of a complex shape consisting of the set of linear, quadratic or cubic segments to create an open or closed curve. The V-trough was then implemented as a *Bézier polygon* consisting of the components shown in Figure 4.22 and described as follows:

- ***A.*** (0,0) to (25,0) representing the 25mm wide horizontally aligned solar PV cell receiver
- ***B.*** (25,0) to (25 + W_x) representing the right-side wall of the V-trough
- ***C.*** (25 + W_x) to (-W_x, 50) going back twice the horizontal component of the reflectors as well as 25mm receiver
- ***D.*** (0, 0) reaching the left-most side of the solar receiver

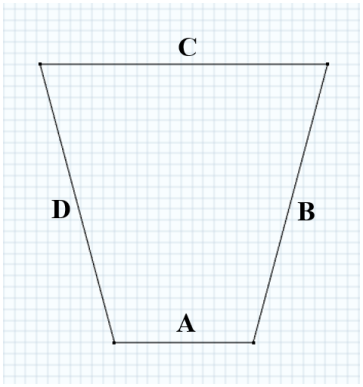

Figure 4.22. Parametric driven 2D V-trough cross-section

4.6.3.2. Compound Parabolic Concentrator

The transformation of the CPC geometry is more complex; due to the rotation of the parabola by the acceptance half angle, the equation of the parabola is changed. Furthermore, since the geometry is no longer manually defined, one cannot create full size CPC parabolas and truncate them by hand. As such the start and end point of the drawn parabola needs to be defined and parametric driven to achieve full geometry-automation.

There are two approaches to rotation: rotation of the axes or rotation of the object (relative to the axes). The project use case requires that the axes and coordinate system remain fixed due to other objects that comprise the CPC and its environment in the model setup, therefore the object themselves were rotated.

A rotation matrix derived from the Euler Formula in two dimensions takes the form:

$$\mathbf{R}_\theta = \begin{bmatrix} \cos\theta & -\sin\theta \\ \sin\theta & \cos\theta \end{bmatrix} \tag{4.21}$$

This is used to get the new *x* and *y* coordinates (denoted as *x'* and *y'*) by multiplication with the column vector:

$$\mathbf{v}' = \boldsymbol{R}_\theta \mathbf{v}_0 \tag{4.22}$$

It should be noted that rotation of a function by an angle θ is not guaranteed to remains a function: a function has one *y* value for each *x* value whereas a rotated function can have multiple *y* values for an *x* value. As such the rotated parabola will take a parametric form so that rather than $x \to y(x)$, the parabola will be described in the form $s \to \big(x(s), y(s)\big)$.

The parametric form of the rotated parabola becomes:

$$\begin{bmatrix} x' \\ y' \end{bmatrix} = \begin{bmatrix} \cos\theta & -\sin\theta \\ \sin\theta & \cos\theta \end{bmatrix} \begin{bmatrix} x \\ y \end{bmatrix} \tag{4.23}$$

This leads to:

$$x' = x \cdot \cos(\theta) - y \cdot \sin(\theta)$$
$$y' = x \cdot \sin(\theta) + y \cdot \cos(\theta)$$

Where (x', y') is the set of coordinates resulting from the rotation of (x, y) by θ degrees counterclockwise. The equation of the parabola is defined as:

$$y = \frac{x^2}{4f} \tag{4.24}$$

The rotated parametric expressions become:

$$x' = s \cdot \cos(\theta) - \frac{s^2}{4f} \cdot \sin(\theta) \tag{4.25}$$

$$y' = s \cdot \sin(\theta) + \frac{s^2}{4f} \cdot \cos(\theta) \tag{4.26}$$

The second challenge was to automate the truncation of the CPC. This was achieved by creating a parametric curve with a minimum and maximum plot value. The maximum represents the height of the (truncated) CPC to be rendered and the minimum corresponds to the absorber aperture of the solar cell.

In order to find both these bounds, the root of the expression for *y'* needs to be calculated. To find the top of the CPC, we substitute *y'* with the CPC height (*y_top*) to get:

$$y_{top} = s \cdot \sin(\theta) + \frac{s^2}{4f} \cdot \cos(\theta) \tag{4.27}$$

It can be seen that the equation (4.25) of the parabola is a quadratic equation. The solution of this equation leads to:

$$y_{top} = x \sin(\theta) + \frac{x^2}{4f} \cos(\theta)$$

$$\Downarrow$$

$$\frac{x^2}{4f} \cos(\theta) + x \sin(\theta) - y_{top} = 0$$

Where:

$$a = \frac{\cos(\theta)}{4f},\ b = \sin(\theta),\ c = -y_{top}$$

$$x = \frac{-b \pm \sqrt{b^2 - 4ac}}{2a} = \frac{-\sin(\theta) \pm \sqrt{\sin^2\theta + \frac{y_{top} \times \cos\theta}{f}}}{\cos\theta / 2f} \tag{4.28}$$

The lower bound of the parametric curve is determined by the focal length of the CPC. This is the *y-value* of the rotated parabola which forms the base of the CPC (absorber aperture). The process is applied again to find the cut-off point of the lower parabolas. Finally, the top and bottom apertures are represented as linear surfaces.

The symmetric CPC was then defined as a set of geometries as follows in sections J-L below:

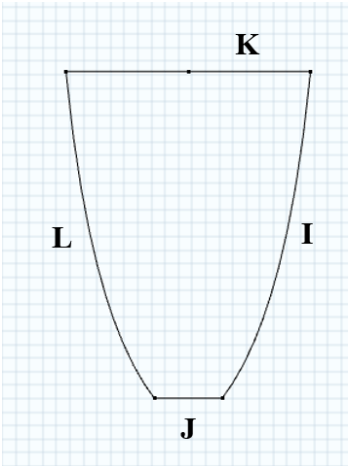

Figure 4.23. Parametric driven 2D CPC cross-section

I. First parabola set up as a *Parametric curve* drawn to top_{root}:

a. $x = \cos(\theta_h)\, s - \sin(\theta_h)\frac{s^2}{4f}$

b. $y = \sin(\theta_h)\, s - \cos(\theta_h)\frac{s^2}{4f}$

Where f is the focal length of CPC parabolas and θ_h the CPC half acceptance angle.

J. Focal lines and absorber aperture set up as a *Bezier polygon* with segments:

a. (0,0) **to** $(-f \sin\theta_h\ , f\cos\theta_h)$

b. $(-fsin\,\theta_h\ , fcos(\theta_h))$ **to** $(-fsin(\theta_h) + W_{abs}\ ,\ fcos(\theta_h))$

c. $(-fsin(\theta_h) + W_{abs}\ ,\ fcos(\theta_h))$ **to** $(-2fsin(\theta_h) + W_{abs}\ ,\ 0)$

K. Inlet half-aperture set up as a 1-step Bezier Polygon:

a. $\left(-fsin(\theta_h) + \frac{W_{abs}}{2}\ , \sin(-\theta_h)\cdot(-top_{root}) + \cos(-\theta_h)\cdot\frac{(-top_{root})^2}{4f}\right)$

to

$\left(\cos(\theta_h)\, top_{root} - \sin(\theta_h)\frac{top_{root}^2}{4f}\ , \sin(\theta_h)\, top_{root} + \cos(\theta_h)\ \frac{top_{root}^2}{4f}\right)$

Where W_{abs} is the absorber width (PV cell width), set as 25mm for the study.

L. For the symmetric CPC, the *mirror transformation* feature was used to get the opposing parabola and inlet aperture. In the case of non-symmetric CPC, a second *parametric curve* going to top_{root} was defined as:

a. $x = \cos(-\theta_h)\, s - \sin(-\theta_h)\frac{s^2}{4f}$

b. $y = \sin(-\theta_h)\, s + \cos(-\theta_h)\frac{s^2}{4f}$

COMSOL Multiphysics can change the geometry and boundary conditions through a set of four core parameters: AoI $angle_{light}$, CPC concentration ratio C_r, PV cell width W_{abs} and truncation level (%). A '*parametric sweep'* was used to run groups of simulations with COMSOL Multiphysics given ranges of each parameter to sweep.

4.6.4. Parametric Sweep

Once the geometry is set up as a set of parametric driven equations, COMSOL can then update the geometry automatically by changing the relevant parameters and remeshing. Under *study*, a "parametric sweep" is added where the parameters to sweep over need to be specified.

Furthermore, the sweep type was set to "all combinations" from the default "specified combinations". To explain the difference, take an example case of 0-20° light angle of incidence and 10-20° V-trough wall angles studies with a parametric sweep. Under "specified combinations", COMSOL first runs 21 simulations for the 0-20° light angle of incidence cases with the wall angle as set by default in the parameter list, it then runs another 11 simulations for the 10-20° V-trough wall angles. What is required is running 0-20° light angle of incidence for each of the V-trough wall angles (10-20°) for a total of $21 \times 11 = 231$ simulations. The "all combinations" sweep type achieves this by running every combination of the parameters provided. This process is visualised in Figure 4.24.

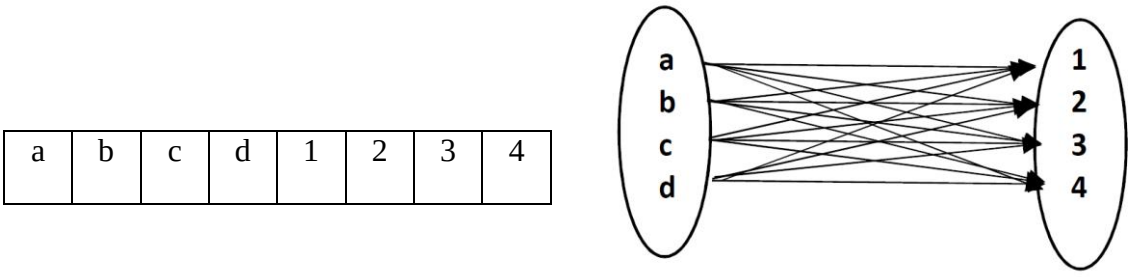

(a) Specified combinations *(b) All combinations*

Figure 4.24. Visual comparison of number of iterations required for a two-parameter (a-d) + (1-4) sweep using (a) specified combinations [8 iterations] and (b) all combinations [16 iterations]

4.6.4.1. V-trough

For the V-trough the parameters selected were *theta*, the reflector wall angle and *angle*, the light angle of incidence. Initial tests were run using coarse sweeps: theta ranging from 0-45° in steps of five and light angle going in steps of 5°. As the area of interest was identified, the step size became more and more fine, in the end going in ½ angle steps from 10-20° wall angle. The light angle of incidence stayed a constant sweep of 0-45° in 1° steps throughout.

4.6.4.2. CPC

There are four parameters which represent the core variables of the simulation, they are angle, the light AoI, C_r, the concentration ratio of the CPC, w_abs, the width of the absorber surface and truncation, the truncation % of the CPC with 1 being full CPC height and 0.5 being a 50% truncation. For the case where the truncation is defined as an absolute height, such as 50mm, the truncation is changed from a value to the expression "50/L" where L is the CPC full height. For example, in the case of a 242 mm CPC height, to truncate to 50mm rather than a %, the variable truncation is evaluated as $\frac{50}{242.06} = 0.20656$.

4.7. Meshing

One of the principle advantages of ray tracing is that rays can propagate over long distances with relatively little computation cost. This is because the mesh need not be fine enough resolve each wavelength throughout its trajectory. With COMSOL version 5.2a and later, it is not necessary to mesh the boundary the rays travel across. This requires the following conditions:

- The medium is homogeneous, isotropic, and does not depend on field variables (such as temperature).
- All unmeshed regions have the same refractive index.
- Advanced mesh-dependent features like domain accumulators are not needed in the unmeshed regions.
- All boundaries that affect ray propagation are meshed. This includes boundary conditions such as material discontinuities, absorbing or scattering walls, diffraction gratings, and optical components such as linear polarizers.

The difference is shown in Figure 4.25 which shows an example model meshed in version 5.2 (a) and version 5.2a (b).

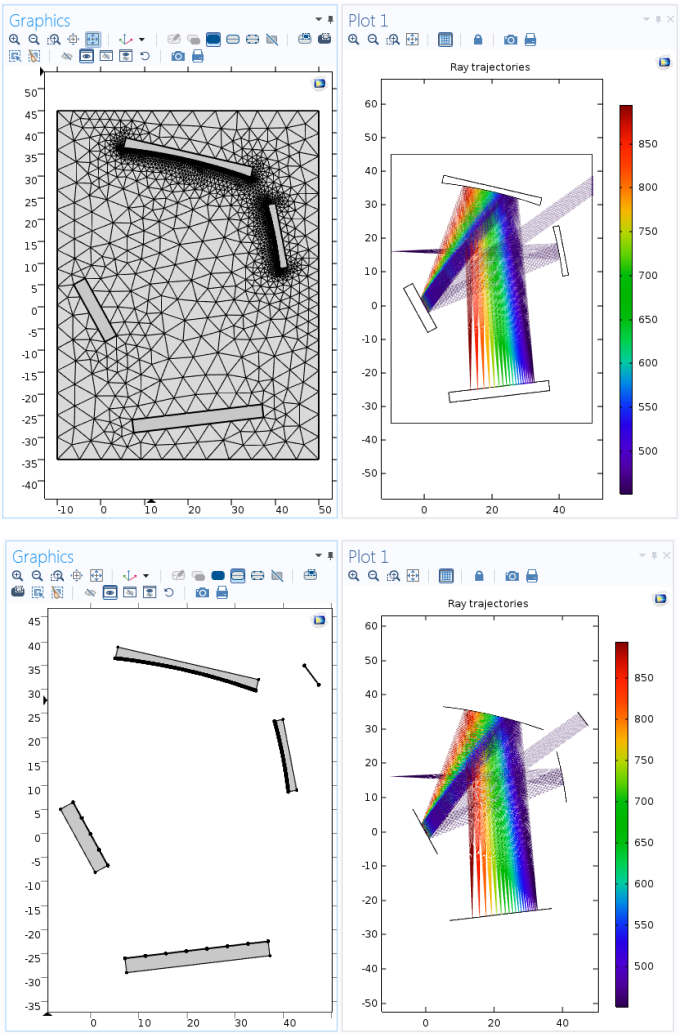

(a)

(b)

Figure 4.25. Mesh and result of the same model with (a) and without domain meshed [164].

For this project, in the decomposed model, only the boundaries need to be meshed because rays will not be travelling through them. The interactions (whether they be freezing, reflecting either specularly or by diffusion) will be happening at the boundaries and rays will not be travelling through the concentrator materials. This significantly reduces the mesh size and allows greater leeway in increasing the resolution at points of interest such as the absorber cell for accurate depiction of distribution of rays absorbed and at the parabolas for better approximation of the curvature. Another reason is that since a parametric sweep was employed, the mesh will not be constant and will evolve throughout the computation.

A *user defined mesh* was selected. An *edge mesh* was added with the boundaries of the CPC and V-trough to be meshed were selected as follows:

- Top inlet aperture
- Two side reflectors

- Bottom absorber plate

For the element parameters, initially the *minimum element size* was set to 0.002 mm and *curvature factor* set to 0.002. This gave us a good resolution of curvature. The inlet and absorber apertures ended up too coarse, something that was not relevant initially but gained significance in later stages where the distribution of light rays on the cell surface became of interest due to cooling and efficiency considerations. As such the *maximum element size* was later set to 0.02 mm.

The resulting CPC mesh consisted of 8090 elements split as shown in Figure 4.26 with minimum quality: 1.0 and average quality: 1.0.

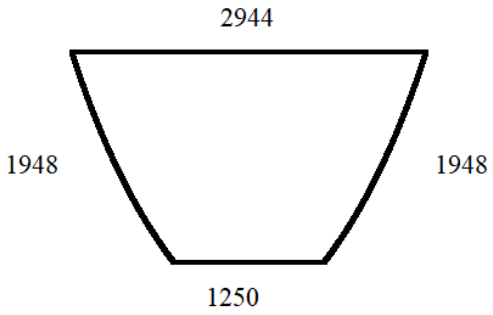

Figure 4.26. CPC boundary mesh breakdown

The V-trough mesh consisted of 9510 elements as shown in Figure 4.27 with minimum quality: 1.0 and average quality: 1.0.

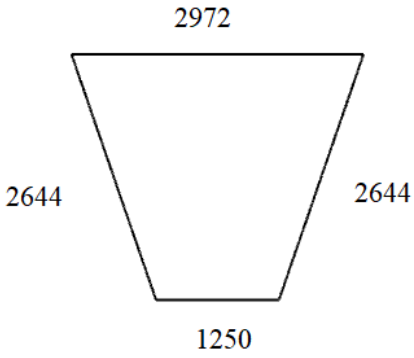

Figure 4.27. V-trough boundary mesh breakdown

4.8. Physics

COMSOL Multiphysics offers a variety of solvers based on the physics being modelled. Examples include Fluid Flow, Heat Transfer, Optics and Structural Mechanics. Optics contains solvers for Ray Optics and Wave optics. Within Ray Optics, the module *Geometric optics*

physics was added to the model (Physics > Optics > Ray Optics > Geometrical Optics). The underlying physics and governing equations are described in section 4.3.3 Ray Optics.

The boundary conditions set as:

- Ray property specified at a wavelength of 660 nm
- Reflector wall boundaries set to:
    - Specular reflection for initial runs
    - Mixed specular and diffusion with a 98% probability of specular reflection based on experimental reflector data

Figure 4.28 demonstrates the difference between a specular and diffuse reflective surface in COMSOL.

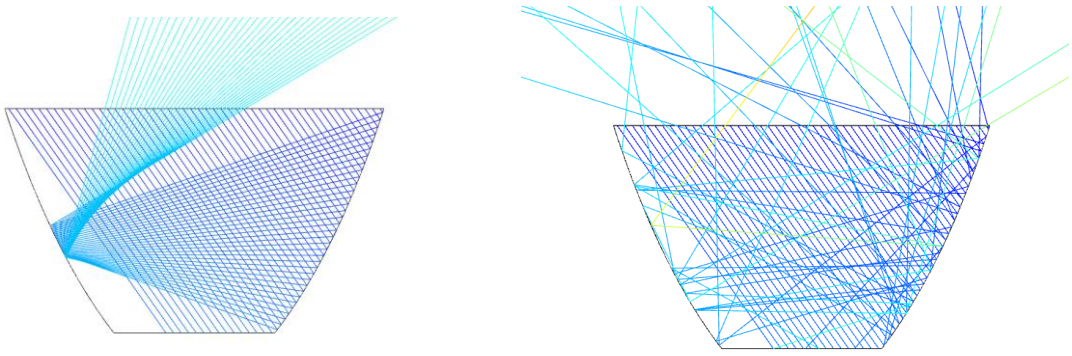

(a) Specular reflection *(b) Diffuse scattering*

Figure 4.28. Comparison of (a) Specular and (b) Diffuse reflections in COMSOL

- Absorber boundaries set to freeze rays
- An accumulator was set on the absorber boundaries to count rays absorbed
    - Accumulator type: *count*
    - Accumulate over: *ray-wall interactions*
    - Source: R = *1* and *dimensionless* (i.e. each ray increases count by 1)
- Inlet boundary
    - Number of rays ranged from *100-100,000*
    - Initial position of rays set to *uniform distribution*
    - Ray direction vector given the *x*, *y* and *z* (for 3D) components of inlet solar rays angle of incidence
    - Environment Boundary set to *freeze* rays with accumulator set using steps as shown for the absorber accumulator to count the number of rays being reflected back out of the concentrator

A schematic of the 2D model is presented in Figure 4.29 with annotated geometries and boundary conditions:

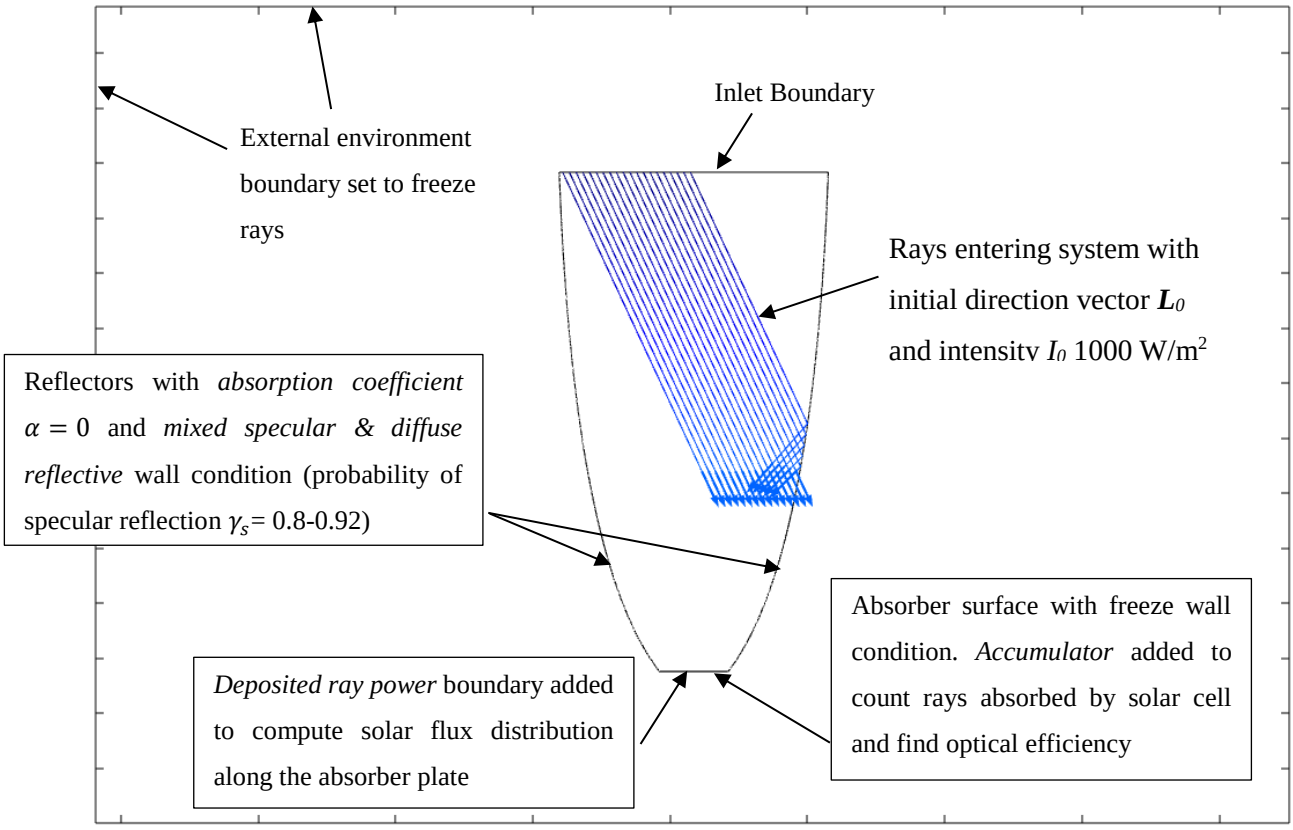

Figure 4.29. 2D schematic of ray tracing model setup in COMSOL Multiphysics

4.9. Concentrator Efficiency Limits

Regardless of the conversion mechanism in solar cells, the laws of thermodynamics impose a theoretical limit on the maximum concentration of sunlight.

Carnot Efficiency:

One way to evaluate the limit is to consider the solar cell by an ideal reversible Carnot heat engine in perfect contact with a high temperature reservoir T_s representing the sun, and a low temperature reservoir T_a representing the ambient Earth atmosphere. The output of the solar cell can be evaluated through the *first law of thermodynamics* as the difference between the energy input of the sun and losses dissipated to its surrounding environment. This is defined as:

$$\eta_c = \frac{W}{Q_1} = \frac{Q_1 - Q_2}{Q_1} = 1 - \frac{Q_2}{Q_1} \tag{4.29}$$

where Q_1 is the incidence solar radiation and Q_2 is the amount of energy leaving the solar cell to the ambient surroundings. *W* is the work done by the solar cell output as electrical energy given by:

$$W = Q_1 - Q_2 \tag{4.30}$$

Total entropy is conserved for a reversible engine, that is $S = S_1 - S_2 = 0$. We therefore get:

$$\frac{Q_1}{T_1} - \frac{Q_2}{T_2} = 0 \tag{4.31}$$

The Carnot efficiency of the system is therefore evaluated by:

$$\eta_c = 1 - \frac{T_a}{T_s} \tag{4.32}$$

Taking the temperature of the sun at *6000K* and the temperature of the ambient at *300K* gives a Carnot efficiency limit of $\eta_c = 1 - \frac{300}{6000} = 0.95$, or 95%. Note this relationship can be used to state that when $T_a = T_s$, the efficiency of the system is 0% and when the solar cell is at *0K* ambient temperature, the efficiency of the system is 100%.

Landsberg efficiency:

Another approach is, called the Landsberg efficiency [165], considers the solar cell as a blackbody converter at temperature T_c, absorbing radiation from the sun, another blackbody, at temperature T_s without creating entropy. The entropy of the system under reversibility condition we get:

$$S_{abs} - S_{emit} - S_a = 0 \tag{4.33}$$

where the absorbed entropy S_{abs} given off is partly emitted back to the sun (S_{emit}) and partly given to the (solar cell) ambient blackbody (S_a). From Stefan–Boltzmann' law of black body, the absorbed heat flow from the sun is evaluated by:

$$Q_{abs} = \sigma T_s^4 \tag{4.34}$$

For a blackbody radiation, the absorbed density of entropy flow is given by:

$$S_{abs} = \frac{4}{3}\sigma T_s^3 \tag{4.35}$$

The energy flow emitted by the solar cell at a temperature T_c is given by:

$$Q_{emit} = \sigma T_c^4 \tag{4.36}$$

The emitted entropy becomes:

$$S_{emit} = \frac{4}{3}\sigma T_c^3 \tag{4.37}$$

This model assumes the blackbody source (sun) surrounds entirely the solar cell at T_c, which is in a contact with the ambient surrounding at T_a. T_c and T_a will therefore reach thermal equilibrium such that $T_a = T_c$. The entropy transferred to the ambient is therefore given by:

$$S_a = S_{abs} - S_{emit} = \frac{4}{3}\sigma(T_s^3 - T_c^3) \tag{4.38}$$

The transferred heat from is given by:

$$Q_a = T_c S_a \frac{4}{3}\sigma T_c(T_s^3 - T_c^3) \tag{4.39}$$

Hence the work of the solar cell can be evaluated by:

$$W = Q_{abs} - Q_{emit} - Q_a \tag{4.40}$$

As such, the Landsberg efficiency is evaluated as:

$$\eta_L = \frac{W}{Q_{abs}} = 1 - \frac{4}{3}\frac{T_c}{T_s} + \frac{1}{3}\left(\frac{T_c}{T_s}\right)^4 \tag{4.41}$$

Since the actual temperature at the solar cell T_c is different from the ambient temperature, $T_c \neq T_a$. To maintain the same assumptions as the Landsberg efficiency calculation, the entropy transferred to the ambient is updated to:

$$Q_a = T_a S_a = \frac{4}{3}\sigma T_a\,(T_s^3 - T_c^3) \tag{4.42}$$

This leads to a general form of the Landsberg efficiency:

$$\eta_L' = 1 - \left(\frac{T_c}{T_s}\right)^4 - \frac{4}{3}\frac{T_a}{T_s}\left(1 - \frac{T_c^3}{T^3{}_s}\right) \tag{4.43}$$

The Landsberg efficiency place the conversion efficiency limit at 93.33%. Both Landsberg efficiency models and the Carnot model are plotted in Figure 4.30.

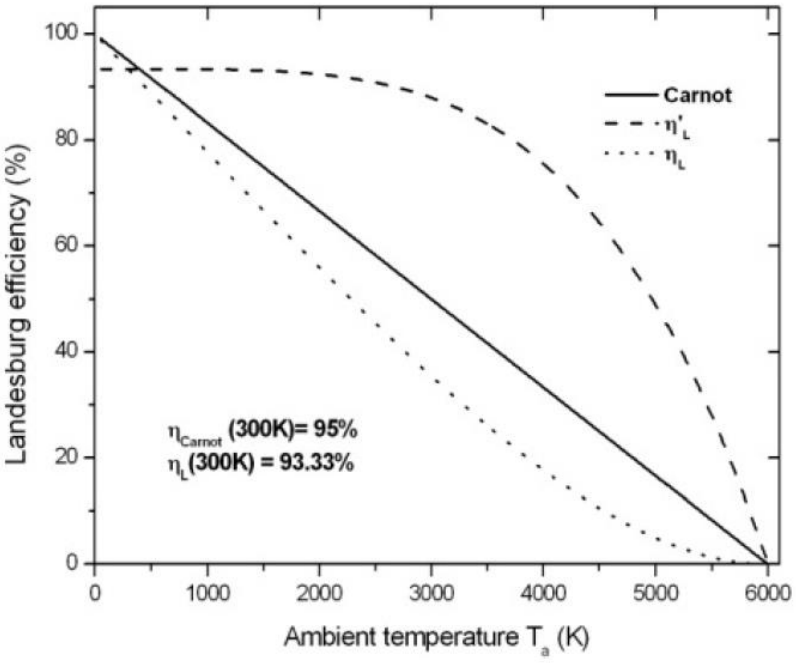

Figure 4.30. Landsberg and Carnot efficiency limits of a solar cell versus ambient temperature T_a [166]

It is possible to split the system into two subsystems each with its own efficiency. A Carnot engine that includes the heat pump of the converter at T_c and the ambient heat sink at T_a, with an efficiency η_c (ideal Carnot engine):

$$\eta_c = 1 - \frac{T_a}{T_c} \tag{4.44}$$

The second part is composed of the sun as an isotropic blackbody at T_s and the converter reservoir assumed as a blackbody at a temperature T_c.

The energy flow falling upon Q_{abs} is given by:

$$Q_{abs} = CfT_s^4 \tag{4.45}$$

and the energy emitted by the solar converter Q_{emit} is given by:

$$Q_{emit} = \sigma T_c^4 \tag{4.47}$$

where *f* is a geometrical factor considering the angle at which solar radiation is incident on the solar cell. Assuming the solar cell operating schematic presented in Figure 4.31, *f* is given by:

$$f = \frac{area\ subtended\ by\ the\ sun}{area\ of\ the\ hemisphere} = \frac{\int_{\omega_s} \cos\theta\, d\omega}{\int_{2\pi} \cos\theta\, d\omega} = \frac{\omega_s}{\pi} \tag{4.48}$$

where ω_s is the sun subtending angle ($6.85 \times 10^{-5}\ sr$) and θ is the solar incidence angle.

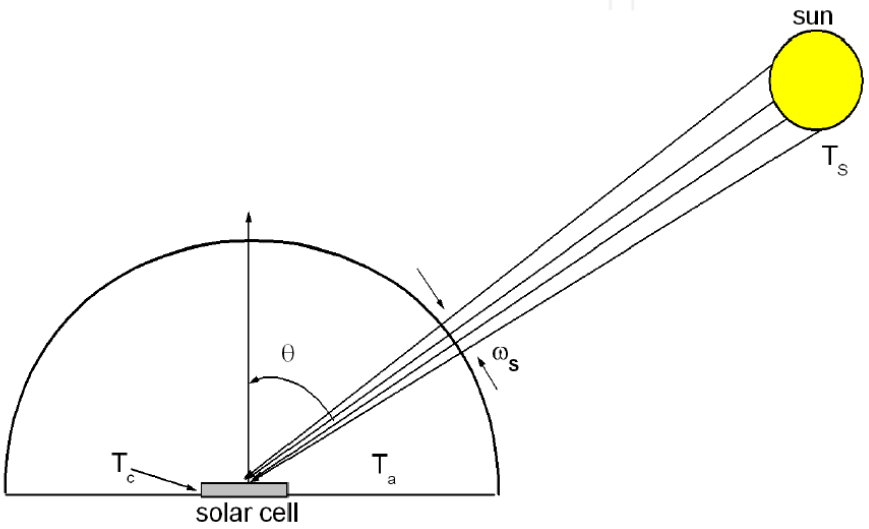

Figure 4.31. Thermodynamics limit of light concentration [167]

The maximum concentration factor can be obtained by taking $T_s = 6000K$, and is given by:

$$\sigma T_s^4 = C_{\max} f \sigma T_s^4 \tag{4.49}$$

$$C_{max} = \frac{1}{f} \approx \mathbf{46200}$$

The efficiency of the absorber part of the system is given by:

$$\eta_{abs} = 1 - \frac{Q_{emit}}{Q_{abs}} \tag{4.50}$$

The overall efficiency becomes the product of the two sub-systems:

$$\eta_{ac} = \eta_c \cdot \eta_{abs} = \left(1 - \frac{T_c^4}{CfT_s^4}\right)\left(1 - \frac{T_a}{T_c}\right) \tag{4.51}$$

Figure 4.32 shows plots of the efficiency limits at various concentrations. At maximum concentration of 46'200, the efficiency limit is given as ~86%.

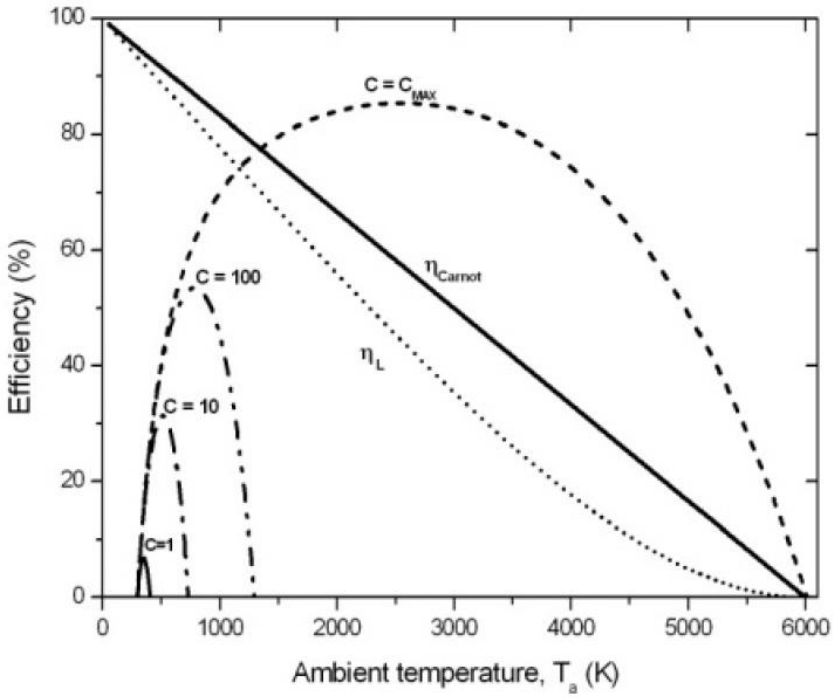

Figure 4.32. Efficiency limits of concentrators based on ambient temperature [166]

In this chapter, a method of approximating the effective concentration ratio has been established analytically through the solution of equations describing the number of reflections or absorbed rays through the V-trough and CPC aperture. It is important to note that this is different from the geometric concentration ratio, the ratio of the inlet aperture to the receiver aperture. This is because not all rays entering the concentrator is absorbed: based on the type of concentrator, the design of the trough walls and the angle of light incidence, some or all the lights entering the concentrator are reflected out.

To do such a task analytically, the aperture width of the V-trough concentrator must be discretised into regions based on the number of reflections required to reach the absorber aperture. CPCs are more difficult to fabricate and analyse, the truncation, optional asymmetry of the parabolas and varying incidence angles add further difficulties. The use of computer modelling does not have these drawbacks and has the advantage of not needing the manufactured system to analyse with lasers, allowing rapid design iterations before even the prototype stage. Table 4.3 shows the advantages and disadvantages of implementing CPV systems.

Table 4.3. Analysis of the strengths and weaknesses of CPV [118].

Strengths	Weaknesses
High efficiencies for direct-normal irradiance	HCPV cannot utilize diffuse radiation LCPV can only utilize a fraction of diffuse radiation
Low temperature coefficients	Tracking with sufficient accuracy and reliability is required
Additional use of waste heat possible for systems with active cooling possible (e.g. large mirror systems)	May require frequent cleaning to mitigate soiling losses, depending on the site
Low CapEx for manufacturing infrastructure enables fast growth	Limited market – can only be used in regions with high DNI, cannot be easily installed on rooftops
Modular – kW to GW scale	Strong cost decrease of silicon flat-plate modules makes market entry very difficult for even the lowest cost technologies
Increased and stable energy production throughout the day due to tracking	Bankability and perception issues due to shorter track record compared to PV
Very low energy payback time	New generation technologies, without a history of production (thus increased risk)
Potential double use of land, e.g. for agriculture. Low environmental impact	Additional optical losses
Opportunities for cost-effective local manufacturing of certain steps	Lack of technology standardization
Less sensitive to variations in semiconductor prices	
Greater potential for efficiency increases in the future compared to single-junction flat plate systems could lead to greater improvements in land area use, system, the balance of system (BOS) costs	

Incorporating CPVs in BIPV is difficult, the biggest problem arises from the sun-tracking required by such systems: since they only operate within specified acceptance angles, CPVs need to track the sun east-west during the day and north-south during the year. Systems integrated in building walls or skyscraper windows would either be impossible or untenably expensive and complicated to manufacture and implement. The existence of moving mechanical parts would bring up maintenance and replacement problems in areas of the building that are hard to reach as well.

LCPVs such as V-trough and CPC can accept light at different angles whilst fixed as compared to parabolic concentrators which need to implement some sort of sun-tracking system. This makes CPCs a great candidate for BIPVs: firstly, because the spread of light over a greater area

leads to better heat generation distribution, secondly because a BIPV CPC can passively track the sun within the acceptance angle.

It was discussed that ray tracing is used to simulate the concentrators due to the physical size of the geometry with respect to the wavelength of the incident light the refraction is taken to be negligible. Second, the distance the incident light travels to the concentrator and within the concentrator is considerable and would be computationally impractical. Finally, within COMSOL ray optics, only the boundaries need to be meshed. This reduces computation time, especially when rays travel large distances such as the sun or light source to a concentrator. From ray tracing analysis, the geometries of CPC and V-trough concentrators are designed to obtain uniform flux distribution and high concentration ratio on the receiver PV panel.

4.10. Conclusion

Drastic advances in commercial multi-junction solar cells have resulted in up to 40% conversion efficiency. As a result, requirement for solar concentrators capable of delivering flux levels of hundreds to thousands of suns at high collective efficiency is a key factor for the success of novel concentrator photovoltaic (CPV) systems.

In this chapter details of solar concentrator technologies have been discussed, comparing different optical performance of CPC and V-trough. However, since the CPVs have recently gained momentum in deployment, there is not enough historical data for the analysis of durability of designs and their performance over years of use.

It was shown that the irradiation pattern for flat concentrators is uniform. However, the concentration ratio in flat concentrators hardly increases above 2, therefore cannot concentrate enough sunlight on the PV receiver. On the other hand, although compound parabolic concentrators (CPCs) increase the maximum intensity, a non-uniform pattern of light is formed on the receiver. This problem is exacerbated by reducing the focal length of the CPC. Further analyses of compound parabolic (CPC) and V-trough are carried out using ray tracing.

COMSOL Multiphysics software has been used to develop ray tracing models for the analysis of CPC and V-trough concentrators. Theoretical results show that the CPC and V-trough exhibit higher variations in non-illumination intensity distributions over the receiver surface for larger incidence angles. In addition, the maximum power output for the cells with CPC and V-trough concentrators varies depending on the location of the cell in the PV module as well as the reflecting surface geometry of the concentrator.

CPC and V-trough collectors can collect solar radiation in the range of $-90° < \theta < 90°$ incidence angle. For comparison of V-tough and CPC in Chapter 6, the concentration ratios and aperture areas are set equal and the angular acceptance function and optical efficiency of both concentrators are analysed for a full range of incidence angles. A 50mm CPV height was set as a constraint for the BIPV width representing the space available in double glazed windows. Within this constraint the V-trough and CPC can have varying geometric concentration ratios (for example due to the angle of the V-trough wall).

The developed ray tracing model in COMSOL Multiphysics is used to predict optical efficiency and solar energy flux distribution along the PV module as well as the maximum power output with the CPC and V-trough collector.

Chapter 5 Experimental Method

5.1. Introduction

There are two reasons for experimentally testing the simulation models. Firstly, it helps validate the results of the modelling results. By comparing the results, the accuracy of the models is verified and also insight is gained on the physical workings of the concentrator that can help improve the model. One example is the back propagation of data regarding the properties of the reflective surfaces of the concentrators: by using the data gathered from the physical medium used to reflect light, the diffuse and specular reflective properties of the boundaries can be better set.

On the other hand, the model can also help improve the experiment. By having rapid analysis of the effect of geometry, topology and test conditions on the results, the number of physical prototypes and test iterations can be reduced manifold. In this case, model results lead to the selection of a 50 mm truncated CPC and a 50 mm V-trough with 19° reflective wall angle.

This chapter explains the steps from concept through fabrication to experimental testing of the CPC and V-trough concentrators.

5.2. CPC and V-trough fabrication

Probably the most important step in the experimental setup was fabrication of the CPC and V-trough bases. The curve of the CPC is incredibly important as small deviations would lead to low quality results. The manufactured parts were measured for accuracy using high precision CNC-probes and digital Vernier Calipers and adjusted as necessary. For this reason, selecting an appropriate manufacturing process was of utmost concern.

For manufacturing the bases three methods were considered:

- Crafting the CPC and V-trough base using wood/metal crafting in the workshops using sawing, milling, bending, turning machines
- Using 3D printing method to build the structures
- Cutting the shapes from blocks of materials using CNC milling machines

Of the three methods, it was decided to fabricate the bases using CNC milling machine. The CPC requires creating rotated parabolic curves (non-circular), something that would be very

difficult and prone to error if hand-crafted. The decision between 3D printing and CNC machining came down to a mix of the availability of high-resolution CNC machines at Brunel University along with the advantage of being able to select the raw material being machines, in contrast 3D printers are limited to a pre-set resin depending on the machine used.

The models were created in SolidWorks as extrusions of the 2D cross-section. Detailed schematic of the concentrators are shown in Figure 5.1 for the V-trough and *Figure* 5.2 for the CPC concentrators.

Interfacing the models with the CNC machines required converting the files to both IGS and STL formats. STL, an abbreviation of *stereolithography,* is not a vector format; rather it creates the model required as close as possible using a series of connected triangles. In order to minimize loss of information when saving as STL files, SolidWorks offers an advanced setting feature under export options and a custom resolution was selected with both the "deviation" and "angle" tolerances and they are set to the smallest unit possible. Figure 5.3 shows the effect of resolution on STL export model.

Another characteristic of STL files is that they are inherently dimensionless. As such the unit needs to be specified in both SolidWorks and any CAD/CAM software used.

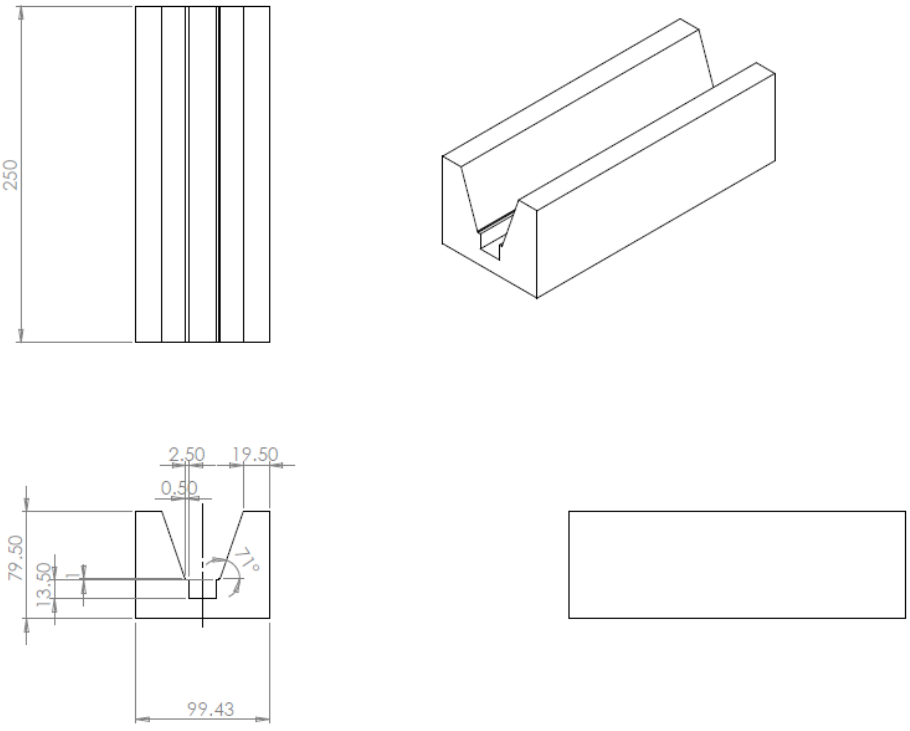

Figure 5.1. V-trough Technical Drawing Schematic (dimensions in mm)

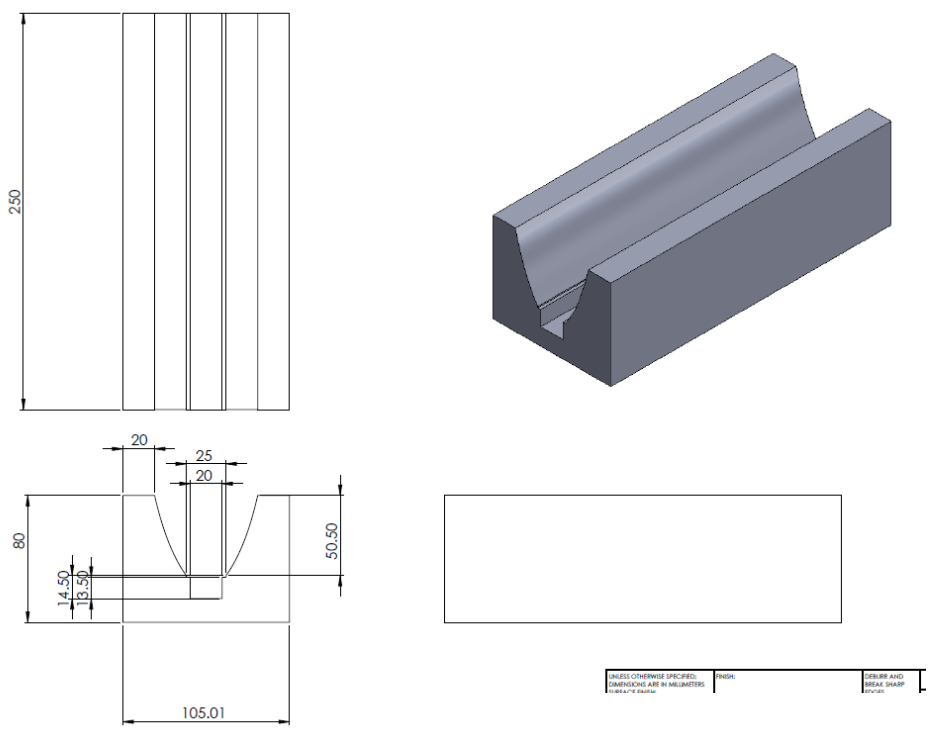

Figure 5.2 CPC Technical Drawing Schematic (dimensions in mm)

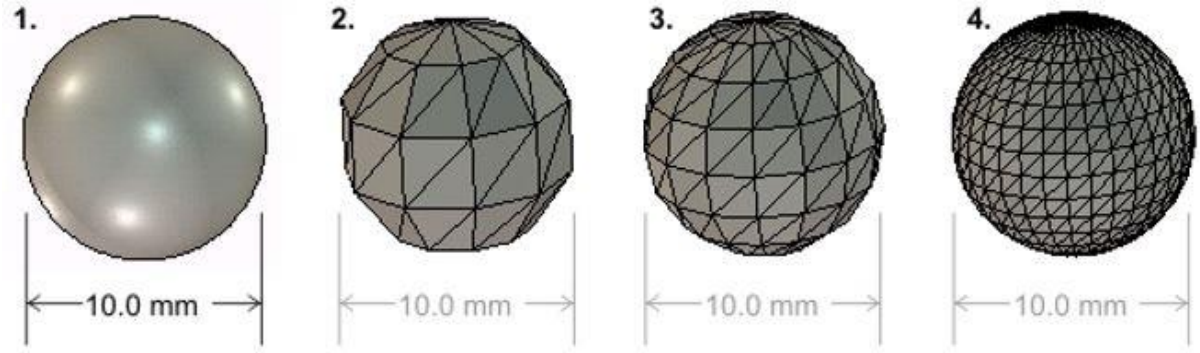

Figure 5.3. The effect of STL resolution on object, (1) ideal and (2-4) coarse to fine [168]

5.2.1. Material Choice

One of the advantages of CNC machining is that the material choice is limited only by the tooltip and spin/feed rates. Considering the use case of the CPC and V-trough concentrators, there is little to no mechanical load, in either tensile or compressive form. The main considerations are the thermal properties of the material and the machinability. Machinability

refers to the ability of the material to be machined to create the finest and smoothest surface, closest matching the input model.

The material used was High Density Polyurethane Model Board, commonly referred to as Uriel. The material can be machined fast, creates smooth curves due to its granularity and is frequently used in prototyping for harder materials due to its affinity to be machined. It is also thermally stable to temperatures up to 130°C, and further beyond with small losses in tensile strength.

When CNC machining the part, a larger block of Uriel was used, this was drilled on four corners and used to bolt down the part to the CNC machine work area as shown in Figure 5.4. The CNC process was divided into two stages, the first stage was a rough cut of the bulk of the material whereas the second stage went over the surfaces of interest (such as CPC, V-trough reflective walls) at slower feed rate, higher speed rate, smaller tool diameter and finer step sizes to ensure a smooth finish.

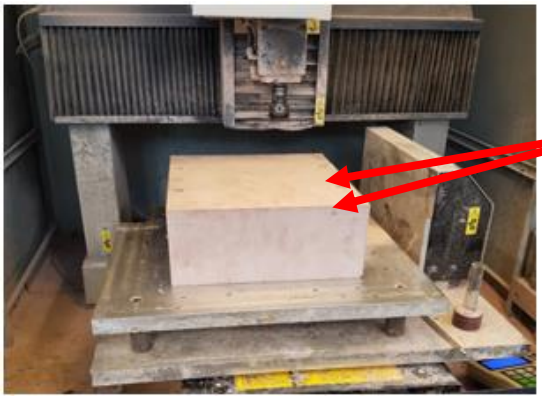

Figure 5.4. Setting up the Uriel on the CNC machine

Figure 5.5. CNC machining in progress (CPC being milled in picture)

Because the simulations and experiments need to match as closely as we can achieve, the physical size of the solar cell needed to be taken into account. On the simulation model, the receiver was virtual and took no physical size, however the solar cell has a physical thickness to it, added to that the copper heat exchange plate and the thermal paste used to transfer the heat between the cell and the plate and therefore a 1 mm allowance is cut underneath both the CPC and V-trough models (shown in their schematics) to ensure the reflective walls have a height of exactly 50 mm.

In order to remove heat from the system, a copper pipe of 12 mm diameter was welded to a 250 mm × 25 mm copper sheet. This would be the base for the solar cell (which would sit on top).

5.3. Solar Cell cutting

The standard size for solar cell blocks is 156 mm × 156 mm. The concentrators are 25mm wide at cell location (receiver) and run a length of 250mm. For this reason, it was decided that two sets of 125 mm × 25 mm cells would need to be cut out and connected using tabbing wire.

Cutting the solar cells was a challenge: the cells used were monocrystalline Silicon cells which are very brittle by nature. The thickness of the cells is 200 µm thick (0.2 mm) and the cells are vulnerable to break, snap or crumble at all stages of the experiment. Three different processes were tried before settling on the method resulting in the highest quality and yield.

5.3.1.1. Hand Scribing

A diamond tipped glass cutter (Figure 5.6) without wheel was used to etch the front Silicon surface of the cells. The solar cells were placed on a clean flat glass surface to minimize cell cracking. The distance required to cut the 25mm × 125mm was measured with a ruler and an allowance was made due to the bulky nature of the cutter tip.

Figure 5.6. Silverline diamond tipped glass cutter

The glass cutter was used to scribe a line along the cutting schema on the solar cell. If enough force was used, the weakness created by the scribing process allows the cell to be *"snapped"* into two sub-cells.

(a) Scribing/Etching the front surface

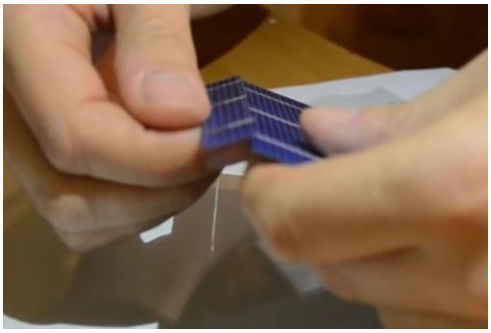

(b) Snapping sub-cells apart.

Figure 5.7. Hand scribing process of solar cell cutting

5.3.1.2. Dremel Milling

An additional method used was to mill the 25 mm × 125 mm parts using a Dremel rotary tool placed in a stand. Various size mill and drill tips were tested before settling on the Dremel 2.0 mm diamond wheel point mill tip. A medium thickness wood surface was placed on the base of the stand on top of which the solar cell blocks were mounted. Because the cells need to be cut through to the back entirely, the top of the wooden base was also milled in the process.

(a) Dremel rotary tool and stand

(b) Dremel 2.0 mm Diamond Wheel Point

Figure 5.8. Dremel 3000 tool and purchased 2.0mm mill tip

This method of cutting the cells chips away at the material: hence the direction of the feed and speed rate need to be considered so that the material being cut is from the side of the cell that would be discarded. The feed rate was manually controlled by hand-pushing the cell from end to end; the primary concern is getting a smooth and straight line without going too fast to ensure a better smoother cut. The spin rate was not straightforward, on slow settings the end result had bigger chipped edges and too slow would straight up destroy the cells. On the other hand,

setting the spin rate too high increased the average likelihood that the cell would crack in the milling process and decrease the yield rate significantly.

Once the cells were cut, the edges of the cell were cleaned with 400 grit sandpaper; this ensures that the milling process has not created a short between the negative and positive junctions of the cell. The cells are then tested to ensure it is producing the correct voltage of roughly 0.5V.

5.3.1.3. Laser Cutting

The third method was laser cutting and came from investigating the best solar cell cutting techniques on the internet. Three different laser types were considered: CO_2, YAG and Fibre lasers.

CO_2 lasers work by passing a current through a gas mix and are used for cutting materials like mild steel, aluminium, paper, wax, plastics and wood. They are the most common type of laser used in engraving systems.

YAG or Nd:YAG (neodymium yttrium-aluminium-garnet) refers to a crystal used as a solid-state lasing medium used in such laser cutters. These are typically stronger and specialize in cutting metals and ceramics.

Fibre lasers are another group of solid-state lasers that is gaining traction in metal cutting. The name is derived from the principal optical fibre doped with rare-earth elements used as the gaining medium. Because the spot size produced by fibre lasers is up to 100 times smaller than CO_2 lasers, they are great for cutting reflective material.

The Si-solar cells used are comprised of silicon wafers with Aluminium back plating. This was a problem when attempting to laser cut by YAG. Also, fibre cutters were hard to hire due to the small scale of the PhD project and a CO_2 laser cutter that agreed to take the project contacted the author to say the project had been cancelled due to the reflectivity of the Aluminium making cutting a damage risk to the laser machines.

Brunel University workshops possess their own low power CO_2 laser machines. The decision was taken to use them to *etch* on the front silicon and snap along the lines. This is similar to the hand etching technique with two major differences: Firstly, the hand scribe has a bulky head which makes it imprecise in practice. Secondly, the nature of the pressure required to create a deep enough scribe to make the cell "snappable" would cause a lot of the solar cells to crack and chip under such pressure, this was especially true near the starting and end edge of the scribing process (where a lot of the cells would be missing triangular bits at their corners).

The cutting process involved creating a 2D CAD drawing of the solar cell and the cut-outs required. This evolved in the end because the cells needed to be cut from *inside* the cell rather than at the edges for the following reasons:

- For consistency of performance it was decided to ensure the collector bus bars would be at the centre of the cut cells
- Because mono-Si solar cells are sliced from Silicon ingots which are circular in shape, they are not a perfect 156mm x 156mm rectangle. Their edges are tapered as shown in Figure 5.9 and hence the rectangular cut-outs needed to be shifted to regions not affected by the tapering.

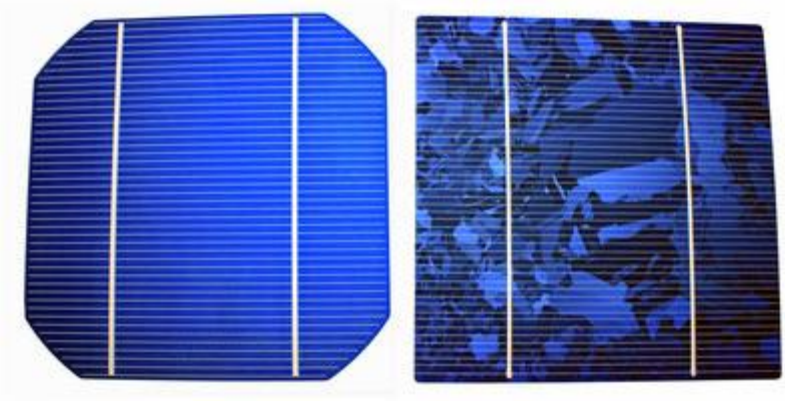

Figure 5.9. Mono (left) vs. poly (right) crystalline silicon solar cells

This meant that rather than just etching the outline of the final cell, the step by step snapping needed to be cut out. As such, the 2D drawing would look as shown in Figure 5.10. Because two batches of different mono-Si solar cells were used, one batch with two bus bars and one larger batch with four busbars, two sets of drawings were needed.

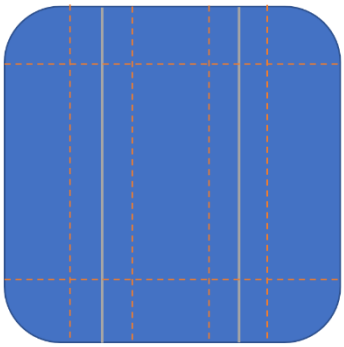

Figure 5.10. 2D Drawing with cut paths shown in dashed orange line.

This was loaded on the laser cutting computer (100W CTR CO_2 laser machine), and a lower power test was run on a wooden backdrop to get the outline of the solar cell. This was used for precise mounting of the actual silicon solar cell and the wooden base was weighed down to stop any small movements that would misalign the CNC laser head.

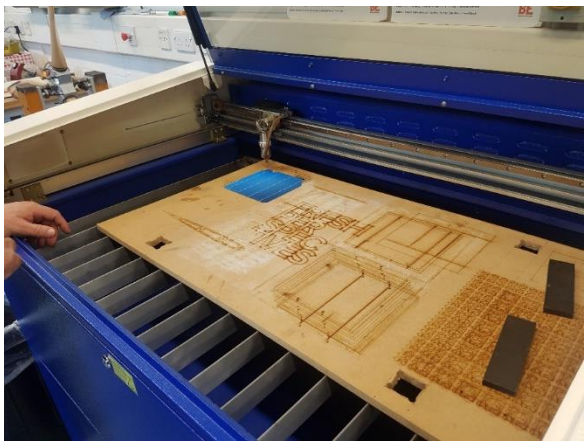

(a)

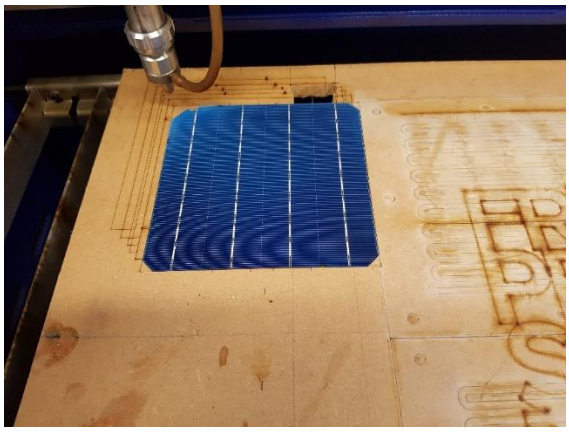

(b)

Figure 5.11. Solar cell placed on laser cutter (a) within bounds engraved on the wooden base (b)

The paths were run over twice under 50.0 power and 30.0 speed settings, the numbers being a relative % of the systems maximum potential. Power refers to the intensity of the laser applied, and speed is the *feed rate* of the laser cutter: the higher the power and slower the speed, the more cutting power and vice versa.

The etched solar cell was then cut into smaller pieces until the solar cells were left as shown in Figure 5.12.

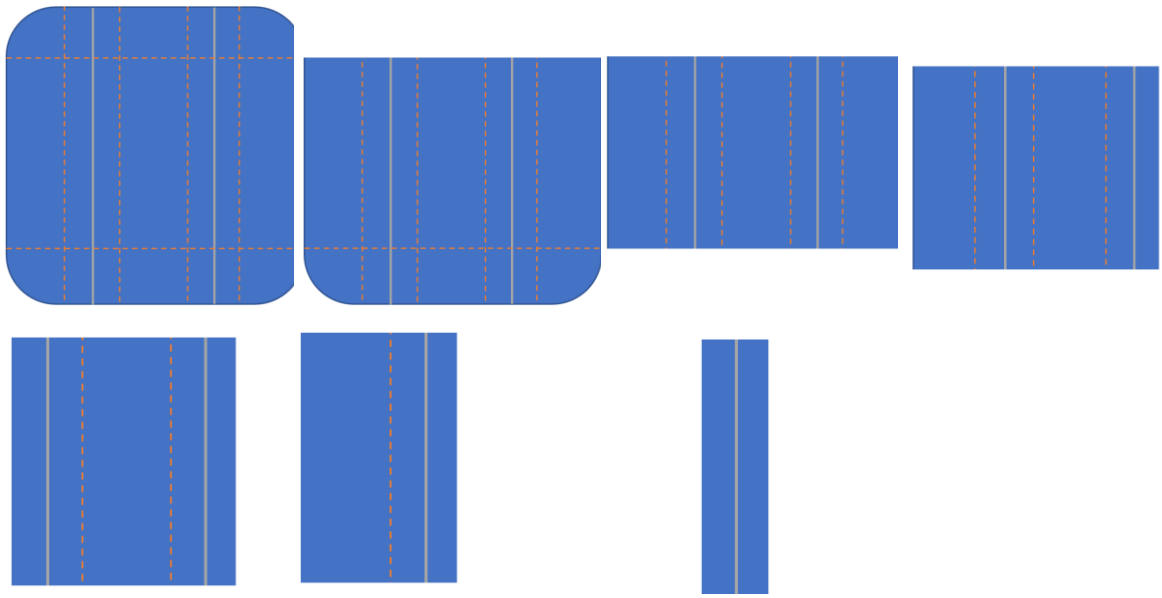

Figure 5.12. Step by step snapping of mono-Si solar cell to get final cells

The result is cells similar to those shown in Figure 5.13.

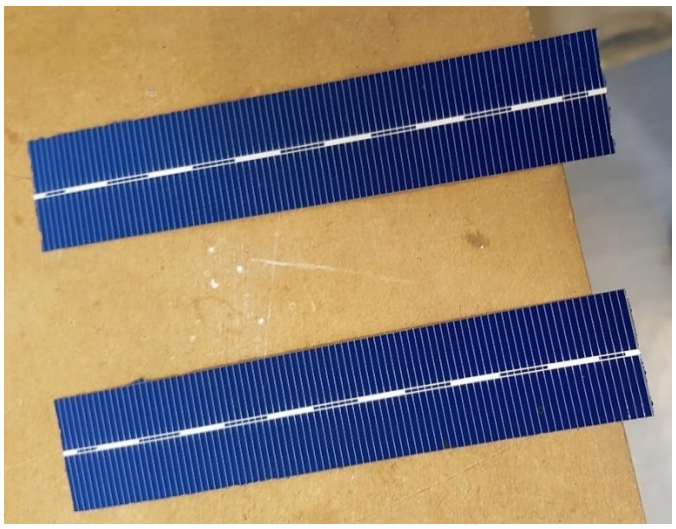

Figure 5.13. Final 25 mm × 125 mm solar cells

Due to the better yields of the laser cutting method, as well as higher quality edges compared to milling, laser cutting was selected as the best method of solar cell cutting.

5.4. Solar Cell connection

Once the solar cells were cut, they needed to be connected. The output of each individual cell was measured at ~0.5-0.6V. As the end result of the LCPV systems is to output electricity for use by the building or the grid, in practice the output voltage would ultimately need to be much higher. If cells are connected in series then the current stays constant whilst the voltage are

added together, the opposite is true when cells are connected in parallel; that is, the voltage remains constant for the whole system whilst the current is added together. For this reason it was decided that the cells in the system should be connected in series.

The positive and negative junctions of the solar cells are on opposite sides, the negative (-ve) junction being the busbar on top of the solar cell and the aluminium backplate acting as the positive (+ve) junction. For this reason, when connecting the cells in series, the top of one cell needs to be connected to the bottom of the next cell. Furthermore, two additional extruding tabbing wires are connected to either side of the solar cell series for connection to the voltmeter. This external connection also needs to be on the opposite side of the tabbing wire connecting the two cells i.e. if the tabbing wire connects from the top of cell A to bottom of cell B, then the external connections needs to extrude from the bottom of cell A, being the +ve connection and also extrude from the top of cell B as the –ve connection. This is shown in Figure 5.14.

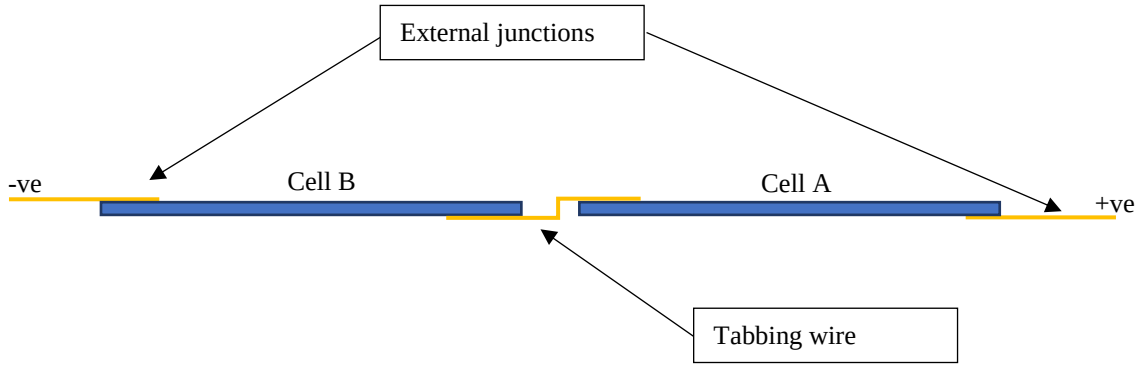

Figure 5.14. Solar cells connected in series with tabbing wire highlighted in yellow

5.4.1. Attaching the solar cells to the system

As explained, when the solar cells are connected in series, the top of one cell needs to be connected to the bottom of the other cell. We also have a copper plate welded to a copper pipe for removal of thermal energy from the solar cell during operation. A problem arises due to the electrical conductivity of the copper pipe: with the solar cell attached, the bottom of cell A and cell B become connected and the cells are *shorted*. With measurements, it was shown that whilst shorted, there is still some electrical output, in fact the output is that of exactly one sub cell. In the example shown in Figure 5.15 for example, when the cell series are placed on the copper plate, the +ve and –ve junctions of cell A are directly connected and hence shorted, however, cell B is still connected correctly and as such can output electricity. Interestingly, this would not be the case if the series were connected in parallel. In fact, the copper pipe can act as the connecting wire for the +ve junctions of the solar cells in such a case.

To solve the problem, the solar cells need to be separated from the copper plate by a material that is electrically insulating, whilst at the same time is thermally conducting. This allows the heat to travel across and be removed from the system whilst allowing both cells to operate as designed.

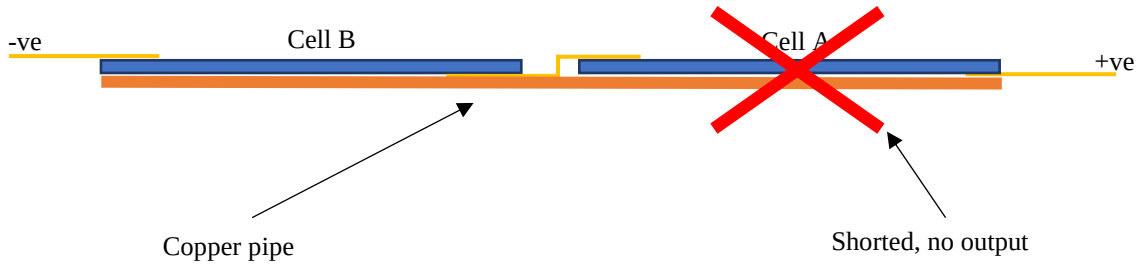

Figure 5.15. Cells in series placed on heat exchanging copper plate. Cell B still functions as the copper pipe acts as a conductor from the +ve connection to the bottom of cell B

Sheet Mica is one such material, specifically its unusual in being a good thermal conductor whilst being an excellent electrical insulator. Additionally, the material is heat resistant, with sheet Mica ordered from RS rated at heat resistant to temperature of 500°C continuously and up to 800°C intermittently. Sheets of MIC-20 were purchased and placed between the solar cells and top of the copper plate. Both sides were applied with thermal paste to ensure good physical contact for transfer of heat. The final system ended as shown in the assembly in Figure 5.16.

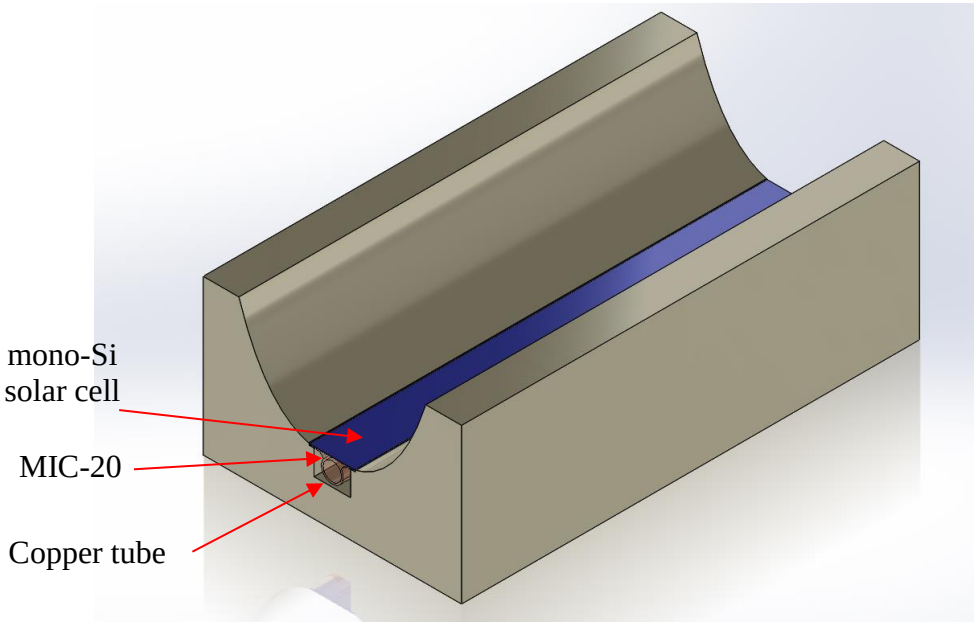

Figure 5.16. Final Assembly of the CPC (and V-trough) systems

5.5. Reflective material

The reflective walls are paramount to the correct performance of the optical concentrator system. The walls need to reflect light specularly to ensure light is reflected as anticipated in theoretical and simulation tests. For this, brushed Aluminium sheets were ordered from Alanod. Alanod specializes in reflective material for lighting and offer a range of surfaces with tailored reflective properties.

Their Miro-Silver 2 4200AG offers a high gloss surface with diffusivity of < 5% with no preferential direction, an optical mirror effect and high brightness. The product is rated at >98% total reflection. Figure 5.17 shows the scattering property of the material (left) and the surface topography (right).

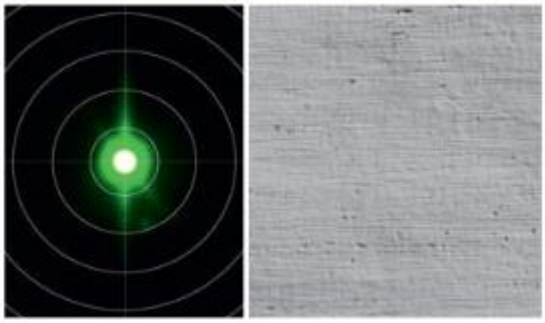

Figure 5.17. MIRO-SILVER 2 | 4200 AG scattering property and surface topography [169]

The sheets were cut to the size as determined by the surface area of the reflective surfaces of the V-trough and CPC. A 0.5mm allowance was given for the thickness of the sheets when calculating the surface area and when machining the concentrator structures.

For the V-trough the surfaces were joined directly using a wood to metal adhesive: the back of the MICRO-SILVER sheets was scratched along with the V-trough side walls to ensure enough surface roughness for the adhesive to grip. For the CPC parabola surfaces, the MICRO-SILVER sheets were first taken to the relevant workshop where a bending machine was used to pre-shape the material to parabola-like curves. This ensured that less pressure is put on the adhesive and the surfaces in the initial *drying phase* of the bonding before the material sets.

The end device is shown in Figure 5.18 before and after application of the reflective surface.

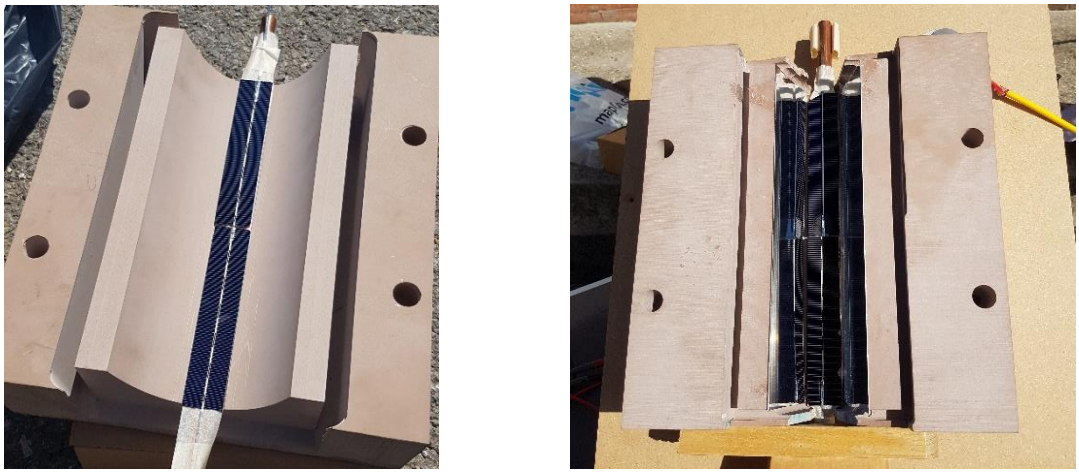

(a) Final setup without reflector *(b) Final setup with reflector*

Figure 5.18. CPC and V-trough with Solar cell, copper pipe, heat transfer plate, busbar junctions (a) without and (b) with reflectors

5.6. Testing Conditions

Figure 5.19 shows the average insolation in London, with a peak around July and a minimum in December solstices and solar insolation for the UK is shown on the map in Figure 5.20.

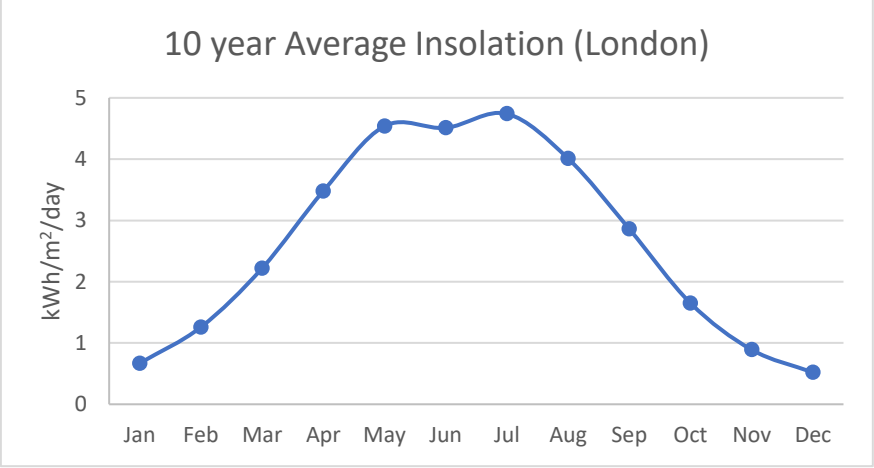

Jan	Feb	Mar	Apr	May	Jun	Jul	Aug	Sep	Oct	Nov	Dec
0.67	1.26	2.22	3.48	4.54	4.51	4.74	4.01	2.86	1.65	0.89	0.52

Figure 5.19. Ten-year average insolation for London. Data courtesy of: NASA - Surface Meteorology and Solar Energy Data Set

Data was gathered in September/October, mid-region of the peak and trough of the yearly solar irradiance. Where possible, the experiments were run on sunny days. In either case two sets of Kipp and Zonen pyranometers were used, one placed on the same plane as the concentrators

during experiment, used to measure the total incident solar radiation falling on the system, and another placed in the shade which would measure the diffuse light. The pyranometers came at 60.5 µV/Wm^{-2} and 80.2 µV/Wm^{-2} sensitivities. The data logger used (Pico TC-08) had a maximum input range of $\pm 70\, mV$, when solar radiation approached 1000 Wm^{-2} if the 80.2 µV/Wm^{-2} pyranometer was connected then the Pico logger would fail to report the out of bounds mV (at 1000 W/m^2, the pyranometer should logically be outputting 80.2 mV). Therefore, it was ensured that the 80.2 µV/Wm^{-2} pyranometer was assigned to measuring the diffuse radiation and the 60.5 µV/Wm^{-2} was assigned to the direct (+diffuse) radiation.

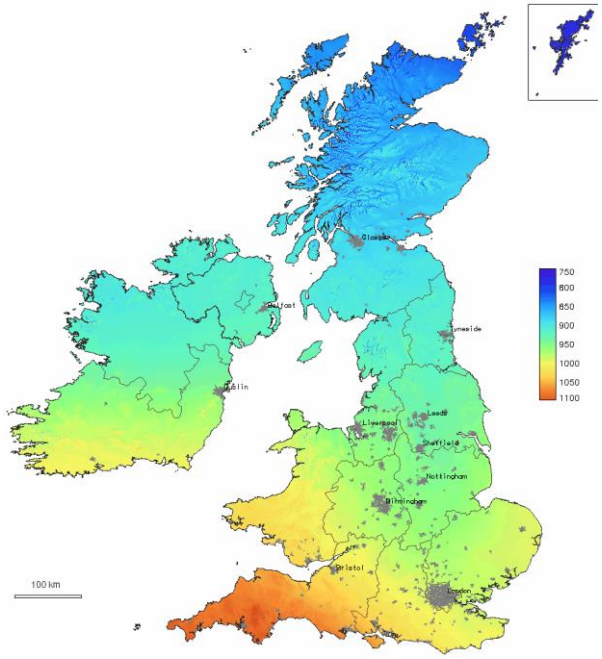

Figure 5.20. Yearly cumulative solar horizontal radiation for the UK and Ireland [kWh/m^2] PVGIS European Communities (re.jrc.ec.europa.eu/pvgis)

Burnett et al. [170] presented impact of diffuse radiation in the UK through the average daily time series of various locations over a period of 5 years (1995-1999).

The monthly average clear sky clearness index $\overline{K}_{clear}$ is defined as:

$$\overline{K}_{clear} = \frac{\overline{H}_{clear}}{\overline{H}_0} \tag{5.1}$$

where $\overline{H}_{clear}$ is the monthly average horizontal surface clear sky irradiance (J/m^2) and $\overline{H}_0$ is the monthly average of daily horizontal extra-terrestrial solar irradiation (J/m^2).

The monthly average daily clearness index $\overline{K}$ is defined as:

$$\bar{K} = \frac{\bar{H}_h}{\bar{H}_0} \tag{5.1}$$

where $\bar{H}_h$ is the monthly average of daily horizontal surface irradiation. $\bar{H}_0$ is calculated by:

$$\bar{H}_0 = \frac{3600 \times 24}{\pi} I_0 \times \frac{\pi h_{ss}}{180} (\sin\phi \sin\delta + \cos\phi \cos\delta \sin h_{ss}) \tag{5.2}$$

where I_0 is the extra-terrestrial solar radiation at normal incidence and h_{ss} is the sunrise/sunset hour angle on a horizontal surface calculated as:

$$h_{ss} = \cos^{-1}(-\tan\phi \tan\delta) \tag{5.3}$$

ϕ is the latitude and δ is the declination of the sun in decrees given by:

$$\delta = 23.45 \sin\left(360 \frac{284 + n}{365}\right) \tag{5.4}$$

where *n* is the day of the year beginning on January 1st.

I_0, the extra-terrestrial solar radiation at normal incidence can be calculated by:

$$I_0 = I_{sc}\left(1 + 0.033 \cos\frac{360}{365} n\right) \tag{5.5}$$

$\bar{K}_{clear}$ values were empirically obtained based on observed solar irradiance data at eighteen Met stations across the UK shown in Figure 5.21. The data is presented in Figure 5.22 with a cubic trend exhibited which is denoted by the dashed line.

Month	***Average*** $\bar{K}_{clear}$
January	0.579
February	0.63
March	0.668
April	0.682
May	0.701
June	0.707
July	0.71
August	0.679
September	0.667
October	0.641
November	0.628
December	0.616

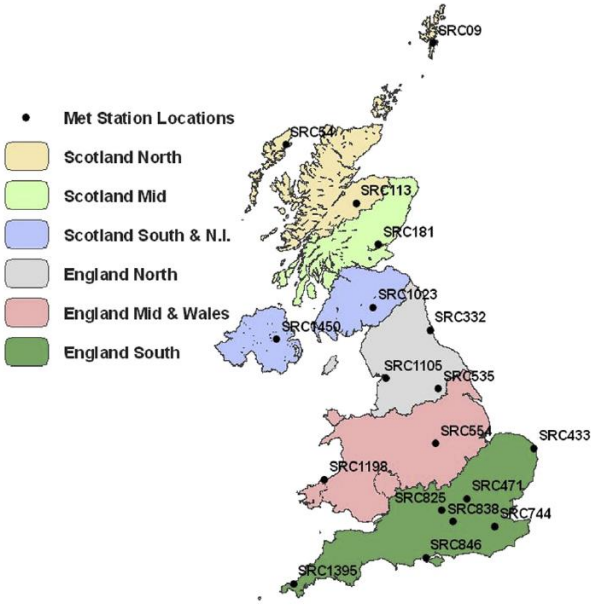

(a) Average monthly $\overline{K}_{clear}$ values for the UK *(b) Locations of measuring met stations*

Figure 5.21. Average monthly $\overline{K}_{clear}$ values for the UK over the 5 years (1995-1999) [170]

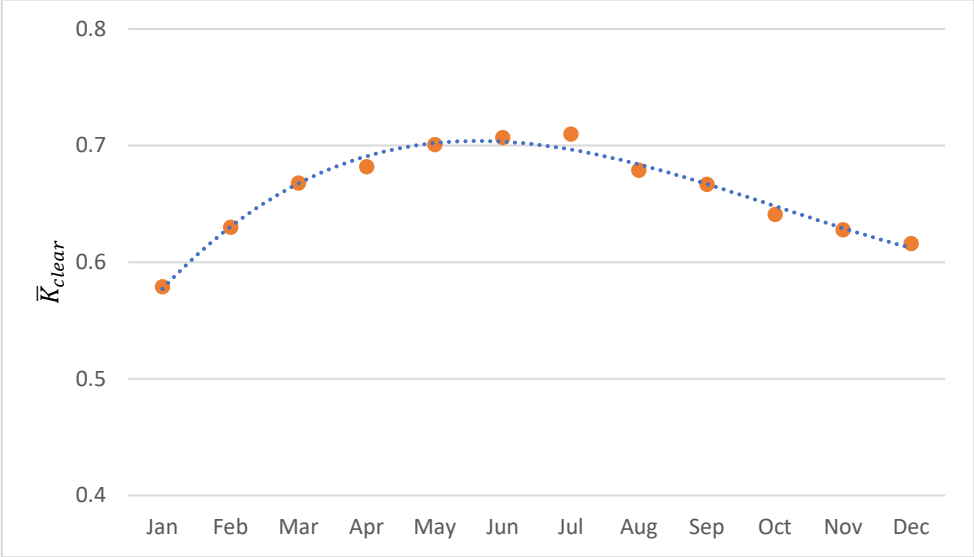

Figure 5.22. Average monthly $\overline{K}_{clear}$ values for the UK (1995-1999)

The monthly average clear sky clearness index, $\overline{K}_{clear}$, was used to find the average diffuse ratio $\overline{K}$ for the UK. Using equation 5.1 and assessing $\overline{H}_0$ values based on equation 5.2, the monthly average of daily horizontal surface irradiation ($\overline{H}_h$) was calculated. The converted measurements were compared to measured irradiance with good correlation shown (Figure 5.23).

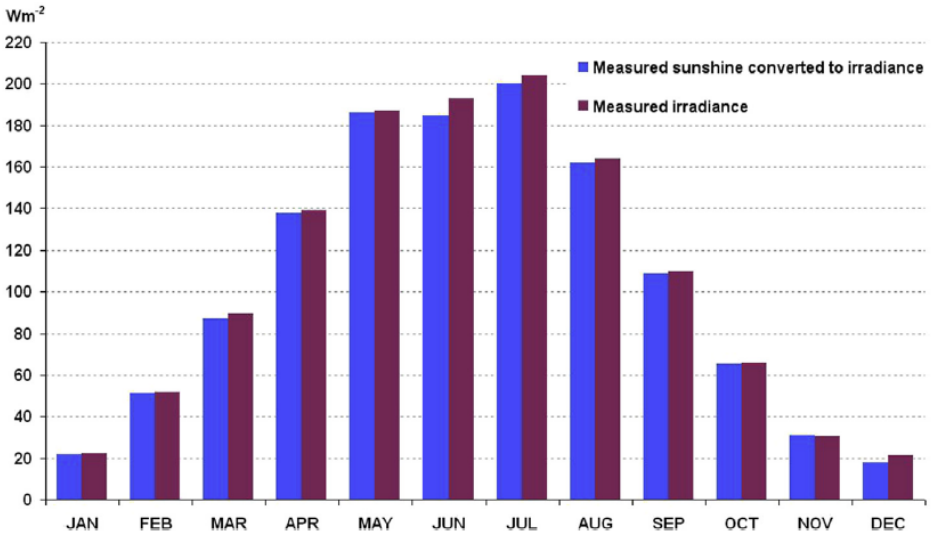

Figure 5.23. Comparison of measured sunshine hour duration converted to irradiance and actual measured irradiance for station SRC535 [170]

Muneer et al. used data from 10 UK locations (Figure 5.24) to propose a regression model linking $\overline{K} - \overline{K}_t$ [171], where $\overline{K}_t$ is the clearness index. The data presented in Figure 5.25 was pooled to obtain the regression model:

$$\overline{K} = 0.89\overline{K}_t^2 - 1.185\overline{K}_t + 0.95 \tag{5.6}$$

	Latitude	Longitude	Observation Period
Camborne	50.21	5.3	1981–1995
Crawley	51.11	0.19	1980–1992
Bracknell	51.42	0.75	1992–1994
London	51.52	0.11	1975–1995
Aberporth	52.13	4.55	1975–1995
Hemsby	52.7	1.69	1981–1995
Finningley	53.48	0.98	1982–1995
Aughton	53.54	2.91	1981–1995
Aldergrove	54.65	6.24	1968–1995
Stornoway	58.22	6.39	1982–1995

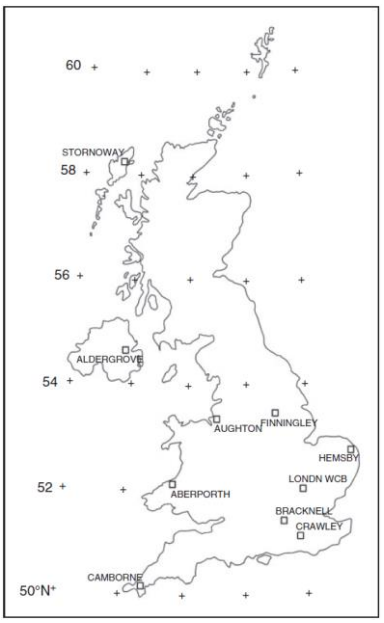

Figure 5.24. Locations investigated by Muneer et al. [171]

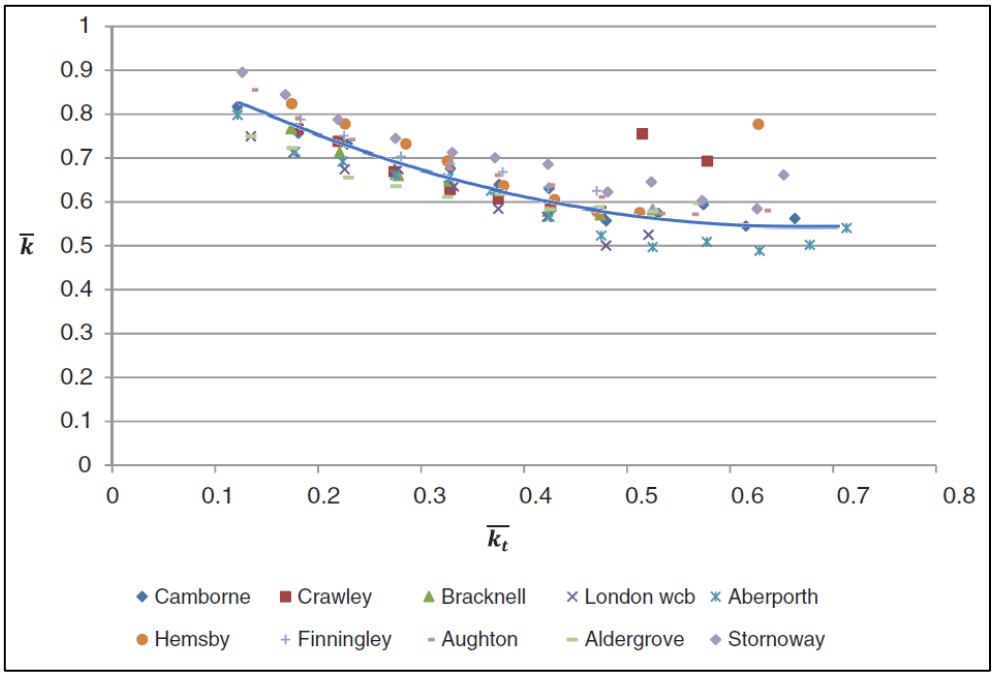

Figure 5.25. Averaged values of diffuse ratio for the UK with locations arranged in an increasing order of latitude [171]. Note regression model added as solid blue line.

Muneer et al. regression model and data put the average diffuse radiation in the UK at between 60-65%.

Dhimish et al. [172] published an assessment of solar resources in the UK in 2018. A series of 27 weather stations were used to collect data and measurements of Direct normal irradiance (DNI), Diffuse horizontal irradiance (DHI) and Global horizontal irradiance (GHI) were provided for years 2015-2017. The terms are related by:

$$GHI = DNI\cos(\theta) + DHI \tag{5.7}$$

The data can be used to find the diffuse ratio using:

$$\overline{K} = \frac{DHI}{GHI} \tag{5.8}$$

Solar resources in England for 2015-2017 are shown in Table 5.1:

Table 5.1. Solar properties for England 2015

Location	Average GHI (kWh/m2)	Average DNI (kWh/m2)	Average DHI (kWh/m2)	Average temp (°C)	Diffuse %
Plymouth	106	114	46	12.5	43.4%
Exeter	96	87	52	12	54.2%
Bristol	95	88	49	12	51.6%
Oxford	92	83	51	10.9	55.4%
London	98	94	50	11.6	51.0%
Cambridge	91	84	51	11.4	56.0%
Norwich	92	88	50	11.4	54.3%
Nottingham	88	79	50	10.5	56.8%
Liverpool	95	94	47	11.2	49.5%
Manchester	85	73	51	10.8	60.0%
Huddersfield	83	75	48	10.4	57.8%
Hull	92	93	49	10.5	53.3%
York	85	78	49	10.2	57.6%
Sunderland	83	83	46	9.6	55.4%
Whitehaven	93	94	44	11.2	47.3%
				Average:	**53.6%**

Table 5.2. Solar properties for England 2016

Location	Average GHI (kWh/m2)	Average DNI (kWh/m2)	Average DHI (kWh/m2)	Average temp (°C)	Diffuse %
Plymouth	102	106	47	12	46.1%
Exeter	95	87	52	11.5	54.7%
Bristol	93	88	49	11.5	52.7%
Oxford	89	80	51	10.4	57.3%
London	97	93	49	11.1	50.5%
Cambridge	90	83	50	10.8	55.6%
Norwich	93	88	50	10.8	53.8%
Nottingham	90	82	51	10	56.7%
Liverpool	96	97	48	10.5	50.0%
Manchester	87	77	50	10.2	57.5%
Huddersfield	87	80	49	9.8	56.3%
Hull	95	99	49	10	51.6%
York	88	84	50	9.7	56.8%
Sunderland	88	94	46	8.9	52.3%
Whitehaven	96	98	45	10.4	46.9%
				Average:	**53.2%**

Table 5.3. Solar properties for England 2017

Location	Average GHI (kWh/m2)	Average DNI (kWh/m2)	Average DHI (kWh/m2)	Average temp (°C)	Diffuse %
Plymouth	101	100	50	12.1	49.5%
Exeter	95	85	53	11.6	55.8%
Bristol	91	81	51	11.6	56.0%
Oxford	89	78	52	10.3	58.4%
London	95	88	51	10.9	53.7%
Cambridge	90	82	51	10.7	56.7%
Norwich	92	85	50	10.8	54.3%
Nottingham	88	79	50	10	56.8%
Liverpool	96	97	48	10.6	50.0%
Manchester	86	76	50	10.3	58.1%
Huddersfield	84	74	49	9.9	58.3%
Hull	94	94	49	10	52.1%
York	87	81	50	9.7	57.5%
Sunderland	86	86	46	9	53.5%
Whitehaven	94	94	46	10.8	48.9%
				Average:	**54.7%**

It can be seen that England averaged between 53-55% Diffuse radiation between 2015-17 with the 3-year average being 53.8%.

The solar properties of Wales are shown below:

Table 5.4. Solar properties for Wales 2015-17

	Location	Average GHI (kWh/m2)	Average DNI (kWh/m2)	Average DHI (kWh/m2)	Average temp (°C)	Diffuse %
2015	Cardiff	102	102	48	12	47.1%
	Aberystwyth	85	69	49	12	57.6%
2016	Cardiff	101	101	48	11.5	47.5%
	Aberystwyth	86	75	48	11.5	55.8%
2017	Cardiff	98	94	51	11.4	52.0%
	Aberystwyth	81	63	49	11.6	60.5%
					Average:	**53.4%**

Wales showed a similar average to England with the 3-year averaged diffuse radiation at 53.4%.

The solar properties for Scotland are shown in Table 5.5 below:

Table 5.5. Solar properties for Scotland 2015-17

	Location	Average GHI (kWh/m2)	Average DNI (kWh/m2)	Average DHI (kWh/m2)	Average temp (°C)	Diffuse %
2015	Glasgow	79	67	48	10.1	60.8%
	Edinburgh	84	94	48	9.6	57.1%
	Aberdeen	79	84	44	9.7	55.7%
2016	Glasgow	83	75	49	9.2	59.0%
	Edinburgh	89	94	48	8.7	53.9%
	Aberdeen	82	84	45	9	54.9%
2017	Glasgow	82	73	49	9.6	59.8%
	Edinburgh	85	82	48	9	56.5%
	Aberdeen	71	78	46	9	64.8%
					Average:	**58.1%**

Unsurprisingly Scotland experiences the higher proportion of diffuse radiation, approaching 60%. Surprisingly however, diffuse radiation in Ireland (north and south) was the same as Scotland, averaging 58.1% over the 2015-17 three-year period.

5.7. Experimental setup

The experiments were carried out in an unobstructed area of the car park adjacent the CSEF (Centre for Sustainable Energy use in Food chains) centre in Brunel University, London, UK (51.53, -0.4697).

Three K-type thermocouples were connected to the base of each solar cell receiver (between the cell and Mica sheet), one at each edge and one at the centre as shown in Figure 5.26.

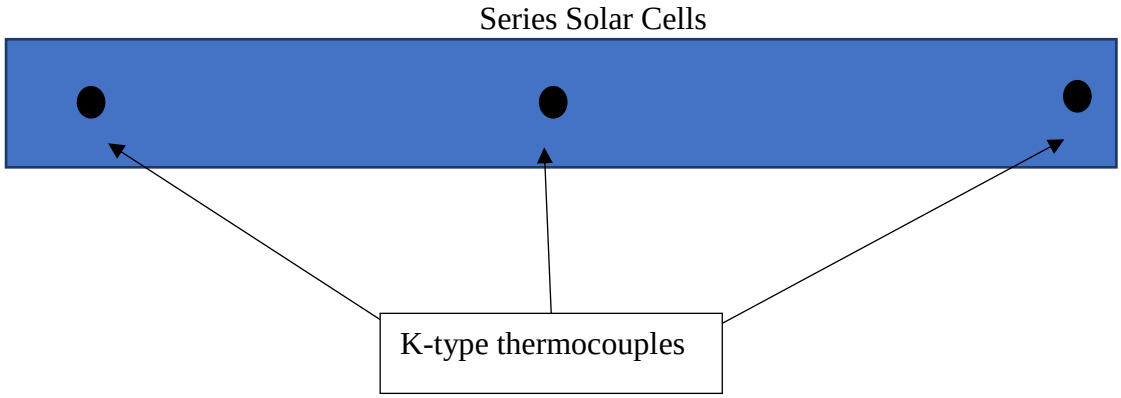

Figure 5.26. Position of thermocouples on the solar cells

To calibrate the thermocouples, a special calibration oil bath was set at the range of temperatures expected during experimental testing. The temperature of the oil bath was separately checked with an accurate thermometer. The thermocouples were submerged, and the corresponding voltage output of each thermocouple was recorded (for each temperature step).

The thermocouples and pyranometers were connected to a Pico TC-08 data logger. The V-trough and CPC systems were placed on a wooden base tilted at an angle based on the sun's altitude such that the projection of the solar radiation would fall exactly on the solar cell. However, this create some uncertainty associated with the accuracy of the manual tracking, which has a direct effect on the electrical output.

A Keithley 2401 Source/Measure Unit (SMU) was used to take the I-V curves of the cells. A test run of the solar cells under dark condition is shown in Figure 5.27.

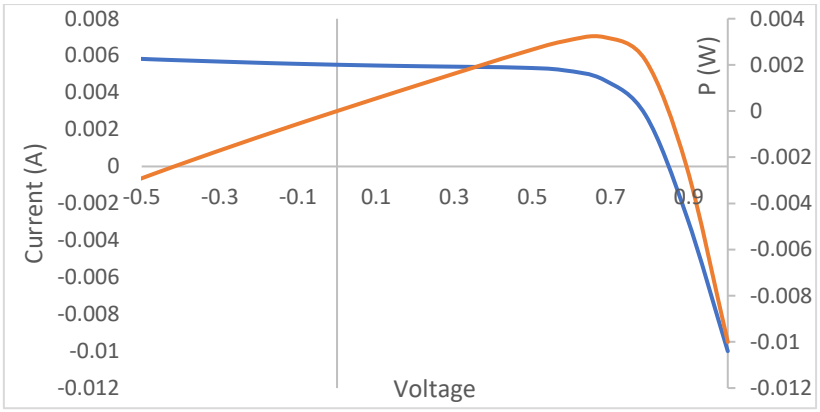

Figure 5.27. I-V and P-V curves of solar cell under dark condition (I-V in blue P-V in orange)

The Instruments used in experimental measurements are shown in Figure 5.28. The schematic presented in Figure 5.29 shows the connectivity of all components in the system. Figure 5.30 pictures the physical setup: the pyranometer attached measures total solar radiation, the second yellow cable running from the Pico data logger connects to the shaded pyranometer for diffuse solar radiation. Here a reference cell is also attached for comparison.

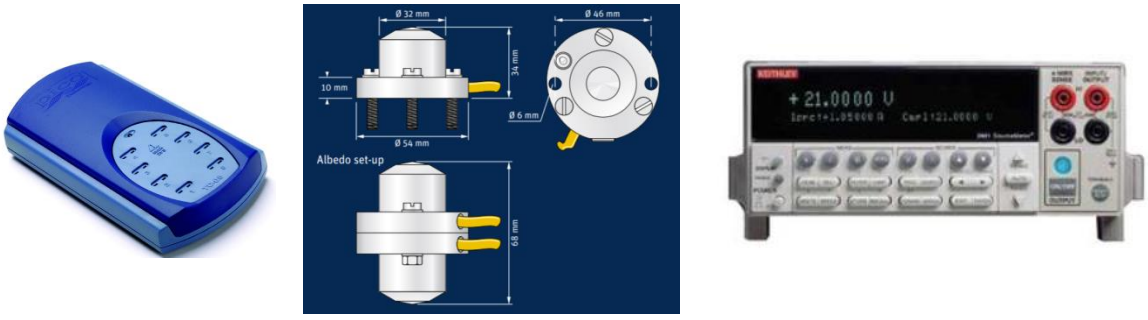

(a) Pico TC-08 (b) SP Lite2 Silicon Pyranometer (c) Keithley 2401 SMU

Figure 5.28. Instruments used in experimental measurements

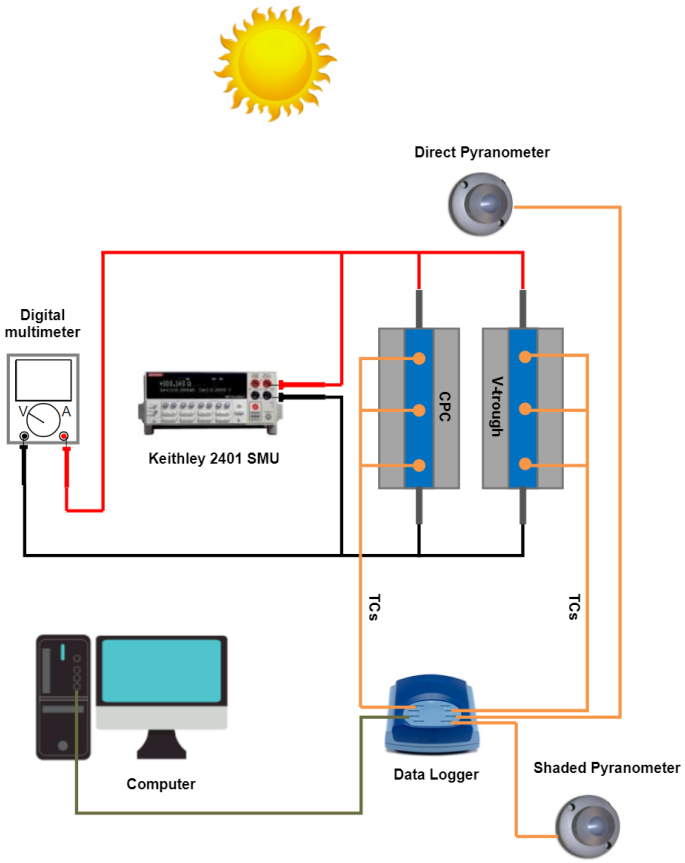

Figure 5.29. Schematic of experimental setup

Crocodile clips connect the solar cell to the Keithley 2401 SMU for I-V measurement, the SMU is located under the wooden board for shading to prevent overheating. Since the Keithley 2401 can only measure one device at a time, the probes need to connect to each device consecutively and take measurements.

Figure 5.30. Experimental setup

5.8. Testing Procedure

For cooled testing, a hose pipe was connected to a water source from accommodating CSEF building, the hose was connected to the tap with an adaptor and tightened to the cooling pipes on the concentrators with jubilee clips. A 2-way manifold was used to allow both connections simultaneously.

Measurements were taken in 15-30 minute intervals. In some instances, when there was a small amount of shading caused by cloud coverage, the measurement was delayed by up to 5 minutes. All data from the multimeter and Keithley 2401 are recorded in these intervals.

Figure 5.31. Pipe connection to tap water supply and 2-way manifold

Chapter 6 Results and Discussion

Based on the theory developed in Chapter 4 and experimental set-up discussed in Chapter 5, in this chapter the results of ray tracing modelling together with the experimental results of CPV and V-trough are presented and discussed.

6.1. Compound Parabolic Concentrator (CPC)

6.1.1. CPC Full Height

The Concentrator parameters were as follows:

- Concentration ratio $C_r = 4$
- Absorber area (width) 25 mm
- Half Acceptance angle $\theta_h = \sin^{-1}\frac{1}{4} = 14.478°$
- Height of CPC: $\frac{w_{abs}+w_{ap}}{2} * cot(\theta_h) = 242.06$ mm

The simulation solved for 3 ns of ray propagation time, the rays are colour-coded by time for clarity with dark blue representing initial ray position (t = 0 ns), going to red (t = 1.8 ns) at ray exit. This is a scaling back of the total time scale of 1-3 ns as most rays were resolved (either accepted or rejected out of the CPC) by 1.8ns. Using original scaling would mark most rays blue and make it difficult to distinguish between the rays coming in and going out. The difference is shown in Figure 6.1.

Looking at the angle of incidence near the acceptance angle region, ray trajectory graphs are shown in Figure 6.2. The ray tracing algorithm initially showed a big drop in ray acceptance between 14-15°. This corroborates with proven literature and theoretical evaluations. In order to evaluate the accuracy of the model, the angle of incidence near the acceptance half angle was cut into finer steps of 0.1°, that is the range of 14-15° was cut into 11 discrete light angles of incidence 14.0, 14.1…14.9, 15. This again showed the model to be successful as the cliff-drop expected of CPC occurred at exactly the half acceptance angle (to $\pm$0.1° accuracy). Taking the model to the extreme, the angle of acceptance was cut into one hundredth of one degree of angle of acceptance and Figure 6.2(e-f) shows the ray trajectories of 14.47 and 14.48, respectively.

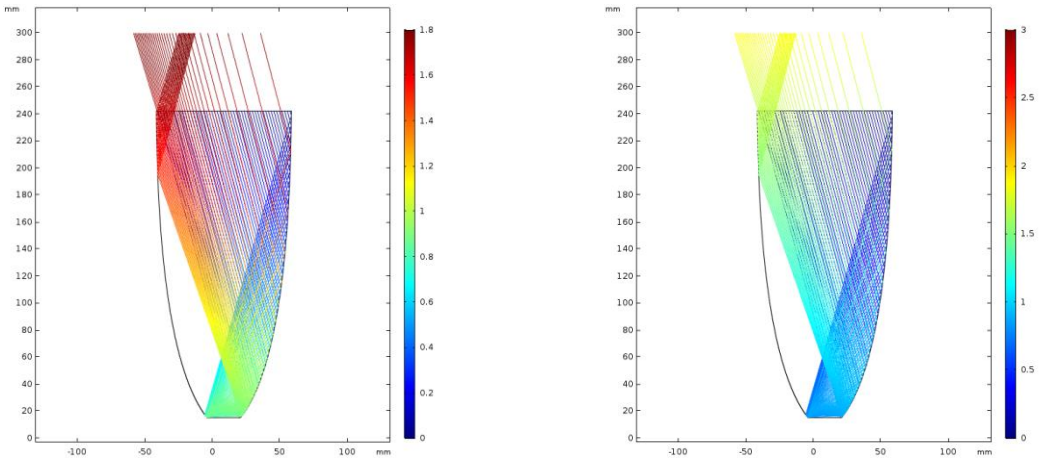

15° Angle of incidence range 0-1.8ns *15° Angle of incidence range 0-3ns*

Figure 6.1. Effect of improving the colour expression range

The results show that there is a big drop in number of accepted rays (those that reach the absorber flat area at the bottom) with most rays being rejected back out. High resolution models were run to get numerical results, they showed 100% acceptance at 14.47° light angle of incidence dropping to 3.84% acceptance at 14.48%, a loss of >96% efficiency. This sudden drop is characteristic of CPCs and is shown in Figure 6.3 for the full height CPC configuration.

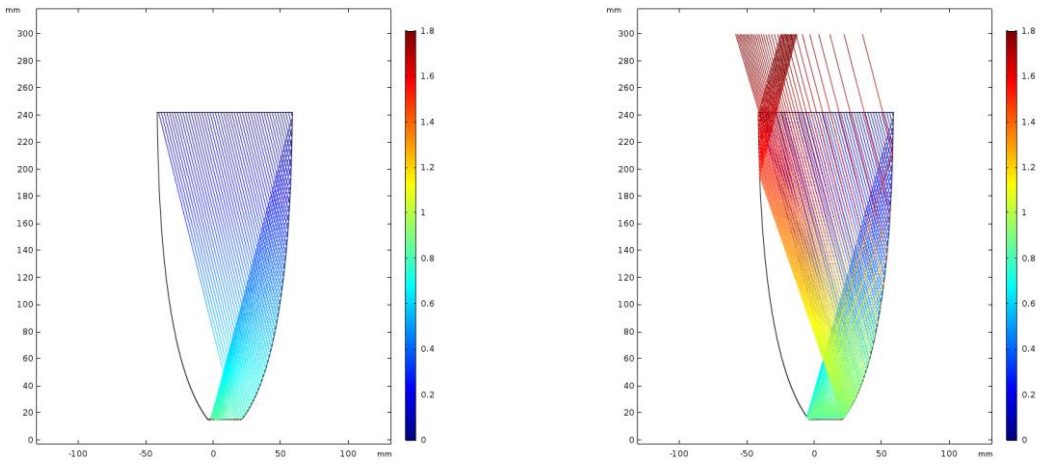

(a) 14° inlet light angle of incidence *(b) 15° inlet light angle of incidence*

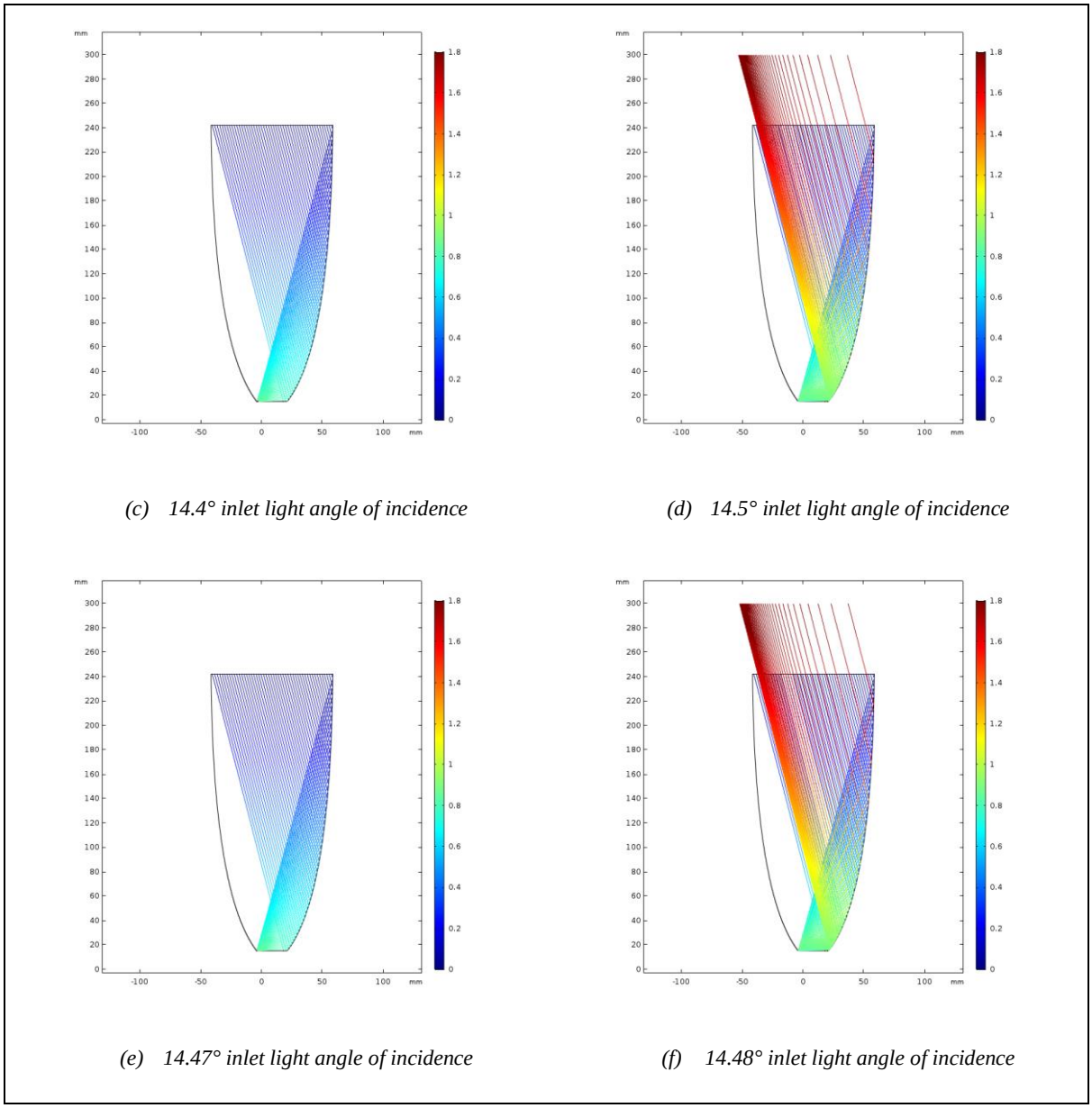

(c) 14.4° inlet light angle of incidence

(d) 14.5° inlet light angle of incidence

(e) 14.47° inlet light angle of incidence

(f) 14.48° inlet light angle of incidence

Figure 6.2. Ray trajectories of Full Height (242mm) CPC at (a) 14° (b) 15° (c) 14.4° (d) 14.5° (e) 14.47° and (f) 14.48° angles of incidence

Up to the half acceptance angle, a CPC should accept 100% of the ray, for the CPC parameters analysed that correlated to 0 - 14.47°. It should be noted that this is considered the acceptance *half* angle, that is, the CPC will accept angles of incidence up to 14.47° from either direction, leading to a total acceptance range of double this (~30°).

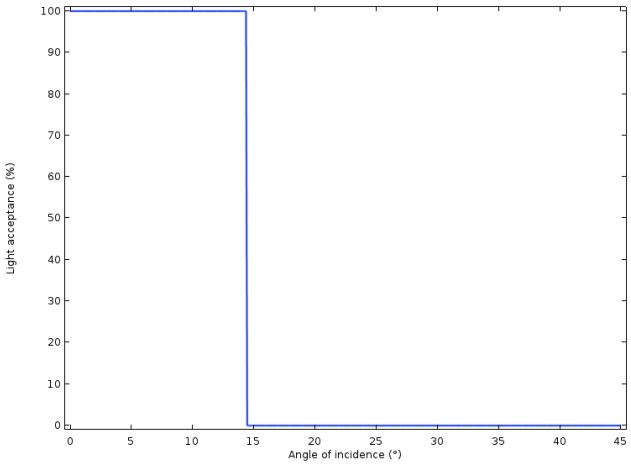

Figure 6.3. Cliff-drop of solar radiation acceptance at CPC design acceptance half angle

Whilst 100% of the radiation reaches the absorber up to the acceptance angle, there is another, important metric to be considered: the distribution of light radiation on the absorber cell area. Light hitting the absorber area is not perfectly distributed. Nor is this distribution constant as the inlet angle of incidence changes, even within the acceptance angle there is a large change in energy flux distribution along the absorber area (solar cell).

Figure 6.4 shows the energy flux concentration along the absorber plate of the CPC at 0°: the x-axis represents the position along the plate and the y-axis is the relative flux concentration. The y-value indicates the number of rays the hit the absorber at that position, therefore the peaks represent regions where the energy flux concentration falling on the cell is highest. Conversely low-lying regions represent areas on the absorber where small amounts of rays reach.

In order to investigate the authenticity of the data and visualise the reasoning for the location of these peaks, a magnified ray tracing graph is shown in Figure 6.5. The propagation of the rays is represented by arrows indicating their direction vector. The arrows pointing vertically downwards represent the light rays travelling directly from the inlet aperture to the absorber at 0° direction. It therefore logically follows and is shown to be perfectly distributed along the absorber. Regions of high energy flux concentration show a greater number of arrows; these arrows are diagonal in direction due to their reflection from the reflective parabolic surfaces.

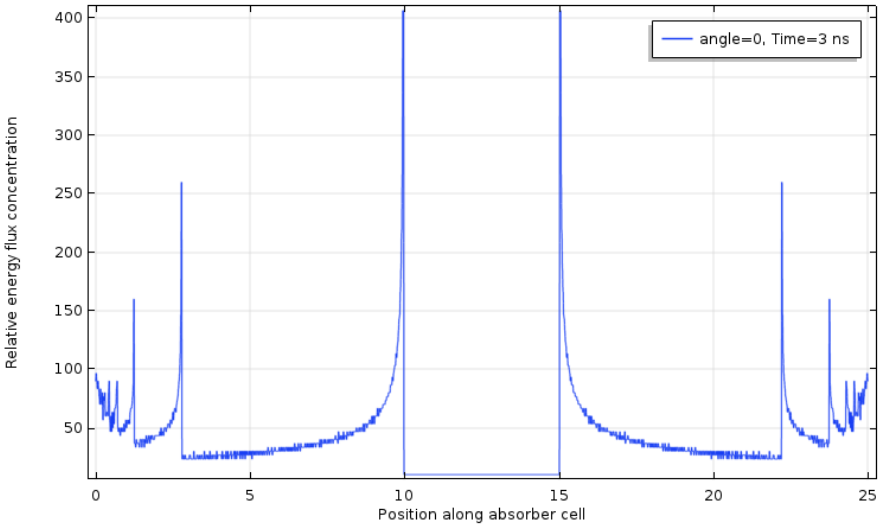

Figure 6.4. Solar energy flux concentration along the absorber plate

It can be seen in Figure 6.5 that there is a high concentration of rays hitting the absorber surface in regions correlating to peaks and highs shown on the light intensity distribution graph (Figure 6.4). These are highlighted in Figure 6.5 by red circles. Figure 6.6 shows the light intensity distribution overlapped on the ray tracing plot.

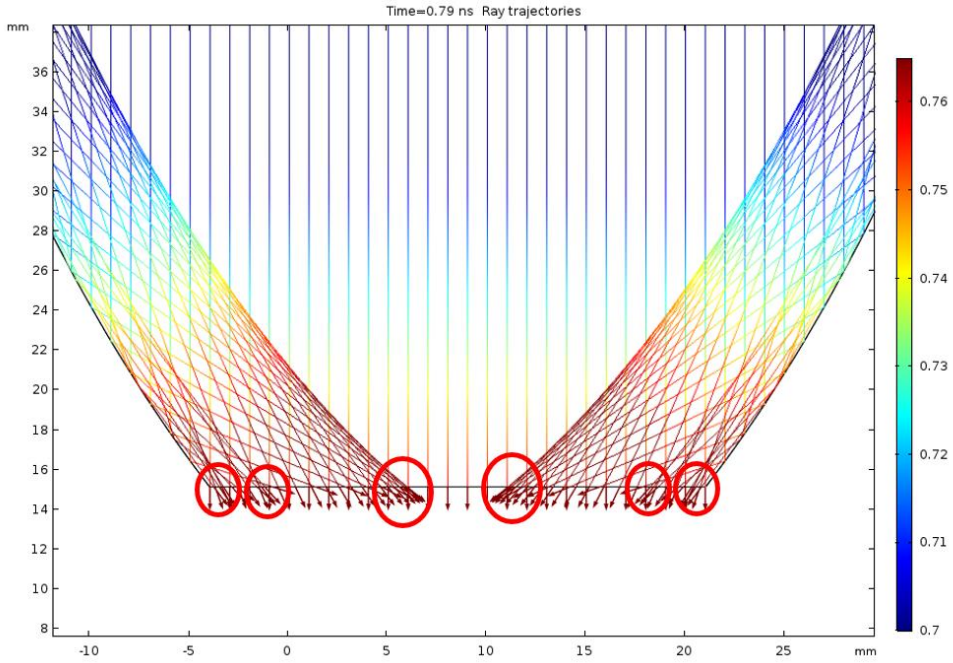

Figure 6.5 Magnified CPC at 0° angle of incidence. Area of high energy flux concentration are highlighted in the red circles.

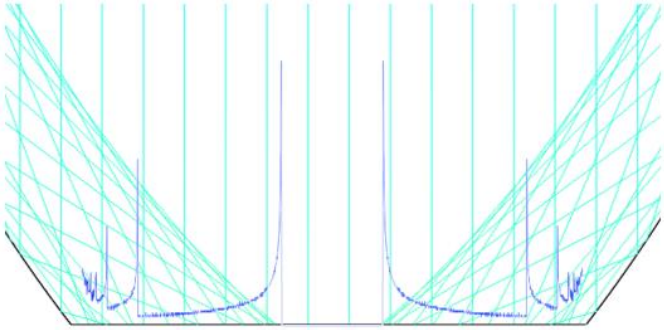

Figure 6.6. Energy flux concentration (light intensity distribution) overlapped on magnified CPC base.

Figure 6.7 shows the ray trace diagrams of the CPC at intervals between 0 to 14.47° inlet light angle of incidence (pre-acceptance angle).

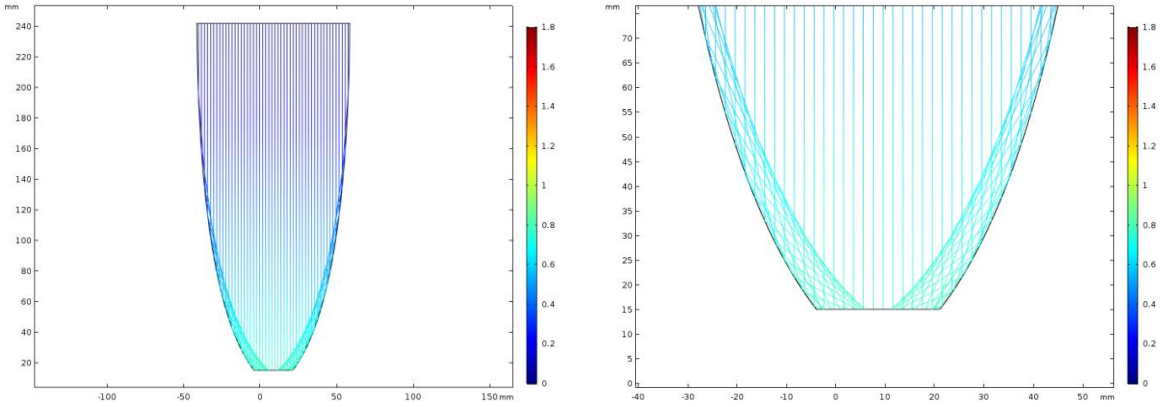

(a) CPC ray trajectories at 0° angle of incidence (whole system in the left and magnified absorber region right)

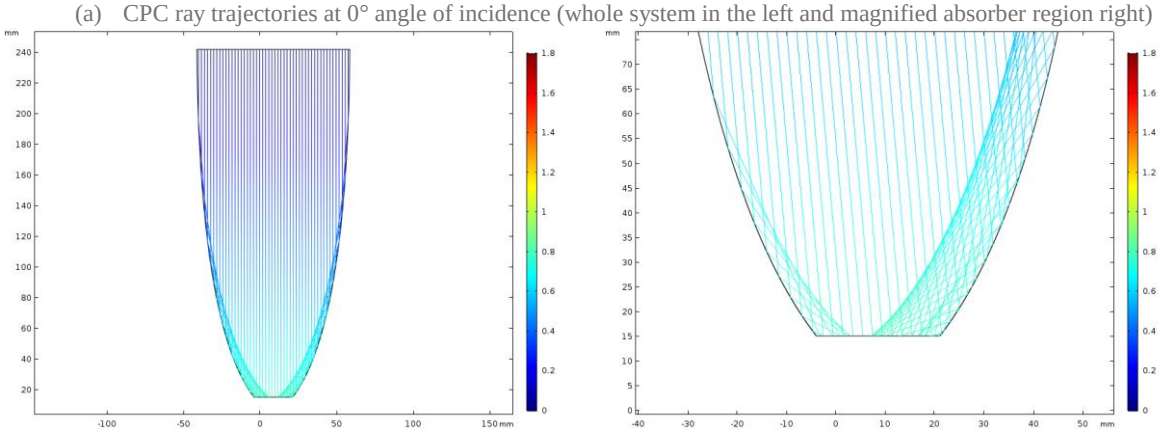

(b) CPC ray trajectories at 5° angle of incidence (whole system in the left and magnified absorber region right)

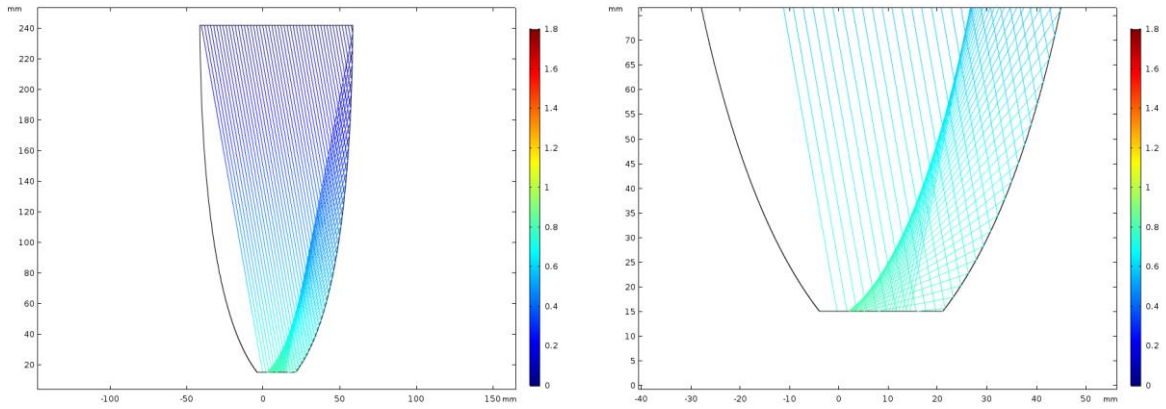

(c) CPC ray trajectories at 10° angle of incidence (whole system in the left and magnified absorber region right)

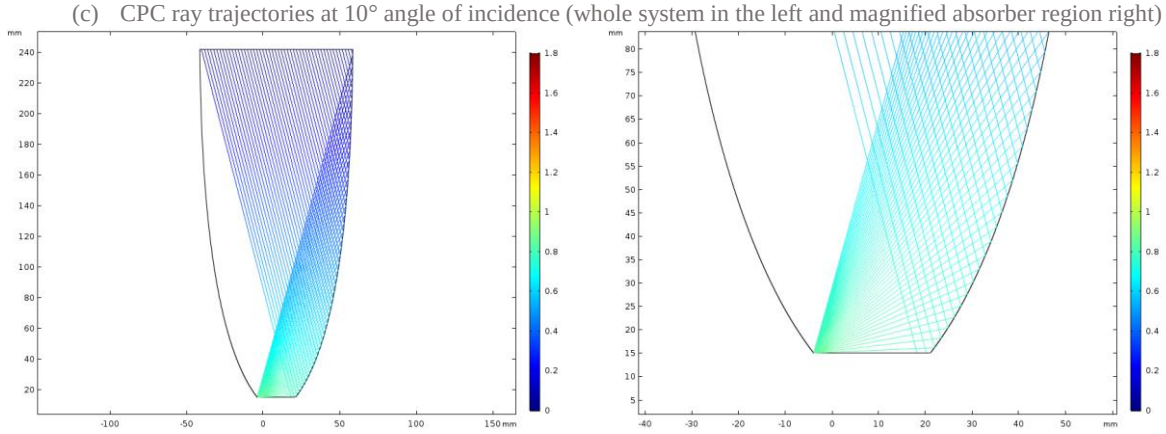

(d) CPC ray trajectories at 14.47° angle of incidence (whole system in the left and magnified absorber region right)

Figure 6.7 Ray trace diagram for Full height CPC at (a) 0° (b) 5° (c) 10° and (d) 14.47° angle of incidence

Attention should be drawn to the magnified section of the absorber region (right) in Figure 6.7. At 0° angle of incidence the rays are more evenly spread, the largest peaks are central and there is symmetry. However, as the angle of incidence increases, the flux concentrations (represented by high density regions on the absorber width) shift left i.e. the opposite direction of the inlet angle. Comparing graph Figure 6.7(a) with Figure 6.7(b) we can see that the two main concentration of light in the centre at 0° shift left in Figure 6.7(b) (5°). Additionally, the intensity of the concentrated regions coming from the right side has increased whilst those from the left side has decreased. This pattern continues to 10° and 14.47° at which point all the rays land on the extreme left edge of the absorber plate shown in Figure 6.7(d).

This relation can be better shown by looking at the ray intensity distribution shown in

Figure 6.8. Because the model is 2D, radiation intensity of unit W/m^2 cannot be calculated. For this reason, the unitless term *relative energy flux concentration* is used to show the distribution of the flux across the absorber area. What this means is that a point on the graph of value 200 is hit with 200x lighter than a point of value 1.

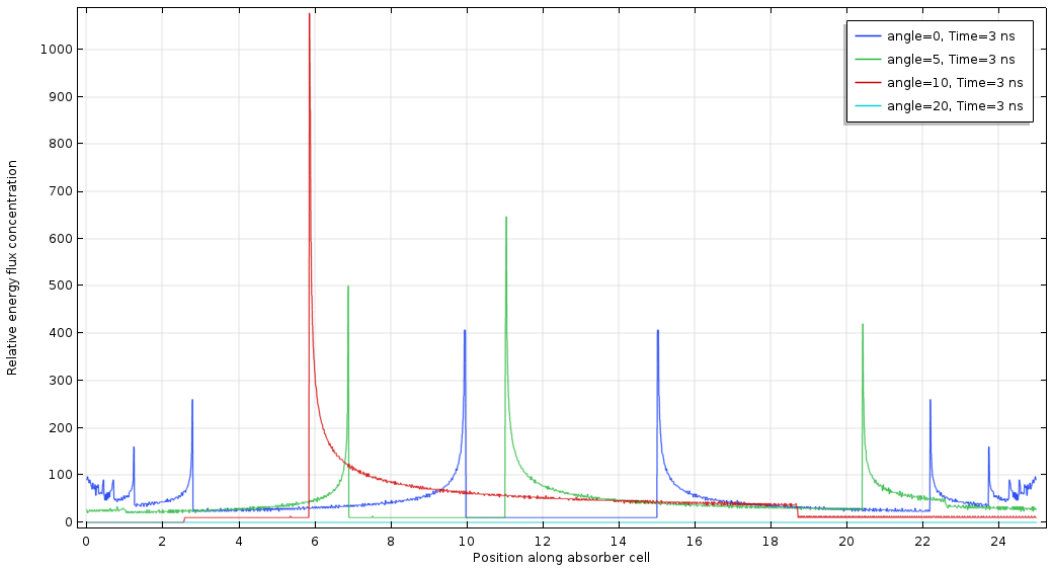

Figure 6.8. Ray intensity distribution (aka energy flux distribution) along the absorber cell of a full height CPC for 0° (blue), 5° (green), 10° (red) and 20° (teal) light angle of incidence

The blue graph representing 0° has a higher number of but a lower concentration of peaks and rises on the graph and better distribution along the absorber cell area. It has 10 notable peaks of maximum 400 relative concentration and large regions of low concentrating plateaus. Moving on to 5° angle of incidence, the number of peaks has reduced to 3 but their intensity is increased (up to 650 relative concentration). The plateaus are also fewer in number and lower in value. At 10° angle of incidence there is only one peak or ~1100 relative concentration representing the bulk of incidence radiation. There is still some distribution of the ray, especially towards the right-hand side where the peak falls off smoothly (it sharply drops on the left-hand side). 20° angle of incidence is also plotted for reference, this graph is zero across the plate correlating to the fact that no rays hit the absorber plate i.e. all the rays were rejected.

At 14.47° the pattern is taken to the most extreme point. Figure 6.9 shows the flux concentration distribution for 14.47° i.e. the CPC design half acceptance angle. At this point there is one peak at the left edge of the absorber plate of enormous magnitude and 0 energy flux landing everywhere else. The graph is drawn separately as the magnitude of the peak (~30,000) would distort the scale of the graphs in Figure 6.8.

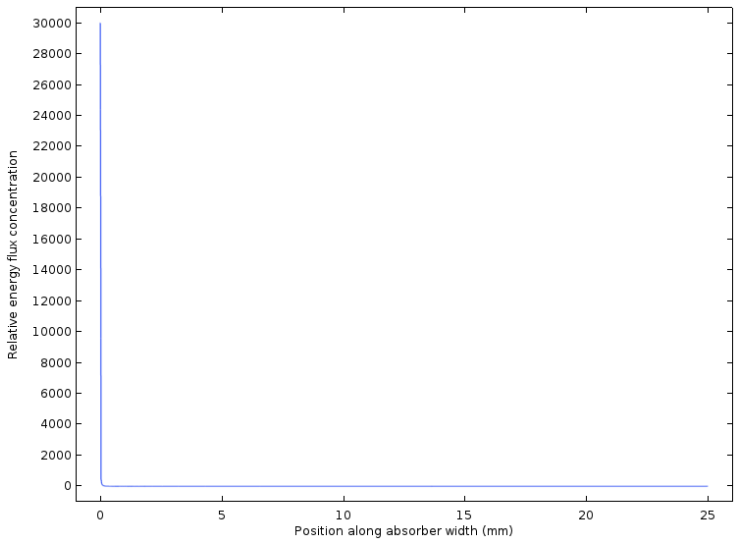

Figure 6.9. Relative energy flux distribution along the absorber plate for 14.47° angle of incidence.

This shift to the left of the bulk of rays explains the sudden drop in efficiency as well. If at 14.47° the rays fall on the leftmost edge of the absorber cell, then any further shifts to the left of the rays would lead to them falling on the left-hand parabola rather than the absorber cell.

Figure 6.10 shows a magnified time lapse of the point of interaction with the absorber cell and left parabola. The rays approach the time of interest at Figure 6.10 (a), the majority of the rays hit the left-parabolic reflector at ~0.8 ns shown in Figure 6.10 (b). The absorber cell is hence missed, and part of the rays are directly reflected out of the CPC whilst the rest are reflected back to the right-hand parabolic reflector before being reflected back out as shown in Figure 6.10 (c). Figure 6.10 (d) shows the complete ray trace diagram with the bulk of the rays rejected back out of the concentrator.

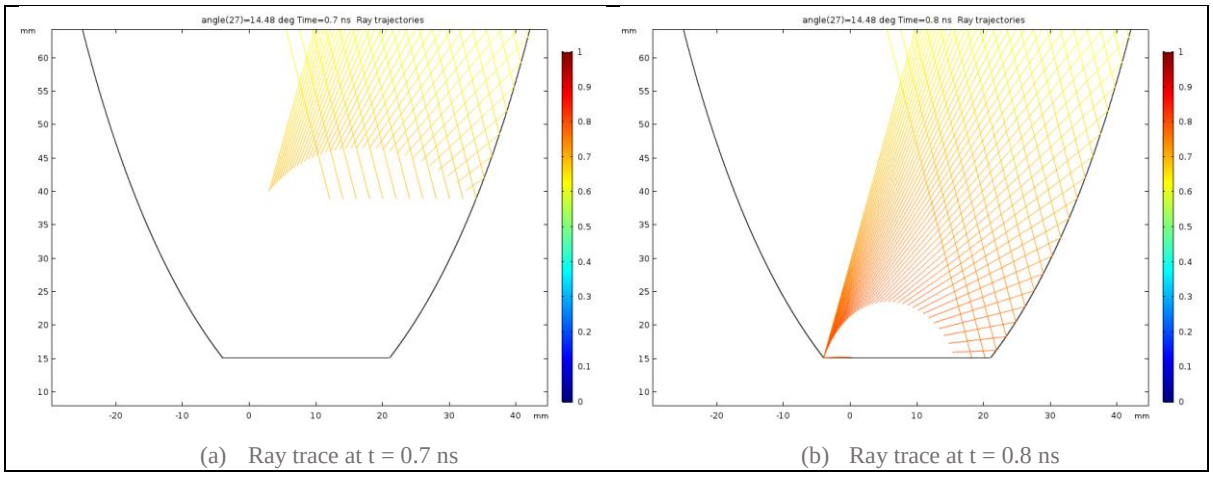

(a) Ray trace at t = 0.7 ns (b) Ray trace at t = 0.8 ns

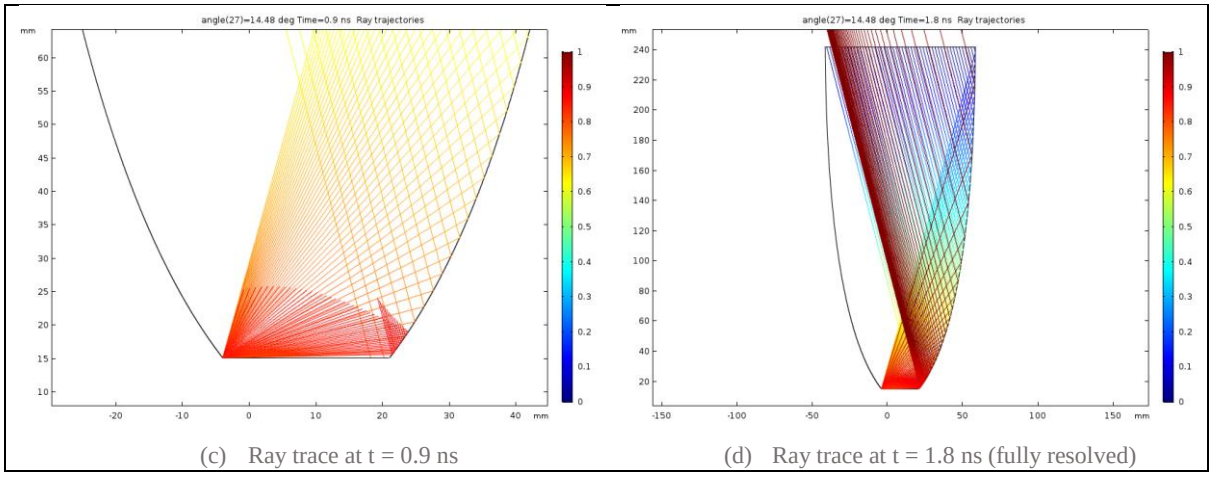

(c) Ray trace at t = 0.9 ns (d) Ray trace at t = 1.8 ns (fully resolved)

Figure 6.10. Magnified ray tracing of 14.48 inlet angle of incidence at a) 0.7 ns, b) 0.8 ns, c) 0.9 ns and d) 1.8 ns

It may not be very apparent even with the magnified images precisely where the rays strike therefore the ray trace diagrams are magnified to 0.01 mm grid size in Figure 6.11. Figure 6.11(a) shows the rays hitting the left-hand parabola before being reflected right and back up. This is in stark contrast to Figure 6.11(b) where the rays hit the absorber cell.

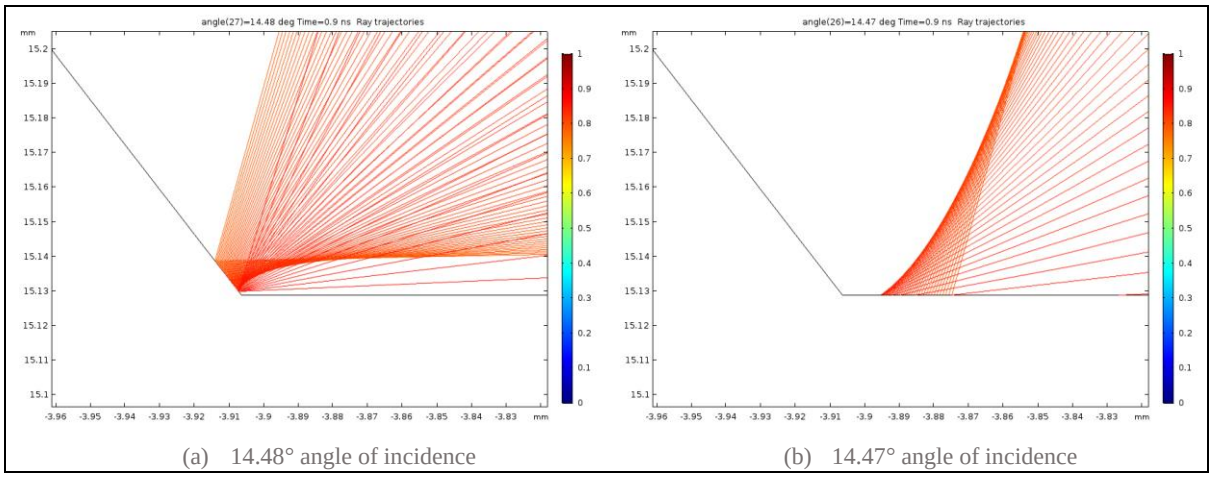

(a) 14.48° angle of incidence (b) 14.47° angle of incidence

Figure 6.11 Magnified ray tracing at time of impact. at (a) 14.48°, and (b) 14.47° angle of incidence for comparison

Finally, Figure 6.12 shows ray trace diagrams for a range of post angle of acceptances 15°-45°. At 15° there is still a small number of accepted rays: 1.63% of rays entering inlet aperture.

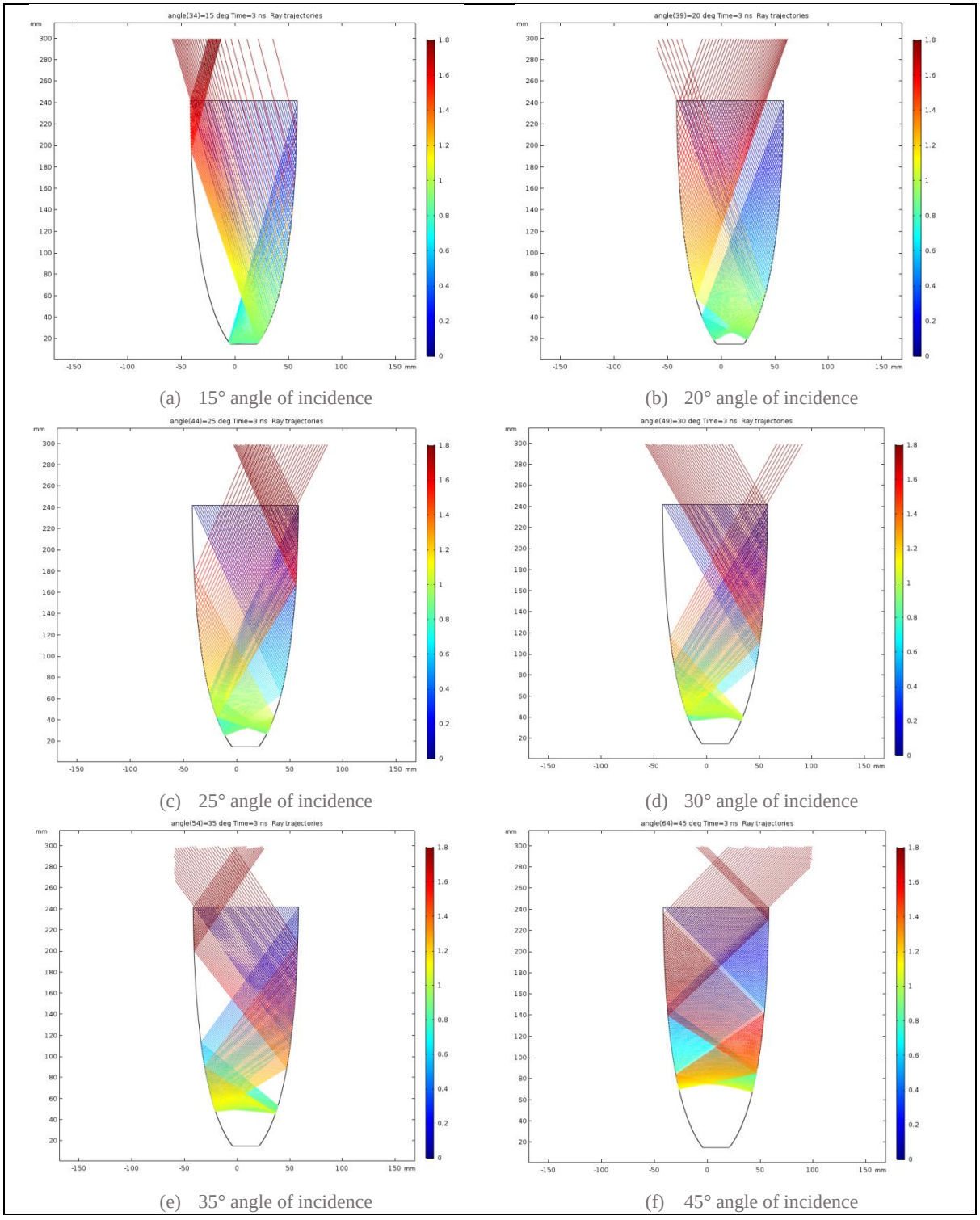

Figure 6.12. Full height CPC ray trace diagrams at (a) 15°, (b) 20°, (c) 25°, (d) 30°, (e) 35° and (f) 45° light angles of incidence.

In all other cases shown above, all rays are rejected. At 20°, the rays reach near the absorber area before being reflected out, at higher angles, the rays are rejected higher up in the CPC due to the sharper angles of the rays.

6.1.2. Half-truncated CPC

The concentrator parameters are as follows:

- Full height CPC was truncated by 50% $\therefore h = 242.06 \times 0.5 = 121.03$ mm
- Absorber area (width) 25 mm
- Aperture area (width) 86.98 mm measured directly from model
- New Geometric Concentration ratio $C_r = \frac{W_{ape}}{W_{abs}} = \frac{90.20}{25} = 3.608$
- Half Acceptance angle $\theta_h \approx 14.478°$

The simulation again solved for 3 ns of ray propagation time. Rays were terminated if passing y>180mm. Since the height of the truncated CPC is 121mm, their rejection is apparent by 180mm, this saves computation time by not resolving the rays any further.

Figure 6.13 shows a sample of ray trace diagrams for half-truncated CPC up to the acceptance angle (14.47°). The results are similar to full height CPC: Figure 6.13(a) shows a more even, mirrored spread of light on the absorber area at 0° angle of incidence. This shifts to the left as the angle of incidence is increased (Figure 6.13 b-d) ending at 14.47° where virtually all the light hits the left most edge of the absorber area.

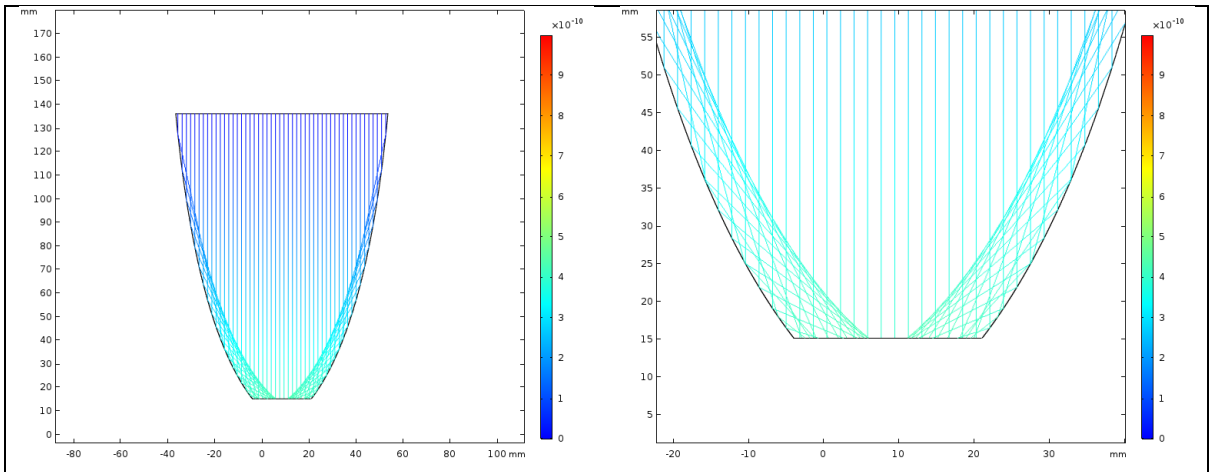

(a) Half truncated CPC at 0° angle of incidence

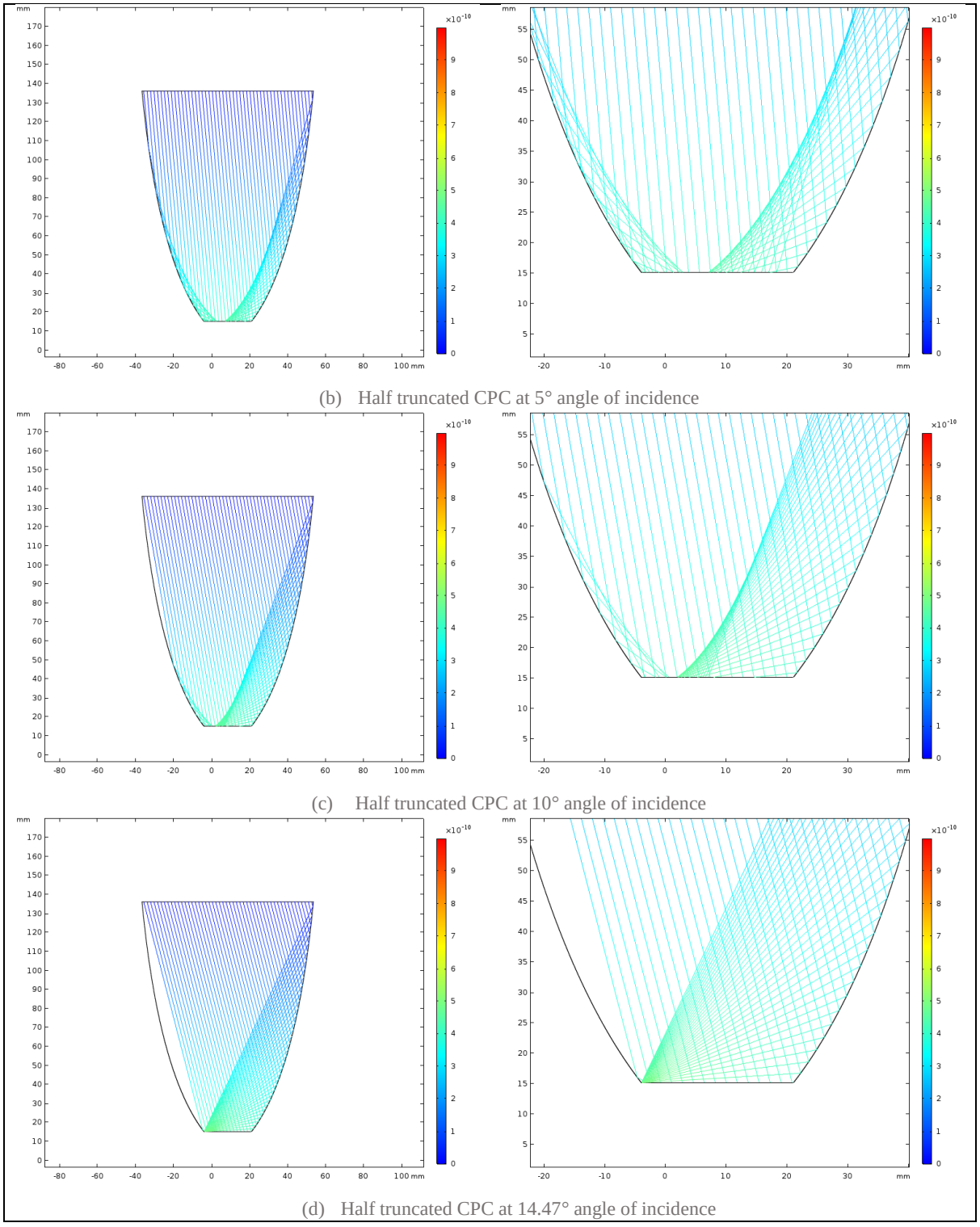

(b) Half truncated CPC at 5° angle of incidence

(c) Half truncated CPC at 10° angle of incidence

(d) Half truncated CPC at 14.47° angle of incidence

Figure 6.13 Ray trace diagrams for half-truncated CPC at (a) 0°, (b) 5°, (c) 10° and (d) 14.47° light angle of incidence

Numerical data from the model support the visual graphs, at 14.47°, 100% of rays are accepted. In effect this means that a 50% truncation of the CPC, results in a 10% (0.4) drop of net (optical) concentration ratio whilst saving 121mm of CPC height, a premium parameter when designing for BIPVs.

Figure 6.14 shows the ray intensity distribution with results being roughly similar to full height CPC. At 0° angle of incidence, there are a larger number of peaks and light is better distributed. As this angle increases, the peaks become fewer in number but greater in height and shift left. At 5° there are two main peaks and at 10° there is one major and one minor peak. Interestingly, at 5° there is now a group of small peaks on the left side, something that was exhibited by the 0° CPC at full height. The half-height CPC at 0° no longer exhibits these large numbers of small peaks and rises near the left (0-1mm) and right (24-25mm) edges of the absorber width. The 10° light incidence model also showed an additional peak at around 5mm position. It now contains two peaks that smooth out in opposite directions.

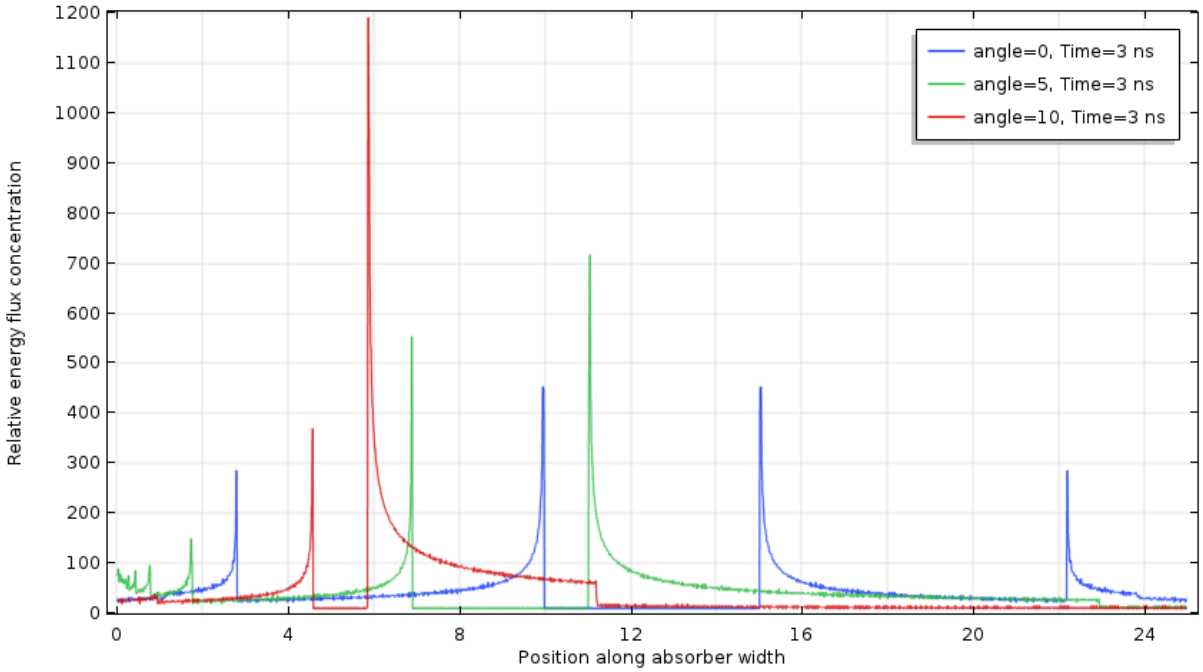

Figure 6.14 Ray intensity distribution along the absorber area of half height CPC for 0° (blue), 5° (green) and 10° (red)

The changes show an improvement in light intensity distribution along the absorber width at higher light angles of incidence (5°, 10° up to 14.47°).

Perhaps the biggest change to the CPC performance is for incident angles above the acceptance angle 14.47°. Figure 6.15 shows ray trace diagrams for models between 15-25° angle of incidence. At 15° there are still accepted rays hitting the absorber width on the half-truncated CPC model. In contrast, the full CPC model had zero accepted rays at 15°. This effect tapers down with less and less accepted rays as the angle increases up to ~25° angle of incidence at which point all light is reflected out i.e. the model results of CPC at full and half truncation re-converge.

The zoomed-out images on the left column of Figure 6.15 show that the accepted light is hitting the absorber width directly from the inlet aperture. This has the other upside of having a perfectly uniform distribution along the absorber width (shown on the right images).

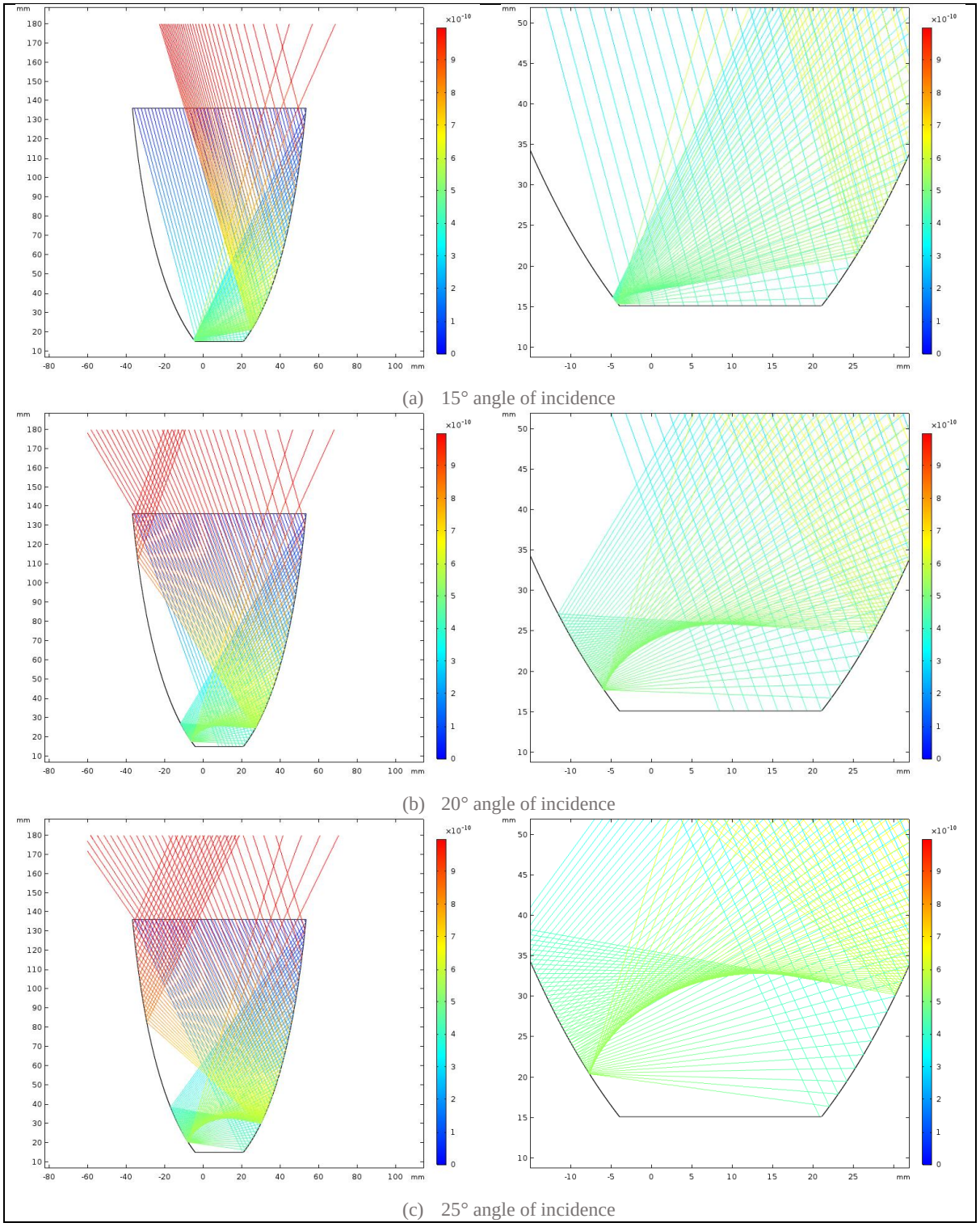

Figure 6.15 Ray trace diagrams for angles (a) 15°, (b) 20° and (c) 25° angles of incidence

Figure 6.16 shows the acceptance rate of the half-truncated CPC for all angles from 0 to 45°. The graph allows a better analysis of the post-acceptance angle effects due to truncation. It shows the acceptance rate is dropping linear to the inlet angle of incidence until it hit zero acceptance at ~25°.

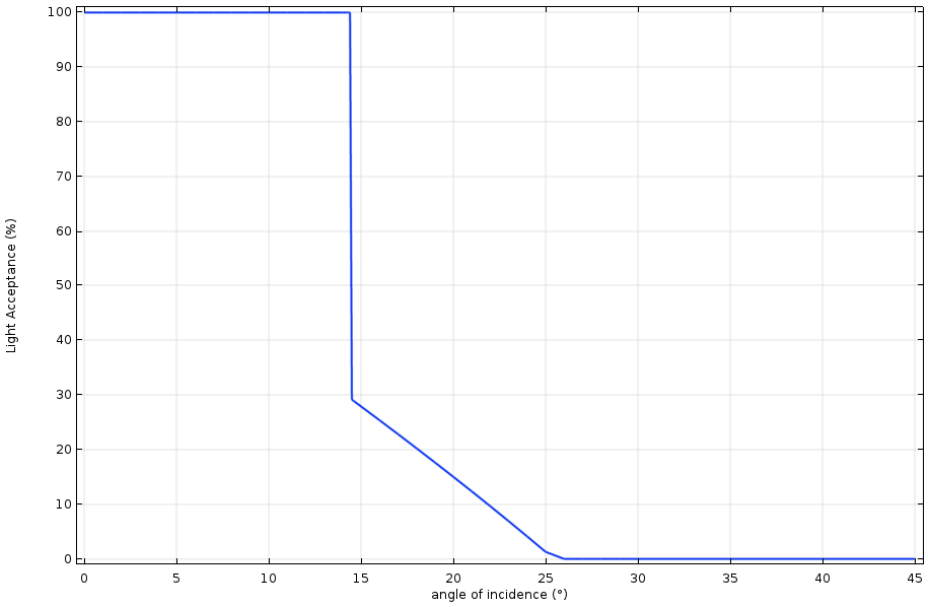

Figure 6.16. Light acceptance of half truncated CPC

The ray trace diagram for 30-45° angle of acceptance is shown in Figure 6.17 for comparison. The results are similar, in all cases rays are reflected out (rejected), the angle of incidence affects the depth at which the rays reach before reflecting back. The higher the angle of incidence, the less depth the rays penetrate before going back out the system.

The biggest difference is not in the relative changes due to angle of incidence increase but the absolute values. For example at 35° angle of incidence, the full CPC rays turn back up at y-axis positions of ~40mm (Figure 6.12e) whilst the truncated CPC rays rebound after reaching ~25mm (Figure 6.17b). Likewise at 45°, the full CPC rays rebound after reaching y-values of ~65mm (Figure 6.12f) on the grid whereas the half-truncated CPC rays at the same angle reach down to 40-45mm (Figure 6.17d) before going back out.

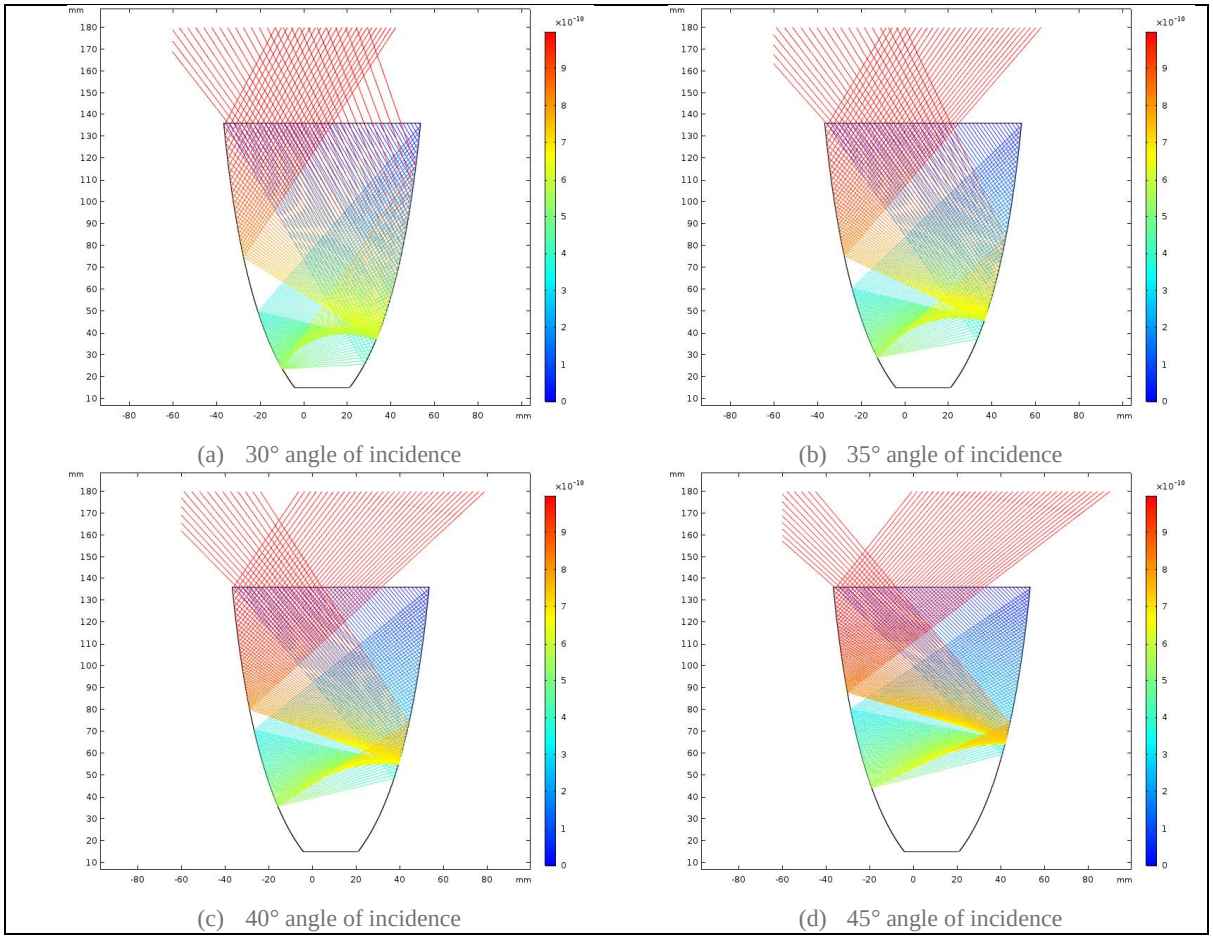

(a) 30° angle of incidence (b) 35° angle of incidence

(c) 40° angle of incidence (d) 45° angle of incidence

Figure 6.17. Ray trace diagrams for 0% acceptance angle of incidences (30-45°)

6.1.3. Truncated CPC to 50 mm Height

The concentrator parameters are as follows:

- Full height CPC was truncated to 50mm $= \frac{50}{242.06} = 20.66\%$. 50mm is designed to represent realistic thickness available for BIPV systems.
- Absorber area (width) 25 mm
- Aperture area (width) 67.48 mm measured directly from model
- New Geometric Concentration ratio $C_r = \frac{W_{ape}}{W_{abs}} = \frac{67.48}{25} = \mathbf{2.699}$
- Half Acceptance angle $\theta_h \approx 14.478°$

The simulation solved for 3 ns light ray propagation time. Rays were terminated if passing y>90mm due to the lower height profile of the 50mm CPC.

Figure 6.18 shows ray trace diagrams of models at 0°, 5°, 10° and 14.47°. The truncation does not affect the acceptance rate up to the half acceptance angle, all the rays still hit the absorber area.

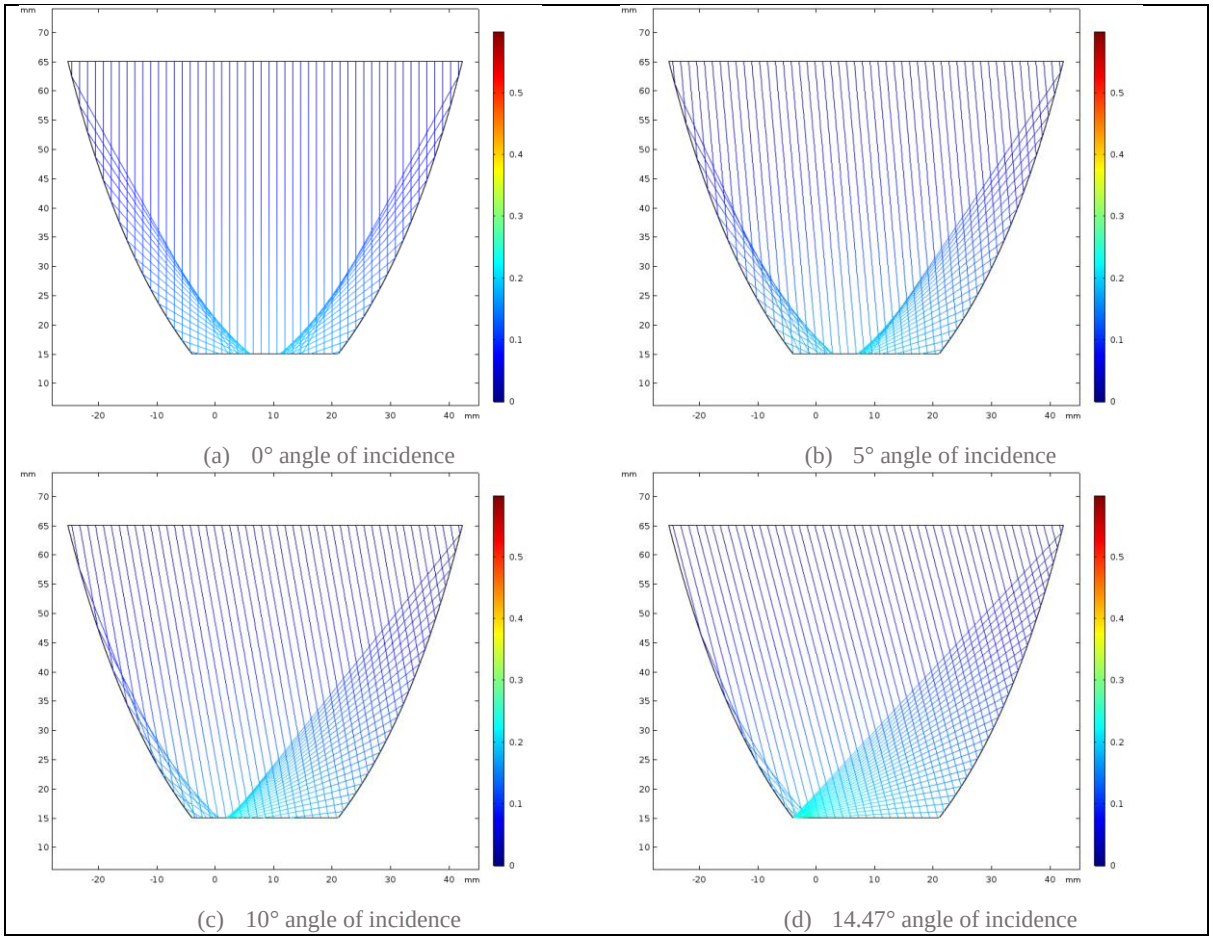

Figure 6.18. Ray trace diagrams at ~5° angle of incidence intervals up to acceptance (half) angle

The concentration is still reduced due to the smaller inlet aperture width. On the other hand, the rate of height truncation far outstrips the rate of concentration loss. In the 50mm case, C_r is reduced from 4.0 to 2.7, a loss of 32.5%, whereas the height of the CPC is reduced by 80%.

Other expected patterns continue, at 0° angle of incidence, the rays are symmetric and relatively evenly distributed. As the angle increases the bulk of rays hitting the absorber width shift left up to 14.47° angle of incidence, at which point almost the entirety of the rays hit the left edge of the absorber area.

Figure 6.19 shows the ray intensity distribution. At 0° there are now only two peaks, this is down from 4 peaks at half truncation CPC (Figure 6.14). Their intensity has increased from 450 at half truncation to 600 at 50mm truncation. As this angle increases, the peaks become fewer in number but greater in height and shift left. In this case both the blue and green graphs have fewer (but taller) peaks whereas the red graph has more peaks than half truncation CPC (3 compared to 2). In the case of the red graph ($\theta = 10°$) however, the intensity has risen from 1200 to 1600.

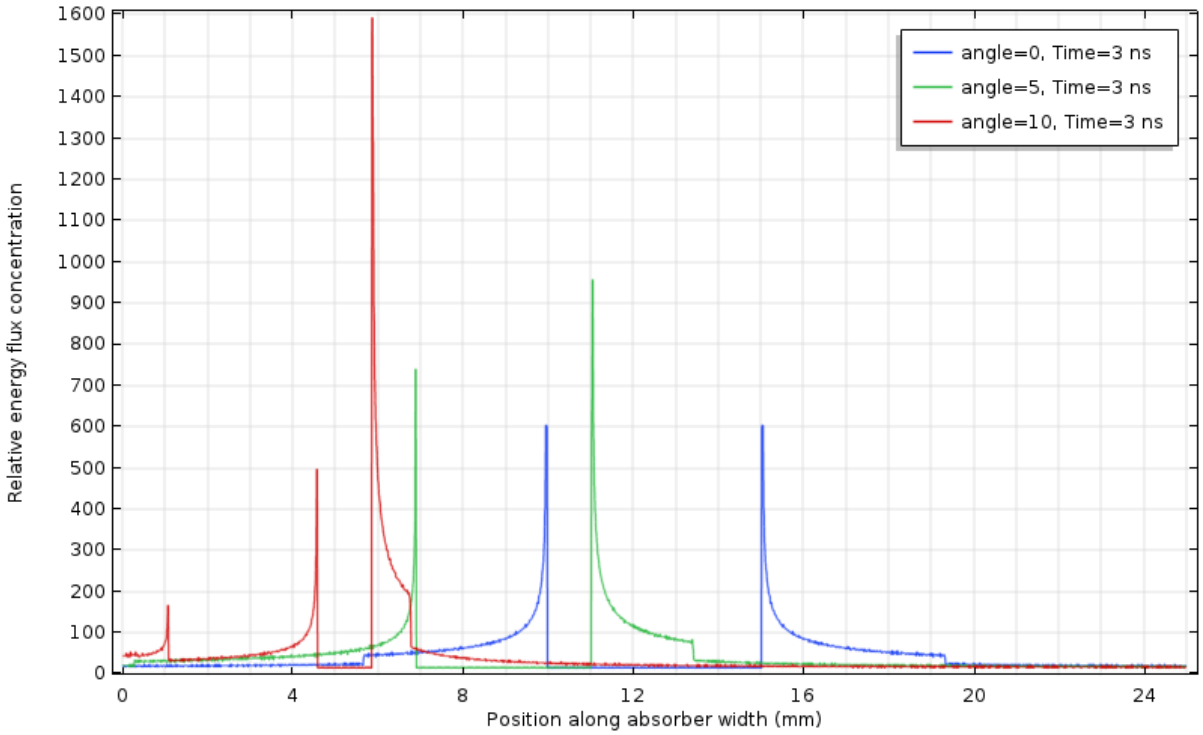

Figure 6.19. Ray intensity distribution along the absorber area of 50mm truncated CPC for 0° (blue), 5° (green) and 10° (red)

Ray trace diagrams for 50mm truncated CPC at post-acceptance angles 15-45° are shown in Figure 6.20. The graphs show an increase in the percentage of rays accepted across all data >14.47°. The range of light incidence after the acceptance angle, for which a proportion of rays were still accepted, also increased significantly. Part of the reason for the increase is the direct radiation falling on the absorber width from the inlet aperture as with the half-truncated CPC. This effect is more pronounced here and tapers off slower, dissipating at ~43° shown in Figure 6.21 (rather than 25° for half-truncation).

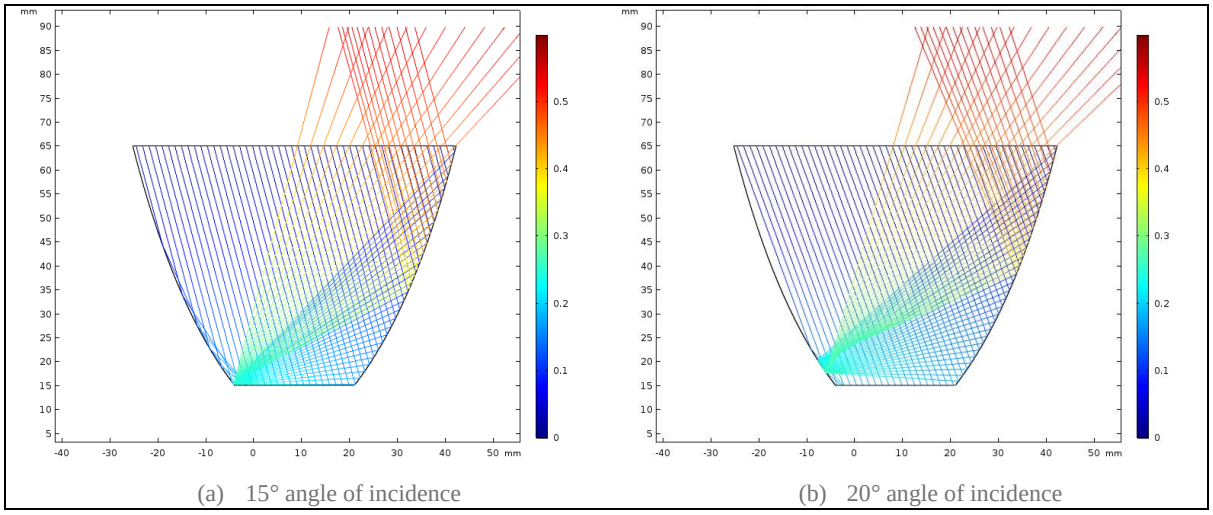

(a) 15° angle of incidence (b) 20° angle of incidence

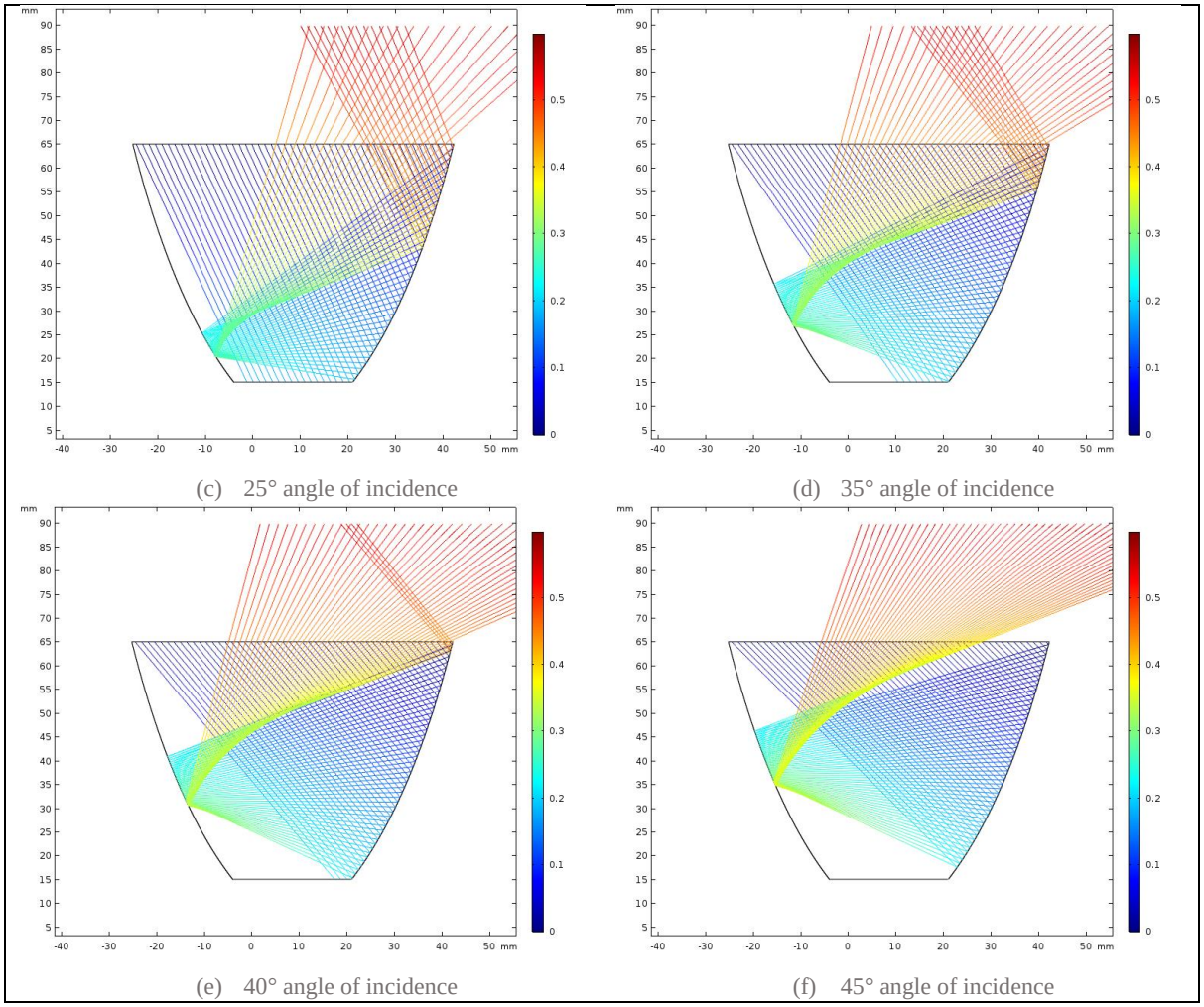

Figure 6.20. Ray trace diagrams for 50mm truncated CPC at post-acceptance angles 15-45°

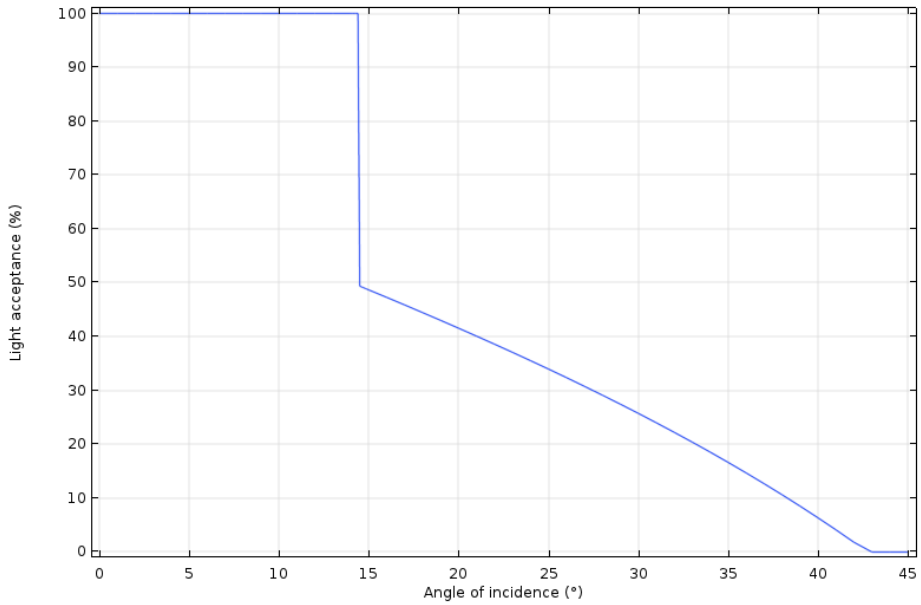

Figure 6.21. Light acceptance of 50mm truncated CPC

Another contribution is from an additional element of rays which hit the left-side reflective parabola and bounce back to the absorber area. This phenomenon occurs due to the shape of the parabola: at the entry aperture the tangential angle of the parabolic wall is less than or equal to the light angle of incidence. Hence, rays parallel or divergent to the parabolic wall enter that then go on to hit the same wall due to the changing angle of the parabola. These rays are highlighted in Figure 6.22 below.

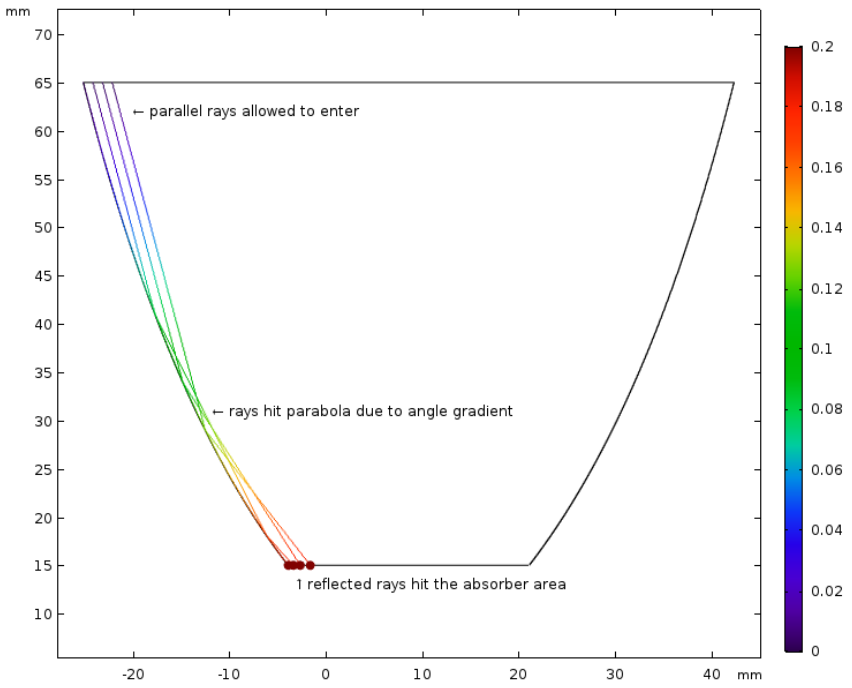

Figure 6.22. 15° angle of incidence ray trace diagram subset demonstrating effect of parabolic curve and truncation on ray acceptance

These regions therefore have a greater than 1 concentration ratio even at such extreme angles of incidence, this is due to not only the direct radiation reaching the absorber surface but also re-directed rays from the same parabola the rays are directed from.

6.2. V-trough Concentrator

Since the V-trough concentrator is constructed from two linear angled walls at either side of the absorber width, the geometric concentration ratio is dependent on the tilt angle of the reflector walls. In effect, the bigger the tilt angle of the reflector walls, the higher the concentration ratio. The limits on either extreme are 0° tilt leading to a geometric concentration ratio of $C_r = 1$, i.e. no concentration, and 90° leading to $\lim_{W_{ape} \to \infty} C_r(W_{ape}) = \infty$.

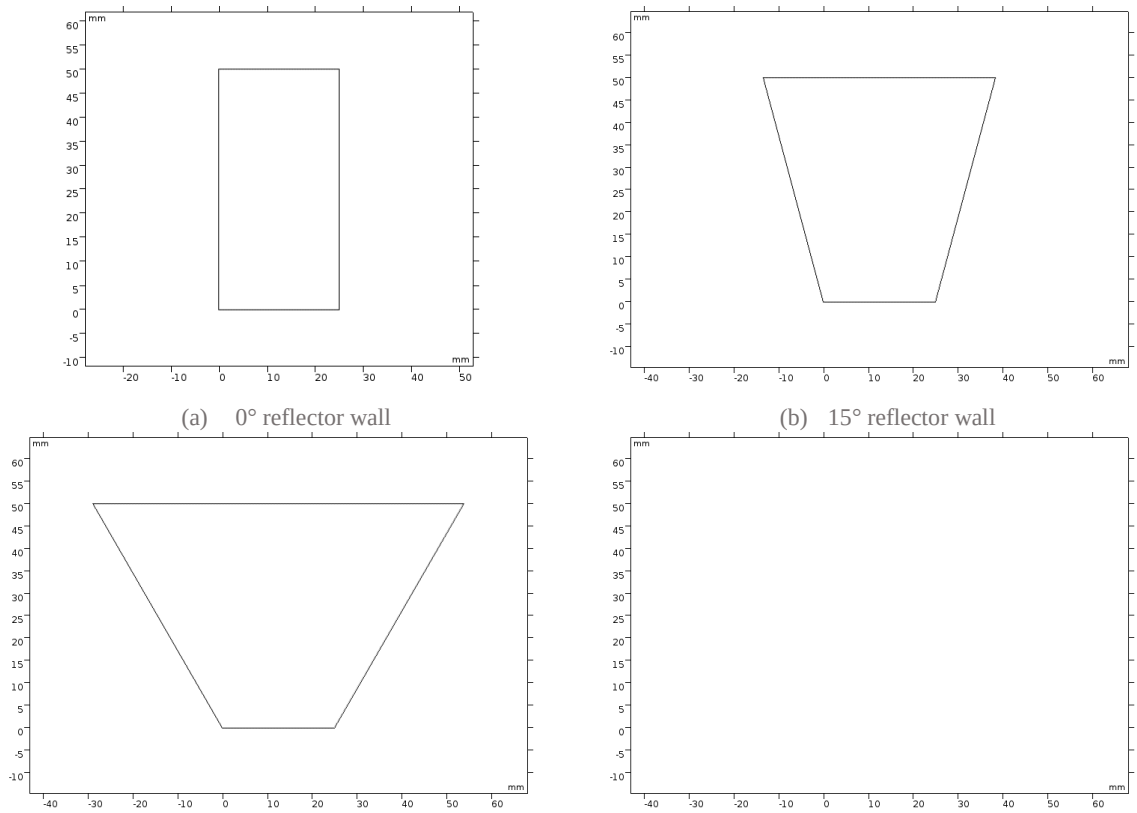

(a) 0° reflector wall (b) 15° reflector wall

(c) 30° reflector wall (d) 90° reflector wall

Figure 6.23 V-trough concentrator generated with (a) 0°, (b) 15°, (c) 30° and (d) 90° reflector wall tilt angle.

At 90° reflector wall angle, the system of equations set up and explained in Chapter 4 for automated geometry generation break down. The equation for the length of the reflector, $(ref)_L = 50/\cos(\phi)$ becomes a *divide by zero* mathematical error as $\cos 90° = 0$.

An early question that arose when comparing the 50 mm CPC and V-trough was how to compare the two systems. Should the concentration ratios be compared? If the concentration ratio of the V-trough can be increased or decreased, should be artificially limit its Cr to 2.7 to be equivalent to the CPC at the same height (50 mm)?

The author believes the answer is to find the best parameters that would generate the highest net concentration for both systems. If a comparison of CPC and V-trough for **BIPV** is to be made, then the only limit should be the 50 mm height limit. This might mean the V-trough will have a higher or lower Cr, mostly dependant on the ray acceptance rate of the various wall configurations.

The ray tracing algorithm was set to run for 2 ns propagation time. The rays are colour-coded based on time to indicate the position of the ray at different time intervals. Here blue represents

just released rays (t = 0 ns) going through yellow to red. The legend will vary based on time taken for rays to resolve.

Figure 6.24 shows the ray tracing diagram for a 15° V-trough with a 0° solar angle of incidence. There are three main observations:

Firstly, all rays are absorbed by the V-trough concentrator. Secondly, the distribution of the rays is very uniform. The direct radiation on the absorber width has perfect uniformity, the indirect radiation – those that hit the reflector walls before reaching the absorber – reduce the uniformity somewhat, but overall the distribution of radiation is better than equivalent CPC. Thirdly, there is a central region in the centre where there are ray contributions from direct, left-reflector and right-reflector. This region appears to have the highest magnitude of incoming radiation.

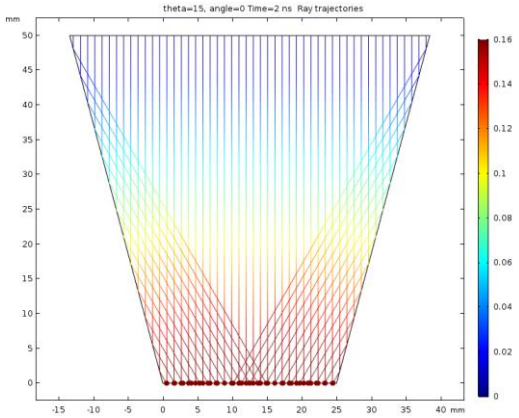

Figure 6.24. 15° V-trough at 0° light angle of incidence

To show a clearer view of the flux concentration on the absorber width, we can look at Figure 6.25. As expected, good distribution is shown, with the flux concentration being mostly horizontal. The region in the centre shows a flux concentration rise for the overlap of reflections from the left and right V-trough walls as explained above.

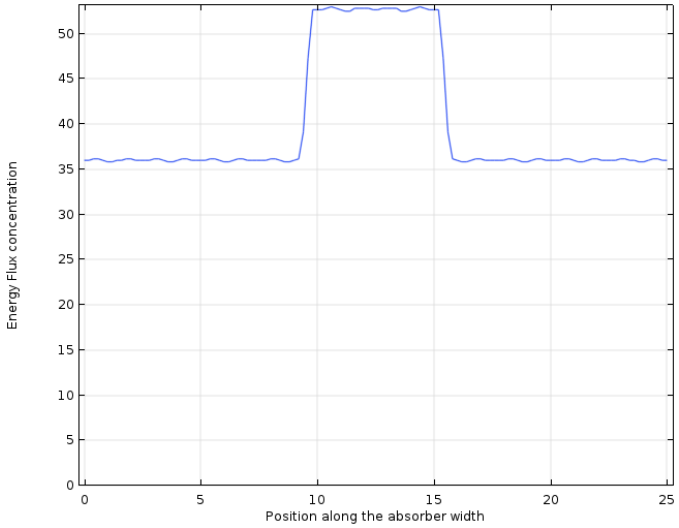

Figure 6.25. Flux concentration distribution of 15° V-trough at 0° light angle of incidence

Next, we look at the changes the V-trough undergoes as the light angle of incidence varies. Figure 6.26 shows the 15° V-trough at 10°, 15°, 20°, 30° and 45° angles of incidence. Their respective flux concentration distribution is displayed to their right.

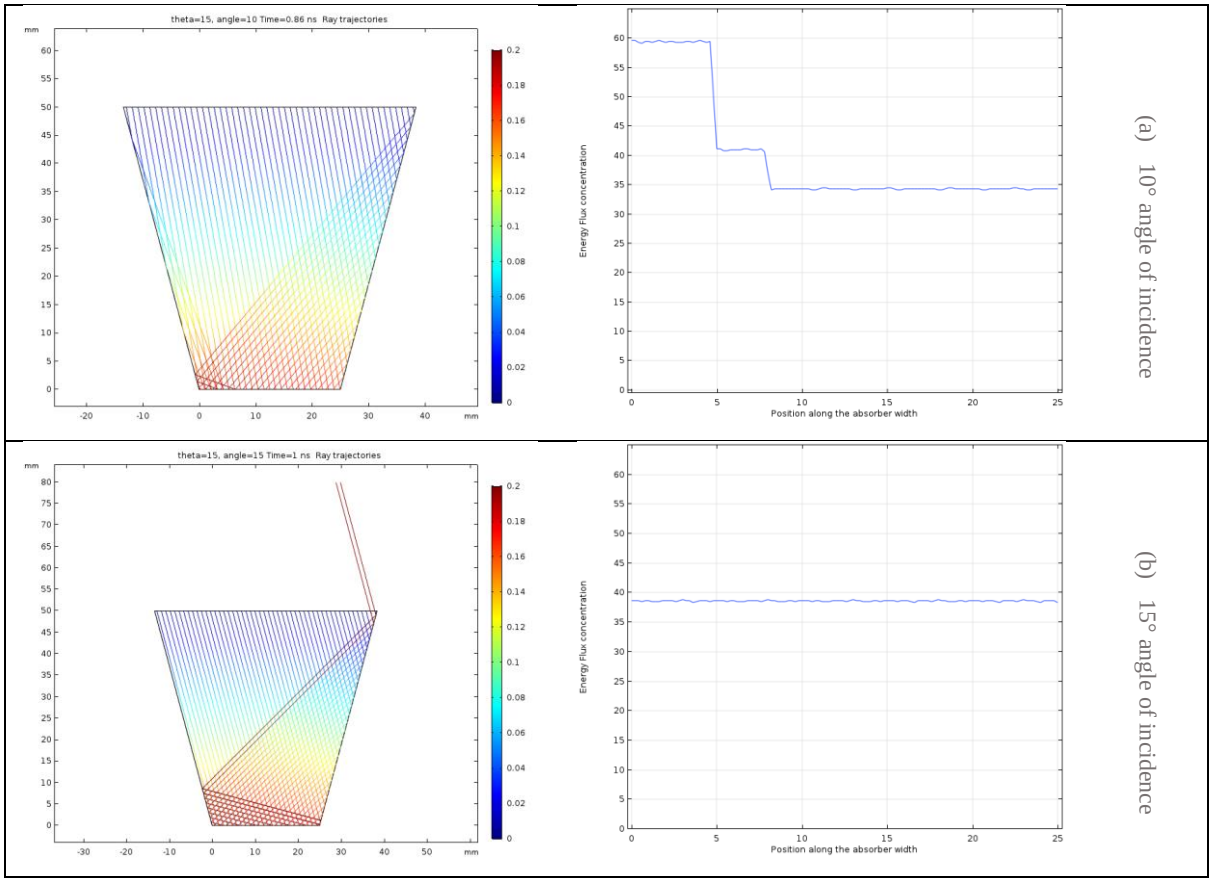

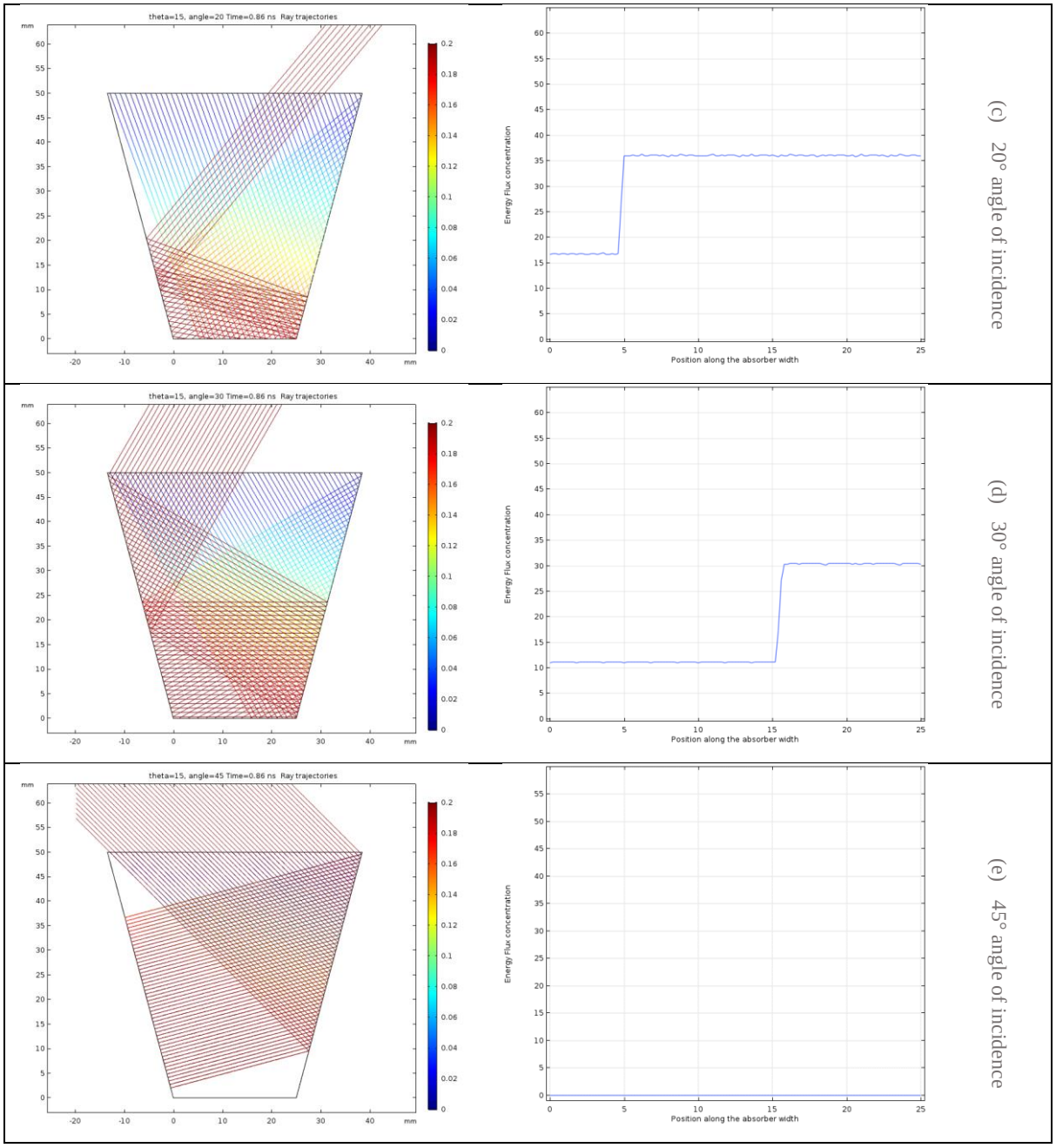

Figure 6.26. 15Deg V-trough concentrator ray trace diagram and radiation distribution graphs at various light angles of incidence.

We can see that at angles below 15°, there is a bigger concentration of light on the left side of the absorber. This shifts to a perfect distribution at 15° angle of incidence (Figure 6.26b) and beyond that the flux distribution is biased to the right-hand side of the absorber width. At 45° all light is reflected out resulting in zero flux concentration on the absorber, furthermore, the light rays leave the V-trough at the exact angle they enter which results in the ray trace of Figure 6.26e being containing all red rays (later rays are drawn on top of prior ones).

Figure 6.27 gives a summary of the performance of a 15° V-trough concentrator. Ray acceptance is the % of rays reaching the absorber.

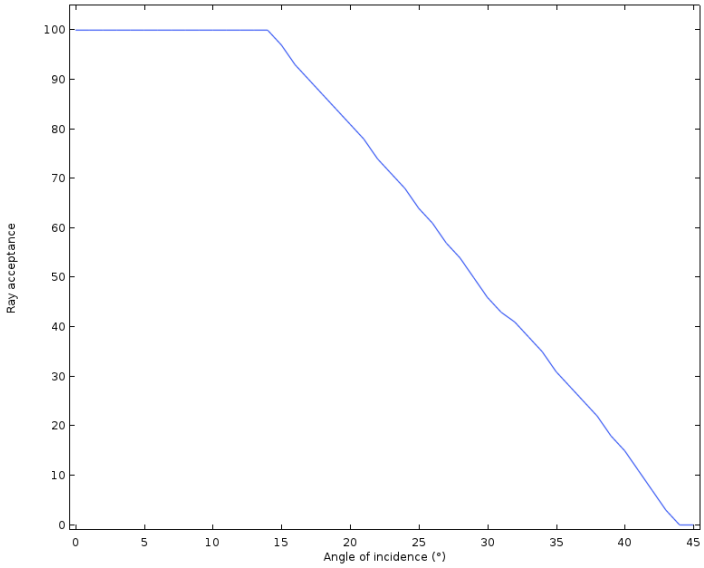

Figure 6.27. Ray acceptance of 15Deg V-trough for 0-45° angles of incidence

The Concentrator has 100% acceptance until around 14°, after which the performance drops linearly to zero at 44° light incidence.

Unlike the CPC, which had only three configurations of Full, Half and 50 mm height, the V-trough concentrator can have a much larger number of configurations based on the angle of the reflector walls. Even at 1° intervals, it would take 46 different configurations to analyse the entire range. Considering the angle of incidence was cut into 1/100th of a degree in some cases for the CPC, the combinations to solve for would get absurd quickly. Consider that for 0-45° V-trough combinations, with 0-45° light incidence angles, even done in coarse steps of 1° would require sections and a huge number of ray trace diagrams to be presented. As such a sample of important angles are highlighted with most data presented in the form of cumulative graphs.

Figure 6.28 shows all results for V-troughs with wall tilt angles from 0-45° in 5° steps. We can see that 0° V-trough concentrator has the best efficiency, running at 100% acceptance at all angles of incidence from 0 to 45. As the angle is increased, a linear drop occurs, where this drop starts is based on the V-trough reflector angle, at 5° the drop begins ~40° light incidence, for 10° V-trough it is ~25° light incidence and so on. 25° V-trough and beyond start below 100% acceptance from the beginning (0° light incidence). 40° and 45° exhibit the most

interesting behaviour, unlike other V-trough configurations they start with low acceptance and improve, up to a peak, before dropping back down again.

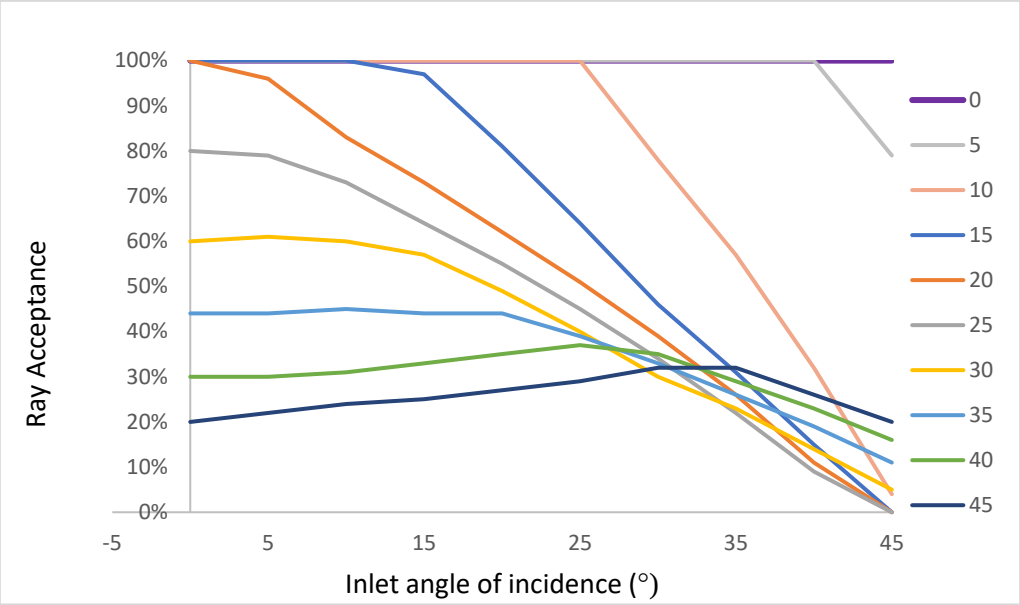

Figure 6.28. Compilation of V-trough configurations performance

There is one important parameter that the above figure does not present: the geometric concentration ratio (C_r). If we consider only the above data, then a wrong conclusion could be made that the best V-trough configuration is 0° V-trough. However as mentioned at the start of section 6.2, the geometric concentration ratio of a 0° V-trough is 1, hence even at 100% acceptance that is still a concentration ratio of 1. On the other hand, the 25° V-trough has $C_r = 2.87$, which operating at 80% acceptance for 0° angle of incidence (~2.23) is still significantly better than the 0° V-trough.

We therefore need to consider the combination of geometric concentration ratio C_r and the acceptance rate to find the effective concentration ratio of the concentrator. This value, called the *optical concentration ratio* is defined as:

$$C_{opt} = \frac{flux\ over\ receiver}{flux\ over\ aperture} = C_r \cdot \eta$$

Where η is the acceptance rate.

Figure 6.29 presents the geometric concentration ratio (C_r) of the various V-trough concentrators studied.

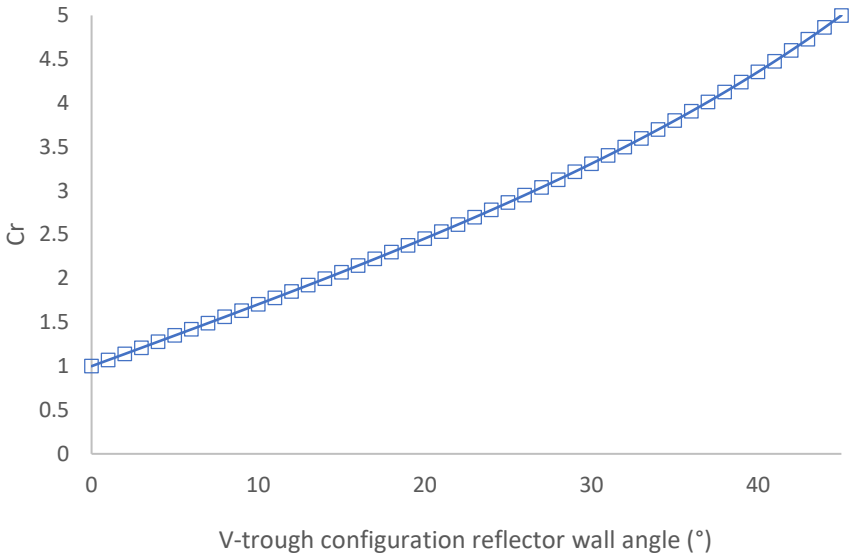

Figure 6.29. Geometric concentration ratio of V-trough configurations from 0 to 45°

Figure 6.30 demonstrates why some V-trough models start at lower efficiency. At 10° V-trough reflector angle, the concentrating rays (those that hit the reflector to fall on the absorber area), land at the same side as their corresponding reflector.

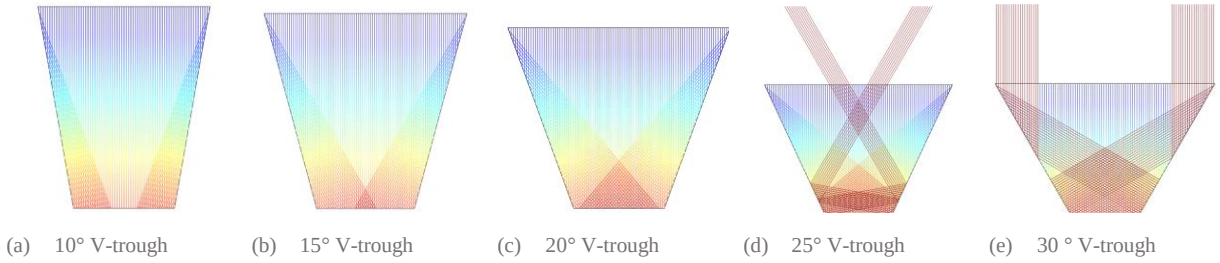

(a) 10° V-trough (b) 15° V-trough (c) 20° V-trough (d) 25° V-trough (e) 30 ° V-trough

Figure 6.30. Ray trace diagram of various V-trough configurations at 0° angle of incidence

As the V-trough angle increases, the concentrating rays are projected further to the other side. For 25° and 30°, part of the concentrating rays begins to hit the opposite side wall, those rays are then reflected out the V-trough concentrator (rejected).

Figure 6.31 shows the optical concentration ratio (C_{opt}) of the V-trough concentrator at 5° wall tilt configuration intervals operating under various light incidence angles.

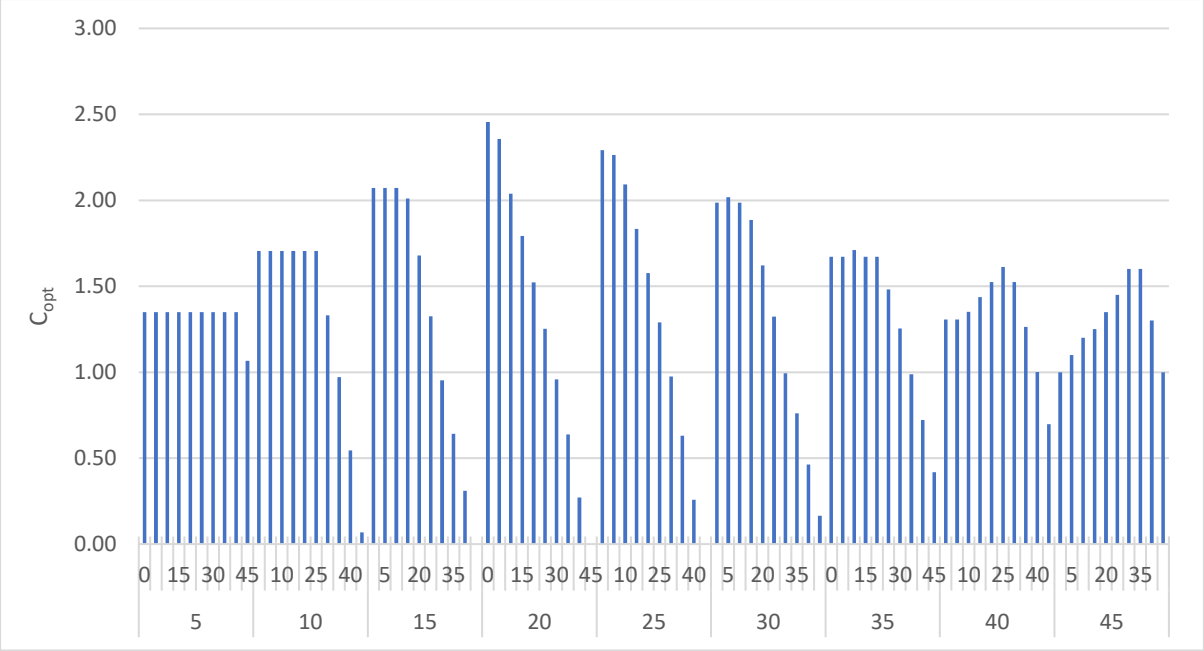

Figure 6.31. C_{opt} of various V-trough wall tilt angle (Major x axis) at different light incidence angles (Minor x axis)

We can average the optical concentration ratio over the angles of incidences provided. Table 6.1 contains the tabulated results and shows slight highs for 20° and 35° V-trough configurations. However, except for 0° V-trough, the numbers are mostly the same.

Table 6.1. Averaged C_{opt} for various V-troughs wall tilt angle at 0° to 45° light incidence angles

V-trough	Avg. C_{opt}
0	1.00
5	1.32
10	1.31
15	1.31
20	1.33
25	1.32
30	1.32
35	1.33
40	1.3
45	1.29

One way to make the results more relevant is to consider when a real V-trough concentrator would be producing its peak power. Assuming the period of 10am – 2pm to be the 4-hour peak production time for solar cells in London, UK, we can hone in on the angles that are of most importance.

The Earth rotates once per 24 hours, hence the sun's position relative to a fixed location on Earth moves $\frac{360}{12} = 15°/h$. Since we assumed 4-hour peak, we consider the most important angles of incidence to be $15 \times 4 = 60°$ wide. This corresponds to a 30° **half** angle of incidence in the models to account for the fact that light rays will be coming from both directions throughout the day.

If we use this to filter out angles of incidence *>30°*, Figure 6.32 is obtained. We now have a better idea of the best performing V-trough design: it would fall somewhere between 15-25° reflector wall tilt angle.

V-trough	Avg. C_{opt}
0	1.00
5	1.35
10	1.65
15	1.74
20	1.77
25	1.76
30	1.69
35	1.59
40	1.44
45	1.28

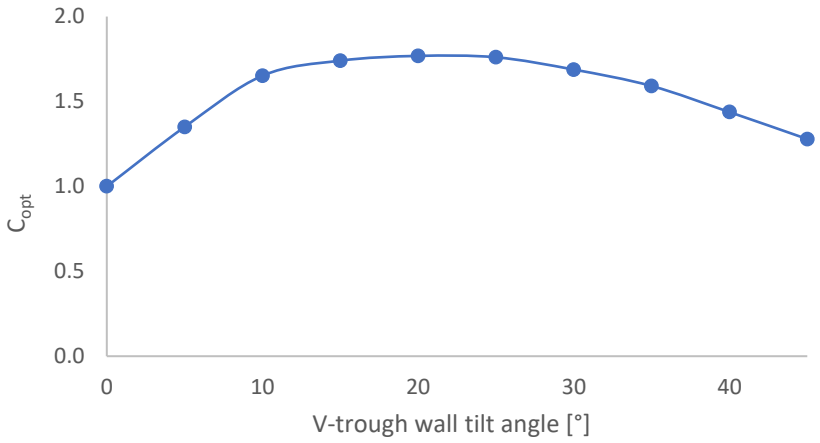

Figure 6.32. C_{opt} of V-trough concentrator at 0-30° angles of incidence

This was used to perform a deeper analysis with more rays and smaller V-trough step sizes. V-trough configurations [15, 16, 17, 18, 19, 20, 21, 22, 23, 24, 25] ° were modelled under 0-30° angles of incidence at 20x resolution. These are tabulated in Table 6.2 with both the average C_{opt} and the peak C_{opt} (at 0° angle of incidence). Most literature presents the value we consider *peak* C_{opt} when talking about the properties of concentrators.

Figure 6.33 presents the results in graphics form on a scatter plot with dual y-axes. The results show the average optical concentration ratio peaks in the 21-23° region with the maximum point at 22° although the difference require four decimal points of differentiation. When considering the peak performance of V-trough concentrators, the differences are more extreme. By peak performance metric, best performance is achieved by the 21° V-trough concentrator. Its performance is higher by 1.17% than the second best performing V-trough, namely the 22 ° V-trough. Which one to use depends on the angle of acceptance which would be of interest for each individual project. Furthermore, it is seen that the answer to the question "which the

best performing V-trough configuration is?" is one with many answers depending on the use case. If for example, a 2-axis tracking system exists that precisely follows the sun, then the best Peak V-trough configuration (21°) would be advised. For this project, it is assumed that the BIPV systems have no tracking; we also consider the peak solar radiation at 10am-2pm. As such the best configuration is deemed to be the 22° V-trough.

Table 6.2. High-resolution results for 15-25 ° V-trough configurations at 0°-30° angles of incidence

V-trough	Avg. C_{opt}	Peak C_{opt}
15	1.7748	2.0718
16	1.7751	2.1470
17	1.7763	2.2229
18	1.7780	2.2997
19	1.7801	2.3773
20	1.7827	2.4559
21	1.7851	2.5355
22	1.7855	2.5062
23	1.7851	2.4011
24	1.7845	2.3387
25	1.7813	2.2865

6.2.1. 22 ° V-trough Concentrator

- Height: 50mm
- Absorber width: 25 mm; Aperture width: 65.4 mm
- Geometric Concentration Ratio C_r: **2.616**
- Optical Concentration Ratio C_{opt}: Average: **1.786**; Peak: **2.506**

Figure 6.34 shows the ray trace diagrams at various angles of incidence ranging from 0° to 45°. We can see that at 0°, there is still a small number of rays leaving the system, roughly 4%. The wave-front is superseded by a series of red points leading the rays. As such, the red dots covering the absorber area on the ray trace diagram represent accepted rays which have successfully hit the absorber. The accepted rays are well distributed and inversely correspond to a growing number of rays leaving the V-trough as the angle of incidence increases.

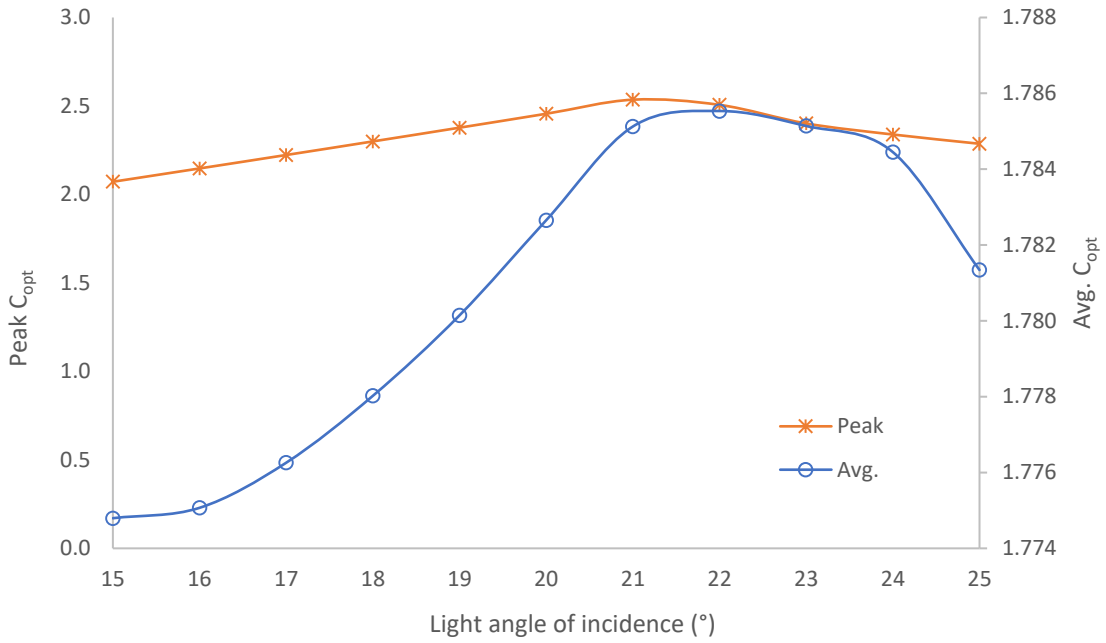

Figure 6.33. High-resolution results for 15-25 ° V-trough configurations at 0°-30° angles of incidence. Peak C_{opt} uses main y-axis, average C_{opt} uses secondary y-axis.

At 25° angle of incidence there is a gap present in the left-side of the V-trough absorber area. Simultaneously there is a small section of rays leaving in the opposite direction of the typical rejected rays. As the angle increases beyond 25°, the left-hand side of the absorber area becomes more bare as less and less light reaches the region. The number of opposite-directed rays also increases proportionally until ~35° where the number of rays leaving in the opposite direction overtakes the original rejected rays. At 40° and 45° very little to no light is accepted in the concentrator.

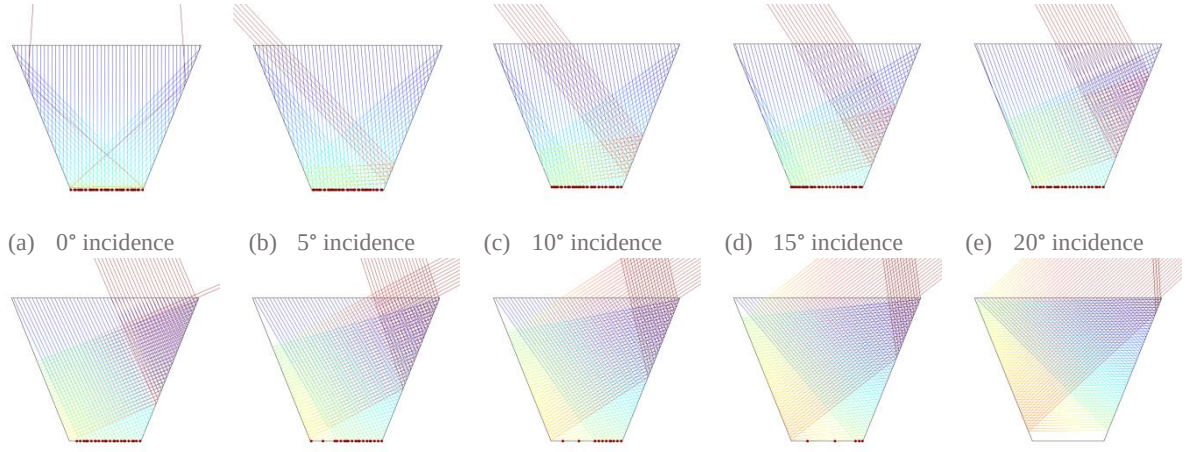

Figure 6.34. Ray trace diagrams for 22 ° V-trough at various angle of incidences

Figure 6.35 shows the ray acceptance of the V-trough concentrator. The acceptance starts at below 100% acceptance rate with a gradual linear decline to 0% acceptance at ~43° light incidence. 21° V-trough is the final model which starts at 100% acceptance. A secondary plot of C_{opt} is overlaid with its vertical axis on the right-hand side.

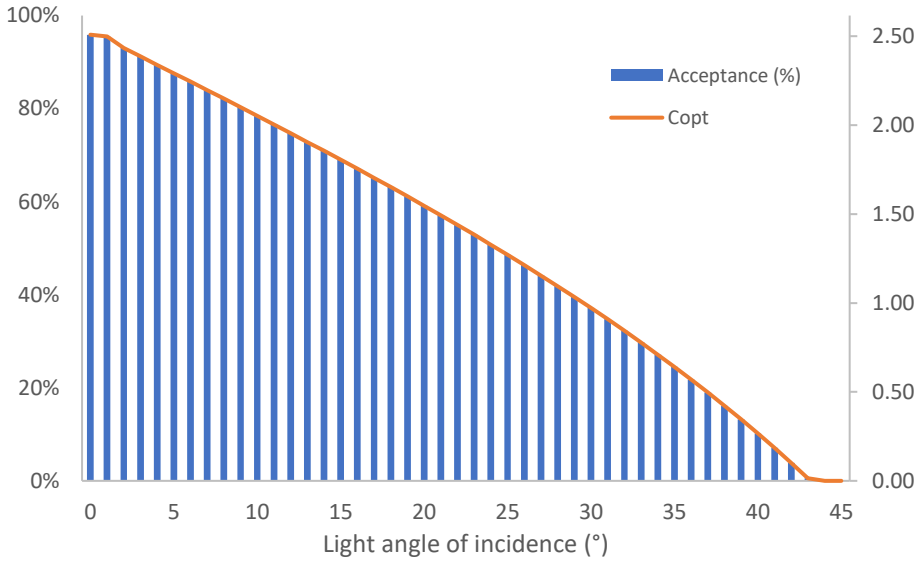

Figure 6.35. Ray acceptance for 22° V-trough concentrator under various light incidences (0-45°)

Figure 6.36 presents the solar radiation flux concentrations on the absorber width at a selection of inlet light angles of incidence. There is perfect uniformity at 0°, with 15° exhibiting a higher concentrated region on the left-side of the absorber and vice-versa at 30° light incidence.

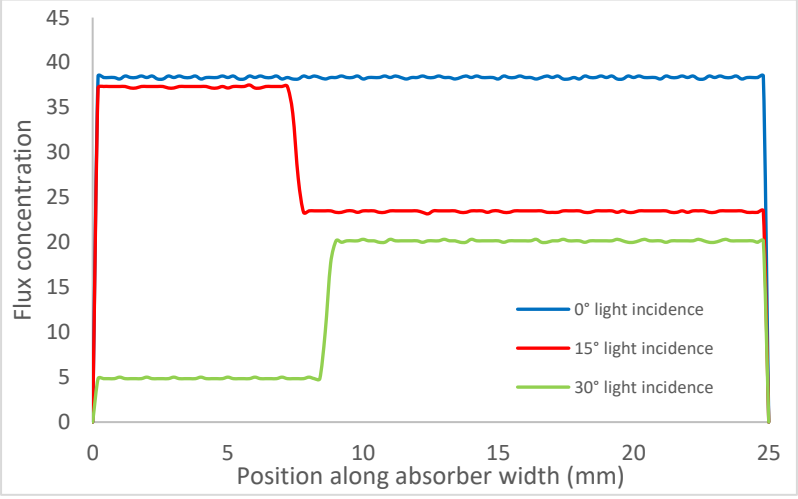

Figure 6.36. Energy flux distribution for 22 ° V-trough at 0°, 15° and 30° inlet light incidences

6.3. Comparison of CPC and V-trough concentrators

Figure 6.37 presents the performance of full and truncated CPCs and the selected V-trough by plotting the C_{opt} as a function of the inlet angle of incidence. The difference here is that whilst all the CPC variants have 100% acceptance rate at 0° light incidence, their final C_{opt} is still different due to their geometric concentration ratio (C_r).

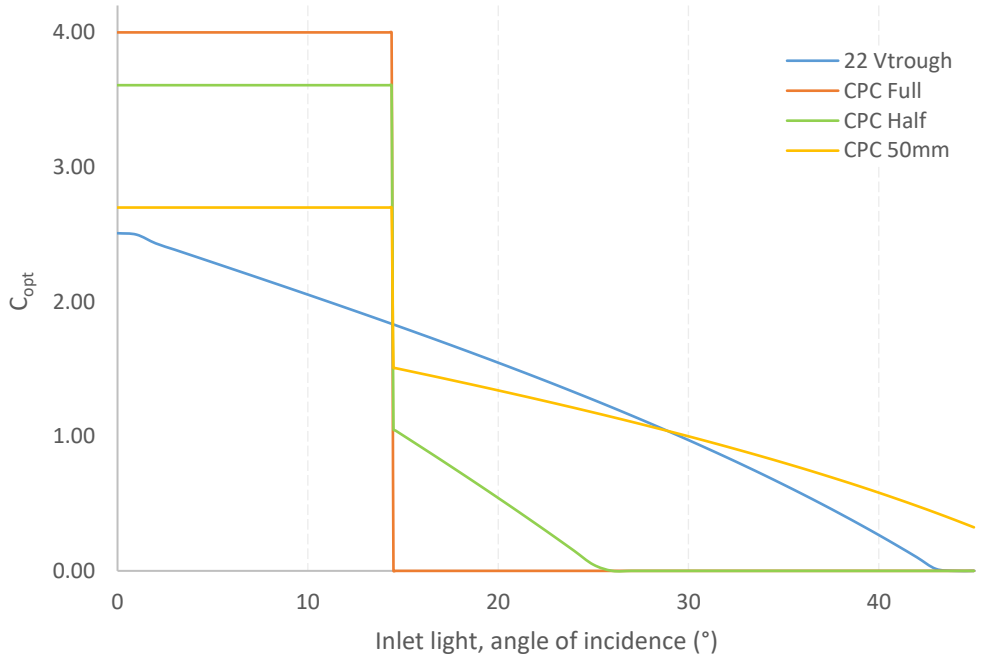

Figure 6.37. Acceptance rate of V-trough concentrator and CPC at various truncations

Figure 6.37 shows that as the CPC is truncated, the optical concentration is reduced, however, the reduction in concentration is far below the truncation, i.e. a 50% truncation only reduced the C_{opt} by 10%. In addition, beyond the traditional acceptance angle, the truncation causes a significant improvement in performance. In effect, the truncated half and 50 mm CPC begin to show *V-trough-like behaviour*. They start to exhibit a gradual linear decline over many angles of incidence. This makes the truncated 50 mm CPC ideal for non-tracking systems required for BIPVs.

The 22° V-trough concentrator was chosen as the candidate for BIPV integration. This was following a thorough analysis of all V-trough configurations with reflector tilt angles from 0-45°. The 22° V-trough presented the best performance during the 4-hour peak production time of 10am – 2pm.

Comparing the 50 mm CPC and 22° V-trough, prior to 14.48°, the truncated CPC shows a greater performance than its counterpart V-trough. At 14.48° the sharp drop in performance

puts the 50 mm CPC below the V-trough, however, the gains of the V-trough between 14.48° and ~30° where their performances re-converge is not enough to overcome the amount the V-trough was lagging. Beyond 30°, the 50 mm CPC again overtakes the V-trough due to the lower gradient of loss. Overall, even when considering up to 30° angle of incidence (the peak 4-hour period), the CPC has 9.4% performance improvement on the V-trough. If larger angles of incidence are taken into consideration, the 50 mm CPC will further its gains, as shown in Figure 6.37, even at 45° angle of incidence the CPC is still accepting light.

The performance is reversed when considering the local energy flux concentration distribution. Figure 6.38 shows the local flux concentration along the absorber area for 0° light angle of incidence. The V-trough has a very good distribution represented by a horizontal line from end to end. All variants of CPCs show non-linearity and non-uniform distributions with peaks, particularly at 10 mm and 15 mm positions, on the absorber. The higher the truncation, the larger is the peaks magnitude.

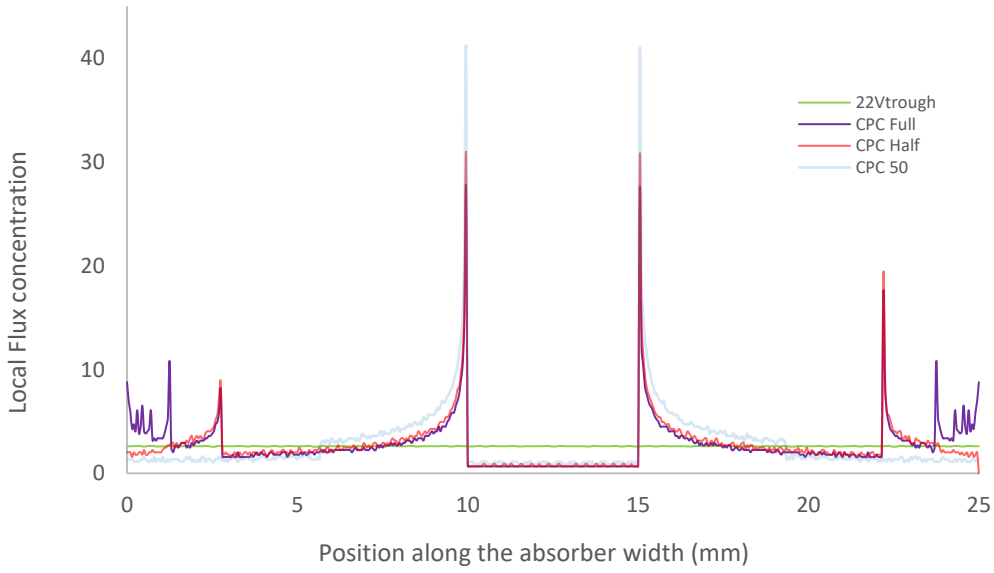

Figure 6.38. Flux concentration distribution of V-trough and CPC at 0° angle of incidence

It should be noted that the flux concentration distributions in this section are no longer relative but present the absolute local concentration factor for each concentrating device. This means at the local flux concentration of 40, the local absorber position is receiving $40x$ the radiation entering the aperture. This transformation allows better comparison between the concentrators.

Figure 6.39 presents the local flux concentrations at 10° light incidence. There CPC devices show a shift to the left of the local flux concentration highs with peaks having risen, meanwhile

the V-trough is still relatively more uniform in distribution, although there are now two tiers of intensity, with a high region of 3.11 local concentration from position 0 mm to ~13 mm and a low region of 2.06 concentration from 13 mm to the right edge (25 mm).

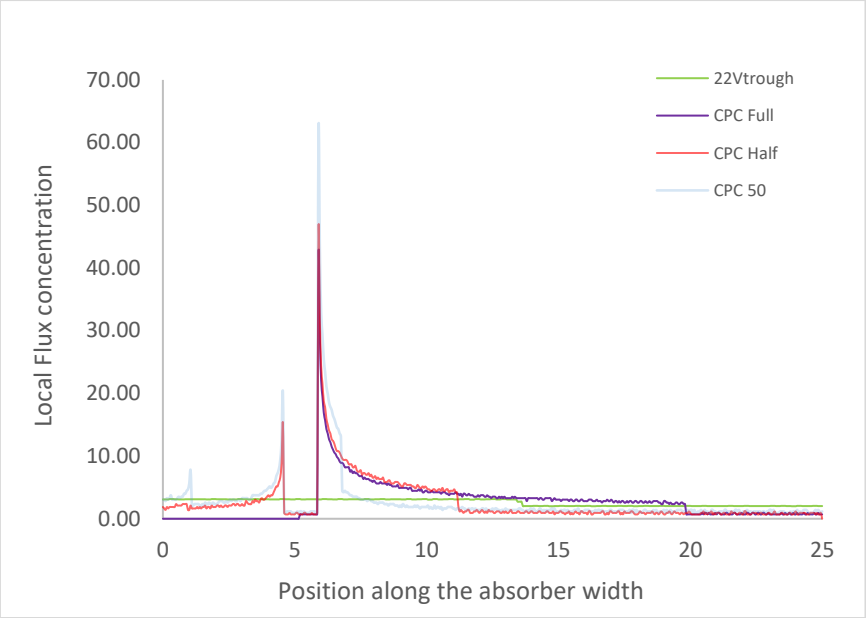

Figure 6.39. Flux concentration distribution of V-trough and CPC at 10° angle of incidence

Figure 6.40 presents the local flux concentration data for 20° light incidence. At this point, the full CPC now has 0 acceptance and hence shows zero flux distribution along the absorber. The half CPC shows a low-lying region at ~12 mm onwards. The V-trough and 50 mm CPC graphs overlap for the most part (~2.5 mm-25 mm). This reinforces the findings that the truncation causes V-trough like behaviour in the CPC systems beyond the acceptance angle. There is still a peak in the region where the V-trough similarly shows a rise, although the V-trough has a steady high-lying region whereas the CPC has an intense peak at ~2 mm which tapers off to the left edge of the absorber.

Finally, Figure 6.41 shows the flux concentration distribution at 30° light incidence. The only two concentrators still operating are the V-trough and 50 mm CPC systems. Their behaviour is also very similar; they both have a low left region and a high right region. The CPC shows zero local flux concentration at 0-7 mm whereas the V-trough shows a small concentration of ~0.9 up to ~8.5 mm position after which it gains to 3.5 concentration up to the right edge.

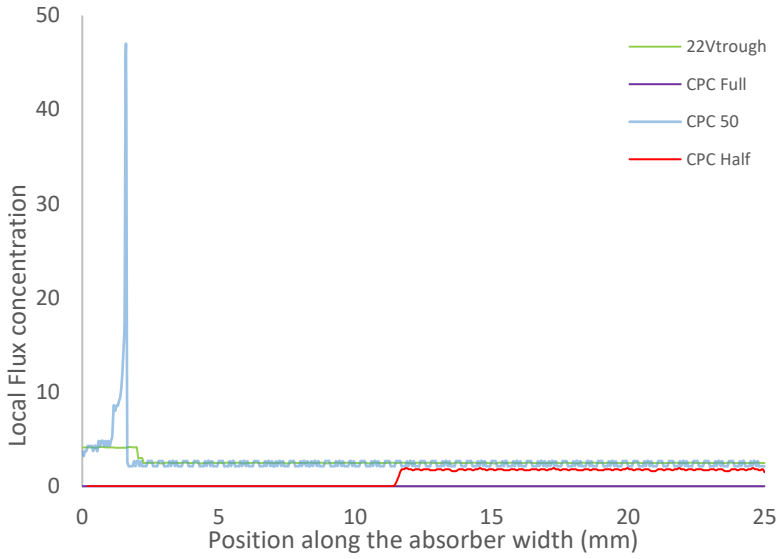

Figure 6.40. Flux concentration distribution of V-trough and CPC at 20° angle of incidence

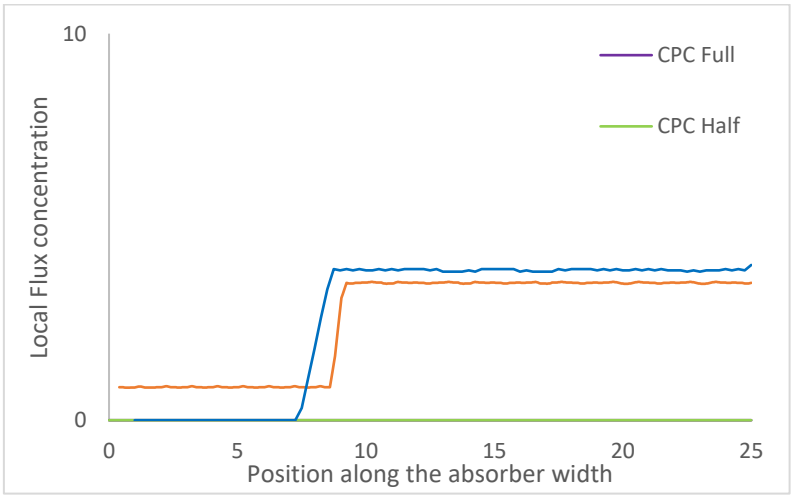

Figure 6.41. Flux concentration distribution of V-trough and CPC at 30° angle of incidence

6.3.1. Summary

In summary, the 50 mm CPC concentrator designed for BIPV shows a greater overall concentrating performance, with significantly improved concentration up to the acceptance half angle, a small loss compared to the V-trough from the acceptance half angle to around 30° light incidence, and again an improvement over the V-trough from ~30° onwards. All truncated CPCs also show V-trough-like behaviour past their acceptance angles, making them suitable for BIPV incorporation. On the other hand, the V-trough concentrator showed better uniformity of flux distribution, this was especially pronounced at lower light angles of incidence.

6.4. 3D Model

Three dimensional studies were also performed on CPC and V-trough concentrators for BIVP application. There are four notable benefits to implementing the 3D models: firstly, the flux distribution along the length of the concentrator can be analysed. Secondly, solar radiation is measured in W/m^2 which is a 3D phenomenon, COMSOL Multiphysics light intensity and power computation only gives legible results on 3D analysis. Thirdly, the concentrators can be analysed under light conditions with direction vectors composing of an additional (z-dimension) component. Finally, the 3D model is a precursor to future work implementing a coupled optical-thermal Multiphysics model in COMSOL.

The results are shown in Figure 6.42 and Figure 6.43. As predicated in 2D models, the V-trough shows much better uniformity of flux distribution on the absorber plate whilst the CPC shows variation on the left and right edges.

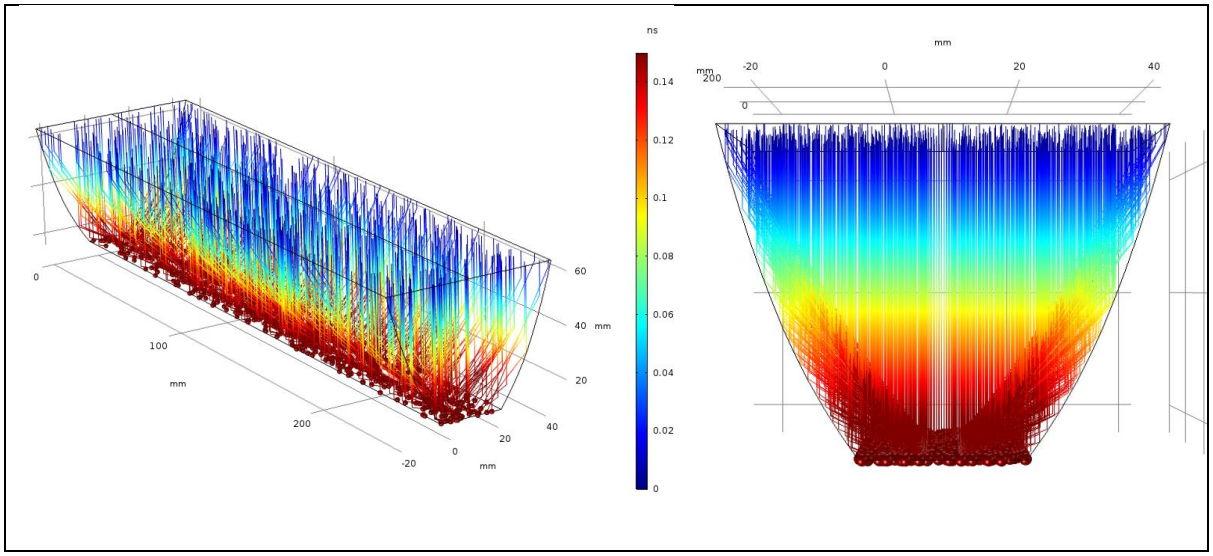

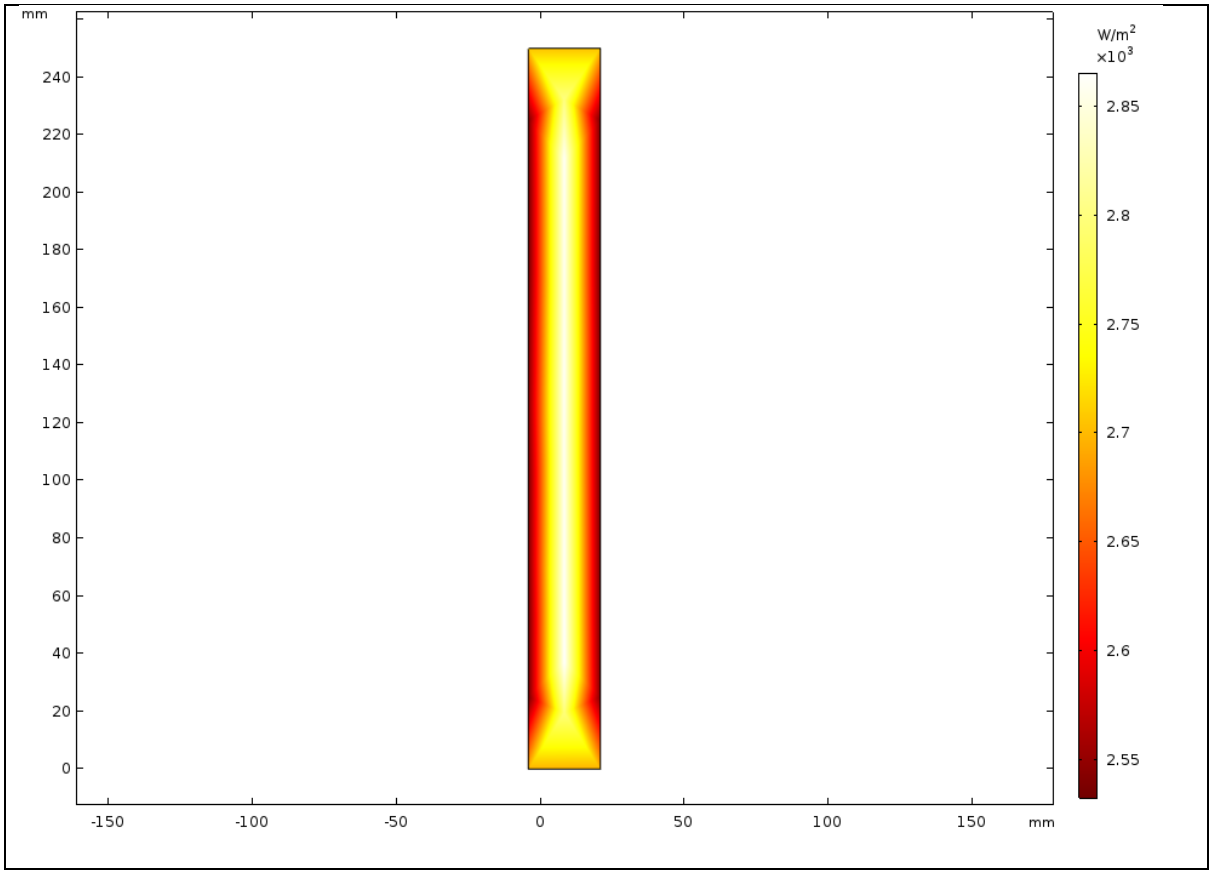

Figure 6.42. 50mm Truncated CPC 3D Analysis under 1000 W/m2 Illumination

There are two

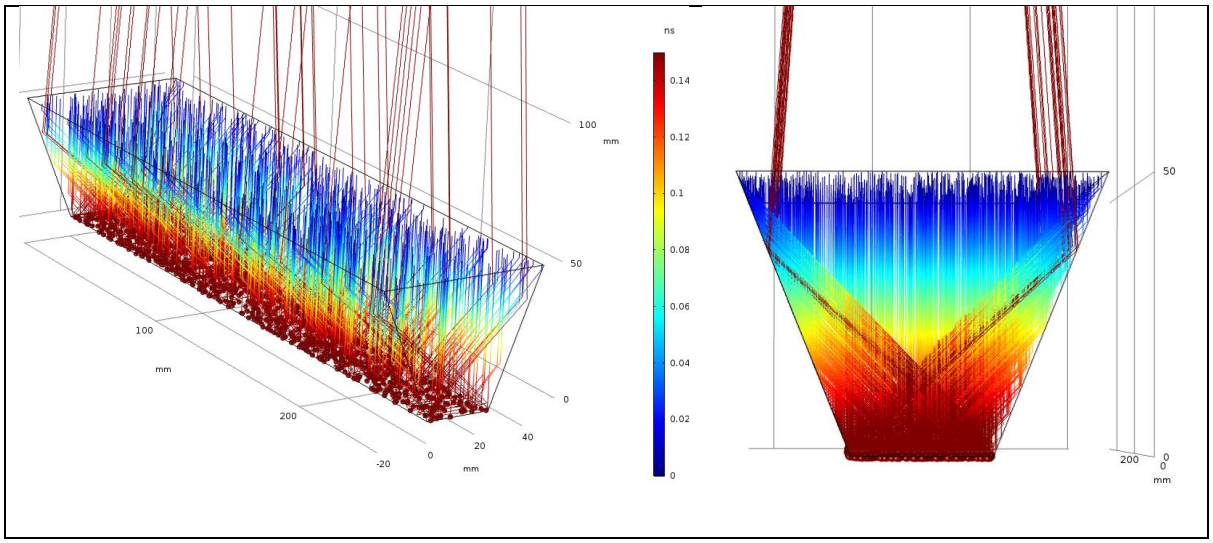

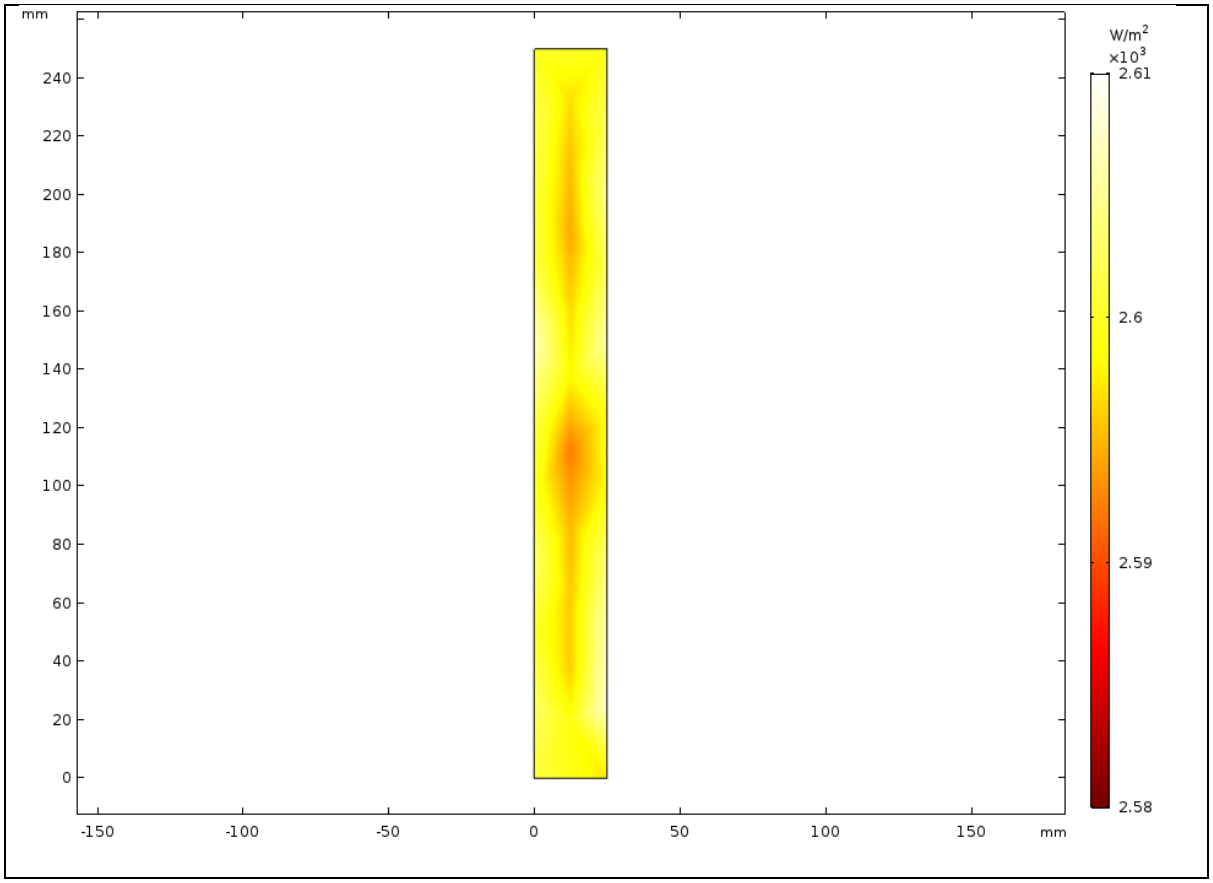

Figure 6.43. 22[Deg] V-trough 3D Analysis under 1000 W/m2 Illumination

6.5. Experimental results

In this section the experimental results for flat-plate (1x concentration), 50mm CPC and 19° V-trough concentrators are discussed. As the fabrication process was performed simultaneous to the modelling work, the V-trough configuration was chosen according to the literature review. For this reason, whilst 22° has been identified as the best performing BIPV V-trough candidate from the outcome of this thesis, 19° side-wall angle was made. On the other hand, the loss in performance is 0.3% average and 5.4% peak.

A 2401 Keithley SMU was used to perform an I-V sweep on the cells at various conditions. Figure 6.44 shows an I-V curve measured from a flat plate mono-Si solar cell under dark testing conditions. Dark testing refers to very low to zero light exposure. The P-V curve is overlaid with its secondary y-axis to the right. The peak power point is the voltage (V_{mp}) and current (I_{mp}) at which maximum power can be obtained from the cells. The y-intercept of the I-V curve is the short circuit current (I_{SC}) and the x-intercept is the open-circuit voltage (V_{OC}).

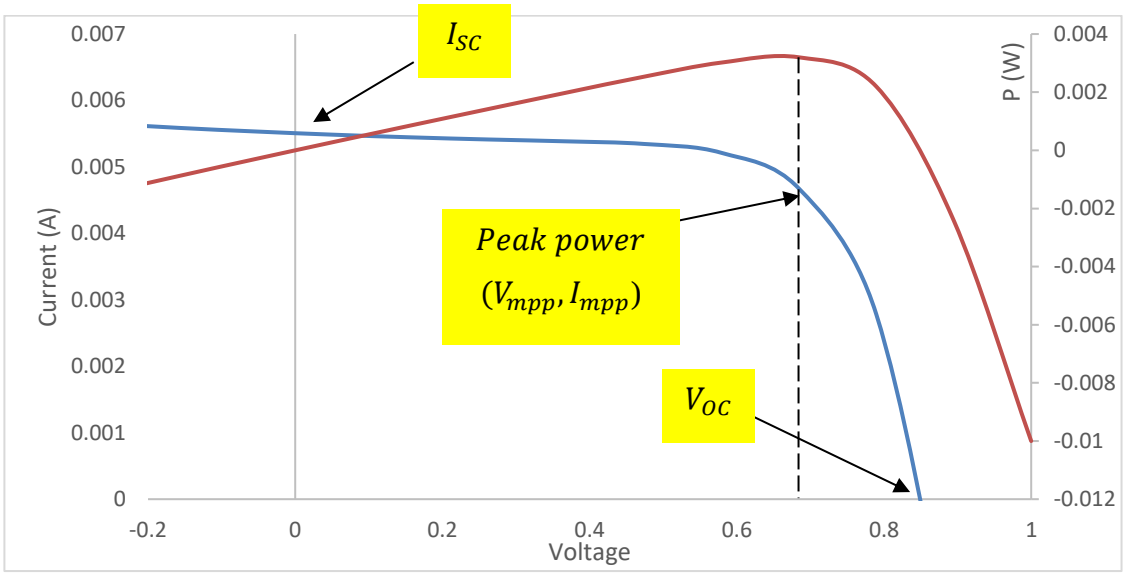

Figure 6.44. I-V curve (blue) and P-V curve of solar cells under dark condition

6.5.1. Cooled vs. non-cooled

As is the case with most electronic devices, the performance of solar cells, which are reverse diodes in effect, varies with temperature. In general, an increase in temperature leads to a decrease in power output of the cells. Based on the work of Varshni [173], the band gap energy changes as a function of temperature based on the equation:

$$E_g(T) = E_g(0) - \frac{\alpha T^2}{T + \beta} \tag{6.1}$$

$E_g(T)$ is the bandgap of the semiconductor and $E_g(0)$ is the bandgap of the semiconductor at 0 Kelvin. α and β are material constants. According to Eq. (6.1) as the temperature rises, the bandgap becomes smaller. This has two effects: first the short circuit current of the solar cell increases as T is increased due to the rising possibility of photon absorption [174] (narrowing gap required for e-h pair generation means photons with lower energy are absorbed). Conversely a reduction in Voc occurs due to the reduction in junction potential and in efficiency as the silicon band gap distances further from the optimum 1.35eV for one sun AM1.5G spectrum. Other effects include the decreasing mobility of electrons with temperature due to atom vibrations and the dependence of the Shockley Read Hall (SRH) recombination and lifetime to temperature.

Ponce-Alcántara et al. [175] performed an experimental study of the effect of temperature variation with the performance of silicon solar cells. They presented the effect of temperature as a temperature coefficient (CTP_{mpp}) with the power output defined as follows:

$$P_{mpp} = P_{mpp}(25°C) \cdot (1 + CTP_{mpp}(T - 25°C))$$

The temperature coefficient for c-Si was reported at ~ -0.45%$/°C$.

Experimental studies were carried out considering the effects of cooling on LCPV performance. The readings were taken as close to solar noon (i.e. 0° angle of incidence) as possible. Unless otherwise stated, where time recordings vary from standard time-reading slots, an allowance was made for skies to clear to make results more comparable.

Table 6.3 presents the results of the CPC concentrator with the cooling pipe turned on and off. Solar noon on the 20th September occurred at 12:53 pm local time.

Readings from the pyranometers were converted from mV to W/m^2 based on the pyranometers' specifications. One pyranometer was certified at 60.5 µV/W/m^2 whilst the second was rated at 80.2 µV/W/m^2. The lower of the two was moved to the direct beam + diffuse radiation due to the Pico TC-08 data logger's limitation in taking readings up to a maximum of $\pm 70mV$. This caused failure of data readings when solar radiation was too high as the 80.2 µV/W/m^2 pyranometer would output expected voltages of up to $80.2 \times 1100 = 88.22\,mV$. The same irradiance would only produce $60.5 \times 1100 = 66.55mV$ output, well within the Pico TC-08 datalogger range. 1100 W/m^2 was the top end of measurements, with most recordings well below such level.

Table 6.3. CPC under cooled and non-cooled conditions 20th Sept 2017

TIME (LOCAL)		CONC	TEMP(°C)	I_{sc}	V_{oc}	P (W)	DIRECT+DIFFUSE (W/m^2)	DIFFUSE (W/m^2)	DIFFUSE (%)
12:45	Cooled	CPC	32.32	1.61	1.2	1.932	1102.61	104.31	9.5%
12:45	Heated	CPC	63.22	1.42	1.2	1.704	1102.61	104.31	9.5%

Results show the non-cooled CPC operates at -12.44% power output (W) due to a temperature rise of 30.9 °C. This translates into a temperature coefficient of -0.40%/°C. Figure 6.45 presents the I-V (and P-V) measurements for cooled and non-cooled CPC concentrator.

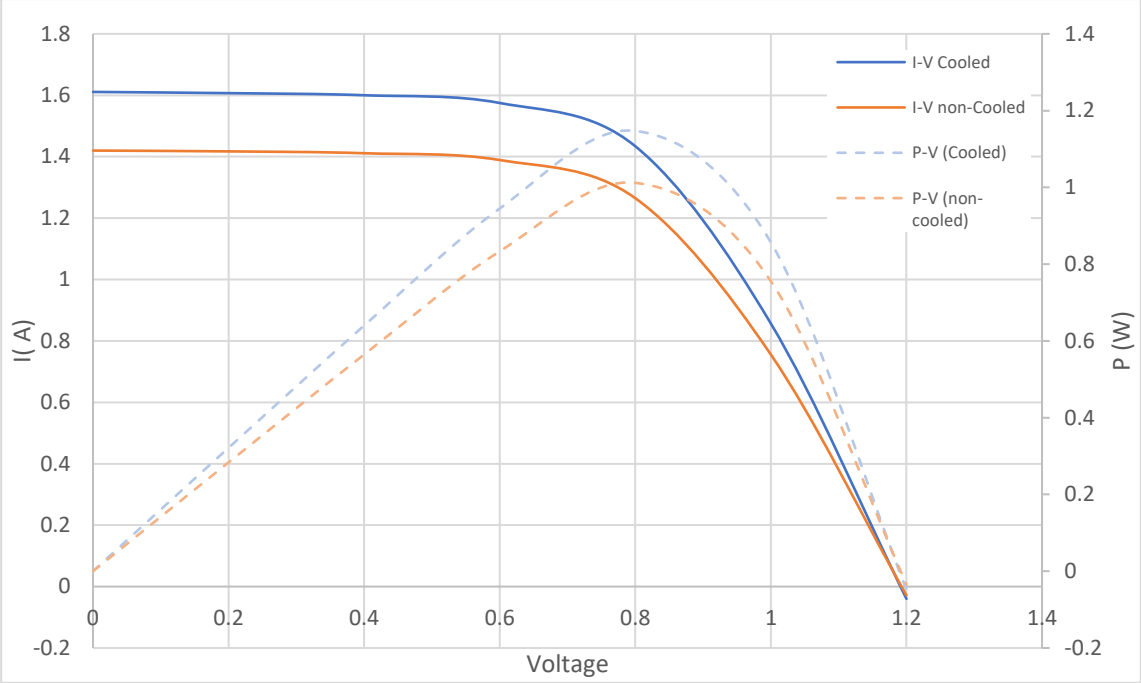

Figure 6.45. I-V and P-V curves of 50mm CPC with and without active cooling

6.5.2. Concentration ratio vs. angle of incidence

The CPC and V-trough concentrators were positioned vertically. This meant the angle of light incidence would vary based on time with the sun moving 15°/hour from East to West. The concentrators were positioned facing due south exactly, using a compass. The tilt angle of the V-trough and CPC concentrators were manually adjusted to the altitude of the sun using the solar projection created by the concentrators on the solar cell: at perpendicular to the sun the concentrator light would start at one edge of the absorber solar cell and end exactly on the other edge of the cell (250mm apart). The sun's position relative to the solar cells is based on two angles, the solar altitude and the azimuth angle (Figure 6.46). When positioned correctly the azimuth angle will represent the light angle of incidence.

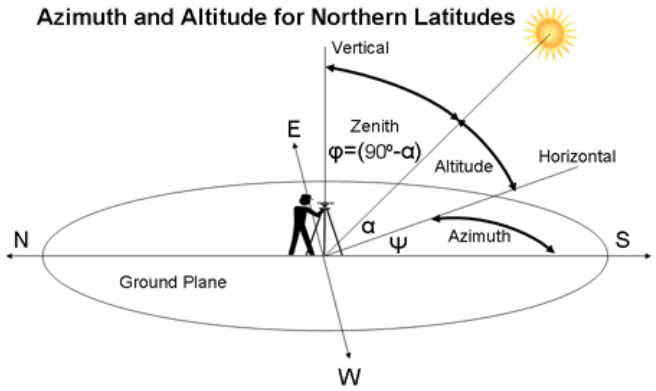

Figure 6.46. Azimuth and Altitude (courtesy of http://www.mpoweruk.com/solar_power.htm)

The local time was converted to solar time to find the solar noon. The table of local time to solar time is provided in the appendix A for the months of September and October 2017, during which experimental measurements were taken. It should be noted that due to daylight saving time, the clocks shifted 1 hour on the 29th October, this is noted on the appendix table.

Figure 6.47 shows the experimental data collected on the 20th Sept 2017, presented due to the clear skies on the day and good solar irradiance. Orange (diffuse) data was collected with a shaded pyranometer, blue (direct) data was total irradiance taken with pyranometer on plane of concentrator with diffuse radiation deducted.

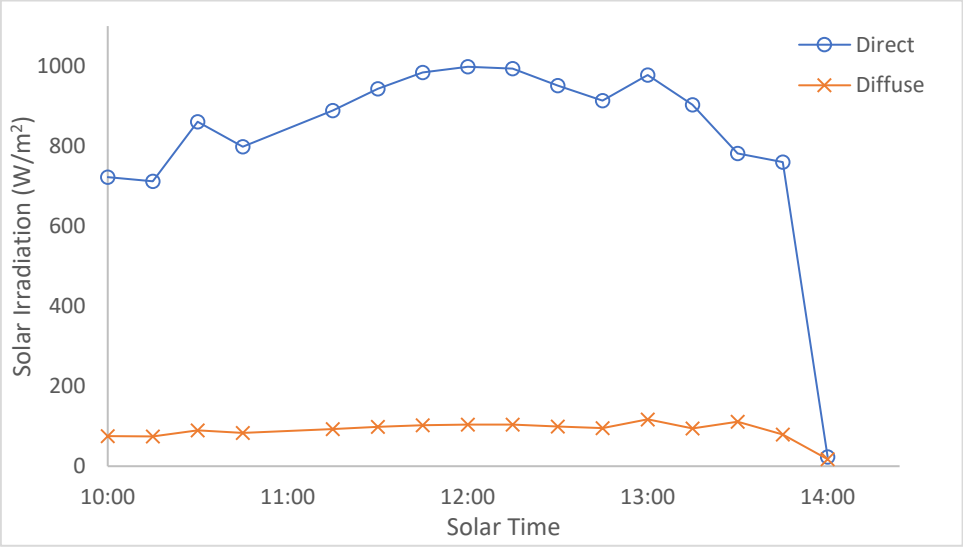

Figure 6.47. Direct and diffuse solar radiation 20th Sept 2017

The diffuse radiation typically accounted for around 9.5% of total solar irradiance. This number shoots up when there is cloud coverage or shading for other reasons, for example at 14:00, diffuse radiation accounted for 43% of total irradiance.

Figure 6.48 shows the power output of the CPC concentrator overlaid on the solar irradiance for that period.

It is clearly noticeable that whilst there is some loss of irradiance on either side of solar noon, the drop-in performance of the CPC is far sharper. This is because of shading and optical efficiency of the concentrator as the angle of incidence is increased.

This can be compared to the flat plate solar cell (non-concentrator) shown in Figure 6.49. Even though the power output is lower, the drop-in performance at higher angles of incidence is significantly lower. The power output generally correlates with the solar irradiance.

Figure 6.50 presents data collected for the V-trough concentrator under the same conditions. The results are somewhat similar to CPC, there is a faster-than-irradiance drop on both ends of the graph. The data is more chaotic, unlike the CPC which had a more consistent performance within its acceptance angle.

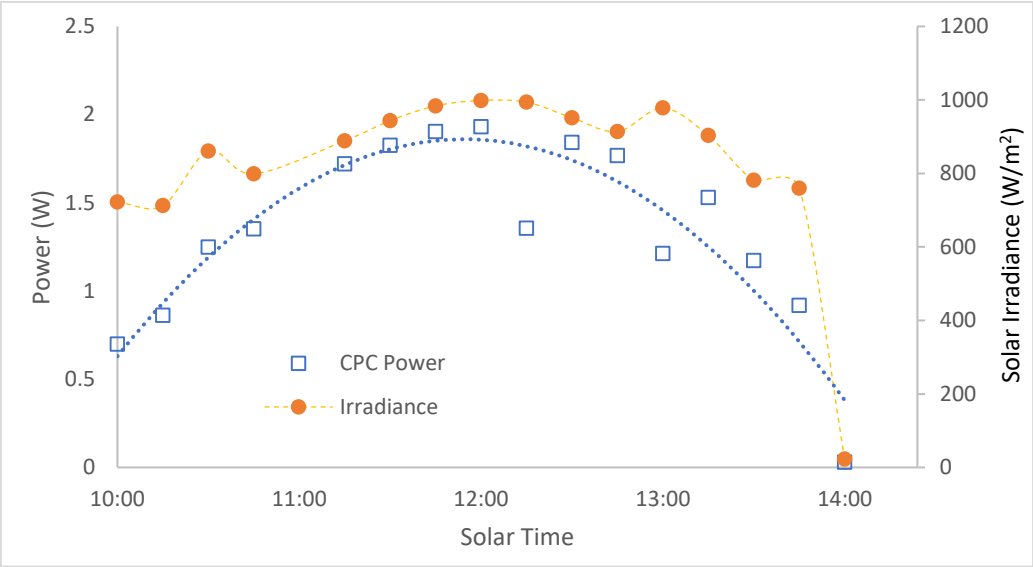

Figure 6.48. Power output and solar irradiance for CPC for period 10:00 to 14:00 solar time

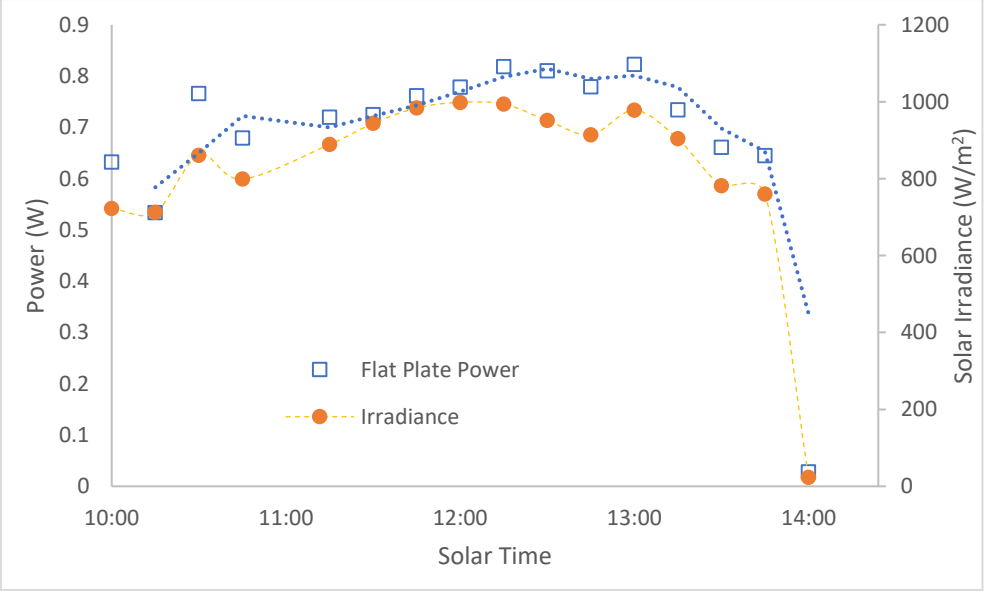

Figure 6.49. Power output and solar irradiance for flat plate solar cell for period 10:00 to 14:00 solar time

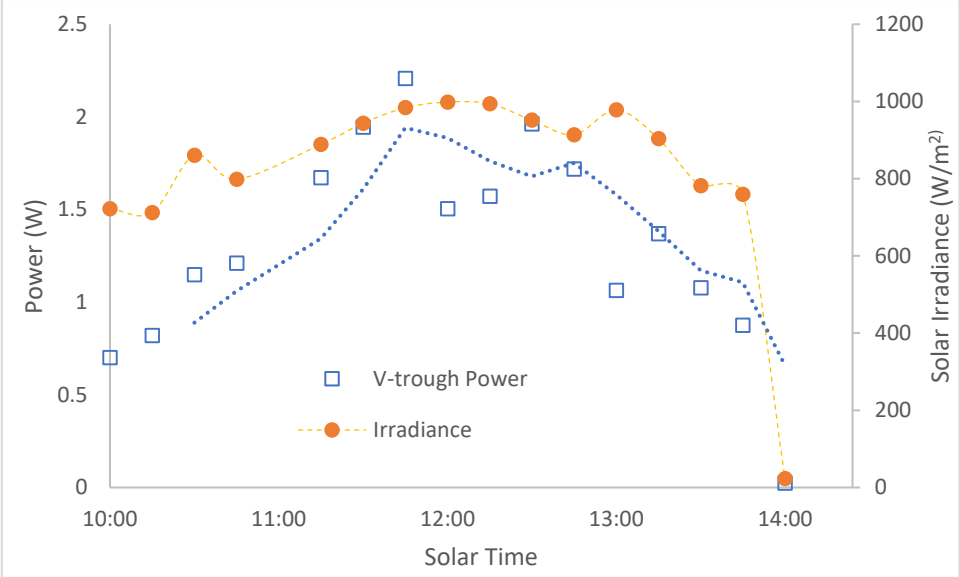

Figure 6.50. Power output and solar irradiance for V-trough concentrator for period 10:00 to 14:00 solar time

6.5.3. I-V Curve abnormalities

During result analysis, some I-V curves did not return expected data. An example I-V curve is shown for V-trough at 14:30 (37.5° angle of incidence) in Figure 6.51. The I-V curves had bad ideality factors, it behaved as though it was affected by bad series resistance. However, as the conditions of the cell returned to default values (lower intensity and smaller light incidence angles), the I-V curves would again return to normal as well. This ruled out physical damage to the solar cells. This was also not limited to V-trough, the CPC showed similar behaviours (Figure 6.52).

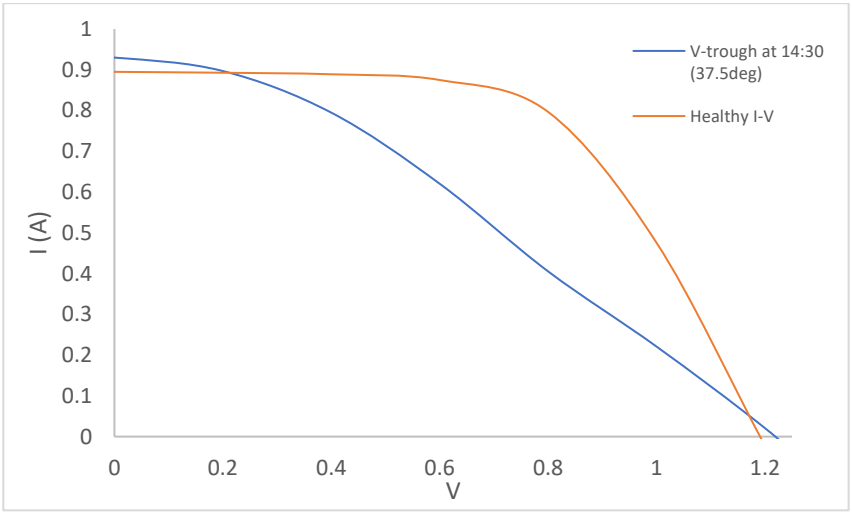

Figure 6.51. I-V curve for V-trough collected at 14:30 vs. typical I-V curve

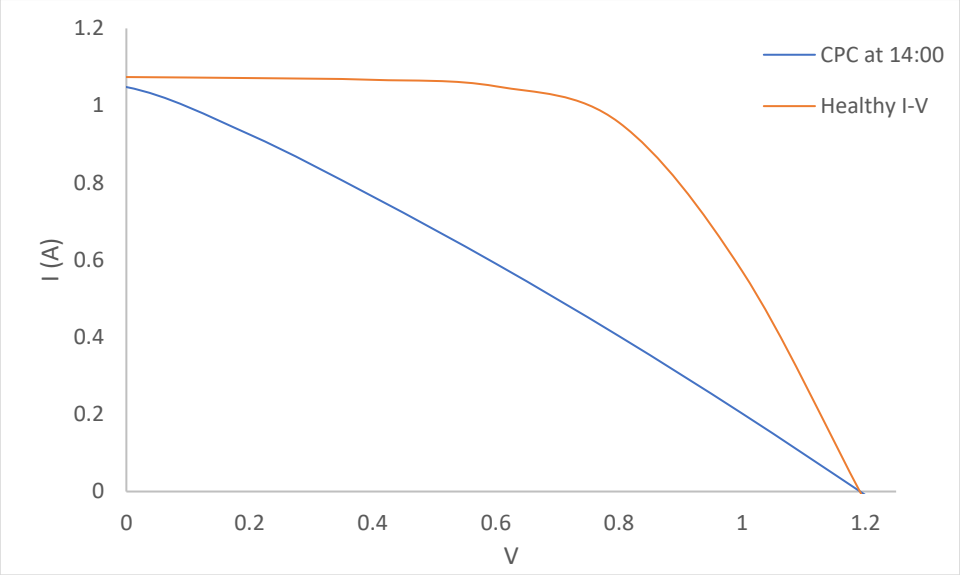

Figure 6.52. I-V curve of CPC at 14:00 (30deg) vs. typical I-V curve

In investigating the issue, in order to determine if an error has occurred in measurement, damage to the cell has happened or other reasons which would explain the loss, the author came across a paper by Saad et al. [176] looking at the effect of shading. I-V curved for PV panels under shading shows behaviour similar to the anomalies recorded. Figure 6.53 shows one of their I-V curves for panels under shading. The *curve* is flattened on both the horizontal and vertical elements.

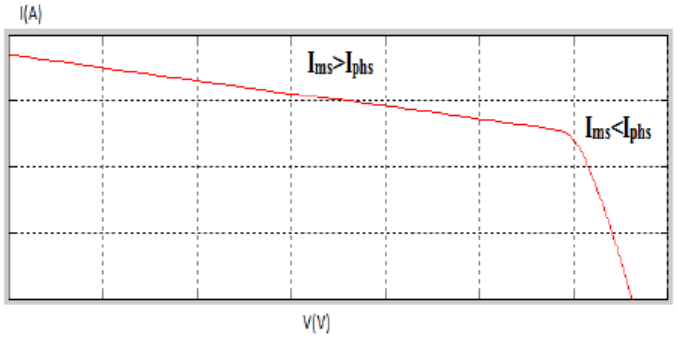

Figure 6.53. I-V curve for PV panel under shading [176]

The author believes one reasonable cause for non-ideal I-V curves is the effect of *localized shading* due to the distribution of solar flux on the absorber width. It was shown in modelling that at high angles of incidence, both CPC and V-trough, though to varying degrees, had regions with big peaks of solar radiation and regions with little to no solar radiation. This would also explain why the I-V curves showing un-ideal behaviour present themselves at high angles of incidences.

6.6. Comparison and Conclusion

For comparison, experimental data was normalized for angle of incidence and power. The CPC and V-trough model results were also overlaid as shown in Figure 6.54. The model output was converted to power using by considering the system's real power conversion efficiency and optical efficiency based on:

$$Power\ (W) = T_{glass} \times R_{spec} \times \eta$$

Where T_{glass} is the glass transmittance, set to 100% for comparison to experimental, R_{spec} is specular losses of the Alanod reflector sheets (92%) and η is the solar cell power conversion efficiency set at 15%.

Results showed good correlation between the experimental measurements and modelling results. The CPC measurements showed linear power output for ~$\pm$15% light angle of incidence, in line with model results of the CPC acceptance angle. The V-trough measurements showed a near linear drop with respect to light angle of incidence in both negative and positive light angle of incidence direction. This was again in good corroboration with the model predictions. On average the CPC showed a 2.38% higher power output than V-trough. This was lower than predicted by the models. The most likely cause of this is the increased energy flux non-uniformity of the CPC concentrators.

Similar studies carried out by Singh et al. [177] also showed that for the V-trough and CPC systems with the same geometrical concentration ratio, the V-trough concentrator had an electrical power output up to 17.2% higher than the CPC system at a specific tilt angle of 30° and the V-trough had a consistently higher receiver plate temperature as it was reflecting larger quantities of solar radiation than the CPC. Redpath et al. [178] also showed that the CPC-PVT had a lower thermal efficiency than the flat plate PVT with a heat removal factor of 0.488 compared to 0.638.

However, results from this study showed a better performance of CPC compared to V-trough. This could be down to geometric optimisations performed using COMSOL, leading to a better prototype design. Another difference is that the CPC fabricated in this study was smaller in scale for BIPV integration, e.g. the absorber width was 25mm compared to Singh et al. [177] absorber width of 125mm, this acts in reducing disparity in the flux distribution due to the side walls being closer together on the CPC.

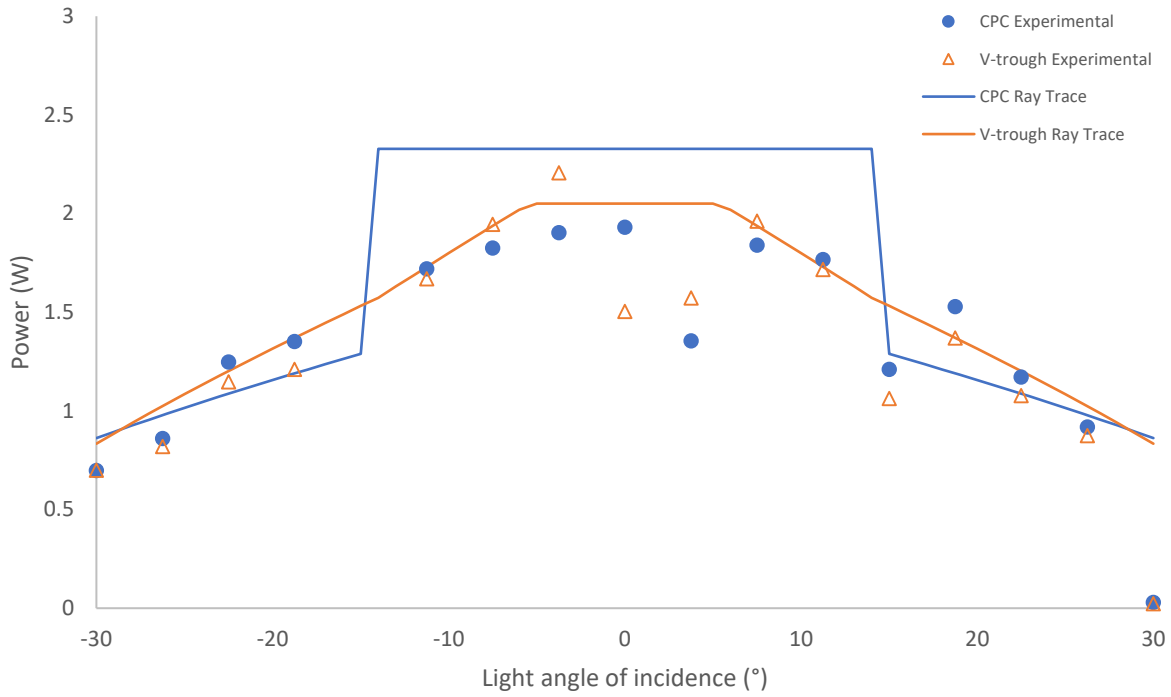

Figure 6.54. Experimental vs. modelling comparison of CPC and V-trough concentrators over various light angles of incidence

6.7. Cost Benefit Analysis

The cost-benefit of the CPV system is dependent on the added expense of the reflector walls (cost) and the improvement provided by the concentration (benefit).

A monocrystalline silicon panel based on the bulk purchase pricing from DAH Solar China has the following product details:

Model: DHM72-335w
Max. Power: 340 W
Efficiency: 17.28%
Size: 1956 x 991 x 40 mm

The cost is \$0.25-0.35/W. Assuming an average price of 0.3\$/W leads to:

$$Solar\ Cell\ Area = 1.956 \times .991$$
$$= 1.938\ m^2$$

$$Price\ of\ module = 0.3 \times 335$$

$$= \$100.50$$

$$\boldsymbol{Price\ (\$/m^2) = 51.85}$$

The reflector walls are brushed laminated aluminium. Pre-treated, pre-laminated sheets of 0.4mm thickness aluminium reflectors are supplied by FastArriver (China) priced at $2300/Metric Tons. The price in *$/m²* can be calculated as follows:

- Price/Tonne ($): 2300
- Aluminium Density: 2710 kg/m3
- Thickness (mm): 0.4
- Thickness (m): 0.0004
- Mass of 1m² x 0.4mm thickness: 1.084
- **Price *($/m²)* = 2.49**

Hence 1m² of solar cell is priced at $51.85 and 1m² of the reflective aluminium material costs $2.49. As such the breakeven cost of the CPV system is reached when $\frac{51.85}{2.49} = 20.80$ times the area of aluminium is used **per concentration factor** provided by the system. The COMSOL models were used to measure the lengths of the reflector and absorber (solar cell). These were used to calculate the ratio of *reflector* to *solar cell* presented in Table 6.4.

Table 6.4. Cost benefit of CPC systems

Concentration Ratio (Cr)	Absorber (mm)	Walls (mm)	Walls x 2 (mm)	Walls/Absorber ratio	Breakeven Ratio
2	25	65.74	131.48	5.3	20.8
3	25	144.8	289.6	11.6	41.6
4	25	247.9	495.8	19.8	62.4
5	25	375.2	750.4	30.0	83.2
6	25	527.2	1054.4	42.2	104.0
2.70 (50mm Truncated CPC)	25	54.68	109.36	4.2	35.3

The terms Walls/Absorber and Breakeven Ratio are dimensionless values (m^2/m^2). The breakeven point increases as the concentration ratio rises due to the increased output of the system and is defined as:

$$Breakeven = (C_r - 1)\left(\frac{price\ of\ reflector\ (\$/m^2)}{price\ of\ solar\ cell\ (\$/m^2)}\right)$$

Figure 6.55 presents the costs of the CPC concentrator of various concentrating designs and their equivalent breakeven points. The 50mm truncated CPC is added for reference, it can be seen that the truncated CPC costs less than its equivalent C_r full height CPC.

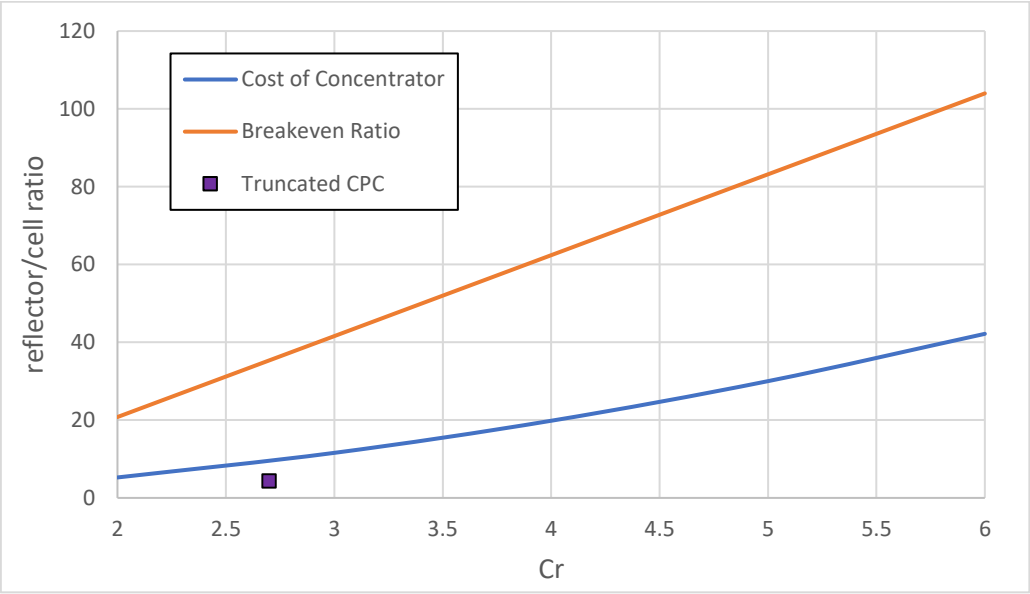

Figure 6.55. Cost of concentrator and breakeven point

6.7.1. Diffuse radiation impact

The above analysis assumes 100% beam radiation. The cost-benefit is affected under real life conditions with mixed diffuse and beam solar radiation. Diffuse radiation can be a significant proportion of total irradiance, especially in cloudy regions. As mentioned in section 5.6, the average proportion of diffused light in the UK ranged from 53% in England and Wales, to 60% for Scotland.

CPC systems have an inverse relation to their efficiency at accepting diffuse radiation with respect to their concentration ratio C_r. The amount of diffused light a CPC accepts is defined as:

$$\eta_D = \frac{1}{C_r}$$

where η_D is the system's efficiency at converting diffused radiation. The results can be tabulated below:

C_r	η_D
1	1.00
1.5	0.67
2	0.50
2.5	0.40
3	0.33
3.5	0.29
4	0.25
4.5	0.22
5	0.20
5.5	0.18
6	0.17

Figure 6.56 shows the effect of diffuse radiation on the *overall* efficiency of CPCs (full beam conversion and partial diffuse conversion) ranging from 1-concentration factor to 6-concentration factor. At 70% diffuse radiation, a 6-factor CPC only operated at 42% efficiency.

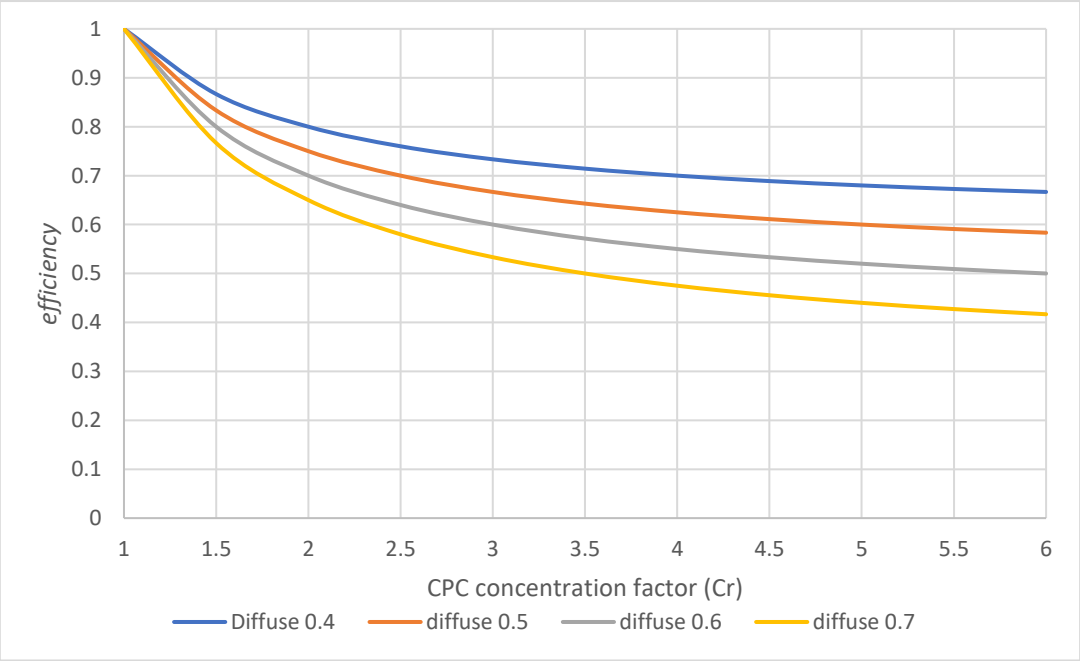

Figure 6.56. Effect of diffused radiation on CPC performance (0.4 - 0.7 diffuse ratios)

Whilst a 6-factor CPC operated at lower efficiency than a 2-factor CPC, the results above can be somewhat misleading as a 6-concentration CPC even at 42% efficiency may provide a

higher output than a 2-factor CPC at 65% efficiency. The results can be normalised for the concentration ratio of the CPC to get the effective concentration of CPCs under cloudy conditions as shown in Figure 6.57. This demonstrates that a 6-factor CPC can operate as low as 2.5-factor CPC when under high diffuse conditions.

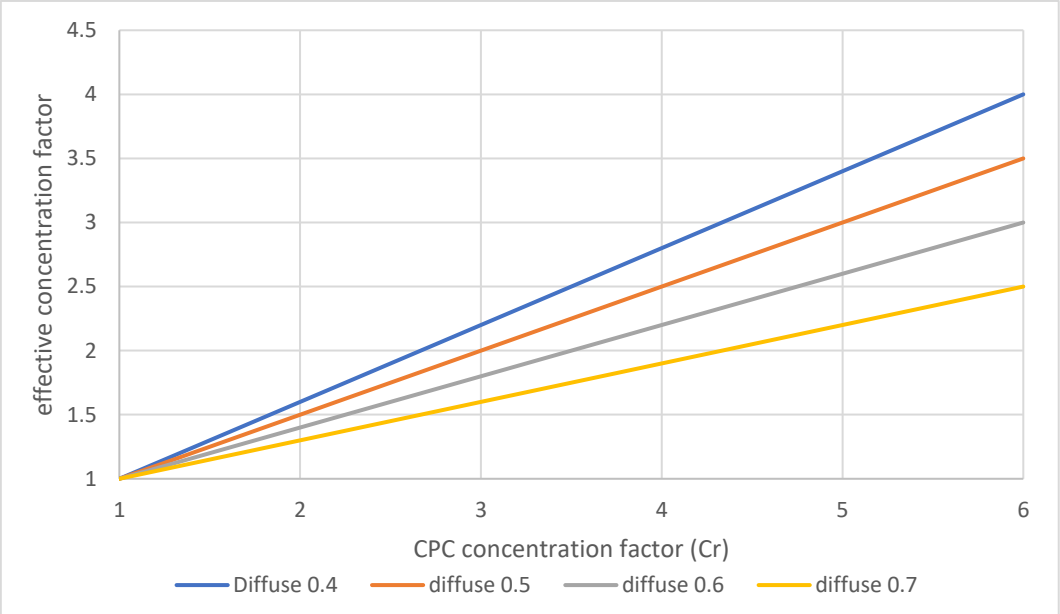

Figure 6.57. Effective concentration factor of CPC for various diffuse ratios

The above data can be applied to the original cost-benefit graph in order to get Figure 6.58. Here, CPC systems ranging from 2-fact to 6-factor concentrations are analysed under ideal (no diffused radiation), 40% diffuse, 50% diffuse, 60% diffuse and 70% diffuse radiations. The breakeven point has been divided into three separate cut-offs based on varying solar cell prices. The UK lies between the 0.5 and 0.6 diffuse radiation region and under assumed cost analysis, using CPC of 4-factor concentration or more provides little to no benefit and at 5+ concentration is financially detrimental depending on the type and price of solar cells employed.

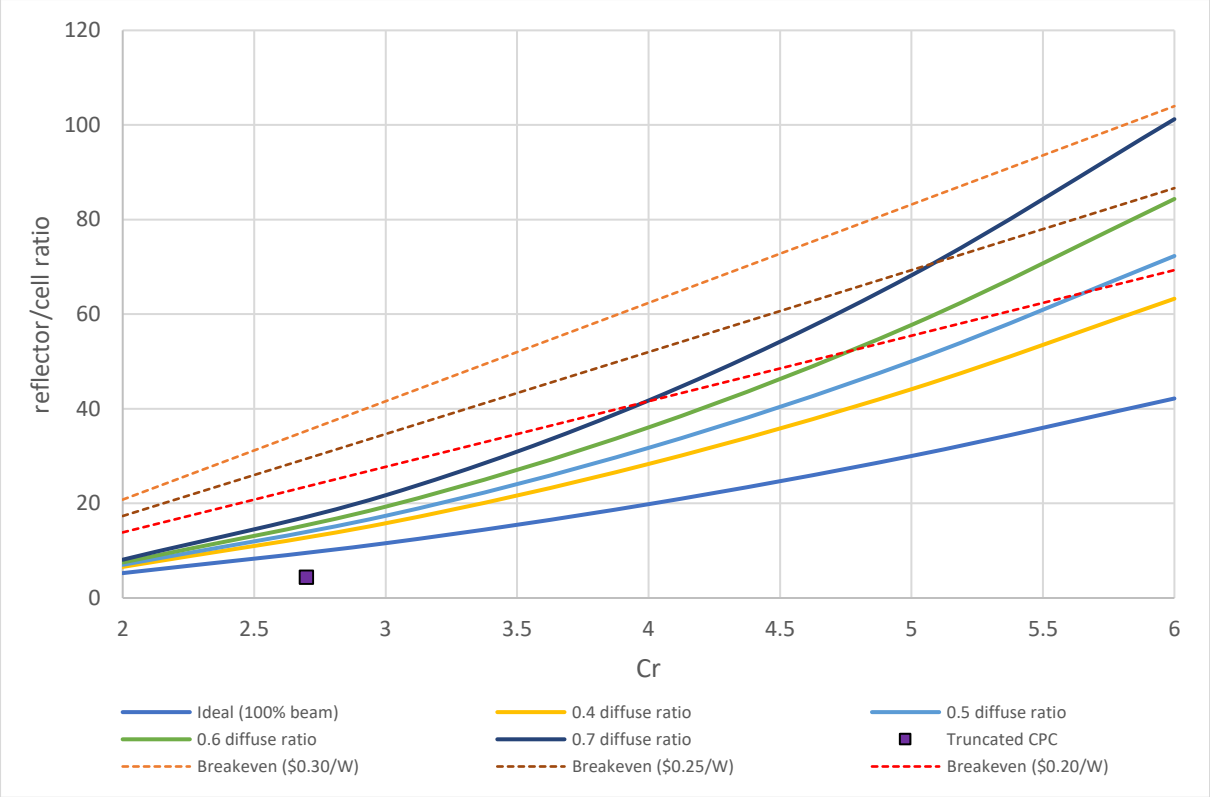

Figure 6.58. Cost of CPC concentrators under ideal and 40-70% diffuse radiation. Breakeven points are expanded for solar cell costs of $0.20/W, $0.25/W and $0.30/W.

Chapter 7 Conclusion and Future work

In this thesis ray tracing modelling, analysis and experimental verification of CPCs and V-trough concentrators are presented. As the intensity of solar radiation reaching the earth's surface is low, minimization of the cost per square meter of aperture is a key requirement for the economical conversion of solar energy into electricity or heat. In concentrated photovoltaic (CPV) technology optics is used for concentrating sunlight onto PV cells. This results in the highest efficiency conversion of sunlight to electricity. Taking this into account, the solar trough was identified as a promising candidate due to its simple design in comparison to more complex three-dimensional configuration. However, two-dimensional CPC and V-trough concentrators are limited to a maximum concentration of ~230× (see Chapter 4). Additionally, higher concentrations improve the economics of the collector by reducing the required receiver dimension for generating power. For high-efficiency triple-junction concentrator cells (TJSC) concentrations above 400× are generally required [179].

7.1. Summary

This researched started by developing and fabricating Dye Sensitized Solar Cells for BIPV integration. Modifications were made to a dye sensitizer known as Black Dye. The modified black dye did not show performance improvements, unfortunately its performance was below the control N719 dye. The results were sent back to the developers of the dye for improvement. This development of dye sensitizers is a focus of chemists.

At the same time, improvements to solar cell efficiencies could be brought about by various methods. It was therefore decided to take a mechanical engineering perspective at the problem posed and look for solution.

The research focus shifted to LCPVs, specifically V-trough and CPC. The area of interest was application of these concentrators in BIPVs. BIPVs pose their own unique problems. The two biggest issues present is the difficulty of installing and maintaining tracking system and the costs associated with such a design, and the minimization of maintaining parts (especially movable parts). The work consisted of modelling for rapid development and analysis of CPC and V-trough geometries and the effect of the geometry, topology and solar irradiance

characteristics on the performance of such concentrators. This was validated through fabrication of V-trough and CPC concentrators and experimental measurements.

7.1.1. The state-of-the-art of nonimaging collectors and applications in BIPVs systems

As with standard PV systems, CPVs are typically warranted for at least 25 years. It is a mandatory requirement for manufacturers of CPVs to certify their product according to the IEC 62108 standard "Concentrator photovoltaic (CPV) modules and assemblies - Design qualification and type approval" issued by the International Electrotechnical Commission (IEC) before entering the market [180]. Additional UL and IEC standards for power and energy rating, module safety, tracker, optics, cell assembly etc., are also exist (see Appendix B for most relevant ones).

Most of efforts in research on photovoltaics aim at increasing the efficiency at all levels from cell to module to system. Figure 7.1 shows the progress made in the increase in efficiency from 1993 to 2019. Significant potential for even higher efficiencies than today is foreseen.

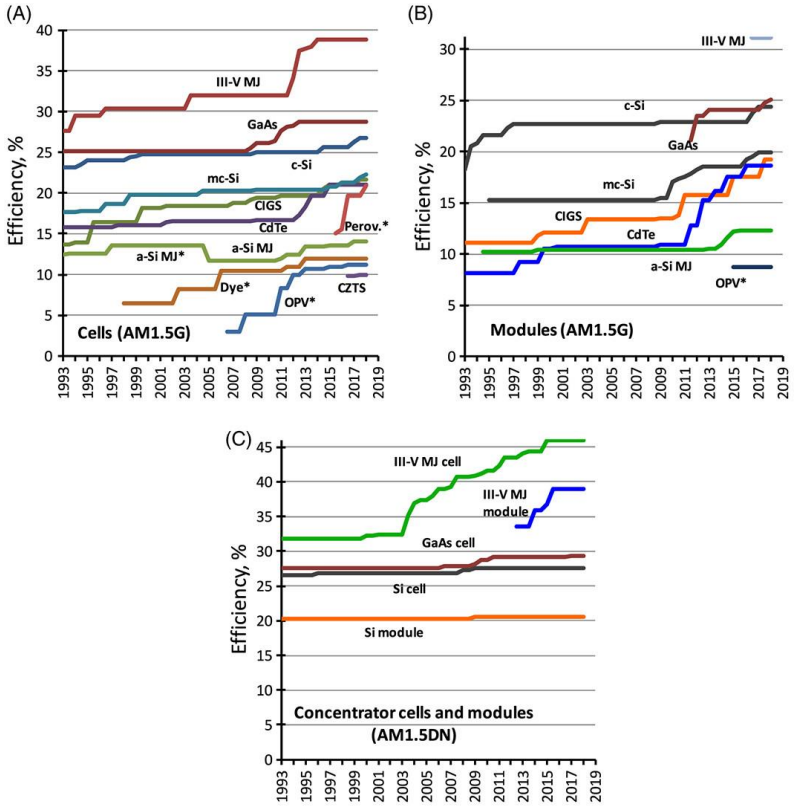

Figure 7.1. Twenty-five years of progress: (A) highest confirmed efficiencies for ≥ 1cm^2 area cells fabricated using the different technologies shown. (B) highest confirmed module results for modules sizes ≥800-cm^2 and (C) highest confirmed concentrator cell and module results [181].

7.1.2. Improvement of Dye Sensitized Solar Cell (DSSC) performance and development of modelling and characterisation techniques

The work set out to fabricate high performing DSSCs. During the literature review, an improvement was made to one of the papers being reviewed with a non-linear interpolation model proposed and compared to the original paper showing favourable results.

The DSSCs fabricated showed poor performance for the novel dye BD-HTB, a modified black dye with the aim of improving the efficiency. Meanwhile the good performance of the control cells created using the N719 dye validated the fabrication process and implied the poor performance was due to the dye themselves. The results were sent back to the chemistry department for evaluation.

7.1.3. Analysis of local irradiance distribution perturbations due to concentrators over a wide range of light incident angles and concentration factors

Work moved to the LCPVs, V-trough and CPC. They were modelled using Ray tracing analysis and their performance was analysed and compared over a wide range of angles of incidences and a variety of configurations. For CPC this involved full height, half truncation and 50mm CPC truncation. For the V-trough the analysis required even more configurations: the tilt angle of the reflector walls could hold an infinite number of configurations.

7.1.4. Developed reliable models using COMSOL software ray-tracing algorithms and investigate the optical efficiency of the selected solar concentrators

The models were iterated over many times, adding increasing complexity including information regarding the reflection mixture (specular and diffuse) which would be exhibited with real-world material. The results were compared to literature for initial validation.

7.1.5. Improvement of optical performance of CPC and V-trough concentrators by modifying the geometry and topology of the concentrators for BIPV applications

These models were then used to propose improved geometric configuration for both CPC and V-trough. For CPC, the truncation analysis showed greatly improved acceptance angles. The loss of concentration factor was significantly smaller than gains in both height saving and material costs. Height was reduced from 242mm to 50mm, a 4.8-fold decrease in one of the most important aspects of BIPV integration. The V-trough analysis showed that for BIPV integration, established parameters are not necessarily best. For example, proposed angles in literature of 19° configuration and 11° configuration were exceeded in performance by new proposals.

7.1.6. Model validation by getting real data from experiments on CPC and V-trough

V-trough and CPC, as well as basic flat plate solar cells were designed and fabricated. The goal was to first validate the results of the modelling work carried out and secondly investigate the challenges and complexities the physical model would experience. Results showed good correlation to the modelling, the experiment also shed light on areas not fully modelled which could be expanded upon in future work.

7.2. Future Work

There are several branches leading out of the results of this work that can be expanded upon:

It is proposed that research is carried out on passive cooling systems for the V-trough and CPC designed for BIPV. Their low concentration and lower heat profile lend well to non-moving and fixed cooling systems such as convective cooling heat sinks. These would lower the operating costs and initial investment required.

For cooling, it is proposed to create larger CPC and V-trough scales. The initial models, whilst well dimensioned for final BIPV implementation were both small in width and short in length. This meant the cooling of the system could not be thoroughly investigated as the mass flow rate required to cool the system was smaller than the most precise rotameters available for lab work.

Further work may also be carried out on the effect of the moment of the sun throughout the year. This research is focused on the properties of CPC and V-trough; however, work can also be carried out on practical application of the BIPV systems, this would take into consideration for example the rotation and geometry of the LCPVs not just during peak season but throughout the year. It may for example be advantageous to design the BIPV for lower overall efficiency, but more stead output throughout the year.

The introduction of Quantum Dots (QDs) has also changed both light emittance and light acceptance devices. There is currently a lot of focus on QD solar cells. One idea proposed is the use of QDs, not as the principle mechanism of the solar cell but as an added layer in the BIPVs for up/downscaling of light coming through the aperture.

Finally, small extensions may be carried out on the integration of glass cover / window cover which would be provided by the BIPV. It is likely the addition of a cover glass would further improve the acceptance angle due to refraction of incoming light. On the other hand, transmittance would then have to be considered. On the reflector side, the effect of softening the light reflection (i.e. more diffuse and less specular reflection) can be considered. Whilst it

may provide a lower overall theoretical concentration and optical efficiency, it is likely the improved flux distribution would in practice improve the performance of such systems.

It was shown in Chapter 6 that distribution of the sun light intensity over the PV receiver is not uniform and this have effect on electrical performance of the cells and high-power losses due to two problems. On the one hand if the cells are in series the lowest cell controls energy production and on the other hand the temperature at the location of high intensity increases sharply. These drawbacks can be alleviated by using cooling systems and developing smart reflecting materials with low-angle scattering. Both two research fields have great potential. On cooling system nanofluid shows great potential in enhancing the heat transfer process. Many works currently underway on enhancing the heat transfer from the PV cells to cooling water [182, 183].

The use of a cover glass in front of reflectors and cells causes high optical losses. Development of more efficient selective coatings for glass cover of the CPC and V-trough with both high solar absorbance (α>0.96) and low thermal emittance (ε<0.07) that are thermally stable in air with enhanced longevity when exposed to polluted air and rain fall in built environment, with reasonable manufacturability and reduced cost can contribute to a more robust CPV product. Research in this area is also very active.

Beam splitting technique is used to separate the concentrated solar radiation into two parts: one for the PV power generation and the other for thermal utility [184]. By this technique it is possible to concentrate solar radiation onto solar cells with high uniformity, which is beneficial to improving the efficiency of solar cells. The thermal receiver is separated to the solar cells, and therefore, the thermal fluid can be heated to a relatively high temperature and does not affect the performance of solar cells.

References

[1] REN21, “Renewables 2017 Global Status Report,” REN21 Secretariat, Paris, 2017.

[2] “Fraunhofer ISE: Photovoltaics Report,” Fraunhofer Institute for Solar Energy, 12 July 2017.

[3] B. Norton, P. C. Eames, T. K. T. K. Mallick, M. J. Huang, S. J. Mc Cormack, J. D. Mondol and Y. G. Yohanis, “Enhancing the performance of building integrated photovoltaics,” *Solar Energy,* vol. 85, no. 8, pp. 1629-1664, 2011.

[4] D. O. Akinyele, R. K. Rayudu and R. H. G. Tan, “Comparative study of photovoltaic technologies based on performance, cost and space requirement: Strategy for selection and application,” *International journal of green energy,* vol. 13, no. 13, pp. 1352-1368, 2016.

[5] G. Siefer, “CPV- Concentrator Photovoltaics Current Status, Challenges & Perspectives,” in *NETRA Conference Green Power - Challenges & Innovation*, Noida, India, 2017.

[6] A. K. Shukla, K. Sudhakar and P. Baredar, “Recent advancement in BIPV product technologies: A review,” *Energy and Buildings,* vol. 140, p. 188–195, 2017.

[7] S. Madala and R. F. Boehm, “A review of nonimaging solar concentrators for stationary and passive tracking applications,” *Renewable and Sustainable Energy Reviews,* vol. 71, pp. 309-322, 2017.

[8] S. Waghmare and N. Gulhane, “Design and ray tracing of a compound parabolic collector with tubular receiver,” *Solar Energy,* vol. 137, pp. 165-172, 2016.

[9] C.-W. Kuo, P.-S. Yen, W.-C. Chang and K.-C. Chang, “The Design and Optical Analysis of Compound Parabolic Collector,” *Procedia Eng.*, vol. 79, pp. 258-262, 2014.

[10] L. Chen, J.-X. Chen and X.-R. Zhang, “Numerical simulation on the optical and thermal performance of a modified integrated compound parabolic solar concentrator,” *Int. J. Energy Res.*, vol. 39, pp. 1843-1857, 2015.

[11] H. Xie, J. Wei, Z. Wang, G. Yang and Q. Ma, “Design and performance study of truncated CPC by eliminating multiple reflections of solar radiation in hybrid CPV/T system: Highest and lowest truncation position,” *Solar Energy,* vol. 136, p. 217–225, 2016.

[12] H. Xie, J. Wei, Z. Wang, G. Yang and Q. Ma, “Design and performance research on eliminating multiple reflections of solar radiation within compound parabolic concentrator (CPC) in hybrid CPV/T system,” *Solar Energy,* vol. 129, pp. 126-146, 2016.

[13] “International energy outlook 2016 with projections to 2040,” U.S. Energy Information Administration, 2016.

[14] E. Becquerel, *C.R. Acad.. Sci. Paris,* vol. 9, p. 561, 1839.

[15] M. Riordan, “The Silicon Dioxide Solution,” *IEEE Spectrum,* 1 12 2007.

[16] N. Roth-Wells, “The Lantern,” [Online]. Available: http://web.colby.edu/thelantern/2017/05/25/a-trip-to-the-science-fair/. [Accessed 20 08 2017].

[17] S. M. Sze and K. K. Ng, Physics of Semiconductor Devices, 2nd ed., New York: Wiley, 1981.

[18] ANDOR, “An overview of the properties of light,” Oxford Instruments, 2017.

[19] S. Fujita, “Wide-bandgap semiconductor materials: For their full bloom,” *Japanese Journal of Applied Physics,* vol. 54, no. 3, 2015.

[20] C. Kittel, Introduction to Solid State Physics, 8th edition, John Wiley & Sons, 2004, pp. 194-196.

[21] M. A. Green, “Intrinsic concentration, effective densities of states, and effective mass in silicon,” *Journal of Applied Physics,* vol. 67, no. 6, pp. 2944-2954, 1990.

[22] W. A. Harrison, Electronic Structure and the Properties of Solids, San Francisco: Dover Publications Inc., 1989.

[23] F. Reif, Fundamentals of Statistical and Thermal Physics, McGraw–Hill, 1965.

[24] A. B. Sproul and M. A. Green, “Improved value for the silicon intrinsic carrier concentration from 275 to 375 K,” *Journal of Applied Physics,* vol. 70, pp. 846-854, 1991.

[25] T. Wasserab, Z. Naturoforsch and A. Teil, vol. 32, p. 746, 1997.

[26] H. F. Wolf, Semiconductors, New York: Wiley, 1971.

[27] W. C. O’Mara, “Semiconductor Materials and Process Technology Handbook,” G. F. McGuire, Ed., Park Ridge, Noyes, 1988, p. 28.

[28] O. D. Trapp, R. A. Blanchard and W. H. Shepperd, Semiconductor Technology Handbook, Portola Valley: Technology Associates, 1980.

[29] P. P. Altermatt, A. Schenk, F. Geelhaar and G. Heiser, “Reassessment of the intrinsic carrier density in crystalline silicon in view of band-gap narrowing,” *Journal of Applied Physics,* vol. 93, no. 3, p. 1598, 2013.

[30] K. . Misiakos and D. . Tsamakis, “Accurate measurements of the silicon intrinsic carrier density from 78 to 340 K,” *Journal of Applied Physics,* vol. 74, no. 5, pp. 3293-3297, 1993.

[31] S. M. Sze and M.-K. Lee, Semiconductor Devices, Physics and Technology, John Wiley & Sons, 2012.

[32] F. A. Lindholm, J. . Fossum and E. . Burgess, “Application of the superposition principle to solar-cell analysis,” *IEEE Transactions on Electron Devices,* vol. 26, no. 3, pp. 165-171, 1979.

[33] J. R. Tumbleston, D. H. Ko, E. T. Samulski and R. . Lopez, “Nonideal parasitic resistance effects in bulk heterojunction organic solar cells,” *Journal of Applied Physics,* vol. 108, no. 8, p. 084514, 2010.

[34] A. . Assi and M. . Al-Amin, “Reducing the parasitic loss of c-Si solar cells,” , 2013. [Online]. Available: http://ieeexplore.ieee.org/document/6734955. [Accessed 19 9 2017].

[35] M. A. Green, Solar Cells - Operating Principles, Technology and System Application, Kensington, Australia: University of NSW, 1992.

[36] P. Auger, “Sur les rayons β secondaires produits dans un gaz par des rayons X,” *C.R.A.S.,* vol. 177, pp. 169-171, 1923.

[37] W. Shockley and W. T. Read, “Statistics of the Recombinations of Holes and Electrons,” *Physical Review,* vol. 78, 1952.

[38] R. N. Hall, “Electron-Hole Recombination in Germanium,” *Physical Review,* vol. 87, p. 387, 1952.

[39] W. Shockley and H. J. Queisser, “Detailed Balance Limit of Efficiency of p-n Junction Solar Cells,” *Journal of Applied Physics,* vol. 32, no. 3, pp. 510-519, 1961.

[40] W. Ruppel and P. Wurfel, “Upper limit for the conversion of solar energy,” *IEEE Transactions on Electron Devices,* vol. 27, no. 4, pp. 877-882 , 1980.

[41] A. de Vos and H. Pauwels, “On the thermodynamic limit of photovoltaic energy conversion,” *Appl. Phys.,* vol. 25, p. 119, 1981.

[42] C. S. Solanki and G. Beaucarne, “Advanced Solar Cell Concepts,” *Interuniversity Microelectronics Center, Belgium.*

[43] S. Ruhle, “Tabulated values of the Shockley–Queisser limit for single junction solar cells,” *Solar Energy,* vol. 130, pp. 139-147, 2016.

[44] A. de Vos, “Detailed balance limit of the efficiency of tandem solar cells,” *J. Phys. D: Appl. Phys.,* vol. 13, pp. 839-846, 1980.

[45] S. Aldous, Z. Yewdall and S. Ley, A peek inside a PV cell. Home Power, (https://www.homepower.com/articles/solar-electricity/equipment-products/peek-inside-pv-cell).

[46] “Photovoltaics Report,” Fraunhofer ISE, 2017.

[47] M. Gratzel, “Perspectives for dye-sensitized nanocrystalline solar cells,” *Progress in Photovoltaics Research and Applications,* vol. 8, no. 1, pp. 171-185, 2000.

[48] W. West, “Proceedings of vogel centennial symposium,” *Photographic Science and Engineering,* pp. 18-35, 1974.

[49] J. Moser, “Monatshefte f□ur Chemie,,” vol. 8, p. 373, 1987.

[50] S. Namba and Y. Hishiki, “Color sensitization of zinc oxide with cyanine dyes1.,” *The Journal of Physical Chemistry,* vol. 69, no. 3, pp. 774-779, 1965.

[51] H. Gerischer and H. Tributsch, “Ber. Bunsenges.,” *Phys. Chem.,* vol. 72, pp. 437-445, 1968.

[52] H. Tsubomura, M. Matsumura, Y. Nomura and T. Amamiya, “Dye sensitised zinc oxide: aqueous electrolyte: platinum photocell,” *Nature,* vol. 261, pp. 402-403, 1976.

[53] W. D. K. Clark and N. Sutin, “Spectral sensitization of n-type titanium dioxide electrodes by polypyridineruthenium(ii) complexes,” *Journal of the American Chemical Society,* vol. 99, no. 14, pp. 4676-4682, 1977.

[54] M. P. Dare-Edwards, J. B. Goodenough, A. Hamnett, K. R. Seddon and R. D. Wright, “Sensitisation of semiconducting electrodes with ruthenium-based dyes,” *Faraday Discuss. Chem. Soc.,* vol. 70, pp. 285-298, 1980.

[55] D. Duonghond, N. Serpone and M. Gratzel, “Integrated systems for water cleavage by visible light sensitization of tio2 particles by surface derivatization with ruthenium complexes,” *Helvetica Chimica Acta,* vol. 67, no. 4, pp. 1012-1018, 1984.

[56] J. Desilvestro, M. Gratzel, L. Kavan, J. Moser and J. Augustynski, “Highly effcient sensitization of titanium dioxide,” *Journal of the American Chemical Society,* vol. 107, no. 10, pp. 2988-2990, 1985.

[57] N. Vlachopoulos, P. Liska, J. Augustynski and M. Gratzel, “ Very efficient visible light energy harvesting and conversion by spectral sensitization of high surface area polycrystalline titanium dioxide films,” *Journal of the American Chemical Society,* vol. 110, no. 4, p. 1216–1220, 1988.

[58] B. O’Regan and M. Gratzel, “A low-cost, high-efficiency solar cell based on dye-sensitized colloidal tio2 films,” *Nature,* vol. 353, no. 6346, pp. 737-470, 1991.

[59] K. Hara, H. Arakawa, A. Luque and H. Arakawa, Dye-Sensitized Solar Cells, John Wiley & Sons, 2005.

[60] J. Villanueva, J. A. Anta, E. Guillen and G. Oskam, “Numerical Simulation of the Current−Voltage Curve in Dye-Sensitized Solar Cells,” *The Journal of Physical Chemistry C,* vol. 113, no. 45, pp. 19722-19731, 2009.

[61] J. Bisquert and V. S. Vikhrenko, “Interpretation of the Time Constants Measured by Kinetic Techniques in Nanostructured Semiconductor Electrodes and Dye-Sensitized Solar Cells,” *The Journal of Physical Chemistry B,* vol. 108, no. 7, pp. 2313-2322, 2004.

[62] J. van de Lagemaat and A. J. Frank, “Nonthermalized Electron Transport in Dye-Sensitized Nanocrystalline TiO2 Films: Transient Photocurrent and Random-Walk Modeling Studies,” *The Journal of Physical Chemistry B,* vol. 105, no. 45, pp. 11194-11205, 2001.

[63] J. A. Anta, J. Nelson and N. Quirke, “Charge transport model for disordered materials: Application to sensitized TiO2,” *American Physical Society Phys. Rev. B,* vol. 65, no. 12, p. 125324, Mar 2002.

[64] J. van de Lagemaat, N. Kopidakis, N. Neale and A. J. Frank, “Effect of nonideal statistics on electron diffusion in sensitized nanocrystalline TiO2,” *American Physical Society Phys. Rev. B,* vol. 70, no. 3, p. 035304, Jan 2005.

[65] J. A. Anta, F. Casanueva and G. Oskam, “A Numerical Model for Charge Transport and Recombination in Dye-Sensitized Solar Cells,” *The Journal of Physical Chemistry B,* vol. 110, no. 11, 2006.

[66] J. Nelson, S. A. Haque, R. David and J. R. Durrant, “Trap-limited recombination in dye-sensitized nanocrystalline metal oxide electrodes,” *American Physical Society Phys. Rev. B,* vol. 63, no. 20, p. 205321, May 2001.

[67] K. D. Benkstein, N. Kopidakis, J. van de Lagemaat and A. J. Frank, “Influence of the Percolation Network Geometry on Electron Transport in Dye-Sensitized Titanium Dioxide Solar Cells,” *The Journal of Physical Chemistry B,* vol. 107, no. 31, pp. 7759-7767, 2003.

[68] P. J. Cameron, L. M. Peter and S. Hore, “How Important is the Back Reaction of Electrons via the Substrate in Dye-Sensitized Nanocrystalline Solar Cells?,” *The Journal of Physical Chemistry B,* vol. 109, no. 2, pp. 930-936, 2005.

[69] K. Sopian, K. S. Yigit, H. T. Liu, S. Kaka and T. N. Veziroglu, "Performance analysis of photovoltaic thermal air heaters," *Energy Convers Manag,* vol. 37, pp. 1657-1670, 1996.

[70] S. A. Kalaogirou, "Solar thermal collectors and application," *Prog Energy Combust Sci,* vol. 30, pp. 231-295, 2004.

[71] R. Daghigh, A. Ibrahim, G. L. Jin, M. H. Ruslan and K. Sopian, "Predicting the performance of amorphous and crystalline silicon based photovoltaic solar thermal collectors," *Energy Convers Manag,* vol. 52, pp. 1741-1747, 2011.

[72] "Renewables 2017 global status report," Paris: REN21 Secretariat, 2017.

[73] "Solar heat worldwide 2017," IEA Solar Heating & Cooling Programme, 2017.

[74] O. Sharaf and M. Orhan, "Concentrated Photovoltaic Thermal (CPVT) solar collector systems: Part I-fundamentals, design considerations and current technologies," *Renewable Sustainable Energy Rev.,* vol. 50, pp. 1500-1565, 2015.

[75] M. Wiesenfarth, S. P. Philipps, A. W. Bett, K. Horowitz and S. Kurtz, "Current status of concentrator photovoltaic (CPV) technology," Fraunhofer ISE/NREL report, 2015.

[76] S. Wenham, Applied photovoltaics, Routledge, 2011.

[77] R. Kunnemeyer, T. Anderson, M. Duke and J. Carson, "Performance of a V-trough photovoltaic/thermal concentrator," *Solar Energy,* vol. 101, pp. 19-27, 2014.

[78] Q. Z. Sharaf and M. F. Orhan, "Concentrated photovoltaic thermal (CPVT) solar collector systems: Part II – Implemented systems, performance assessment, and future directions," *Renewable and Sustainable Energy Reviews,* vol. 50, pp. 1566-1633, 2015.

[79] W. G. J. van Helden, R. J. C. Van Zolingen and H. Zondag, "PV thermal systems: PV panels supplying renewable electricity and heat," *Photovoltaics Res. Appl. Prog.,* vol. 12, pp. 415-442, 2004.

[80] J. E. Kern and M. C. Russell, "Combined photovoltaic and thermal hybrid collector systems," in *Proceedings of the 13th IEEE photovoltaic specialists; p. 1153–57.*, Washington DC, USA, 1978.

[81] M. Y. Othman, A. Ibrahim, G. L. Jin, M. H. Ruslan and K. Sopian, “Photovoltaic-thermal (PV/T) technology–the future energy technology,” *Renew Energy,* vol. 49, pp. 171-174 , 2013.

[82] X. Ju, C. Xu, Z. Liao, X. Du, G. Wei, Z. Wang and Y. Yang, “A review of concentrated photovoltaic-thermal (CPVT) hybrid solar systems with waste heat recovery (WHR),” *Science Bulletin ,* vol. 62, p. 1388–1426, 2017.

[83] B. M. Ziapour, V. Palideh and F. Mokhtari, “Performance improvement of the finned passive PVT system using reflectors like removable insulation covers,” *Appl Therm Eng,* vol. 94, pp. 341-349, 2016.

[84] L. T. Kostic, T. M. Pavlovic and Z. T. Pavlovic, “Influence of reflectance from flat aluminum concentrators on energy efficiency of PV/Thermal collector,” *Appl Energy,* vol. 87, no. 2, pp. 410-416, 2010.

[85] Y. Tripanagnostopoulos, M. Souliotis, R. Battisti and A. Corrado, “Energy, cost and LCA results of PV and hybrid PV/T solar systems,” *Prog Photovolt: Res Appl,* vol. 13, pp. 235-250, 2005.

[86] Y. Yupeng Wu, P. Eames, T. Mallick and M. Sabry, “Experimental characterisation of a Fresnel lens photovoltaic concentrating system Author links open overlay panel,” *Solar Energy,* vol. 86, no. 1, pp. 430-440, 2012.

[87] C. Feng, H. Zheng, R. Wang and X. Ma, “Performance investigation of a concentrating photovoltaic/thermal system with transmissive Fresnel solar concentrator,” *Energy Conversion and Management ,* vol. 111, no. 1, pp. 401-408, 2016.

[88] R. Eke and A. Senturk, “Performance comparison of a double-axis sun tracking versus fixed PV system Author links open overlay panel,” *Solar Energy,* vol. 86, no. 9, pp. 2665-2672, 2012.

[89] R. Tripathi, G. N. Tiwari and V. K. Dwivedi, “Overall energy, exergy and carbon credit analysis of N partially covered Photovoltaic Thermal (PVT) concentrating collector connected in series,” *Solar Energy,* vol. 136, pp. 260-267 , 2016.

[90] M. Abdelhamid, B. K. Widyolar, L. Jiang, R. Winston, E. Yablonovitch, G. Scranton, D. Cygan, H. Abbasi and A. Kozlov, “Novel double-stage high-concentrated solar

hybrid photovoltaic/thermal (PV/T) collector with nonimaging optics and GaAs solar cells reflector," *Applied Energy,* vol. 102, no. 15, pp. 68-79, 2016.

[91] M. Y. Othman, B. Yatim, K. Sopian and M. N. A. Bakar, " Double-pass photovoltaic-thermal solar air collector with compound parabolic concentrator and fins," *J Energy Eng,* vol. 132, no. 3, pp. 116-120, 2006.

[92] P. Raghuraman, "Analytical prediction of liquid and air photovoltaic/thermal flat plate collector performance," *J Sol Energy Eng,* vol. 103, pp. 291-298, 1981.

[93] C. H. Cox and P. Raghuraman, "Design considerations for flat-plate photovoltaic/thermal collectors," *Sol Energy,* vol. 35, pp. 227-241, 1985.

[94] S. A. Hamid, M. Y. Othman, K. Sopian and S. H. Zaidi, "An overview of photovoltaic thermal combination (PV/T combi) technology," *Renewable and Sustainable Energy Reviews,* vol. 38, pp. 212-222, 2014.

[95] Y. Tripanagnostopolous, T. Nousia and M. Souliotis, "Low cost improvements to building integrated air cooled hybrid PV–Thermal Systems," in *Proceeding of the 16th European PV Solar Energy Conference, Vol. 2, 1874–1899.,* Glasgow, UK, 2000.

[96] X. Ju, Z. Wang, G. Flamant, P. Li and W. Zhao, "Numerical analysis and optimization of a spectrum splitting concentration photovoltaic–thermoelectric hybrid system," *Sol Energy,* vol. 86, no. 6, pp. 1941-1954, 2012.

[97] J. A. Duffie and W. A. Beckman, Solar Engineering of Thermal Processes, John Wiley & Sons, 2013.

[98] P. Pérez-Higueras, E. Muñoz, G. Almonacid and P. G. Vida, "High concentrator photoVoltaics efficiencies: present status and forecast," *Renewable and Sustainable Energy Reviews,* vol. 15, no. 4, pp. 1810-1815, 2011.

[99] V. Jebasingh and G. Joselin Herbert, "A review of solar parabolic trough collector," *Renewable & Sustainable Energy Reviews,* vol. 54, pp. 1085-1091, 2016.

[100] Flabeg, "Reflecting the Future – Solar Mirrors for all CSP Applications," http://www.flabeg-fe.com/en/solar-mirrors.html.

[101] M. Geyer, E. Lüpfert, R. Osuna, A. Esteban, W. Schiel, A. Schweitzer, E. Zarza, P. Nava, J. Langenkamp and E. Mandelberg, "EUROTROUGH - Parabolic Trough Collector Developed for Cost Efficient Solar Power Generation," in *11th SolarPACES International Symposium on Concentrated Solar Power and Chemical Energy Technologies*, Zurich, Switzerland, Sept 4-6, 2002.

[102] H. Hijazi, O. Mokhiamar and O. Elsamni, "Mechanical design of a low cost parabolic solar dish concentrator," *Alexandria Engineering Journal,* vol. 55, pp. 1-11, 2016.

[103] C. S. Sangani and C. S. Solanki, "Experimental evaluation of V-trough (2 suns) PV concentrator system using commercial PV modules," *Solar Energy Materials & Solar Cells,* vol. 91, p. 453–459, 2007.

[104] W. A. Al-Shohani, R. K. Al-Dadah, S. . Mahmoud and A. . Algareu, "Optimum design of V-trough concentrator for photovoltaic applications," *Solar Energy*, vol. 140, no. , pp. 241-254, 2016.

[105] M. Tian, Y. Su, H. Zheng, G. Pei, G. Li and S. Riffat, "A review on the recent research progress in the compound parabolic concentrator (CPC) for solar energy applications," *Renewable and Sustainable Energy Reviews,* vol. 82, no. 1, pp. 1272-1296, 2018.

[106] A. Wilson and R. Ross, "ANGLE-OF-INCIDENCE EFFECTS ON MODULE POWER AND ENERGY PERFORMANCE," [Online]. Available: https://www2.jpl.nasa.gov/adv_tech/photovol/ppr_81-85/Angle%20of%20Incid%20Effects%20-%2021PIM1983.pdf. [Accessed 10 10 2018].

[107] b. solar, "Technical Data," [Online]. Available: https://www.bsqsolar.com/product/productscpv-tracking-system/. [Accessed 10 10 2018].

[108] S. A. Kalogirou, "CHAPTER 2 Environmental Characteristics," in *Solar Energy Engineering*, Elsevier, 2014.

[109] J. Kwangbok, H. Taehoon, K. Choongwan, O. Jeongyoon, L. Minhyun and K. Jimin, "A Prototype Design and Development of the Smart Photovoltaic System Blind

Considering the Photovoltaic Panel, Tracking System, and Monitoring System," *Applied Sciences,* 2017.

[110] K. Araki, T. Yano and Y. Kuroda, "30 kW concentrator photovoltaic system using dome-shaped Fresnel lenses," *Opt Express,* vol. 18, p. 53–63, 2010.

[111] F.-L. Siaw, K.-K. Chong and C.-W. Wong, "A comprehensive study of dense-array concentrator photovoltaic system using non-imaging planar concentrator," *Renew Energy,* vol. 62, p. 542–55, 2014.

[112] M. Grätzel, "Dye-sensitized solar cells," *Journal of Photochemistry C: Photochemistry Reviews,* vol. 4, pp. 145-153, 2003.

[113] ACS, "Ultrathin, dye-sensitized solar cells called most efficient to date," *American Chemical Society,* 2006.

[114] GCell, "Gcell," G24 Power, [Online]. Available: http://gcell.com.

[115] S. Min-Kyu, H. Seo, L. Kyoung-Jun, K. Soo-Kyoung, K. Byung-Man, P. Songyi, P. Kandasamy and K. Hee-Je, "A simple method for modeling dye-sensitized solar cells," *Thin Solid Films,* vol. 554, pp. 114-117, 2014.

[116] S. N. Laboratories, "The dakota project," Sandia National Laboratories, 2014.

[117] K. R. Dalbey, B. M. Adams and W. J. Bohnhoff, "Dakota Manual version 5.2 edition," Sandia National Laboratories, 2014.

[118] M. Wiesenfarth, S. P. Philipps, A. W. Bett, K. Horowitz and S. Kurtz, "Current status of concentrator photovoltaic (CPV) technology," Fraunhofer Institute for Solar Energy Systems ISE in Freiburg and NREL, Germany, Version 1.3, April 2017.

[119] S. Madala and R. F. Boehm, "A review of nonimaging solar concentrators for stationary and passive tracking applications," *Renewable and Sustainable Energy Reviews,* vol. 71, p. 309–322, 2017.

[120] K. Shanks, S. Senthilarasu and T. K. Mallick, "Optics for concentrating photovoltaics: Trends, limits and opportunities for materials and design," *Renewable and Sustainable Energy Reviews,* vol. 60, pp. 394-407, 2016.

[121] R. M. Swanson, “The Promise of Concentrators,” *Progress in Photovoltaics: Research and Applications,* vol. 8, pp. 93-111, 2000.

[122] Y. Amanlou, T. T. Hashjin, G. B, N. G and R. Mamat, “A comprehensive review of uniform solar illumination at low concentration photovoltaic (LCPV) systems,” *Renewable and Sustainable Energy Reviews,* vol. 60, pp. 1430-1441, 2016.

[123] M. Khamooshi, H. Salati, F. Egelioglu, A. H. Faghiri, J. Tarabishi and S. Babadi, “A Review of Solar Photovoltaic Concentrators,” *International Journal of Photoenergy,* vol. 2014, p. Article ID 958521, 2014.

[124] P. Pérez-Higueras, E. E. Munoz, G. Almonacid and P. Vidal, “High Concentrator PhotoVoltaics efficiencies: Present status and forecast,” *Renewable and Sustainable Energy Reviews,* vol. 15, pp. 1810-1815, 2011.

[125] K.-K. Chong, S.-L. Lau, T.-K. Yew and P. C.-L. Tan, “Design and development in optics of concentrator photovoltaic system,” *Renewable and Sustainable Energy Reviews,* vol. 19, pp. 598-612, 2013.

[126] A. D. Vos, “Detailed balance limit of the efficiency of tandem solar cells,” *Journal of Physics D: Applied Physics,* vol. 13, no. 5, p. 839, 1980.

[127] S. Kurtz, D. Myers, W. E. McMahon, J. Geisz and M. Steiner, “A comparison of theoretical efficiencies of multi-junction concentrator solar cells,” *Progress in Photovoltaics: Research and Applications,* vol. 16, no. 6, pp. 537-546, 2008.

[128] M. Adsten and B. Hellstrom, “Measurement of radiation distribution on the absorber in an asymetric CPC collector,” *Solar Energy,* vol. 76, no. 1-3, pp. 199-206, 2004.

[129] H. Hatwaambo and H. Hakansson, “Angular characterization of low concentrating PV-CPC using low-cost reflectors,” *Solar Energy Materials and Solar Cells,* vol. 92, no. 11, pp. 1347-1351, 2008.

[130] D. I. Paul, M. Smyth, A. Zacharopoulos and J. Mondol, “The design, fabrication and indoor experimental characterisation of an isolated cell photovoltaic module,” *Solar Energy,* vol. 88, pp. 1-12, 2013.

[131] W. T. Welford and R. Winston, The Optics of Non-Imaging Concentrators, New York, NY, USA: Academic Press, 1978.

[132] F. Reis, Brito, V. Corregidor, J. Wemans and G. Sorasio, "Modeling the performance of low concentration photovoltaic systems," *Solar Energy Materials & Solar Cells,* vol. 94, p. 1222–1226, 2010.

[133] C. Solanki, C. Sangani, D. Gunashekar and G. Antony, "Enhanced heat dissipation of V-trough PV modules for better performance," *Solar Energy Materials,* vol. 92, pp. 1634-1638, 2008.

[134] H. Singh, M. Sabry and D. Redpath, "Experimental investigations into low concentrating line axis solar concentrators for CPV applications," *Solar Energy,* vol. 136, pp. 421-427, 2016.

[135] R. Tang and X. Liu, "Optical performance and design optimization of V-trough concentrators for photovoltaic applications," *Solar Energy,* vol. 85, pp. 2154-2166, 2011.

[136] N. Fraidenraich and G. J. Almeida, "Optical properties of V-trough concentrators," *Solar Energy*, vol. 47, pp. 147-155, 1991.

[137] M. Irshid and M. Otham, "V-troughs with high concentation ratios for photovoltaic concentrator cells," *Solar Cells,* vol. 23, pp. 159-172, 1988.

[138] G. Burkhard, G. Strobel and D. Burkhard, "Flat-sided rectilinear trough as a solar concentrator: an analytical study," *Applied Optics,* vol. 17, pp. 1870-1883, 1978.

[139] N. Fraidenraich, "Analytic solutions for the optical properties of V-trough concentrators," *Applied Optics,* vol. 31, pp. 131-139, 1992.

[140] N. Fraidenraich, "Analytic solutions for the optical and radiative properties of nonaccepted light radiation of V-trough concentrators," *Solar Energy,* vol. 47, no. 3, pp. 147-155, 1995.

[141] S. Shams, M. Mc Keever, S. Mc Cormack and B. Norton, "Design and experiment of a new solar air heating collector," *Energy,* vol. 100, pp. 374-383, 2016.

[142] S. Farooqui, “A vacuum tube based improved solar cooker,” *Sustain. Energy Technol. Assess.,* vol. 3, pp. 33-39, 2013.

[143] M. Sabry, “Prismatic TIR (total internal reflection) low-concentration PV (photovoltaics)-integrated facade for low latitude,” *Energy,* vol. 107, pp. 473-481, 2016.

[144] F. Patiño-Jiménez, Y. Nahmad-Molinari, V. Moreno-Oliva, F. Santos-Garcia and A. Santiago-Alvarado, “Construction and optical testing of inflatable membrane mirror using structured light technique,” *Int. J. Photoenergy,* p. ID 196186.

[145] A. Maccari and M. Montecchi, “An optical profilometer for the characterization of parabolic trough solar concentrators,” *Solar Energy,* vol. 81, pp. 185-194, 2007.

[146] A. Rabl, “Comparison of solar concentrators,” *Solar Energy,* vol. 18, no. 2, pp. 93-111, 1973.

[147] A. Rabl, “Optical and thermal properties of compound parabolic concentrators,” *Solar Energy,* vol. 18, no. 6, pp. 497-511, 1976.

[148] H. Hinterberger and R. Winston, “Efficient light coupler for threshold Cerenkov counters,” *Rev. Sci. Instrum.,* vol. 37, pp. 1094-1095, 1966a.

[149] H. Hinterberger and R. Winston, “Gas Cerenkov counter with optimized light-collecting efficiency,” *Proc. Int. Instrum. High Energy Phys.,* pp. 205-206, 1966b.

[150] V. Baranov, “A paper in Russian that introduces certain properties of CPCs,” *Opt. Mekh. Prom.,* vol. 6, pp. 1-5, 1965a.

[151] V. Baranov and G. Melnikov, “Study of the illumination characteristics of hollow focons,” *Sov. J. Opt. Technol.,* pp. 408-411, 1966.

[152] V. Baranov, “[Eng transL: Parabolotoroidal mirrors as elements of solar energy concentrators. Appl. Sol Energy 2, 9-12.],” *Geliotekhnika,* vol. 2, pp. 11-14, 1966.

[153] R. Winston, “Principles of solar concentrators of a novel design,” *Sol. Energy,* vol. 16, pp. 89-95, 1974.

[154] J. J. O'Gallagher, “Retrospective on 30 years of nonimaging optics development for solar energy at the University of Chicago,” in *Proc. SPIE 9955,* 2016.

[155] A. Timinger, A. Kribus and H. Ries, “Faceted concentrators optimized for homogeneous radiation.,” *Appl Opt,* vol. 39, no. 7, pp. 1152-1158, 2000.

[156] Lourens van Dijk, E. Pepijn Marcus, A. Jolt Oostra, Ruud, Ruud E.I. Schropp and Marcel Di Vecea, “3D-printed concentrator arrays for external light trapping on thin film solar cells,” *Solar Energy Materials and Solar Cells,* vol. 139, pp. 19-26, 2015.

[157] T. Cooper, F. Dahler, G. Ambrosetti, A. Pedretti and A. Steinfeld, “Performance of compound parabolic concentrators with polygonal apertures,” *Solar Energy,* vol. 95, pp. 308-318, 2013.

[158] M. Brogren, “Optical efficiency of low-concentrating solar energy systems with parabolic reflectors,” PhD Thesis, Acta Universitatis Upsaliensis, Uppsala, Sweden, 2004, 2004.

[159] D. Grimmer, “A comparison of compound parabolic and simple parabolic concentrating solar collectors,” *Sol Energy,* vol. 22, pp. 21-25, 1979.

[160] P. P. Mondal and A. Diaspro, “Ray Optics, Wave Optics and Imaging System Design,” in *Fundamentals of Fluorescence Microscopy*, Dordrecht, Springer, 2014, pp. 3-31.

[161] L. S. Pedrotti, “Fundamentals of Photonics,” in *Basic Geometric Optics*, 2008, p. 77.

[162] R. K. Luneburg, Mathematical Theory of Optics, Providence, Rhode Island:: Brown University. Graduate School, 1944, p. 189–213.

[163] C. Boucher, “The Basics of Ray Optics Modeling in COMSOL Multiphysics”.

[164] C. Boucher, “Using the New Ray Tracing Algorithm in COMSOL Multiphysics® 5.2a,” COMSOL, 2016.

[165] L. P. T. B. P. P. J. E. De Vos A, “Entropy fluxes, endoreversibility and solar energy conversion,” *J. Appl. Phys.,* vol. 74, pp. 3631-37, 1993.

[166] A. Belghachi, “Theoretical Calculation of the Efficiency Limit for Solar Cells,” *IntechOpen,* 2014.

[167] R. Winston, “Nonimaging Optics,” *Scientific American,* pp. 76-81, 1991.

[168] Solidworks, “Preparing SOLIDWORKS Models for 3D Printing,” Solidworks, [Online]. Available: http://blogs.solidworks.com/tech/2015/05/preparing-solidworks-models-3d-printing.html. [Accessed 15 01 2018].

[169] Alanod, “MIRO-SILVER® product catalog”.

[170] D. Burnett, E. Barbour and G. P. Harrison, “The UK solar energy resource and the impact of climate change,” *Renewable Energy,* vol. 71, pp. 333-343, 2014.

[171] T. Muneer, S. Etxebarria and E. Gago, “Monthly averaged-hourly solar diffuse radiation model for the UK,” *Building Services Engineering Research & Technology,* 2014.

[172] M. Dhimish, V. Holmes, P. Mather and M. Sibley, “Preliminary assessment of the solar resource in the United Kingdon,” *Clean Energy,* vol. 2, no. 2, pp. 112-125, 2018.

[173] Y. Varshni, “Temperature dependence of the energy gap in semiconductors,” *Physica,* vol. 34, no. 1, 1967.

[174] M. A. Green, “General temperature dependence of solar cell performance and implications for devide modeling,” *Prog. In Photovoltaics,* vol. 11, pp. 333 - 340, 2003.

[175] S. Ponce-Alcántara, J. Patrick Connolly, G. Sánchez, J. Manuel Míguez, V. Hoffmann and R. Ordás, “A statistical analysis of the temperature coefficients of industrial silicon solar cells,” *4th International Conference on Silicon Photovoltaics, SiliconPV 2014,* vol. 55, p. 578 – 588, 2014.

[176] S. Motahhir, e. g. Abdelaziz and A. Derouich, “Shading Effect to Energy Withdrawn from the Photovoltaic Panel and Implementation of DMPPT Using C Language,” *International Review of Automatic Control,* 2016.

[177] H. Singh, M. Sabry and D. Redpath, “Experimental investigations into low concentrating line axis solar concentrators for CPV applications,” *Solar Energy,* vol. 136, pp. 421-427, 2016.

[178] D. A. G. Redpath, H. Singh, C. Tierney and P. Dalzell, “An Experimental Comparison of two Solar PhotovoltaicThermal (PVT) Energy Conversion Systems for Production of Heat and Power,” *Energy and Powet,* vol. 2, no. 4, pp. 46-50, 2012.

[179] T. A. Cooper, “High-concentration solar trough collectors and their application to concentrating photovoltaics,” PhD Thesis, ETH, DISS. ETH NO. 21840, Switzerland, 2014.

[180] S. P. Philipps, A. W. Bett, K. Horowitz and S. Kurtz, “Current status of concentrator photovoltaic (CPV) technology,” Fraunhofer Institute for Solar Energy Systems ISE in Freiburg, , Germany, 2015.

[181] M. A. Green, Y. Hishikawa, E. D. Dunlop, D. H. Levi, J. Hohl-Ebinger and A. W. Y. Ho-Baill, “Solar cell efficiency tables (version 51),” *Progress in Photovoltaics 26,* vol. 26, no. 1, pp. 3-12, 2018.

[182] M. S. Y. Ebaid, A. M. Ghrair and M. Al-Busoul, “Experimental investigation of cooling photovoltaic (PV) panels using (TiO2) nanofluid in water- cetyltrimethylammonium bromide mixture,” *Energy Conversion and Management,* vol. 155, no. 1, pp. 324-343, 2018.

[183] Y. Khanjari, F. Pourfayaz and A. B. Kasaeian, “Numerical investigation on using of nanofluid in a water-cooled photovoltaic thermal system,” *Energy Conversion and Management,* vol. 122, no. 15, pp. 263-278, 2016.

[184] P. Hu, Q. Zhang, Y. Liu, C. Sheng, X. Cheng and Z. Chen, “Optical analysis of a hybrid solar concentrating Photovoltaic/Thermal (CPV/T) system with beam splitting technique,” *Science China Technological Sciences,* vol. 56, no. 6, pp. 1387-1394 , 2013.

[185] EN61730-1, “European committee for Electrotechnical Standardizations. Photovoltaic (PV) module safety qualification-Part 1: requirements for construction,” European Standard, 2007.

[186] E. 61215, “European committee for Electrotechnical Standardization. Crystalline SiliconTerrestrial Photovoltaic (PV) modules-design qualification and type approval,” European Standard, 2005.

[187] E. 61215, “European committee for Electrotechnical Standardization. Crystalline Silicon Terrestrial Photovoltaic (PV) modules-design qualification and type approval,” European Standard, 2005.

[188] EN61730-2, “European committee for Electrotecnical Standardization. Photovoltaic (PV) module safety qualification-Part 2: requirements for construction,” European Standard, 2007.

[189] E. 61646, “ European committee for Electrotechnical Standardization. Thin-film terrestrial photovoltaic (PV) modules - design qualification and type approval,” European Standard, 2008.

[190] UL1703UL, “standard for safety flat-plate photovoltaic modules and panels,” Underwriters Laboratories Inc., 2002.

[191] A. Rabl and P. Bendt, “Effect of Circumsolar Radiation on Performance of Focusing Collectors,” *Journal of Solar Energy Engineering,* vol. 104, no. 3, pp. 237-250., 1982.

[192] R. Winston, J. C. Minano, P. G. Benitez, N. Shatz and J. C. Bortz, Nonimaging Optics, Burlington: Elsevier Academic Press, 2005.

[193] G. Smestad, H. Ries and R. Winston, “The thermodynamic limits of light concentrators,” *Solar Energy Materials ,* vol. 21, pp. 99-111, 1990.

[194] C. Sangani and C. Solanki, “Experimental evaluation of V-trough (2 suns) PV concentrator system using commercial PV modules,” *Solar Energy Materials & Solar Cells,* vol. 91, pp. 453-459, 2007.

Appendix A

Table A.0.1. Sunrise, Sunset and Solar Noon for London Sep 2017

2017	Sunrise/Sunset		Daylength	Solar Noon
Sep	**Sunrise (heading)**	**Sunset (heading)**	**Length**	**Time (altitude)**
1	06:13 ↑ (76°)	19:46 ↑ (284°)	13:33:17	13:00 (46.6°)
2	06:14 ↑ (76°)	19:44 ↑ (283°)	13:29:28	13:00 (46.2°)
3	06:16 ↑ (77°)	19:42 ↑ (283°)	13:25:38	12:59 (45.9°)
4	06:18 ↑ (77°)	19:39 ↑ (282°)	13:21:48	12:59 (45.5°)
5	06:19 ↑ (78°)	19:37 ↑ (282°)	13:17:56	12:59 (45.1°)
6	06:21 ↑ (79°)	19:35 ↑ (281°)	13:14:05	12:58 (44.8°)
7	06:22 ↑ (79°)	19:33 ↑ (280°)	13:10:14	12:58 (44.4°)
8	06:24 ↑ (80°)	19:30 ↑ (280°)	13:06:22	12:58 (44.0°)
9	06:25 ↑ (81°)	19:28 ↑ (279°)	13:02:30	12:57 (43.6°)
10	06:27 ↑ (81°)	19:26 ↑ (279°)	12:58:38	12:57 (43.3°)
11	06:29 ↑ (82°)	19:23 ↑ (278°)	12:54:44	12:57 (42.9°)
12	06:30 ↑ (82°)	19:21 ↑ (277°)	12:50:51	12:56 (42.5°)
13	06:32 ↑ (83°)	19:19 ↑ (277°)	12:46:58	12:56 (42.1°)
14	06:33 ↑ (84°)	19:17 ↑ (276°)	12:43:04	12:55 (41.7°)
15	06:35 ↑ (84°)	19:14 ↑ (275°)	12:39:10	12:55 (41.4°)
16	06:37 ↑ (85°)	19:12 ↑ (275°)	12:35:16	12:55 (41.0°)
17	06:38 ↑ (85°)	19:10 ↑ (274°)	12:31:22	12:54 (40.6°)
18	06:40 ↑ (86°)	19:07 ↑ (274°)	12:27:28	12:54 (40.2°)
19	06:41 ↑ (87°)	19:05 ↑ (273°)	12:23:33	12:54 (39.8°)
20	06:43 ↑ (87°)	19:03 ↑ (272°)	12:19:39	12:53 (39.4°)
21	06:45 ↑ (88°)	19:00 ↑ (272°)	12:15:43	12:53 (39.0°)
22	06:46 ↑ (89°)	18:58 ↑ (271°)	12:11:49	12:53 (38.6°)
23	06:48 ↑ (89°)	18:56 ↑ (270°)	12:07:54	12:52 (38.3°)

24	06:49 ↑ (90°)	18:53 ↑ (270°)	12:04:00	12:52 (37.9°)
25	06:51 ↑ (90°)	18:51 ↑ (269°)	12:00:05	12:52 (37.5°)
26	06:53 ↑ (91°)	18:49 ↑ (269°)	11:56:10	12:51 (37.1°)
27	06:54 ↑ (92°)	18:47 ↑ (268°)	11:52:14	12:51 (36.7°)
28	06:56 ↑ (92°)	18:44 ↑ (267°)	11:48:20	12:51 (36.3°)
29	06:58 ↑ (93°)	18:42 ↑ (267°)	11:44:25	12:50 (35.9°)
30	06:59 ↑ (94°)	18:40 ↑ (266°)	11:40:31	12:50 (35.5°)

Table A.0.2. Sunrise, Sunset and Solar Noon for London Oct 2017

heading	**heading**		**heading**	**heading**
Oct	**Sunrise (heading)**	**Sunset (heading)**	**Length**	**Time (altitude)**
1	07:01 ↑ (94°)	18:37 ↑ (265°)	11:36:36	12:50 (35.1°)
2	07:02 ↑ (95°)	18:35 ↑ (265°)	11:32:42	12:49 (34.8°)
3	07:04 ↑ (95°)	18:33 ↑ (264°)	11:28:48	12:49 (34.4°)
4	07:06 ↑ (96°)	18:31 ↑ (264°)	11:24:53	12:49 (34.0°)
5	07:07 ↑ (97°)	18:28 ↑ (263°)	11:21:00	12:48 (33.6°)
6	07:09 ↑ (97°)	18:26 ↑ (262°)	11:17:06	12:48 (33.2°)
7	07:11 ↑ (98°)	18:24 ↑ (262°)	11:13:13	12:48 (32.8°)
8	07:12 ↑ (99°)	18:22 ↑ (261°)	11:09:20	12:47 (32.5°)
9	07:14 ↑ (99°)	18:19 ↑ (261°)	11:05:27	12:47 (32.1°)
10	07:16 ↑ (100°)	18:17 ↑ (260°)	11:01:35	12:47 (31.7°)
11	07:17 ↑ (100°)	18:15 ↑ (259°)	10:57:42	12:47 (31.3°)
12	07:19 ↑ (101°)	18:13 ↑ (259°)	10:53:51	12:46 (30.9°)
13	07:21 ↑ (102°)	18:11 ↑ (258°)	10:50:00	12:46 (30.6°)
14	07:22 ↑ (102°)	18:09 ↑ (258°)	10:46:09	12:46 (30.2°)
15	07:24 ↑ (103°)	18:06 ↑ (257°)	10:42:18	12:46 (29.8°)
16	07:26 ↑ (103°)	18:04 ↑ (256°)	10:38:29	12:46 (29.5°)

17	07:28 ↑ (104°)	18:02 ↑ (256°)	10:34:39	12:45 (29.1°)
18	07:29 ↑ (105°)	18:00 ↑ (255°)	10:30:50	12:45 (28.7°)
19	07:31 ↑ (105°)	17:58 ↑ (255°)	10:27:02	12:45 (28.4°)
20	07:33 ↑ (106°)	17:56 ↑ (254°)	10:23:14	12:45 (28.0°)
21	07:34 ↑ (106°)	17:54 ↑ (253°)	10:19:27	12:45 (27.7°)
22	07:36 ↑ (107°)	17:52 ↑ (253°)	10:15:42	12:44 (27.3°)
23	07:38 ↑ (108°)	17:50 ↑ (252°)	10:11:57	12:44 (27.0°)
24	07:40 ↑ (108°)	17:48 ↑ (252°)	10:08:12	12:44 (26.6°)
25	07:41 ↑ (109°)	17:46 ↑ (251°)	10:04:29	12:44 (26.3°)
26	07:43 ↑ (109°)	17:44 ↑ (250°)	10:00:47	12:44 (25.9°)
27	07:45 ↑ (110°)	17:42 ↑ (250°)	09:57:06	12:44 (25.6°)
28	07:47 ↑ (110°)	17:40 ↑ (249°)	09:53:26	12:44 (25.3°)
Note: hours shift because clocks change backward 1 hour.				
29	06:48 ↑ (111°)	16:38 ↑ (249°)	09:49:47	11:44 (24.9°)
30	06:50 ↑ (112°)	16:36 ↑ (248°)	09:46:10	11:44 (24.6°)
31	06:52 ↑ (112°)	16:35 ↑ (248°)	09:42:34	11:44 (24.3°)

Appendix B

International standards for Photovoltaic (PV) module and CPVs [185, 186, 187, 188, 189, 190].

International standards for PV/CPV/BIPV module	Scope/Remarks
IEC 61215	Crystalline silicon terrestrial photovoltaic modules-design qualification and type approval.
IEC 61277	Terrestrial photovoltaic (PV) power generating systems.
IEC 61345	UV test for photovoltaic (PV) modules.
IEC 61646	Thin-film terrestrial photovoltaic (PV) module-design qualification and type approval.
IEC 61701	Salt mist corrosion testing of PV modules.
IEC 61730-1	Photovoltaic module safety qualification-part-1: requirements for construction.
IEC 61730-2	Photovoltaic module safety qualification-part-2: requirements for construction.
IEC 61829	Crystalline silicon photovoltaic (PV) array on-site measurement of I–V characteristics.
IEC 61853-1	Irradiance and temperature performance measurements and power rating, which describes requirements for evaluating PV module performance in terms of power (watts) rating over a range of irradiances and temperatures.
IEC 61853-2	Spectral response, incidence angle, and module operating temperature measurements, which describes test procedures for measuring the effect of varying angle of incidence and sunlight spectra as well as the estimation of module temperature from irradiance, ambient temperature, and wind speed.
IEC 61853-3	Energy rating of PV modules, which describes the calculations for PV module energy (watt. hours) ratings.
IEC 61853-4	Define the standard time periods and weather conditions that can be utilized for calculating energy ratings.

IEC 62108	Concentrator photovoltaic (CPV) modules and assemblies - Design qualification and type approval
IEC 62670-1	Photovoltaic concentrators (CPV) - Performance testing - Part 1: Standard conditions
IEC 62670-2	Photovoltaic concentrators (CPV) - Performance testing - Part 2: Energy measurement
IEC 62670-3	Photovoltaic concentrators (CPV) - Performance testing - Part 3: Performance measurements and power rating
IEC 62716	Ammonia corrosion testing of PV modules.
IEC 62759	Transportation testing of PV modules.
IEC 62782	Dynamic mechanical load testing of PV modules.
IEC 62787 ED1	Concentrator photovoltaic (CPV) solar cells and cell-on-carrier (COC) assemblies - Reliability qualification
IEC 62804	System voltage durability test for crystalline silicon modules.
IEC TS 62989 ED1	Primary optics for concentrator photovoltaic systems
IEC 63104 ED1	Solar trackers - Safety requirements
IEC TC82 WG7	Concentrator modules - To develop international standards for photovoltaic concentrators and receivers. These standards will be in the general areas of safety, photoelectric performance and environmental reliability tests.
UL 1703	UL standard for safety flat-plate photovoltaic modules and panels.

Figure 2.8. Fermi-Dirac distribution F(E) vs. (E-E_F) MATLAB Code

```
x = -0.5:0.01:0.4;
y0 = 1./(1 + exp(x/(8.6173303*10^(-5)*0)));
y1 = 1./(1 + exp(x/(8.6173303*10^(-5)*100)));
y2 = 1./(1 + exp(x/(8.6173303*10^(-5)*300)));
y3 = 1./(1 + exp(x/(8.6173303*10^(-5)*500)));
figure
plot(x,y0,x,y1,x,y2,x,y3)
legend('K = 0','K = 100','K = 300','K = 500')
```